THE UNIVERSITY OF QUEENSLAND

AUSTRALIA

INDUCED PLURIPOTENT STEM CELLS FROM PATIENTS WITH ATAXIA–TELANGIECTASIA

SAM NAYLER (B.Sc Hons)

A thesis submitted for the degree of Doctor of Philosophy at
The University of Queensland in 2014

School of Medicine

Abstract

A-T (Ataxia-Telangiectasia) is a multi-systemic, rare genetic disorder hallmarked by predisposition to cancer, immune deficiency and most notably progressive neurodegeneration [1]. A-T results from mutation of the *ATM* gene (11q22.3). ATM is a protein kinase belonging to the phosphatidylinositol 3-kinase-like family [2]. ATM exerts control over genomic integrity by recognizing and responding to DNA damage, through phosphorylation of substrates involved in cell cycle control and DNA damage repair [1]. The ATM protein is involved with numerous cellular processes and as such, A-T represents a paradigm for neurodegenerative disorders, as well as cancer.

Experimental models of ATM function have been restricted to systems of limited context to understanding ATM biology and its potential role in development and tissue formation. Animal models have failed to faithfully recapitulate the full spectrum of A-T symptoms including the neurodegenerative aspect, which remains poorly understood. Existing human cellular models (such as fibroblasts and lymphoblastoid cell lines from patients) allow analysis of ATM in limited contextual space. Little is known about the involvement of ATM or its downstream substrates have in the mechanisms that exist to direct and protect development within the embryo. Perturbed regulation of DNA damage at critical temporal junctures within the developing embryo could lead to the progressive degenerative characteristics observed in this disorder. Further to this, accumulating evidence points to involvement of ATM in areas outside of its canonical role of orchestrating the DNA damage response including; meiosis [3], proteasome-mediated protein degradation [4], mitochondrial function [5], insulin resistance and glucose metabolism [5, 6], modulation of synaptic functions in neurons [7], vesicle trafficking [8], pentose-5 pathway signaling [9], HDAC4 localization [10] and as a sensor and responder to oxidative stress [11, 12]. Emerging evidence also suggests that ATM has tissue specific functionality and is required during development [13, 14].

hESCs (human embryonic stem cells) constitute a powerful tool for modeling of development and disease. To date only one report describes the effect of ATM knockout in hESCs by BAC-mediated transgenesis [15]. The authors show that ATM knockout results in cells that display hypersensitivy to IR (ionizing radiation) and show lack of G2M cell cycle

arrest after DNA damage, recapitulating aspects of the phenotype seen in existing cellular A-T models and demonstrating that ATM is a critical responder to DNA damage in this context. A recent technology to emerge from Japan has made it possible to reprogram terminally differentiated somatic cells, such as fibroblasts, into cells which resemble hESCs, in terms of self-renewal and their ability to generate cells of all three germ layers [16] and are so named induced pluripotent stem cells (iPSCs).

To date, studies on A-T have failed to answer the fundamental question of why certain cell types are seemingly more affected than others. As access to pluripotent stem cells becomes mainstream, it becomes possible, to a degree, to recreate and study *in vitro* processes giving rise to various cell types, including neurons, using directed differentiation protocols.

We hypothesized that ATM deficient cells may be difficult or impossible to reprogram without intervention or assistance, and that this difficulty may be at least in part due excessive levels of reprogramming-induced or existing DNA damage, to the poor growth characteristics of A-T cells or the inability to participate in certain pathways necessary for reprogramming. We show that it was indeed possible to generate iPSCs from A-T patients albeit at reduced efficiency. This thesis describes the first generation and characterization of *bona fide* iPS cells from patients with A-T. Additionally we use this model system to explore the role and functionality of ATM in an embryonic setting, showing that ATM signaling is vitally required for the maintenance of cell cycle control and DNA fidelity after DNA damage. We have defined the transcriptional landscape of pluripotent stem cells from patients with A-T and point to novel findings regarding oxidative phosphorylation pathways. Further to this, we have used this model system to explore the role of ATM in neurogenesis and neuronal activity. We provide evidence that fosters support for the theory that A-T involves aspects of mitochondrial dysfunction and explore whether calcium trafficking is defective in neurons generated from patient iPSCs. Importantly we have illustrated the proof of concept that genetic manipulation of neuronal cells is possible by delivery of full length ATM, which also restored a functional DNA damage response.

Finally, we utilized a neuronal differentiation protocol to generate neural progenitors characteristic of the developing cerebellum, and describe the transcriptome of these cells in the absence of ATM. These data present unique and novel insights into the developing A-T brain and recapitulate many of the existing findings regarding the molecular pathways that

may underpin the neurodegeneration in A-T. We speculate that this dataset will be a useful tool in understanding the growth requirements required for further expansion and study of these cell types *in vitro*, which could be harnessed to identify and screen drugs useful for the treatment of A-T patients.

Declaration by author

This thesis is composed of my original work, and contains no material previously published or written by another person except where due reference has been made in the text. I have clearly stated the contribution by others to jointly-authored works that I have included in my thesis.

I have clearly stated the contribution of others to my thesis as a whole, including statistical assistance, survey design, data analysis, significant technical procedures, professional editorial advice, and any other original research work used or reported in my thesis. The content of my thesis is the result of work I have carried out since the commencement of my research higher degree candidature and does not include a substantial part of work that has been submitted to qualify for the award of any other degree or diploma in any university or other tertiary institution. I have clearly stated which parts of my thesis, if any, have been submitted to qualify for another award.

I acknowledge that an electronic copy of my thesis must be lodged with the University Library and, subject to the General Award Rules of The University of Queensland, immediately made available for research and study in accordance with the *Copyright Act 1968*.

I acknowledge that copyright of all material contained in my thesis resides with the copyright holder(s) of that material. Where appropriate I have obtained copyright permission from the copyright holder to reproduce material in this thesis.

Publications during candidature

Nayler, S., Gatei, M., Kozlov, S., Gatti, R., Mar, J.C., Wells, C.A., Lavin, M., and Wolvetang, E. (2012). Induced pluripotent stem cells from Ataxia–Telangiectasia recapitulate the cellular phenotype. Stem Cells Transl Med *1*, 523-535. (Work from this publication appears in chapters two and three of this thesis that include additional details and experimental results).

Nayler S[1,2*], Gatei M[2], Kozlov S[2], Gatti R[4], Mar J[5], Wells C[1], Lavin M[2,3] and Wolvetang E[1]

A Human iPSC model of Ataxia–Telangiectasia recapitulates the cellular phenotype
Conference abstract and talk - ATW, New Delhi, India (2012)

Barry G, Briggs JA, Vanichkina DP, Poth EM, Beveridge NJ, Ratnu VS, **Nayler SP**, Nones K, Hu J, Bredy TW, Nakagawa S, Rigo F, Taft RJ, Cairns MJ, Blackshaw S, Wolvetang EJ, Mattick JS. The long non-coding RNA Gomafu is acutely regulated in response to neuronal activation and involved in schizophrenia-associated alternative splicing. *Molecular Psychiatry* (2013).

Briggs JA, Sun J, Shepherd J, Ovchinnikov DA, Chung TL, **Nayler SP**, Kao LP, Morrow CA, Thakar NY, Soo SY, Peura T, Grimmond S, Wolvetang EJ. Integration-free induced pluripotent stem cells model genetic and neural developmental features of down syndrome etiology. *Stem Cells* (2013).

Publications included in this thesis

Nayler, S., Gatei, M., Kozlov, S., Gatti, R., Mar, J.C., Wells, C.A., Lavin, M., and Wolvetang, E. (2012). Induced pluripotent stem cells from Ataxia–Telangiectasia recapitulate the cellular phenotype. Stem Cells Transl Med *1*, 523-535. - Work from this publication appears in chapters two and three of this thesis that include additional details and experimental results.

Contributor	Statement of contribution
Sam Nayler	Conception and design (50%), Collection and assembly of data (90%), Data analysis and interpretation (75%), Manuscript writing (90%)
Magtouf Gatei	Collection and assembly of data (1%)
Sergei Kozlov	Collection and assembly of data (2%)
Louise Marquart	Data analysis and interpretation (1%)
Richard Gatti	Collection and assembly of data (1%)
Jessica Mar	Collection and assembly of data (5%), Data analysis and interpretation (10%), Manuscript writing (2%)
Christine Wells	Data analysis and interpretation (1%), Final approval of manuscript
Martin Lavin	Conception and design (25%), Financial support, Provision of study material/patients, Data analysis and interpretation (6%), Manuscript writing (2%), Final approval of manuscript
Ernst Wolvetang	Conception and design (25%), Financial support, Provision of study material/patients, Collection and assembly of data (1%), Data analysis and interpretation (7%), manuscript writing (6%), Final approval of manuscript.

Contributions by others to the thesis

Chapter 2.0 – Generation and characterization of lentivirally generated A–T iPSC
Ernst Wolvetang and Martin Lavin: Conception and design (50%), Data analysis and interpretation (10%), Manuscript writing (10%); Sam Nayler: Conception and design (50%), Collection and assembly of data (90%), Data analysis and interpretation (90%) Manuscript writing (90%); Jian Sun: Collection and assembly of data (3%); Stemcore: Collection and assembly of data (2%).

Chapter 3.0 – iPS cells from patients with Ataxia–Telangiectasia recapitulate the cellular phenotype
Ernst Wolvetang and Martin Lavin: Conception and design (50%) Data analysis and interpretation (10%), Manuscript writing (10%); Sam Nayler: Conception and design (50%), Collection and assembly of data (88%), Data analysis and interpretation (78%) Manuscript writing (89%); Magtouf Gatei: Collection and assembly of data (1%); Sergei Kozlov: Collection and assembly of data (3%); Louise Marquart: Data analysis and interpretation (1%); Richard Gatti: Collection and assembly of data (1%); Jessica C Mar: Data analysis and interpretation (5%), Manuscript writing (1%); Christine A Wells: Data analysis and interpretation (2%); Jian Sun: Collection and assembly of data (2%), Data analysis and interpretation (2%).
Jason Cullen; Collection and assembly of Data (3%), Data analysis and interpretation (2%); Jian Sun: Collection and assembly of data (1%) Provision of study material/patients; Katia Nones: Collection and assembly of data (1%)

Chapter 4.0 – A basic model for neurogenesis in A–T derived iPS cells
Ernst Wolvetang and Martin Lavin: Conception and design (47.5%) Data analysis and interpretation (10%), Manuscript writing (10%); Sam Nayler: Conception and design (47.5%), Collection and assembly of data (95%), Data analysis and interpretation (80%) Manuscript writing (90%); James Briggs: Conception and design (5%); Margreet Ridder; Collection and assembly of data (1%), Irina Vetter; Collection and assembly of data (3%), Alejandro Hidalgo Gonzalez; Collection and assembly of data (1%).

Chapter 5.0 – A developmentally relevant model system for Neurogenesis in A–T

Ernst Wolvetang and Martin Lavin: Conception and design (50%) Data analysis and interpretation (10%), Manuscript writing (10%); Sam Nayler: Conception and design (50%), Collection and assembly of data (90%), Data analysis and interpretation (70%) Manuscript writing (85%); Darya Vanichkina; Collection and assembly of data (10%), Data analysis and interpretation (20%), Manuscript writing (5%).

Statement of parts of the thesis submitted to qualifty for the award of another degree

None

Acknowledgements

At the start of my undergraduate degree, someone very wise told me to treat my studies as if they were a job and to simply make the decision to try and be the best at whatever task was in front of me. These words have had an enormous impact on shaping my outlook on the challenges, successes and failures that I have faced over the last four years. I have found that life in general requires a thick skin, but this is especially true in the world of science, where we must make ourselves utterly resilient in the face of constant difficulty and embrace the continual search for clarity, criticism and self-improvement. I am pleased and thankful to have enjoyed these challenges, successes and failures with the people in my life.

Nilay Thakar — you have been a constant companion, competitor, collaborator and friend. My time in the lab would certainly not have been the same without you. Please take care near large bodies of water.

Ernst Wolvetang, who refers to me as Samwise, you are truly Gandalf the wizened wizard by comparison. You have helped me on the road to becoming the scientist that I aspire to be. I have deeply appreciated your presence on this adventure and value your indomitable spirit, thirst for knowledge, but above all, your unending generosity and kindness.

Jian–Sun, you truly have kept the lab together with your organizational skills and tireless work ethic. You make the success of many people possible through your hard work.

Alejandro-Hidalgo Gonzalez, your analytical approach to problem solving and willingness to give up your time to help others, expecting nothing in return, inspired me greatly. James Briggs — the only word that comes to mind is paragon. Your insight is boundless and I was glad to share but a small part of it. Patrick Fortuna, when you arrived in the lab, I knew we would be friends for a long time. Many of us are moving on and we leave the lab in your capable hands. Owen Hawksworth, you always had a fresh perspective and I enjoyed our brainstorming sessions. Steve Dingwall, your thirst for scientific knowledge is second only to your thirst for tasty (or available) beer. You contribute greatly to making the group smarter as a whole. Samah Alharbi and Suad Alateeq, you are two of the toughest and most determined women that I know.

To all the other members of the Stem cell engineering group (and by extension Tissue engineering and microfluidics) in its current and previous forms (Rachel, Stu, Drew, Betty, Jenny, Vani, Dmitry, Dee, Suad, Lauren, Jack, Paul, Tania, Jess, Huaying, Nick, Benoit and any anyone else I may have forgotten) thank you for making the lab an excellent place to be. To everyone else at UQ and QIMR (Tara, Aine, Romal, Hazel, Abrey, Amanda, Olivier, Magtouf & John) who helped, whether in the lab or just making life in general more pleasant, thank you. I must extend massive appreciation to the people who have assisted with statistics (Louise Marquadt) and the black art of Bioinformatics (Jess Marr, Christine Wells, Ryan Taft, Rowland Mosbergen, Othmar Korn & Darya Vanichkina).

Sergei Kozlov, thank you for your commitment and persistence on all fronts. Martin Lavin, thank you for providing the opportunities that you have. Jason Cullen - if I ever reach even half of the talent and scientific rigor you possess I will consider this a great achievement - thank you for all your help in the lab and advice besides.

To the Roebig family and BrAshAT, you are a constant reminder why we do what we do. Thank you for all your support and inspiration.

To everyone at Ronin Jiujitsu and the UQ MMA club, especially Stefan, John, Jarek, Amir, Chris and Ryan, thank you for providing an escape and outlet from the scientific world and teaching me lessons that extended well beyond the mat.

Finally, and most importantly — to my beloved family. To my brother Ben, your unwavering help and support in all things helped me get across the line. I could not have done this without you. To my father Gary and mother Jenny, you continue to be the biggest sources of inspiration in my life. Gary you are the most patient person that I know. Jenny, you have and always will teach me important lessons. To my partner Cora, thank you for making the sacrifices that you have and always giving me your support.

Keywords

Induced pluripotent stem cells, pluripotency, DNA damage, cell cycle, ATM, Ataxia–Telangiectasia, neurodegeneration, disease model, cerebellar neurogenesis

Australian & New Zealand standard research classifications (ANZSRC)

100404 Regenerative medicine (incl. Stem cells and tissue engineering) – 50%

060103 Cell development, proliferation & death – 25%

110902 Cellular Nervous System – 25%

Fields of Research (FoR) Classification

0601 Biochemistry and cell biology – 100%

"*From the standpoint of daily life, however, there is one thing we do know: that we are here for the sake of each other - above all for those upon whose smile and well-being our own happiness depends, and also for the countless unknown souls with whose fate we are connected by a bond of sympathy. Many times a day I realize how much my own outer and inner life is built upon the labors of my fellow men, both living and dead, and how earnestly I must exert myself in order to give in return as much as I have received.*"

-Albert Einstein

Table of contents

List of abbreviations

ATM – Ataxia–Telangiectasia-Mutated

ATP – Adenosine TriPhosphate

ATR – Ataxia–Telangiectasia-Related

A–T – Ataxia–Telangiectasia

BER – Base excision repair

Brdu – Bromodeoxyuridine

CCCP - Carbonyl cyanide *m*-chlorophenyl hydrazone

CldU – Chlorodeoxyuridine

CNS – Central Nervous System

CTMIO - 5-carboxy-1.1.3.3-tetramethylisoindolin-2-yloxyl

DAPI – 4',6-diamidino-2-phenylindole

DMEM – Dulbecco's minimal essential medium

DMSO - Dimethylsulfoxide

DSB – Double strand break

EB – Embryoid body

ECM – Extra-cellular matrix

FAT - FRAP-ATM-TRRAP

FCS – Fetal calf serum

FGF – Fibroblast growth factor

FLIPR - Fluorometric imaging plate reader

GC – Granule cell

HEAT - Huntington Elongation factor 3 protein phosphatase 2A PI3-kinase Tor1

HB – Hindbrain

hESC – Human embryonic stem cell

HRR – Homologous repair & recombination

IEG – Immediate early gene

IdU – Ioxodeoxyuridine

IPA – Ingenuity Pathway Analysis

iPSC – Induced pluripotent stem cell

IR – Ionizing radiation

IsO – Isthmic organizer

KD - Kinase Domain

KEGG – Kyoto Encyclopedia of Genes and Genomes

KSR – Knockout serum replacement

MEF – Mouse embryonic fibroblast

MHB – Mid-hind brain

MMP – Mitochondrial membrane potential

MR – Mismatch repair

mtDNA – Mitochondrial Deoxyribonucleic Acid

NBS1 – Nijmegen's breakage syndrome

NER – Nucleotide excision repair

NHEJ – Non-homologous end joining

PC – Purkinje cell

PD – Parkinson's disease

PNS – Peripheral nervous system

PRD - PIKK-regulatory domain

RA – Retinoic acid

RDS – Radioresistant DNA synthesis

ROS – Reactive Oxygen species

SCID – Severe combined immunodeficiency

TMRM – Tetramethylrhodamine, methyl ester

TUNEL – Terminal deoxynucleotidyl tansferase mediated dUTP Nick End Labelling

1.0 Literature review

1.1 History of embryonic stem cell research

International stem cell research has endured a tumultuous past that has been plagued with a host of technical, ethical and political complications - many of these played out in the American political arena, which has set the world stage for this area of research. Since the early 1970s, The American Congress has imposed bans and restrictions on federally funded embryonic and fetal tissue research that have been continually contested, overturned and appealed. Despite this, extensive progress has been made on a number of fronts including the first clinical trial of hESC (human embryonic stem cells) for treatment of acute spinal injuries (Geron, 2009). hESCs serve extensively as disease models where they are useful in understanding development and also facilitate the procurement of cells and tissues that are normally difficult to acquire. Recently the remarkable finding that terminally differentiated somatic cells could be reprogrammed to an embryonic-like state emerged from the laboratory of Shinya Yamanaka in Kyoto, Japan [16].

hESCs are harvested from the developing embryo five days post fertilization, resulting in destruction of this embryo. These cells are derived from the inner cell mass (ICM) of the blastocyst, an embryonic structure comprising approximately 100 cells and that represent an intermediate stage between the morula (a clump of cells which grows by embryonic cleavage) and the gastrula (in which germ layers begin to form and organize before organogenesis) (See Figure 1.1). hESCs are pluripotent, meaning that they are capable of differentiating into cell and tissue types from all three germ layers (ectoderm, mesoderm and endoderm) that go on to constitute the entire human body. As well as this, hESCs are theoretically capable of infinite self-renewal [17]. hESCs differ from adult stem cells which reside within the human body in stem cell ‘niches’ and are referred to as multipotent.

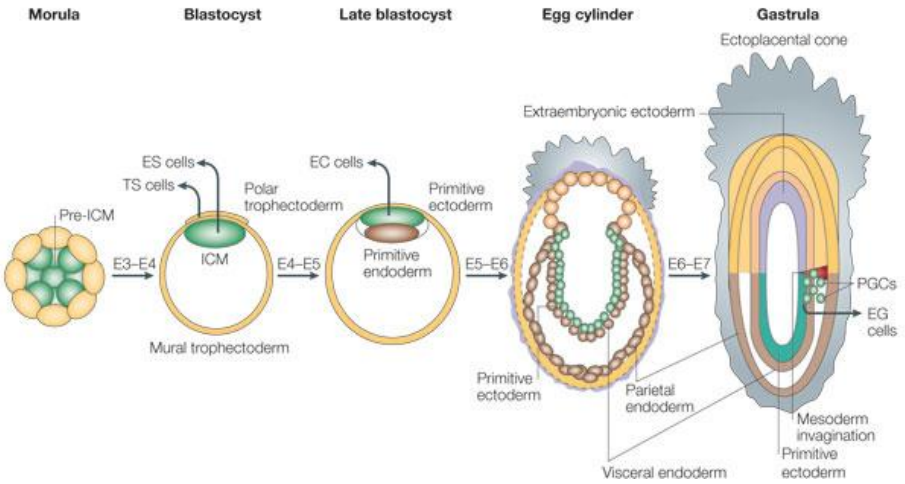

Figure 1.1 **–** Embryonic stem cells are harvested from the inner cell mass of a blastocyst. These cells are pluripotent, meaning they can form any cells or tissue within the human body (with the exception of the placenta). Figure adapted from [18].

In 1998, a group led by James Thomson published for the first time, a method for isolation and propagation of hESC using *in vitro* culture methods [17]. Following on from Gail R Martin's work in mouse embryonic stem cells [19], and pioneering work in hESC isolation [20], Thomson and colleagues showed that hESCs isolated from IVF-donated embryos cultured to the blastocyst stage could be expanded on mitotically-inactivated mouse embryonic fibroblasts. These cells were described as possessing a *'high ratio of nucleus to cytoplasm, prominent nucleoli, and a colony morphology similar to that of rhesus monkey ES cells"* [17]. In addition, they were shown to have 46, XX & XY karyotypes, and the capability of extended growth in culture, free from signs of replicative crisis. Notably, a high level of telomerase expression was observed in these cells. Telomerase expression is associated with cell immortality and normally absent in diploid somatic cells [17].

Because of their ability to self-renew and differentiate into other cell types, ESCs have long been touted as a panacea to a range of congenital and acquired illnesses. In reality their utilization has largely been as a research tool for examining development and disease, although these two issues are inextricably intertwined. ESCs were recently used to treat Stargardt's Macular Dystrophy and age-related macular degeneration with promising results [21]. A range of

technical, ethical and political challenges exist with respect to their ongoing use and this has spurred researchers to investigate alternate sources of pluripotent stem cells.

Given their provenance, a major limitation of ESCs is immune rejection of ESC based grafts by the host, potentially limiting their clinical relevance. Currently, a theoretical therapy might hope to replace a damaged cell or tissue type that is subsequently recognized by the body as foreign and targeted by the immune system, with major implications for the health of the patient and success of the graft. While immunologists seek to further understand or circumvent this process by either deleting MHC molecules from the hESCs [22] or re-educating the host immune system, a simpler solution would be to harness tissue originating from the host. One strategy proposed to circumvent graft rejection is the use of Somatic cell nuclear transfer (SCNT), in which an enucleated egg from a donor is injected with the nucleus of a patient, resulting in a blastocyst which is genetically compatible with the donor from whom it is taken [23]. This process however is complex, labor intensive and while it addresses certain ethical and technical issues, it is not without those of its own, including the acquisition of donor eggs and the intrinsic low efficiency of the process.

1.2 Discovery of induced pluripotent stem cells

In 2006, a breakthrough emerged from a laboratory in Kyoto, Japan [16]. Yamanaka and Takahashi demonstrated that it was possible to return terminally differentiated cells back to a pluripotent state using novel methodology. This was achieved through combinatorial screening of 24 important stem cell genes, introduced into mouse fibroblasts using retroviruses and subsequent antibiotic selection linked to the *Fbx15* locus, which is associated with an undifferentiated embryonic state [24]. The Yamanaka group uncovered a combination of transcription factors, *Oct4*, *Sox2*, *c-Myc* and *Klf4* which when introduced into mouse fibroblasts and combined with proper culture conditions, gave rise to cells remarkably similar to ESCs, which he called induced pluripotent stem cells (iPSCs). The process is depicted in figure 1.2. Although these cells initially failed to produce chimaeric offspring and still maintained certain residual epigenetic artefacts of origin, they displayed many of the characteristics of ESCs [16]. This study paved the way for an explosion of interest into the field.

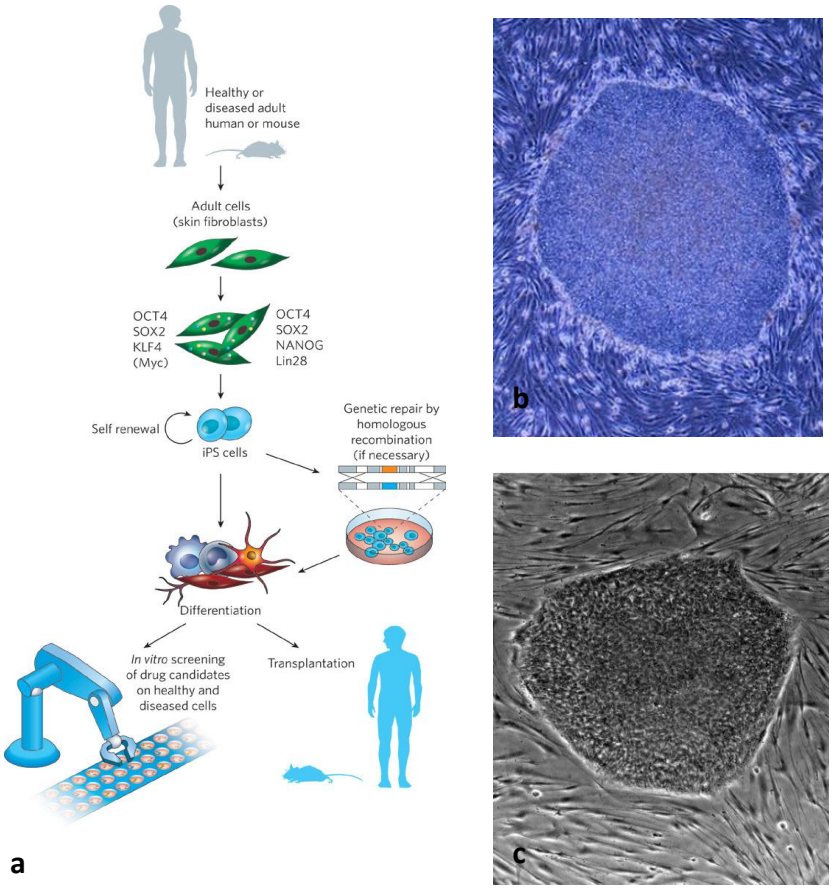

Figure 1.2 - a) Diagramatic representation of the iPSC generation process, including harvesting tissue from healthy/diseased patient, establishment of fibroblasts, introduction of reprogramming factors and downstream analysis b) induced pluripotent stem cell colony c) human embryonic stem cell colony. Figure a is adapted from [25]. Figure b from [26]. Figure c from Wikipedia commons.

The following year, Yamanaka and colleagues published a follow-up work outlining successful generation of mouse iPSCs that could form chimaeras and had an epigenetic profile at certain loci resembling that of embryonic stem cells, by using a modified selection strategy [27]. This study was accompanied by two independent publications reporting similar findings [28, 29]. Translation to a human clinical situation was alluded to cautiously, with the finding that one of

the reprogramming factors *c-Myc* (a known oncogene) caused cancer in one in five mice. *c-Myc* was proven to be dispensable for reprogramming, at the cost of greatly reduced efficiency [30].

Later that year, both Yamanaka and another group (led by Jamie Thomson) would independently reach the same conclusion – that it was possible to adapt this system for use with human cells [31, 32]. Jamie Thomson led work that closely resembled that of Yamanaka but instead used a lentiviral based delivery system and substituted two different reprogramming factors, *Lin28* and *Nanog*, in place of *Klf4* and *c-Myc*. Yamanaka had made the most significant discovery in regenerative medicine since the discovery of embryonic stem cell isolation and culture, by essentially showing that it was possible to re-awaken the dormant endogenous pluripotentcy network in a terminally differentiated cell. In addition to drastically changing the way in which the field regarded pluripotency and cell state, this discovery held promise in addressing two of the major hindrances associated with embryonic stem cell research - the ethical and political issues in destruction of embryos and also the issue of tissue sourcing with regards to donor compatibility and immune rejection of allogeneic tissue.

Numerous variations and combinations of the reprogramming factors have since been used to generate iPSCs in a range of human and animal cellular models, with a myriad of results (See Figure 1.3). Fears for the feasibility of these retrovirally derived cells as a clinical tool have driven approaches to generate iPSCs free from viral integration sites including the use of Adenovirus [33], Cre/LoxP excisable elements [34], tagged proteins [35], episomal vectors [36], RNA [37, 38] and recently a piggyBac transposon system [39]. These systems have reported a wide variety of results including variable reprogramming efficiency and reproducibility.

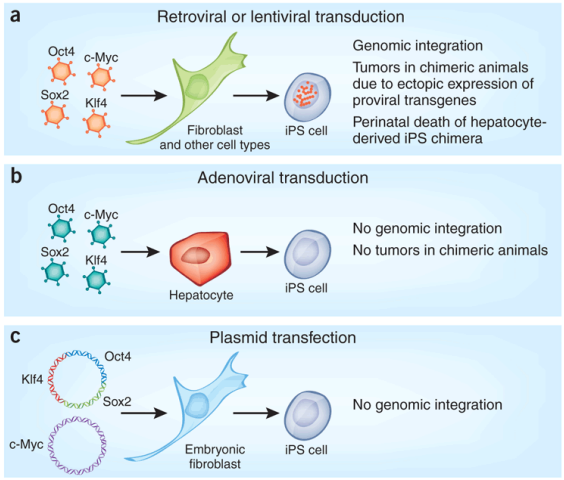

Figure 1.3 – Comparison of three different methodologies to generate iPSC a) Retroviral transduction uses viral particles to randomly integrate copies of transgene into the genome b) Adenoviral transduction uses non-integrative infection to deliver reprogramming factors c) Plasmid transfection uses episomes to deliver reprogramming factors to target cells. Image adapted from [25].

It is now widely accepted that potential utilization of iPSCs as clinical entities will require non-integrating methodologies which do not rely on transgene insertion into the genome. A separate issue remains the current lack of understanding of the process that drives this reversion to pluripotency and consequently, the degree or completeness to which cells are reprogrammed. Accumulating evidence suggests that iPSCs must overcome a barrier to be reprogrammed and in doing so undergo a genome-wide epigenetic remodeling, which may happen to various degrees based on a number of criteria including culture conditions, starting material and method of reprogramming [40, 41]. Interestingly, it was shown that iPSC possessed an 'epigenetic memory' of their tissue type of origin, and that this epigenetic state could modulate the ability of iPSC to differentiate effectively into certain tissues/lineages [42].

1.3 Utilization of induced pluripotent stem cells

Owing to the fact they have been synthetically derived and propagated in continuous culture, and also the fact that there has been no comprehensive definition of what is a truly reprogrammed iPSC, concerns remain which still prohibit these cells from being utilized in clinical settings. iPSCs are however, now widely being used as models for human disease and development, in an effort to further understand the onset and pathogenesis of a range of disorders, from schizophrenia [43] to amyotrophic lateral sclerosis [44] (See Figure 1.4).

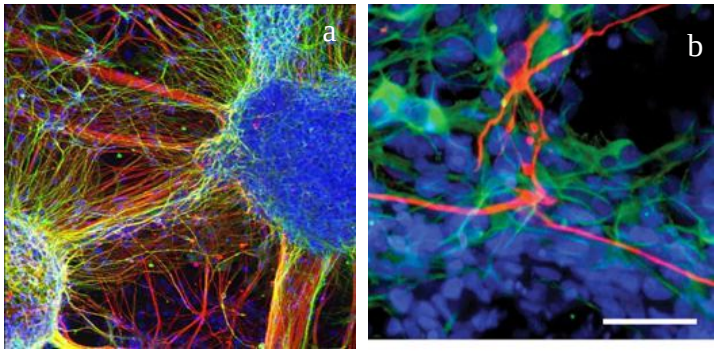

Figure 1.4 – a) Neurons generated from a patient with Schizophrenia [43] b) Motor neurons generated from patients with ALS [44].

The precise number of hESC lines worldwide is indeterminate but believed to exceed 100, each of which possesses a certain distinct genetic background. iPSC technology has made it possible to generate the hESC equivalent from patients with various genetic backgrounds and diseases, with relative ease. This now allows for more accurate, patient-specific modeling of diseases, and takes into account genomic contexts of mutations, rather than conventional gene knockdown methodology. iPSCs are model systems which can be differentiated into a range of tissue types which may help address problems associated with obtaining suitably relevant material for studying specific diseases. For example, it is not always feasible or possible to obtain relevant biopsied material from living patients, but propagated cells from a relatively painless skin biopsy can be reprogrammed to generate iPSCs, and then differentiated into the desired cell type to study. Recently it has been shown that a vast array of cell types can be reprogrammed, including

blood [45], dermal papilla from hair follicles [46] and even renal tubule cells extracted from urine [47]. This might provide a system to generate easily sourced and immunologically matched tissue that could be re-implanted with lessened chance of immune rejection than tissue derived from an unrelated donor embryo. Additionally, the process by which these cells take in differentiating can be scrutinized and may reveal insights into development and disease pathology.

1.4 Pluripotent cells in modeling development and disease

Just as mice and humans share significant genetic homology, mouse and human stem cell research shares many similarities. Mouse embryonic stem cell research is free from many of the ethical and technical experimental constraints that surround human research (ie generation of chimaeras, tissue transplantation). To understand the state of current ESC research, both must be viewed critically. There are many gaps in our understanding of human ESC behavior where mice must stand in and available information must be appraised. In many cases mice provide relevant models with which to study human disease, however due to large cross-species differences in processes such as neurogenesis, direct comparison between mouse and humans with respect to neural pathology is often not suitable [48].

Pluripotent stem cells hold enormous potential for aiding our understanding of development of the body and the onset and molecular basis of disease. The defining feature of embryonic stem cells, the ability to form any cell of the human body, has allowed researchers to direct these cells into targets of interest to study and those that may have clinical relevance. Researchers in this field have made numerous achievements, but in keeping with brevity and relevance, this document will focus mainly on studies relating to neural development, given its relevance to A–T and this work.

1.4.1 Models of neurological disease

The two main constituents of the human nervous system are the CNS (central nervous system), largely comprised of the brain and spinal cord and the PNS (perhipheral nervous system), the nerves and ganglia outside of the brain and spine.

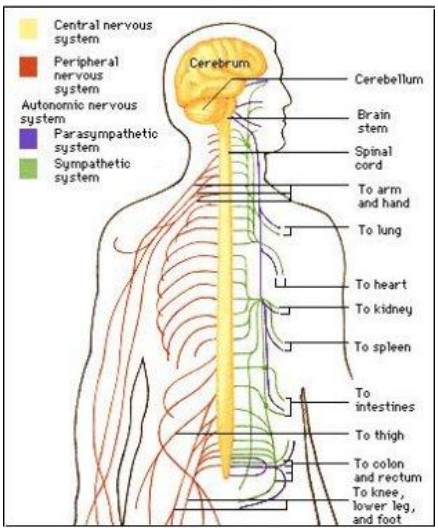

Figure 1.5 – The CNS is comprised of the brain and spinal cord, while the PNS consists of nerves and ganglia outside this area**.** Figure adapted from http://universe-review.ca/R10-16-ANS.htm

ESCs have been used to artificially recreate several of the complex cell types from the CNS, especially the brain, for study or transplantation therapy purposes aimed at restoring lost functionality. The problem with respect to these approaches is determining how ESCs can be efficiently directed towards the specific cell type of interest. In many cases of transplantation therapy, groups have attempted to implant undifferentiated ESCs, with variable and sometimes dangerous results [49, 50]. In past instances this has resulted in tumour formation and so a strategy to bypass this has been to reduce the tumorigenic potential by partially or fully differentiating the cells to be transplanted into a committed cell type or an upstream precursor. A prime example of this is shown in recent work on Parkinson's disease (PD)[51, 52]. PD is associated with the loss of dopaminergic neurons from the substantia nigra, which secretes dopamine to regulate cortical and thalamic behavior – defects in which cause the symptoms associated with PD, such as loss of motor control and dementia [53]. To safely replace the damaged cell type by transplantation would be the gold standard for treatment of this disorder; however to do this completely has remained elusive. Although these studies have shown some level of efficacy, they bring to light several of the limitations of current technologies, being safety and our knowledge of manipulation of this technology including efficiency and functional

incorporation of transplanted material. While iPSCs and their derivatives serve as viable disease models to study onset and treatment of disease, their use in the clinic may still be far away.

1.4.2 Additional induced pluripotent stem cell disease models including chromosomal instability syndromes

An increasing number of diseases have been modeled using iPSC technology including diabetes type 1 [54], Parkinson's [55], Amyotrophic lateral sclerosis [44], spinal muscular atrophy [56], Rett syndrome [57], Huntington's [58] amongst a long list of others.

Two papers explored iPSC models of complex and multisystemic disease relating to chromosomal instability syndromes; Friedreich Ataxia (FRDA), an autosomal recessive disorder caused by trinucleotide (GAA) repeat expansion in the *FXN* gene and involving cardiomyopathy and neurodegeneration [59, 60], as well as Fanconi anaemia – caused by mutations in genes from the FA pathway and involving bone marrow failure and other malignant developments [61]. iPSC modeling of Friedrich Ataxia demonstrates the underlying promise of this technology. FRDA is manifested most notably in neuronal and cardiac cells, resulting in ataxia and cardiomyopathy respectively. Liu et al. were able to demonstrate that iPSC could be generated from two patients and subsequently differentiated into the cell types affected in FRDA; sensory neurons from the dorsal root ganglia and representative cardiomyoctes. Both the iPSCs and the differentiated cells recapitulated the disease-causing reduction in FXN protein level. This has provided a model that may allow for deeper insights into the progression of this disease, which is poorly understood. Part of this is due to the fact that animal models of FRDA do not fully recapitulate the symptoms seen in human patients [62, 63], and so in addition to revealing developmental insight into this disorder, this technology may provide a relevant and useful system for the screening of drugs that could be used to treat FRDA patients.

1.5 Ataxia–Telangiectasia

Another autosomal recessive ataxia, the focus of this document, is Ataxia–Telangiectasia (A–T)- named so because of the ataxia (prominent unsteady gait), and oculocutaneous telangiectasia (the dilation of blood vessels around the eyes) [64].

1.5.1 Symptoms and underlying etiology of A–T

Patients with A–T suffer from radiosensitivity, predisposition to malignancies (particularly lymphomas), infertility, elevated risk of diabetes type 1, immune deficiency and pronounced cerebellar degeneration [65]. Because of this, most A–T patients are wheelchair bound by their early years, and many do not live beyond the age of 20, with sinopulmonary infections and cancer being the leading cause of mortality [66]. The multisystemic nature of A–T has caused some speculation about the potential for ATM involvement in activities other than DNA damage response. While the nuclear localization and involvement of ATM in response to DNA damage has been extensively characterized, and loss of this activity correlated with chromosomal breakage and malignancy, several groups have postulated theories and provided evidence that explain the symptoms of A–T which might fall outside of this paradigm. These include involvement of ATM in meiosis [3], proteasome-mediated protein degradation [4], insulin resistance and glucose metabolism [5, 6], modulation of synaptic functions in neurons [7], vesicle trafficking [8], pentose-5 pathway signaling [9], HDAC4 mislocalization [10] and most recently as a sensor and responder to oxidative stress [11, 12, 42]. Perturbation of ATM may disrupt these processes resulting in the symptoms observed in A–T, however the exact mechanisms in doing so are unclear.

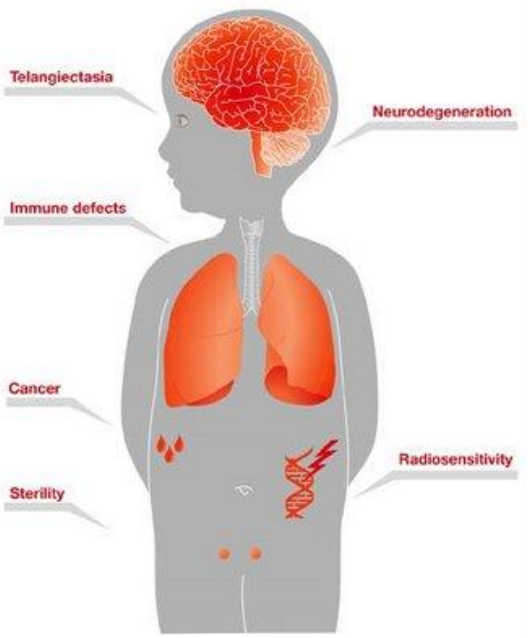

Figure 1.6 – Schematic representation of A–T symptom manifestation; Telgangiectasia affecting the eyes, Neurodegeneration affecting the brain/cerebellum, systemic radiosensitivity, immune defects and cancer, sterility in the gonads [67].

1.5.2 ATM & the and molecular basis of A–T

A–T is caused by mutational inactivation of the *ATM* gene, which was localized to 11q22-q23 in 1988 [68] and first cloned and identified in 1995 [69]. *ATM* belongs to the phosphatidylinositol 3-kinase like (PIKK) family of serine threonine kinases that also includes *ATR* ('Ataxia–Telangiectasia Mutated and Rad3 related'), *DNA PKcs* ('DNA-dependent protein kinase catalytic subunit') and hSMG-1 [70], all of which are involved with DNA repair. ATM also shares homology with *tel1* and *rad3* in yeast and the *TOR* genes in yeast/mammals that are involved with cell cycle progression and meiotic recombination [71]. The ATM protein is comprised of five domains, containing from (N-C terminus) HEAT (**H**untington **E**longation factor 3 protein phosphatase 2**A** PI3-kinase **T**or1), FAT (**F**RAP-**A**TM-**T**RRAP), KD (**K**inase **D**omain), PRD (**P**IKK-**r**egulatory **d**omain) and FATC domains. The HEAT domain is known to function by binding to NBS1, another DNA damage surveillance protein. The FAT domain is theorized tointeract with the KD in ATM to enhance stability of the C-terminus of the protein.

The KD is responsible for the extensive kinase activity of ATM, which is regulating by PRD and FATC domains.[72].

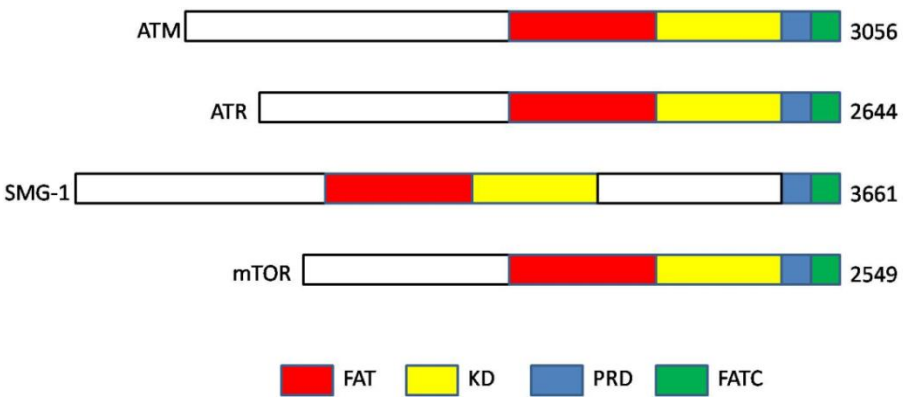

Figure 1.7 – ATM protein shares homology with ATR, SMG-1 and mTOR, containing FAT (**F**RAP-**A**TM-**T**RRAP), KD (**K**inase **D**omain), PRD (**P**IKK-**r**egulatory **d**omain) and FATC domains. Also present towards the N-terminus but not shown, the HEAT (**H**untington **E**longation factor 3 protein phosphatase 2**A** PI3-kinase **T**or1) domain. Figure taken from Cellular Biochemistry II.

ATM is involved with the response to DNA damage by phosphorylating a large number of substrates to control the cell cycle and initiate DNA damage repair [65, 73].

1.5.3 Animal and cellular models of A–T

A wealth of research exists on A–T, however much is still unknown about the true nature of this disease. As with the case of FRDA, A–T animal models [74] have failed to accurately recapitulate the full spectrum of symptoms from this disorder - while mouse models of A–T demonstrate sterility, predisposition to malignant developments, neurologic manifestations, radiosensitivity and checkpoint signaling aberrations, they fail to reliably reproduce the most pronounced and debilitating aspect of A–T, which is the ataxia thought to arise from the loss of Purkinje cells (PCs) and granule cells (GCs) in the cerebellum [75]. Human cellular models of

A–T exhibit hypersensitivity to radiation, defective cell cycle arrest (G1, G2 and intra-S-phase radioresistant DNA synthesis) as well as culture stress and predisposition to chromosomal breakage and aberrations [73]. ATM has been shown to be largely nuclear in fibroblasts [76], while evidence points to some cytoplasmic localization in neuronal cell types [13, 14] indicating that ATM might play varying roles in different cellular contexts. Animal models are able to provide the opportunity to study ATM in integrated and differing cellular contexts, however the cross-species differences have prevented this approach from yielding answers that are vital – such as the reason for why some A–T symptoms are specifically manifested in certain cell types and not others. Access to pluripotent stem cells may help bridge this gap by offering insight into the relationship that ATM has with development and networks in a cell-type specific manner.

1.5.4 Potential for modeling A–T in induced pluripotent stem cells

Conventional disease models, such as fibroblasts and lymphoblastoid cell lines are restricted to demonstrating a limited range of contextual information which may be only partially relevant to the actual disease phenotype. This is why pluripotent stem cells are useful, as they allow the examination of what might be a valid model for the development of the embryo with respect to a particular disease, but also the unfolding of processes that occur downstream, such as neurogenesis, hematopoiesis and cardiogenesis. An embryonic knockout model of ATM could be expected to closely resemble the processes that occur during blastocyst stage, allowing insight into what role ATM might have in this and subsequent developmental contexts. ATM is a known DNA damage regulator and is extensively characterized in somatic cell models [73, 75, 77], however due to the technical and ethical constraints of working with such models, very little is known about the function of ATM in an embryonic context.

1.6 The cell cycle and DNA damage in pluripotent and somatic cells

Pluripotent stem cells must preserve their genome, as unrepaired damage will be passed on to daughter cells. This is achieved in three distinct ways; up-regulation of DNA-repair processes, increased efficiency of DNA repair and removal of cells from the pluripotent pool by either apoptosis or differentiation [78].

To focus on the canonical role of ATM as a key player in protection of the genome as a transducer of DNA damage and cell cycle signaling in ESCs is a logical, but complicated place to start. Any system that is artificially cultivated *ex vivo* is at risk of developing karyotypic abnormalities, however it seems that there is a large burden of proof on ESCs and iPSCs in this regard, which may be in part due to the manner in which they are perceived as potential clinical entities. ESCs and iPSCs are by their very nature, culture artefacts and are propagated in highly synthetic conditions meaning that karyotypic abnormalities are bound to arise, and even as relevant precautions are taken, must be considered as transient or fragile models.

The involvement of ATM in an embryonic context is only recently receiving attention. ATM has been demonstrated to activate signaling pathways in ESCs and iPSCs in response to DNA damage [79-81] and to be vital for G2M arrest in hESCs after introduction of DNA damage by treatment with IR [15, 80], however IR may not accurately represent the normal levels and type of DNA damage which occur within the cellular environment.

Several recent findings highlight the phenomena of elevated levels of DNA damage signaling and repair gene expression in ESCs and iPSCs in comparison to somatic cells, which was attributed to the elevated need for protection of the genome [79, 82]. Maintaining a stable genome within the developing embryo is an important requirement for the survival and viability of an organism – similarly, the stability of ESCs and iPSCs relate directly to their applicability as clinical entities and disease models. Recent work outlines the high degree of similarity in response to DNA damage between ESCs and iPSCs with respect to cell cycle arrest, double strand break repair and gene expression [79]. Further to this, it was illustrated that pluripotent and somatic cells utilize DNA damage repair pathways via distinctly different methods which makes sense given the different nature of these cells and their requirements for growth [83]. It has been suggested that ESCs primarily utilize HRR (homologous repair and recombination) rather than error prone NHEJ (non-homologous end joining), which is supported by the observation of 10-fold higher formation of RAD51 foci in ESCs when compared to differentiated astrocytes [84]. HRR is dependent on sister chromatids for repair templates - as

ESCs spend 70% of their time in S and G2M phase, they are more easily able to initiate this more stringent form of repair [79]. ESCs have a doubling time of approximately 20-30 hours [85] and cycle rapidly due to an abbreviated G1 phase and facilitated G1 to S transition [86]. Due to this accelerated rate of DNA replication and also mitotic division, ESCs and iPSCs may be at a greater risk of replication errors, especially in the context of genomic instability syndromes, such as A–T. In somatic cells, ATM phosphorylates p53 to arrest G1/S cell cycle transition in the presence of DNA damage [87] however this mechanism functions differently in ESCs because they lack a conventional restriction point in late G1 [88]. Filion et al.showed that ESCs lack a conventional G1 checkpoint in response to IR [81, 89]. This group and others [15, 80] show supporting data and demonstrate that ESCs arrest in the G2 phase after IR in an ATM dependent manner.

Numerous papers report that ESC are hypersensitive to environmental insult, resulting in elevated levels of apoptosis [90, 91]. Filion et al.demonstrated that ESCs undergo caspase-related mitochondrial apoptosis, demonstrating a mechanism for the removal of irreparably damaged cells [81].

Due to the highly stringent need for faithful repair and fidelity within the embryo, there may be several levels of inbuilt redundancy that exist to take over in the absence of ATM. This is evidenced by findings that a BAC recombineered ATM knockout hESC line maintained normal karyotype for extended periods of culture. This is speculated to be because ATM independent pathways were sufficient to maintain genomic fidelity in normal culture conditions [15]. Adams et al. provide evidence showing that the repair pathways that dominate in the pluripotent state are ATR-driven HRR in comparison to ATM-driven NHEJ in differentiated cells [78]. The apparent contrast between the necessity for ATM in maintaining genomic integrity between somatic and pluripotent stem cells demonstrates that ATM related and unrelated DNA repair pathways behave in contextually dependent manners depending on cell state.

ATM was recently shown to act in a chromatin-state dependent manner, with respect to repair of DNA DSB. It was found that ATM signaling increased proportionally to the heterochromatic

state of the genome [92]. ESCs are primarily euchromatic [93], and as Adams et al.pointed out, this may explain why ATM dependent DNA repair pathways appear to be dispensable to hESCs in some regards [78]. Analysis of these pathways in iPSCs and differentiated cells from patients with A–T will allow insight into these processes.

1.6.1 DNA damage during reprogramming

In addition to the way in which ATM deficient stem cells might provide interesting clues as to the developmental onset of this disorder, it remains to be seen what involvement this protein might have in the role of reprogramming cells to a pluripotent state. The DNA damage response has been shown to be one of the earliest initiated activities in cells that are undergoing reprogramming, but it is not clear as to how ATM might participate in this process [40, 94]. It has been shown that *ATM* knockout mouse tail-tip fibroblasts undergo reprogramming at a greatly reduced efficiency [95]. This group showed that it was not possible to produce mouse *ATM* knockout iPSC that maintained stable karyotypes. This is inconsistent with findings by Song et al. who generated stable *ATM* knockout hESCs [15]. This conflict could be because ATM is more active in mouse ESCs, or simply due to intrinsic culture instability or that insufficient numbers of clones were expanded under sub-optimal conditions. These comparisons should be viewed as speculation due to the cross species difference and also the different methodologies that each group used to derive these models. Interestingly, a recent paper showed that intermediate passage iPSCs show a reduced rate of copy number variations when compared to parental fibroblasts, early passage iPSCs and hESCs, suggesting that these cells undergo a selection against mutations over time [96].

1.7 Neurodegeneration in A–T

Although there is some clinical variability of A–T symptoms [97], all A–T patients suffer from progressive neurodegeneration of the cerebellum. This process and the underlying mechanisms are poorly understood, largely because of the difficulty associated in generating relevant human cellular models and the cross species difference in animal models. A number of *Atm* knockout mice models have been generated which produced a range of degrees with which they were able to recapitulate symptoms of human A–T [98-101]. The neurodegeneration associated with A–T

contributes to the most debilitating aspect of this condition, being the ataxia which leaves patients wheelchair bound and indirectly results in contributing to the largest cause of death, which is recurrent sinopulmonary infections that arise partially as a result of failing to swallow breathe and eat properly.

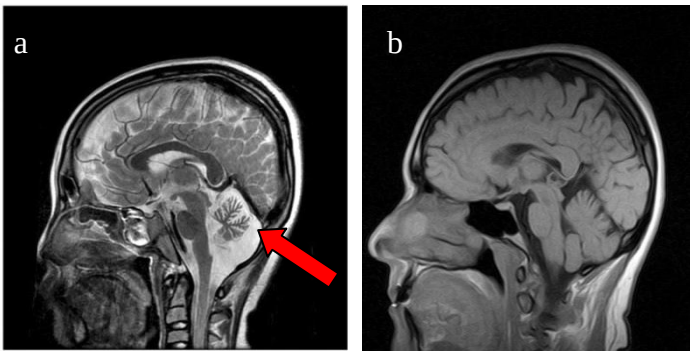

Figure 1.8 – a) MRI of juvenile A–T patient (age 11), showing pronounced and specific cerebellar degeneration, compared to a b) normal brain MRI. Pictured are child (a) [102] and adult (b).

1.7.1 ROS and neurodegeneration

ROS have been implicated in several other neurological disorders, including Parkinson's and Alzheimer's [103]. At least two publications [98, 101] show evidence linking ROS with specific degeneration of Purkinje cells in the cerebellum in A–T models. The former of these groups speculates that ATM acts outside of its canonical role as a DNA damage regulator in participating in the defense against ROS. ATM has shown to be involved in a specific and distinct form of ROS surveillance [11]. Indeed, it has been shown that A–T models display elevated levels of ROS and constitutive activation of multiple oxidative stress pathways, in a range of different cell types [104].

Recently, it was shown that p38 MAPK acts as a negative regulator to control neural stem cell proliferation (NSC) through activation by oxidative stress and may offer some insight into the

mechanism behind the neurodegeneration in this disorder (ie a potential failure of ATM deficient cells to properly regulate ROS) [105].

Given the large metabolic requirements and also the fact that a large proportion of the cells in the brain are post mitotic, the burden of ATM in neuronal cells may be chiefly in response to ROS, rather than DNA damage related cell cycle regulation. This remains a difficult hypothesis to prove, which might be assisted by using pluripotent stem cells to generate neural cell types in large scale to examine the process by which these cells take to differentiate, and where an absence of ATM might contribute to their degeneration.

1.7.2 Other theories to explain neurodegeneration

Although the central paradigm of DNA damage regulation has been used to explain the neurodegeneration in A–T, to different degrees, certain other theories have risen to prominence, including the recent phenomena of inter-cellular differences in aneuploidy [106] as well as ATM's role in apoptosis signaling [107] and development. *In situ* hybridization experiments of the developing mouse CNS show dynamic patterns of ATM expression, showing high levels during early development which later taper off suggesting that problems with neural development might happen early as a consequence of ATM deficiency [108]. This was also proven to be the case in *Xenopus* development [109]. A similar study confirmed this in humans and provided evidence for a role of cytoplasmic ATM in developing cerebellar neurons [13]. In support of this, Allen et al.showed that ATM was required for normal development and differentiation of adult neural progenitor cells and hint at other physiological roles for this protein [110]. A recent paper implicates ATM in neural activity by showing that in its absence, cultured neurons lacking ATM exhibited defective LTP (Long Term Potentiation), while also showing slower rates of spontaneous vesicular dye release [7]. This group showed that ATM could be isolated from synaptosomal preparations, postulating that the ATM protein physically associated with phosphorylated versions of VAMP2 and Synapsin-1 in the pre-synaptic nerve terminal. Interestingly this group demonstrated a physical association between ATM and ATR, predominantly occurring in the cytoplasm of neuronal cells.

A relatively unexplored notion is that of defective calcium handling contributing towards the symptoms in A–T. Calcium is a versatile second messenger which co-ordinates a range of cellular processes, particularly in neurons where it is involved with neuronal survival, activity and signaling. Calcium levels are important in regulating processes such as cell death and migration during the development of the CNS. Khanna et al. showed defective calcium signaling in lymphoblastoid cells isolating from A–T patients [111]. There is an increasing body of literature implicating calcium and mitochondrial aberrations in a range of neurological and metabolic conditions. One such study demonstrates via patch-clamp-recording of murine Purkinje cells, an electrophysiological deficit caused by a significant decrease in calcium currents [112, 113].

The second major site of intracellular calcium storage is the mitochondria. The mitochondria are receiving increasing amounts of attention relating to a range of neuropathologic conditions [114, 115]. A handful of papers provide evidence that ATM may be involved in regulating mitochondrial homeostasis [113,60, 116], however none propose a mechanism that may explain the involvement of mitochondria with the neurodegeneration in A–T.

It seems likely that rather than any one of these theories being correct, there may be an over-arching connection between these that incorporates the role of ATM in development, responding to and repairing DNA damage, sensing ROS, metabolic signaling, apoptosis regulation and the possibility of unknown functions. To elucidate precisely why cells of the cerebellum are targeted remains the challenge.

1.8 Purkinje and granule cells

Purkinje cells, being the only cerebellar cortex projection neurons, are responsible for coordinating cerebellar motor control and motor learning [117]. This neural cell type represents a highly desirable target to study due to its implication in a range of diseases in addition to A–T, including Niemann-Pick syndrome [118], autism [119], Unverricht-Lundborg disease [120], and

certain spinocerebellar ataxias [121, 122]. In the mouse cerebellum, PCs constitute <0.1% of the population [123], meaning that even in mouse models, where tissue can be obtained by sacrifice, studying this cell type is difficult. Additionally, PCs extracted from neonatal mice exhibit poor survival and failure to extend dendrites in culture [124]. There is evidence that an abnormal pattern of dendritic arborization and structural arrangement within the cerebellar molecular layer is associated with the ataxia in A–T patients [125, 126].

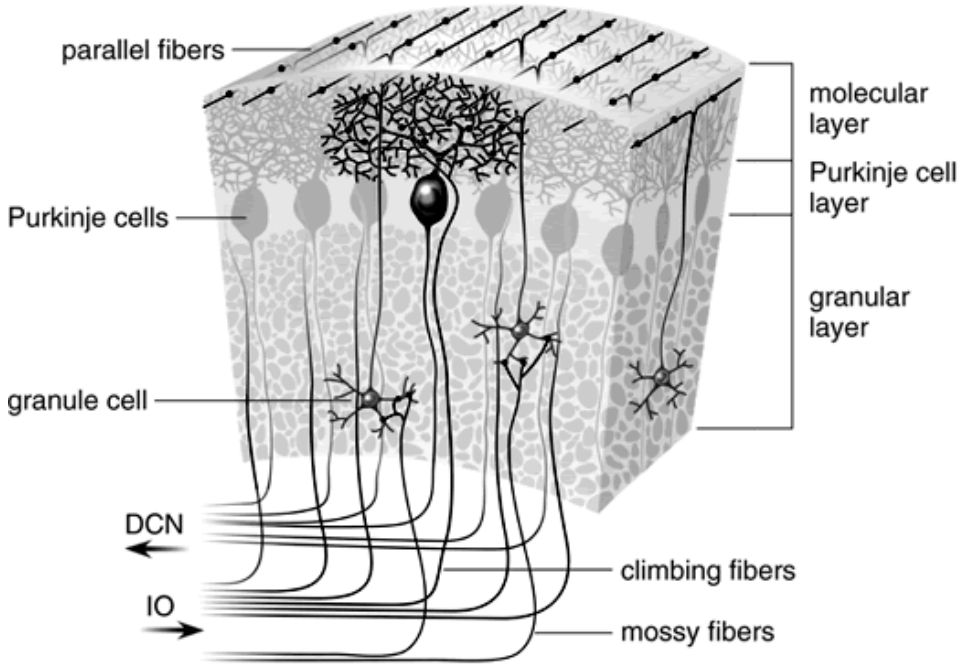

Figure 1.9 – Schematic representation of sagittal cerebellar slice showing Purkinje and granule cells [127].

1.8.1 Purkinje cell differentiation

Specific neural subtypes can be derived *in vitro* from ESC by generating neural precursors, and then directing differentiation to mimic *in vivo* regional, temporal and chemical changes associated with particular neural cell types. These cells can be assayed at time points to examine developmentally relevant processes. Recently, a Japanese group was able to generate mature cerebellar PC from mouse ESC by treating serum-free embryoid bodies with BMP4, Fgf8b and Wnt3a, in combination with feeder cells derived from neonatal mouse cerebellum [117]. FGF8 is a regional regulator which acts on the anteroposterior axis and is expressed in the boundary of

the MHB (mid-hind brain) to control cerebellar development through ras-ERK signaling [128], while BMP and WNT proteins regulate dorsal pattern formation [129]. These, and other secreted factors are involved in the development and regionalization of the early vertebrate brain. By delivering these factors at certain concentrations at given times, Tao et al. were able to induce mouse ESC to form cerebellar neuronal precursors, as similarly reported elsewhere [130], but then went on to amplify these GC precursors using SHH, before adding neurotrophic factors BDNF, NT3 and T3 to differentiate these cells into PCs and GCs. These cells were further matured using a co-culture system comprised of whole-cerebellum dissociations. Recently, Erceg et al. showed it was possible to produce cells with cerebellar characteristics from human ES&iPS cells [131].The ability to translate this system for use with human stem cells may allow for insight into A–T pathogenesis at a never before seen resolution.

2.0 Generation and characterization of lentivirally generated A–T iPSCs

Introduction

Reprogramming of cells from various sources occurs with a wide range of efficiencies [132]. These varied efficiencies are likely to be the culmination of a variety of intrinsic and extrinsic factors including the tissue of origin, the passage number and culture history of the target cells (which has bearing on the epigenetic and proliferative status of the target cells). Another major factor affecting reprogramming is the methodology and quality of the reprogramming process itself (including for conventional viral based approaches; viral titer and subsequent viral transduction efficiency, including downstream transgene insertion and stoicheometry) [133, 134]. Genetic background is an important parameter affecting the efficiency of the reprogramming process with reports that cells from individuals with particular mutations are more difficult to reprogram than their control counterparts. These observations support the theory that modulation of pathways can either enhance or inhibit reprogramming [40].

Given findings that p53 abrogation increased the efficiency of reprogramming [40, 94] it was reasonable to assume the existence of a barrier or roadblock which might prevent cells with excessive levels of DNA damage passing unfettered through this process. Evidence shows that DNA damage pathways are activated early during the reprogramming process [135]. We speculated that given the role of ATM in the maintenance of genomic stability that A–T fibroblasts might navigate this roadblock differently. On one hand, the role of ATM as a tumor suppressor with marked similarities to p53, might suggest that these cells should behave analogously to those reported in the above publications by passing through or skipping this roadblock, regardless of levels of DNA damage. Alternatively, the accumulation (before or during reprogramming) of DNA damage in the absence of ATM may contribute to difficulty in cellular reprogramming. Indeed it has been shown that the introduction of reprogramming factors (both virally and non-virally mediated) introduces genotoxic stress. Given the fact that ATM has been increasingly cited as a contributor to various metabolic pathways, and also the fact that somatic cells which lack ATM show intrinsic culture stress/elevated growth factor requirements [136], we postulated that this might also affect reprogramming efficiency.

To address this, we examined the response of A–T cells to various cell culture conditions after lentiviral transduction with reprogramming factors *Oc4/Sox2 (*pSIN4-EF2-O2S; and *Klf4 /c-Myc (*pSIN4-CMV-K2M), including media type (KSR or serum-containing DMEM), treatment with a p53 inhibitor (small molecule pifithrin-α) and either a low or high concentration of basic FGF. Post-transduction, equivalent numbers of cells from heterozygote and homozygote patients (family 1) were plated in six-well plates and assessed by microscopy at regular intervals for survival and proliferation.

We initially used lentiviral transduction with two separate plasmids carrying *Oct4/Sox2 (*pSIN4-EF2-O2S; Addgene plasmid 21162), and *Klf4 /c-Myc (*pSIN4-CMV-K2M; Addgene plasmid 21164, [36] to generate iPS cells from two families (heterozygotes and homozygotes) as well as wild-type controls.

Although there is a broad knowledge gap regarding the mechanism by which a terminally differentiated cell is reprogrammed back to a pluripotent state, the general consensus is that wide-scale remodeling of the epigenetic landscape occurs [29, 137]. This coincides with the newfound ability of these cells to re-express stem cell gene products and is facilitated by specific loss or gain of modifications of the DNA ultra-structure (ie methylation, ubiquitination, acetylation of DNA sequence or histone proteins). These modifications enforce chromatin dynamics that define the cell's identity largely through transcriptional regulation. Although forced expression of reprogramming factors, which are master regulator stem cell transcription factors, can give rise to colonies with stem-cell-like properties, not all stem-cell-like colonies arising from these experiments are deemed fully reprogrammed induced pluripotent stem cells [138]. Often, cells are incompletely reprogrammed, that is, the epigenetic landscape resembles to a degree that of a pluripotent stem cell, with several critical regions retaining the mark of their tissue of origin [139]. This may result in something that looks like a stem cell, but may have aberrant proliferation and differentiation properties. A major challenge for the field remains to isolate 'good-quality' or *bona-fide* iPS cells for cultivation and experimentation. We examined a range of properties to identify and isolate good quality iPS cells including the expression status of important stem cell transcription factors and surface proteins, methylation levels at stem cell

associated regulatory loci, persistence of transgene, karyotype status and teratoma forming ability

This chapter describes work that was published in *Stem cells & Translational Medicine* that describes the first report of generation of iPS cells from patients with Ataxia–Telangiectasia. Additionally contained herein are further details regarding the optimization of generation and characterization of these cell lines.

Materials and methods

Generation of iPSCs using lentiviral factors

Primary fibroblasts isolated from dermal punch biopsies from patients with Ataxia–Telangiectasia were collected through the A–T Clinic, Royal Children's Hospital & UQ Centre for Clinical Research. Biopsies were dissected into small pieces and incubated under coverslips in DMEM (Invitrogen) with 12% FCS (fetal calf serum) until fibroblasts grew out. Primary human fibroblasts were harvested with TrypLE select (Invitrogen) and expanded in DMEM (GIBCO) with 15% FCS until cryopreservation at passage 2. Lentivirus carrying *OCT4*/IRES/*SOX2* and *KLF4*/IRES/*c-MYC (*Addgene plasmid 21162: pSIN4-EF2-O2S & plasmid 21163: pSIN4-EF2-N2L)[36], (plasmid maps are shown in appendices) was produced by transfection of HEK293 cells with plasmids in 500 µg/ml Geneticin at 70-90% confluency. Before transfection, fresh media without geneticin was added. Following this warm *Optimem* media, *Lipofectamine PLUS reagent* were allowed to warm to room temperature before application at the manufacturer's specifications with (per reaction) 2.5µg Lentiviral vector (O2S or K2M), 2.5 µg pVSVG and 5 µg of pCMR delta-8.2 packaging vector. Virus was collected the following day by filtering supernatant with a 0.45 µm filter.

Target fibroblasts were transduced with lentiviral constructs by application of reprogramming virus for 24 hours. After transduction, >50,000 A–T fibroblasts were allowed to recover for between 24-48 hours before transferring to matrigel coated plates or mouse embryonic fibroblast

(MEF) feeder plates (36,000/cm^2). We observed distinct patterns of recovery and proliferation after viral transduction and were able to quantitatively assess these patterns to design a strategy to facilitate and optimize generation of iPS cell colonies from A–T patient fibroblasts.

Transduced A–T fibroblasts were weaned from DMEM with 15% FCS to 100% hESC culture medium over a period of 4 days, at 25% per day, as this was shown to greatly increase their survival and proliferation. In accordance with a recent attempt to standardize nomenclature across hESCs and iPSCs [140], we have named these lines UQ0001i-ATh47, UQ0002i-AT34, UQ0003i-ATh41 and UQ0004i-AT30 where UQ refers to the institution in which they originated, the subsequent four-letter number refers to the order in which they were generated, i denotes iPSC origin, and AT (Ataxia–Telangiectasia)/ATh (Ataxia–Telangiectasia heterozygote) nomenclature previously developed for naming A–T cell lines, followed an internal patient identifier and a blank space for clone number. A shortened version of this nomenclature is used henceforth to refer to these lines. All work was carried out with informed consent from patients under the approval of the Human Research Ethics Committee (HREC/09/QRCH/103).

Cell Culture Conditions

hESCs and iPSCs were grown in knock out serum (KSR) replacement hESC culture medium (80% DMEM F12 (GIBCO), 20% KnockOut-Serum replacement (GIBCO), 2 mM L-glutamine (GIBCO), 1% non-essential amino acids (NEAA) (GIBCO), 0.1 mM 2-mercaptoethanol and between [50-100 ng/ml] basic fibroblast growth factor) (Invitrogen) at 37°C at 5% CO_2 and at high humidity. Cells were maintained on MEF feeder layers supplied by the Australian Stem Cell Centre. For experimentation, cells were cultured in feeder-free conditions on Matrigel™ (BD) in MEF conditioned hESC culture medium. Cells were passaged as previously described [17] before replating at a seeding ratio of between 1:2 and 1:6. hESC media was replaced daily and cells were split at approximately 80% confluence on days 6-7.

Screening of clones

iPSC colonies were picked at early (2 weeks) and late time points (5 weeks) and sub-cultured clonally on MEFs in organ culture dishes. Clones were screened for expression of TRA-1-60 and Hoechst dye efflux, transgene persistence by RT-PCR, stem cell marker expression and methylation status at *Oct4/Nanog* promoters. Karyotypic stability was assessed via G-band analysis (>15 metaphases analyzed per sample) by a commercial genotyping service (Sullivan Nicolaides Pathology, QLD, Australia). Transgene silencing in selected clones was later confirmed by quantitative RT-PCR.

Teratoma formation

iPSCs grown on MEFs were collected by collagenase IV treatment, and approximately 2 million iPSCs resuspended in 50 μL DMEM/F12 supplemented with 30% BD Matrigel™ were injected into hind limb muscles of Methoxyflurane anaesthetised 6-week-old-immune compromised SCID mice (CB17-SCID mice from the Animal Resource Centre (ARC) in Western Australia). After eight to ten weeks, teratomas were dissected and fixed in 4% paraformaldehyde. Samples were embedded in paraffin, stained with haematoxylin and eosin and examined for the presence of representatives of the three germlayers by an independent pathologist. All mouse procedures were conducted under local ethical guidelines and after gaining permission from the local animal ethics committee (University of Queensland, QLD, Australia).

Bisulfite sequencing

Live iPSCs were sorted by flow cytometry for TRA-1-60 and genomic DNA was isolated. 1-2 μg of DNA was bisulfite converted using EpiTect Bisulfite kit (QIAGEN) before PCR of *Oct4/Nanog* promoter regions and cloning into the PCR2.1 vector. Clones were screened and selected for sequencing (primers are listed in appendices). Synthetically hypermethylated HeLA cells and H9 hESCs were also included as controls.

Immunostaining

For immunostaining cells were washed in PBS and fixed in 4% paraformaldehyde for 15 minutes at 4°C. For nuclear staining samples were permeabilized in 0.1% TritonX100 at room temperature for 10 minutes, before blocking with 10% goat serum and incubation with the relevant antibodies overnight at 4°C. Antibodies and dilutions used were OCT4 (Millipore) [1:1000], SSEA-4 [1:100], TRA-1-60 (Millipore) [1:1000], NANOG (Millipore) [1:400], TRA-1-81 (all from Millipore, USA) or OCT4 [1:1000] (Santa-Cruz). Following washing with PBS (3 times 5 minutes at room temperature) secondary antibodies goat anti-mouse IgG_1, goat anti-mouse IgG_{2B}, goat anti-mouse IgM and Donkey anti-rabbit IgG (Alexa fluor) [1:1000] were used. Nuclei were stained with DAPI or Hoechst. This preparation minus the addition of primary antibody was used to confirm specificity of staining.

Cryopreservation

A four-well vitrification plate was prepared with wells containing 1) 1mL ES Hepes media, 3) 1ml 10% vitrification solution and 4) 1ml 20% vitrification solution (well 2 left blank). Plate was equilibrated in incubator at 37^oC 5% CO_2. 5mL cryovials (with needle-punched bottom) were inserted into a cryocane within a small liquid nitrogen canister. Colonies were manually dissected using a 22 gauge needle and transferred into well 1 of the vitrification plate using a 20µL pipette. 8-10 pieces were moved into well 3 of the vitrification plate for no more than 1 minute. A new pipette tip was used to transfer 20 µL of 20% vitrification solution to the lid of the well-plate creating a high drop. Pieces were taken from well 3 in minimal volume and transferred gently to well 4. Pieces were left for no more than 30 seconds before transferring to the 20 µL drop. A second small drop containing as many pieces as possible in 5 µL was generated on the well-plate lid. Capillary action drew these pieces into a cryostraw by placing the straw at a 30-45 degree angle touching the droplet/plate, before immediate transfer to the cryovial/cryostraw. A diagram below illustrates aspects of the procedure.

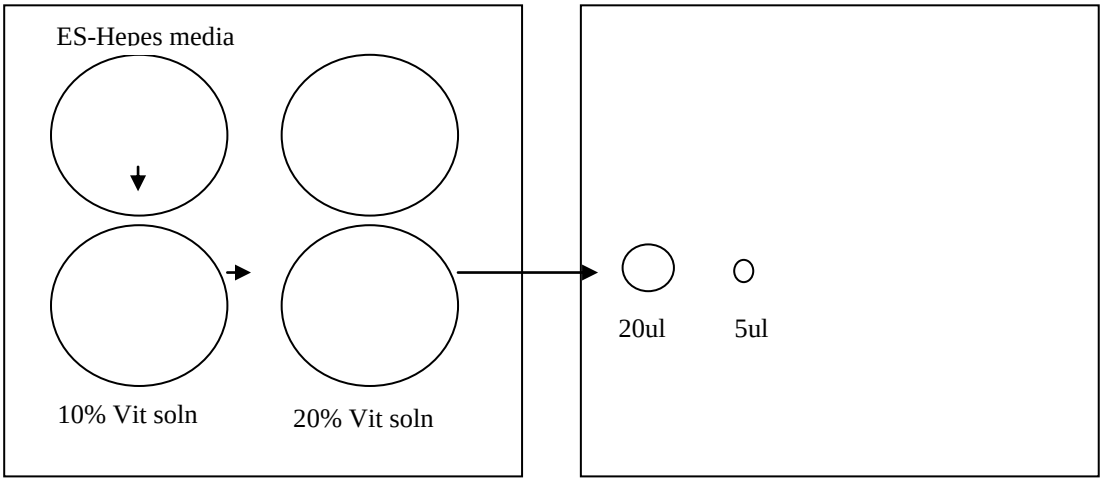

RNA isolation, cDNA synthesis, PCR and Q-PCR

RNA was isolated using RNeasy isolation kit (QIAGEN). Concentration and 260/280 ratios were quantified using a NanoDrop 1000 spectrophotometer before synthesis of cDNA using iscript cDNA synthesis kit (Biorad) according to the manufacturer's specifications (500ng). RT-PCR was performed for *OCT4* (657bp) and *SOX2* (498bp) transgenes according to the following conditions; 94°C 5 mins, 32 cycles (94°C 1 min, 58°C 30 sec, 72°C 1 min), 72°C 7min and *KLF4 (*563bp), *c-MYC (*350bp) transgenes as well as *GAPDH (*152bp) according to the following; 94°C 5 mins, 32 cycles (94°C 1 min, 57°C 30 sec, 72°C 1 min), 72°C 7min. Primers are listed in the appendices. qPCR was performed for *OCT4* transgene, endogenous *OCT4* and □*-Actin* using a C1000 thermal cycler (Biorad) (Ssofast evagreen qPCR mix) (Biorad), according to the following conditions; 95°C 3 mins, 30 cycles (95°C 10 sec, 60°C 30 sec). Expression data was calculated using the ΔΔCt method.

Results

Growth and proliferation of cells after viral transduction

Proliferation and survival after viral transduction was monitored by observing cells in culture in random fields of view by microscopy. An ImageJ cell counting algorithm was used to quantify the number of cells per field of view. Growth was noted to be generally greater in heterozygote line ATh47 when compared with homozygote line AT34, across most conditions (Figures 2.1A &2.1B). Within the range of conditions tested for heterozygote line ATh47, growth and proliferation was markedly increased in media containing FCS when compared to KSR (Figure 2.1A). In the presence of KSR, cyclic-pifithrin-α induced p53 inhibition resulted in increased growth (Figure 2.1A). This same effect was also observed in cells grown in the presence of FCS (Figure 2.1A). Similarly in heterozygote line ATh47, homozygote line AT34 showed a marked response in growth to the presence of FCS (Figure 2.1B) and a similar trend for increased growth in the presence of p53 inhibitor was noted, however this was more subtle.

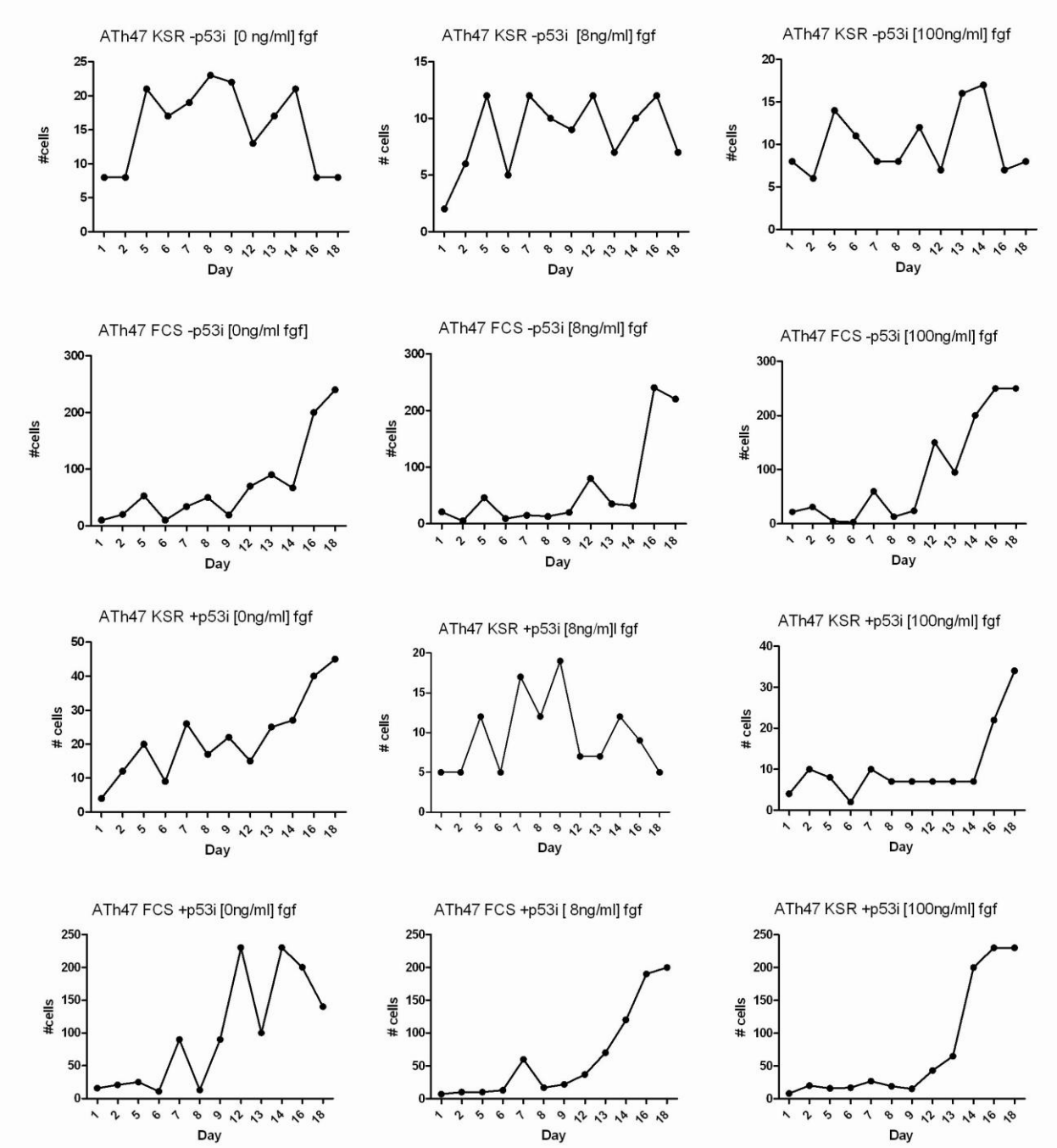

Figure 2.1A – Graphs depicting proliferation rate of A–T heterozygote (family 1 – Ath47) after viral transduction in a range of growth conditions.

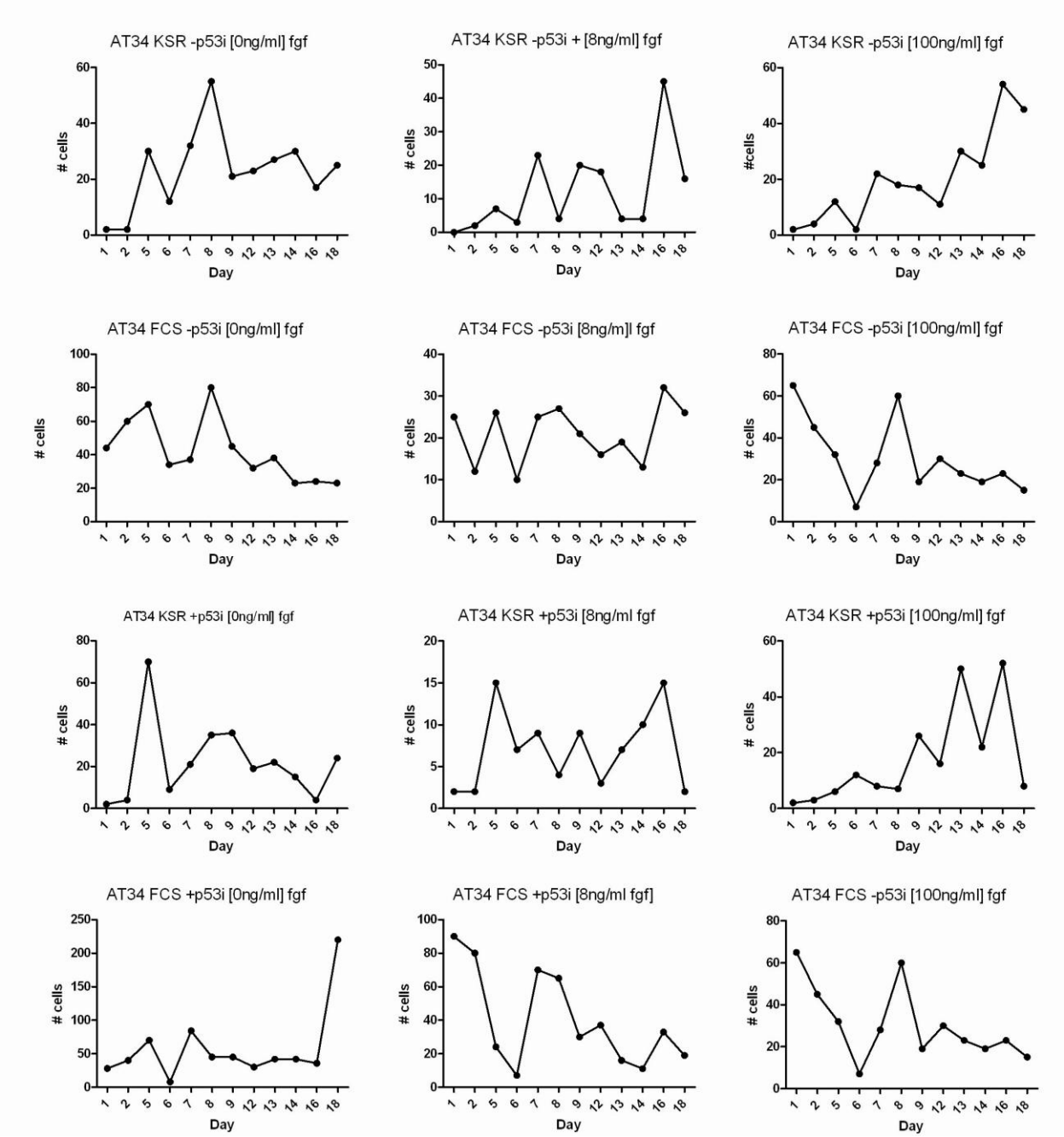

Figure 2.1B – Graphs depicting proliferation rate of A–T homozygote (family 1 – AT34) after viral transduction in a range of growth conditions.

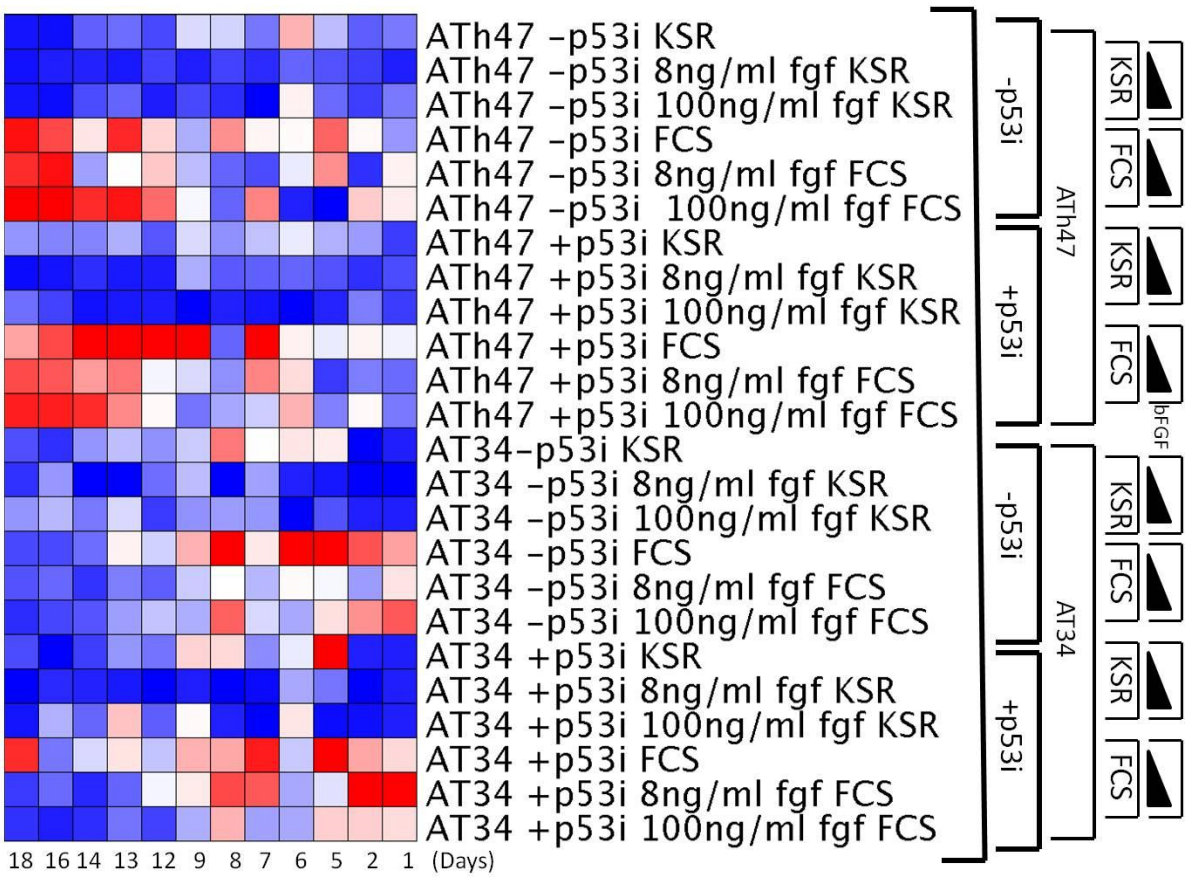

Figure 2.1C – Heatmap representative of data from figures 2.1A&B detailing proliferation after viral transduction in variety of conditions (note heatmap timed data reads right to left from growth condition label). Color indicates cell density/viability ranging from blue (lowest) to white (intermediate) to red (highest).

Interestingly, while growth of cells was remarkably low, the addition of KSR gave rise to colony type structures with densely packed cells reminiscent, but distinct from human embryonic stem cell colonies (see figure 2.1D iii & iv) which we hypothesized to be cells that were experiencing some selective advantage in the stem cell media KSR. These colonies were not observed in media containing FCS. Given the fact that media containing FCS seemed to favor growth and expansion of cells post-transduction, but did not result in the formation of any pseudo-colony type structures we speculated that a strategy involving stepwise weaning of transduced cells from FCS containing media to that of KSR would give them sufficient selective advantage to grow but also form colonies.

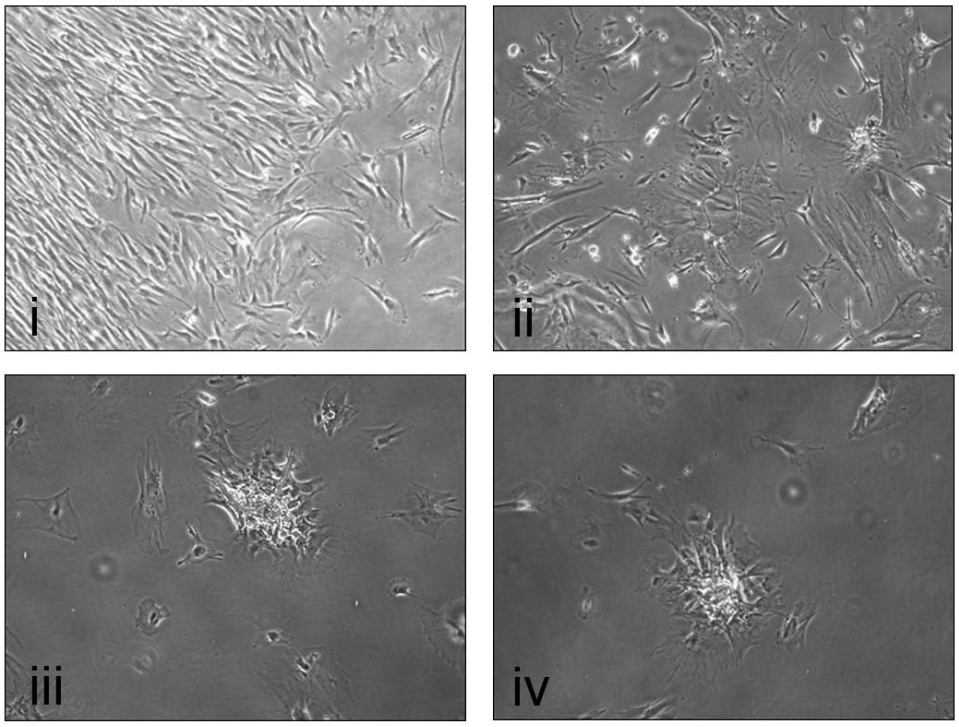

Figure 2.1D - Representative phase-contrast photographs are shown from growth experiment of A–T heterozygote ATh47 (i) and A–T homozygote AT34 (ii) in FCS containing media and also ATh47 (iii) and AT34 (iv) in KSR media.

In parallel to this experiment, transduced fibroblasts were treated as outlined in materials and methods to derive iPS cell colonies. This involved plating ≥50,000 cells onto mouse embryonic fibroblasts feeder (MEF) layers at a MEF density of 36,000 cells/cm^2. Given the above data showed that survival of transduced cells was much higher in the presence of FCS, but KSR was required for formation of pseudo-colony type structures, we adopted an approach to wean transduced cells from 100% DMEM with FCS (15%) to 100% KSR over a period of four days, at a rate of 25% per day.

Isoloation of putative iPSC colonies

The sporadic appearance of clusters of large refractile cells was observed, which were identified as adipocytes (See figure 2.1E vii). After 2 weeks, we also noticed small clusters of cells resembling human embryonic stem cell colonies that were identified as putative iPS colonies (Figure 2.1E iix).

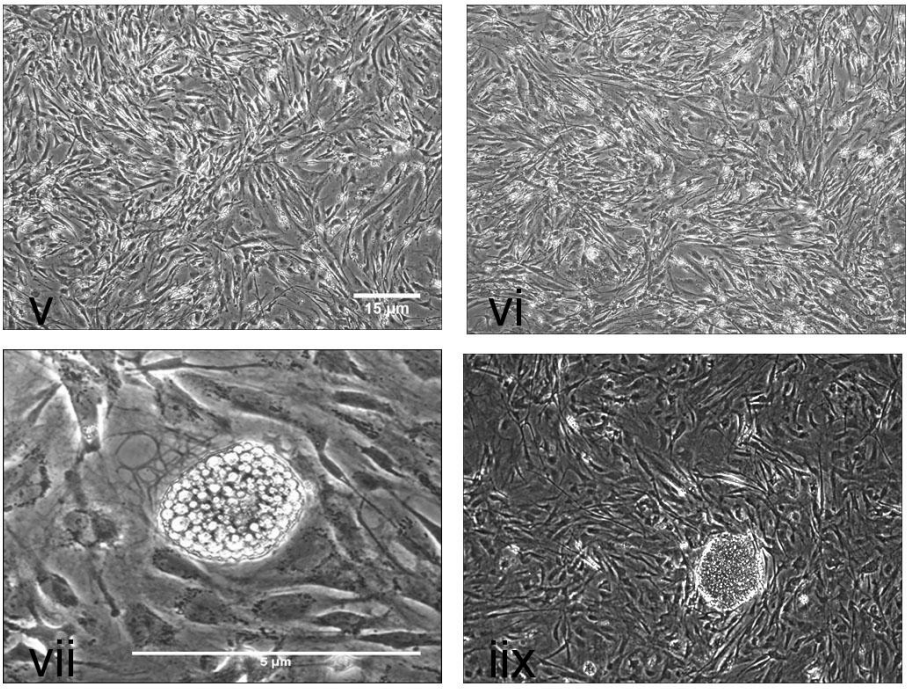

Figure 2.1E - Transduced fibroblasts were seeded onto MEFs. ATh47 (v) and AT34 (vi) are shown. We noticed formation of adipocytes (vii) and early iPS cell colonies (iix). Scale bar is 15 µm (v,vi & iix) and 5 µm for vii.

These putative iPS cell colonies were 'picked' by cutting with a 22 gauge needle attached to a 1ml syringe and transferred to organ culture dishes on MEFs at a density of 36,000/cm^2 for clonal expansion. A vitrified stock was cryopreservered initially (outlined in materials & methods) and then colonies were subject to screening for characteristics of properly reprogrammed cells [41].

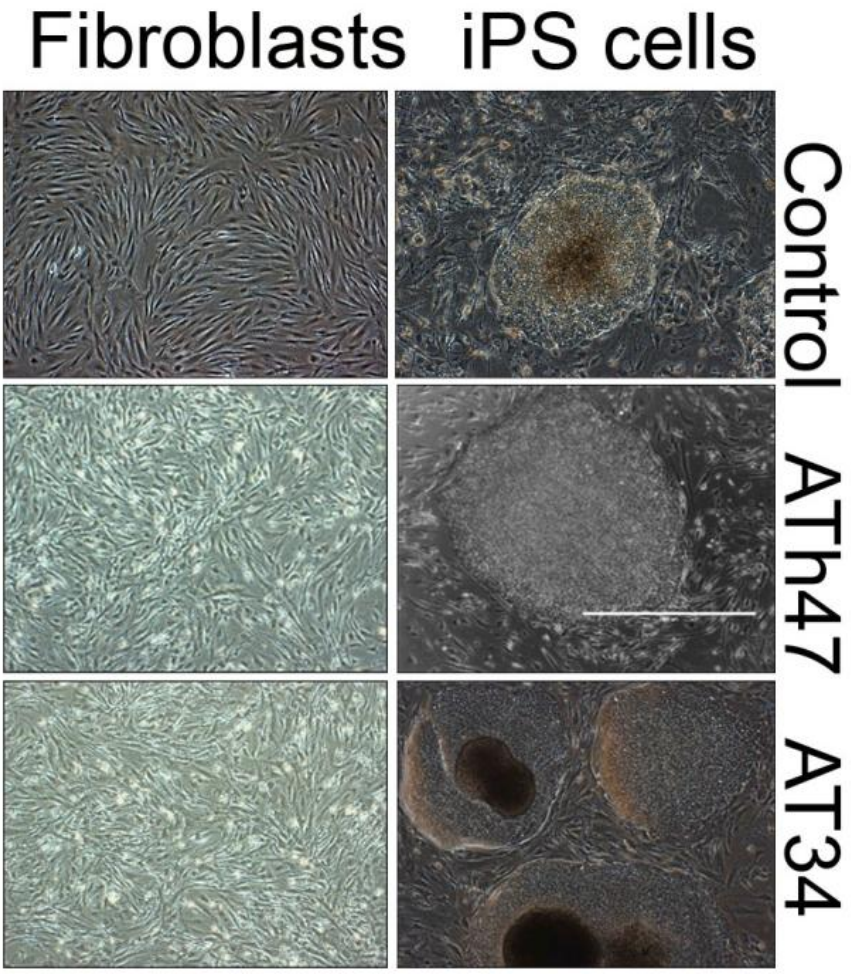

Figure 2.1F – Morphology of fibroblasts (ATh47, AT34 and control CRL2429) and intermediate/early passage iPS cell colonies. Scale bar is 50 μm.

Reprogramming efficiency

After 3 weeks of growth under reprogramming conditions, the gross number of colonies which exhibited human embryonic stem cell-like appearance was recorded. Relative to wild-type controls, heterozygote and homozygote lines ATh47 and AT34 gave rise to fewer colonies, despite seeding of equivalent numbers of transduced cells. Reprogramming efficiency of homozygote AT34 was approximately 4% relative to controls, in contrast to ATh47 that was 15%, indicating a potential role for ATM during reprogramming. A second family (ATh41 and AT30) displayed a greater number of colonies in both heterozygote and homozygote lines relative to controls, although the efficiency of homozygotes compared to heterozygotes was

drastically reduced consistent with the first set of reprogramming experiments (Figure 2.2). We observed that reprogramming of cells from a second A–T family (AT41 & AT30) could occur without the stepwise addition of FCS containing media, however this was not as efficient (Figure 2.2).

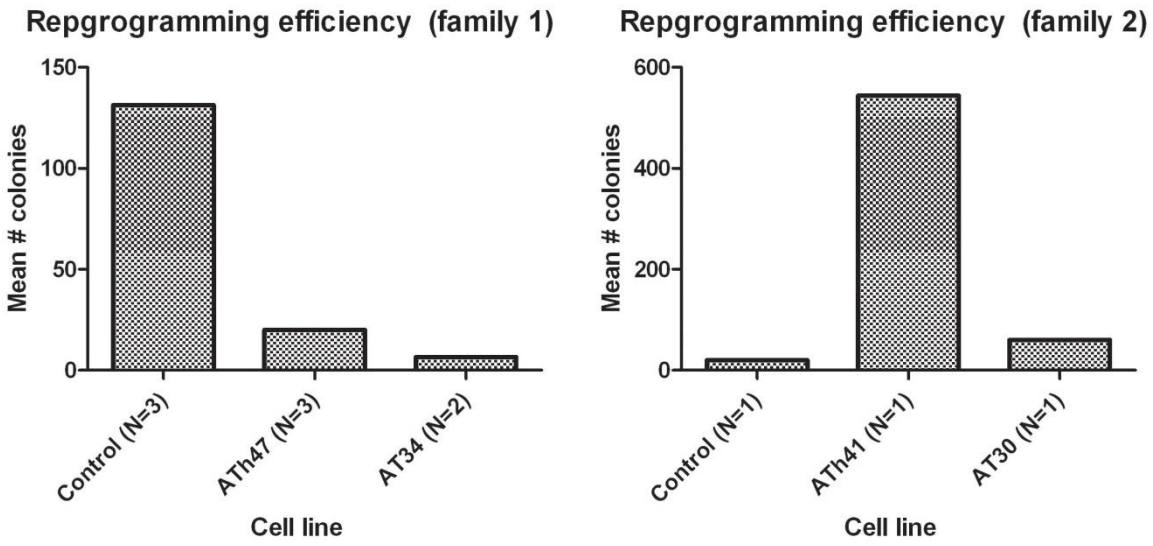

Figure 2.2 – Reprogramming efficiencies in family 1 (ATh47 heterozygote and AT34 homozygote) relative to controls. Family 2 (ATh41 heterozygote and AT30 homozygote).

iPSC nomenclature

According to a recent attempt to standardize nomenclature across hESCs and iPSCs [141], we named these lines UQ0001i-ATh47, UQ0002i-AT34, UQ0003i-ATh41 and UQ0003i-AT30. UQ refers to the institution in which they were generated, the subsequent four-letter number refers to the order in which they were generated, i denotes iPSC origin, and AT (Ataxia–Telangiectasia)/ATh (Ataxia–Telangiectasia heterozygote) nomenclature previously established for naming AT cell lines [142] and finally a blank space for clone number. A shortened version of this nomenclature is used henceforth to refer to iPS cell clones used for experimentation.

Initial screening of iPSCs for criteria pertaining to a fully reprogrammed state (TRA-1-60/Hoescht efflux & pluripotency marker expression)

Live immunostaining was performed to assay for immuno-reactivity of early pluripotency marker TRA-1-60, in combination with Hoescht efflux (ie active pumping out of Hoescht staining agent) (Figure 2.3). Clones were selected that exhibited TRA-1-60 expression and exhibited a Hoescht-dim phenotype.

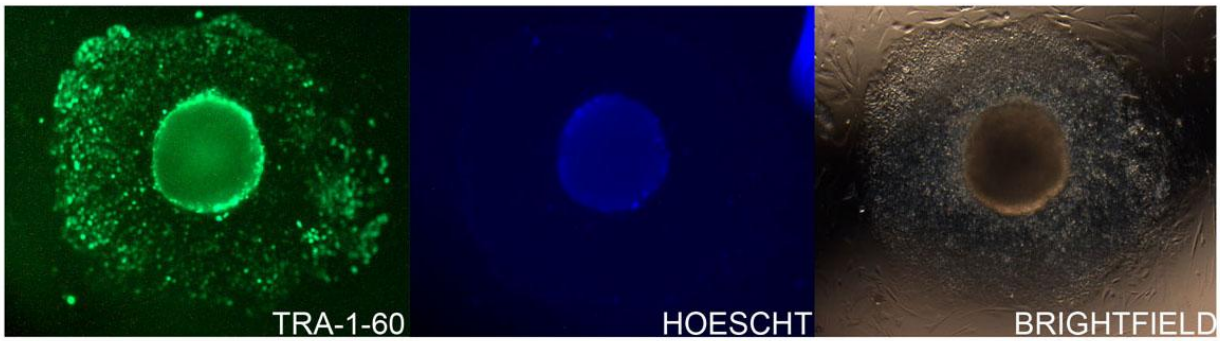

Figure 2.3 – Criteria for selection as bona-fide iPS colonies begins with testing immunoreactivity with TRA-1-60 (left panel) and Hoescht dye efflux (middle panel). Brightfield photograph also shown (right panel).

Selected clones were further expanded and fixed to assay for immunoreactivity with a broader suite of markers including OCT4, NANOG, TRA-1-60, TRA-1-81 and SSEA-4 (Figure 2.4A). Additionally, flow cytometric analysis confirmed the robust and uniform expression of pluripotency marker TRA-1-60 (Figure 2.4B).

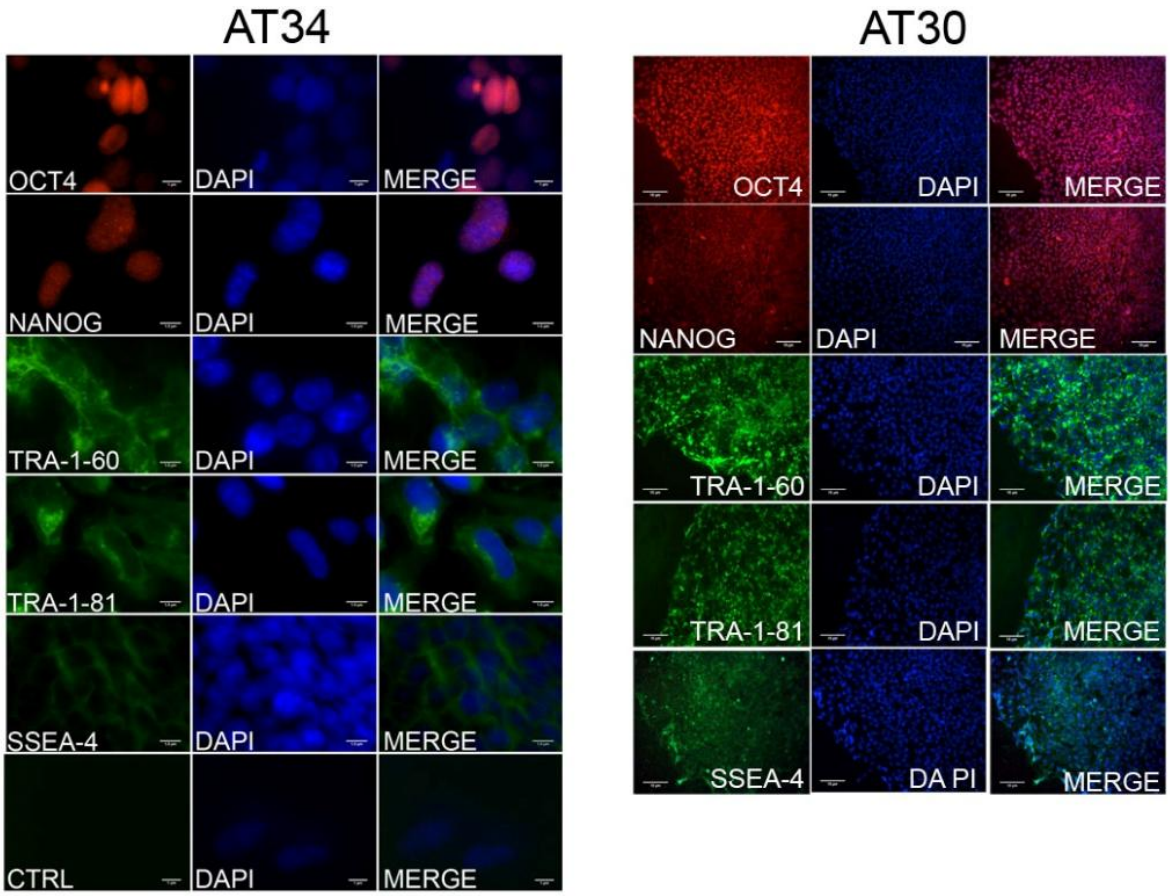

Figure 2.4A – iPS cell colonies exhibited nuclear stem cell markers OCT4 and NANOG in addition to surface markers TRA-1-60, TRA-1-81 and SSEA-4. Scale bars are 10 µm (left panel set – high magnification) and 1 µm (right panel set – low magnification) respectively. A negative control featuring an identical preparation with omission of primary antibody was included (bottom row).

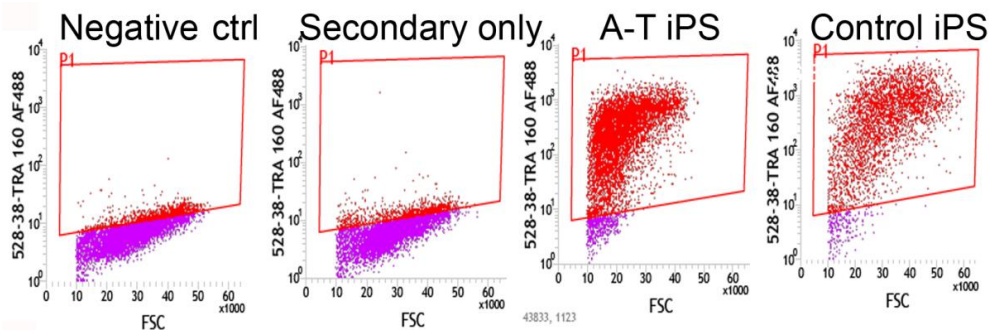

Figure 2.4B – Flow cytometric analysis further exemplifies robust and uniform expression of pluripotency marker TRA-1-60 in A–T (AT34) and control iPSCs.

From the selected clones, RT-PCR was used to ascertain whether the transgenes used in generation of the iPS cells were actively expressing after 13 weeks in culture (Figure 2.5A). Clones showing diminished levels of transgene activity were sought after as this was taken to indicate silencing of these genes and resultant acquisition of a pluripotent phenotype independent from the exogenous factors. Validation of iPS cells from control and a second family (AT30/ATh41) was employed using the same methodology (data not shown).

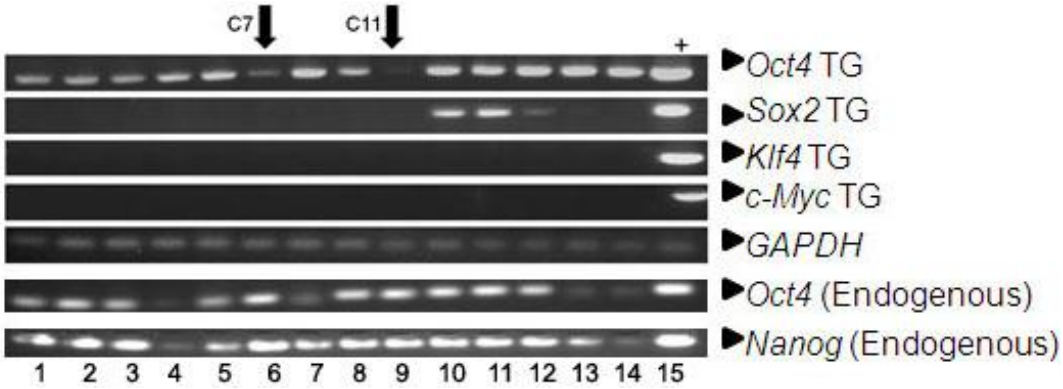

Figure 2.5A – RT-PCR shows by passage 10 most clones (AT34) robustly expressed Oct4/IRES transgene, with the exception of C7 (lane 6) & C11 (lane 9). Silencing of most other transgenes had occurred by this stage with the exception of two clones expressing *Sox2/IRES* (clones 12&13, lanes 10&11). Most clones expressed endogenous *Oct4* and *Nanog*. Amplification of *GAPDH* was used as a loading control. Positive controls (lane 15) were plasmid DNA and H9 human embryonic stem cell line in the case of *GAPDH*.

Screening and monitoring of karyotypic stability

Because of the role for ATM in maintenance of genome integrity, cell lines were examined for gross karyotypic abnormalities at regular intervals (Figure 2.6 and Table 2.6B shows karyotype spreads and table summarizing results). Although three out of the eight clones examined developed chromosomal abnormalities, five A–T iPSC clones displayed normal karyotypes between passage 11-16 and this was maintained out to passage 31 in the case of one clone.

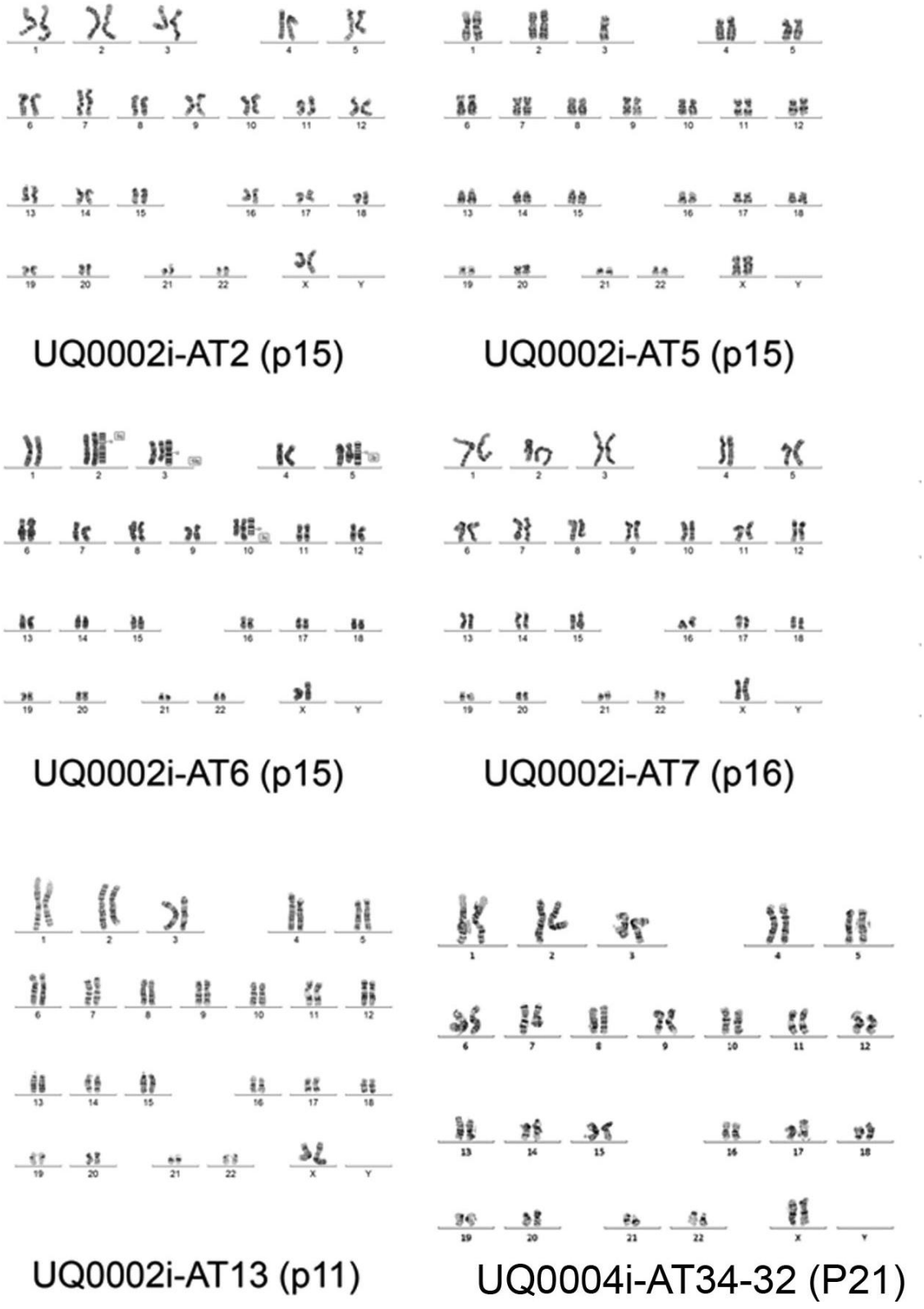

Figure 2.6 – Karyotypes of selected iPS cell lines

Figure 2.6 (cont.) – Karyotypes of selected iPS cell lines

Name	Clone#	Passage	Karyotype
UQ0002i-AT34	2	15	46,XX[15]
UQ0002i-AT34	5	15	46,XX[15]
UQ0002i-AT34	6	15	46,XX,t(2;5)(p13;q13),t(3;10)(112;q22)
UQ0002i-AT34	7	16	46,XX[15]
UQ0002i-AT34	7	25	46,XX[15]
UQ0002i-AT34	7	31	46,XX[15]
UQ0002i-AT34	11	15	45,XX 14,der(20)t(14;20)(q11.2;p11.2)
UQ0002i-AT34	12	11	46,XX[15]
UQ0002i-AT34	13	11	46,XX[15]
UQ0004i-AT30	17	21	46,XX,+14,der(14;14)(q10;q10)[15]
UQ0004i-AT30	32	21	46,XX[15]

Table 2.6B – Summary of Metaphase spreads/karyotypes depicted in Figure 2.6

Further characterization & screening of iPSC for criteria pertaining to a fully reprogrammed state (Transgene qPCR, Bisulfite sequencing of *Oct4/Nanog* promoters & teratoma formation assay)

Transgene extinction in samples C7 and C11 (AT34) was confirmed after 30 weeks in culture by qPCR amplification with primers specific for the 3' end *Oct4* and adjacent *IRES* sequence (Figure 2.7). Transgene transcript could be detected in virally transduced cells at 168 & 208 hours after viral infection but not in untransduced fibroblasts. We failed to detect any residual *Oct4* transgene expression in AT34 (C7 &C11) after 30 cycles but could easily detect robust expression in a transgene expressing positive iPS cell line. No amplification of transcript was observed in no template or minus reverse transcriptase controls.

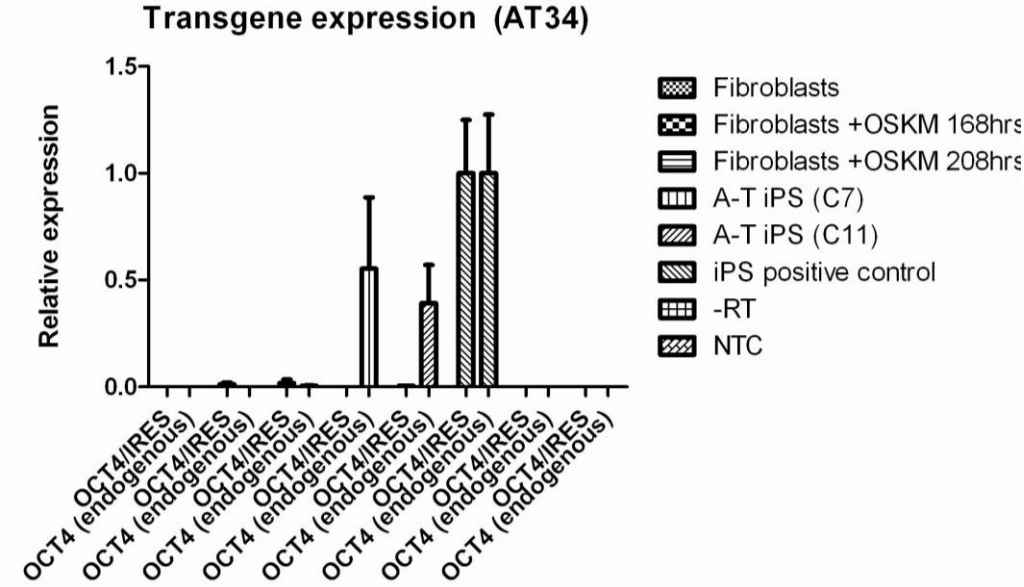

Figure 2.7 – qPCR analysis of gene expression demonstrates transcript from the *Oct4*/IRES transgene was detected within 168 hours of lentivirally transducing fibroblasts. We confirmed silencing of the *Oct4/IRES* transgene and also active expression of endogenous *Oct4* in samples C7 & C11 (AT34). Untransduced fibroblasts, a minus reverse transcriptase and also no template reactions were run as controls.

We next determined the methylation status of the *Oct4* & *Nanog* promoter loci, given that demethylation of CpG islands in this region is associated with a fully reprogrammed state [36]. We used bisulfite modification of genomic DNA and PCR amplification at promoter loci to ascertain the methylation status of these promoters in our iPS cells and controls relative to their corresponding parental fibroblasts by sequencing of these loci (Figure 2.8).

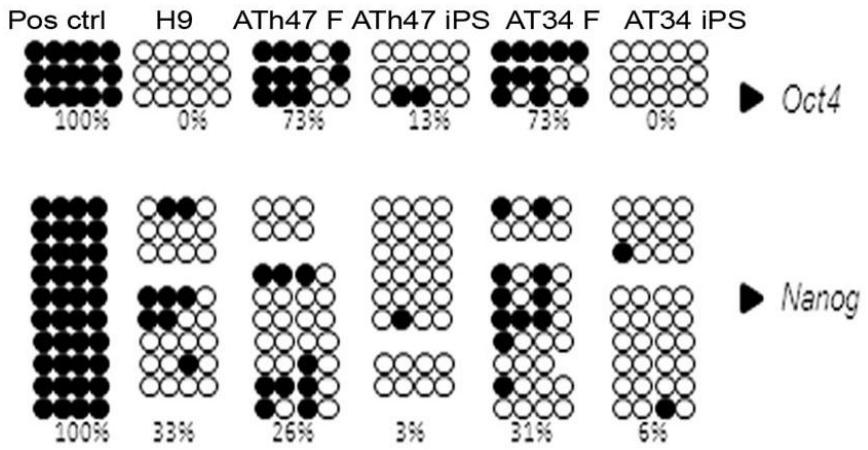

Figure 2.8 – CpG islands in the promoter regions of Oct4 and Nanog undergo hypomethylation as part of their transition from fibroblasts to iPS cells. Fully methylated HeLa cells were used as a positive control and H9 human embryonic stem cells used as a negative control. Open circles depict unmethylated CG diresidues. Full circles represent methylated CG diresidues.

In A–T heterozygote line ATh47, the *Oct4* CpG island containing promoter region underwent a transition from 73% to 13% methylation. Similarly *Oct4* transitioned from 26% to 3% methylated indicating that hypomethylation of this locus had occurred as part of the reprogramming process. Likewise in A–T homozygote AT34 we observed a 73% to 0% and 31% to 6% shift, respectively. Between five and ten clones were isolated and sequenced to encapsulate the spread of methylation that was present within the given cell population.

A standard test for pluripotency was used to assess the potential of our derived iPS lines to contribute into all three germ lineages (endoderm, ectoderm and mesoderm) by injecting approximately $2x10^6$ iPS cells resuspended in 50 μL DMEM/F12 supplemented with 30% BD Matrigel™. iPSCs from both A–T homozygotes (AT34 and AT30) and A–T heterozygote parents (ATh47) formed teratomas when injected into SCID mice comprising tissue types from all three germ layers (endoderm, mesoderm and ectoderm), indicating capacity for pluripotential tri-lineage differentiation (as shown in Figure 2.9).

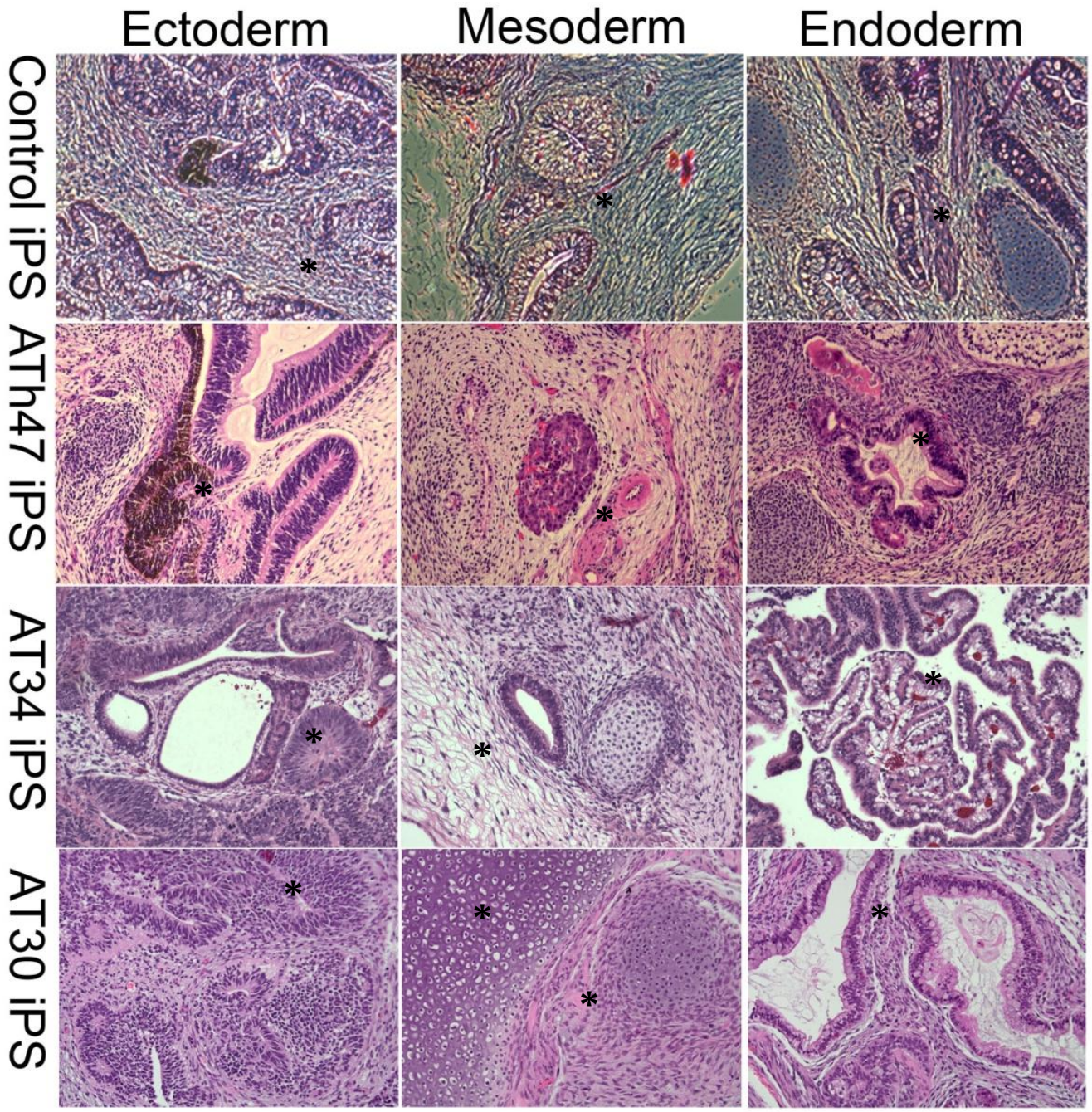

Figure 2.9 – H&E stains of paraffin embedded teratoma sections from control, ATh47, AT34 and AT30 iPSCs that show presence of all three germ lineages, indicating pluripotentcy.

We observed structures representative of all three germ lineages including glandular epithelium (endoderm), cartilage (mesoderm) and pigmented epithelium (ectoderm) (UQ0001i-control1), retinal epithelium (ectoderm), liver (mesoderm) and endodermal glands (endoderm) (A–T heterozygote UQ0001i-ATh47.1), neuroepithelium (ectoderm), cartilage (mesoderm) and intestinal tissue (endoderm) (A–T homozygote UQ0002i-AT34), neuroepithelium (ectoderm), stroma and cartilage (mesdoderm) and glandular epithelium (endoderm) (A–T homozygote UQ0004i-AT30. We conclude from this that no gross interference with pluripotency was evident in iPS cells generated from A–T patients.

Discussion

Emerging evidence suggests that the DNA damage pathways are activated early during reprogramming and may pose a barrier to iPSC generation [40, 94, 135]. The generation of iPSCs from chromosomal instability syndromes has indeed proven to be difficult without gene manipulation. Raya et al. showed that somatic cells from patients with the rare recessive chromosomal instability disorder Fanconi anaemia could be reprogrammed to pluripotency to generate patient-specific iPSCs only after correction of the defective gene with cDNA [61]. We have shown that this is not necessary, by demonstrating for the first time that fibroblasts from patients with A–T, a syndrome characterized by genome instability, can be reprogrammed to pluripotency and meet all the established criteria for *bona fide* iPSCs.

We observed survival and proliferation of virally transduced fibroblasts to be vastly enhanced by the stepwise addition of KSR stem cell media to the native FCS containing fibroblast media (Figures 2.1A.B&C) but showed that neither this, nor the addition of p53 inhibitor was essential for the generation of iPS cells from A–T patient fibroblasts (Figures 2.1/2.2).

The efficiency of reprogramming A–T fibroblasts (family 1) to iPSCs was approximately 4% of that seen with controls, with heterozygotes of intermediate efficiency (Figure 2.2). This is in keeping with the observation that reprogramming of mouse *Atm*-deficient tail-tip fibroblasts occurs with efficiency less than 2% of that of wild-type fibroblasts [95]. Reprogramming of a

second family with a distinct genetic background showed results consistent with this – generation of colonies from homozygotes yielded markedly fewer colonies to those of heterozygotes (Figure 2.2). Interestingly reprogramming efficiency was drastically reduced in controls from these experiments indicating a natural intrinsic variability in this process. This serves to illustrate the point that reprogramming kinetics may vastly differ across experiments and tissue sources. For the purpose of detailed investigation into reprogramming kinetics, these data highlight the need for approaches that encompass simultaneous reprogramming of multiple cell lines with experimental replicates.

During the process of reprogramming, cells may be less tolerant to the presence of DNA damage where p53 may play an important role in removing these cells by inducing apoptosis [40]. It is likely that the accumulation of DNA DSB during reprogramming of A–T fibroblasts renders these cells more susceptible to apoptosis or makes them otherwise unavailable for reprogramming. Short telomeres may also contribute to the barrier of cell reprogramming imposed by p53 [143]. This is also significant for A–T since fibroblasts and lymphoblastoid cells from these patients are characterized by abnormally short telomeres [144, 145]. Together this might explain the reduction in observed reprogramming efficiency in fibroblasts from A–T patients.

This chapter is a description of an optimized methodology for the complete production and characterization of iPS cells from patient fibroblasts using lentiviral factors. Also outlined are experiments monitoring the growth and response of cells in the period between transduction and successful establishment of iPS cell colonies, with a variety of conditions postulated to enhance the reprogramming process through survival and selection. We used this data to adapt a protocol that allowed a more efficient acquisition of iPS cells from A–T fibroblasts by the stepwise addition of serum-containing media, rather than the stark addition of media that is reported in the literature.

Further we outline techniques necessary to meet the stringent criteria required to validate these clones as *bona-fide* iPS including CpG island methylation status interrogation at specific gene

promoters (Bisulfite sequencing), assays for transgene silencing (PCR/qPCR), testing expression of pluripotency genes/proteins (PCR, qPCR, immunostaining and FACS respectively) and teratoma formation. We show that it was possible to not only derive but maintain karyotypically stable iPS cell cultures from A–T patients.

Finally and importantly, this chapter provides validation of iPS cell lines that are used in subsequent work to investigate the role of ATM in pluripotent context and also as a model of this disease. In addition to the lentivirally-derived iPSC described in this chapter, in subsequent chapters we have utilized iPSC generated episomally within our lab (by Jian-Sun). The methodology concerning generation and characterization of these lines is described in [146].

3.0 A–T iPSC recapitulate the cellular phenotype

Introduction

Conventionally available disease models commonly used in laboratory investigations, such as fibroblasts, lymphoblastoid cells and other immortalized cell lines are restricted to providing a limited range of contextual information, which may be only partially relevant to an actual disease phenotype. Human pluripotent stem cells are useful, as they allow as close a model system of the developmental state of the embryo as possible. This may be extended to explore early mechanisms of disease pathogenesis and also developmental processes that occur downstream, such as neurogenesis, hematopoiesis and cardiogenesis. An embryonic knockout model of ATM could be expected to closely resemble the processes which occur during the blastocyst stage of an individual with A–T, allowing insight into what role ATM might have in this and subsequent developmental contexts.

Although ATM is a known DNA damage regulator and is extensively characterized in somatic cell models [73, 75, 77], due to the technical and ethical constraints of working with such models, very little is known about the function of ATM during early embryonic development. In the previous chapter the generation, screening and characterization of iPS cells from patients with A–T was described. The relative breadth of knowledge on the role of ATM in somatic cells in contrast to pluripotent stem cells presents a large knowledge gap. This chapter describes the use of iPS cells from A–T patients in an investigation into the role of ATM in human pluripotent cells to aid in the elucidation of early events which may help define the onset of this disease.

These cells recapitulate important aspects of the A–T phenotype, including exhibition of various aberrant cellular responses to DNA damage, such as apoptosis and cell cycle control. We also have for the first time defined the transcriptional landscape of ATM deficient pluripotent cells and show deregulation of molecular pathways previously associated with *ATM*, as well as gene expression changes in the pentose phosphate and mitochondrial oxidative phosphorylation pathways. These findings provide novel insights into early developmental consequences of *ATM* deficiency that may contribute to A–T pathogenesis.

This chapter describes work that was published in *Stem cells & Translational Medicine [147]*.

Materials and methods

Immunoblotting

Cell extracts were prepared as previously described [148]. Proteins were separated using SDS-PAGE and transferred to nitrocellulose using Towbin's buffer and 100V for 1h at 4^{o}C prior to immunoblotting. Membranes were blocked with PBS blocking buffer containing 5% skim milk and 0.05% Tween20 for 1 hour at room temperature and incubated for 16 hours with antibodies to SMC1 [1 µg/ml] , SMC1pS5957 [1 µg/ml], KAP-1 [1 µg/ml] and KAP-1pS824 [1 µg/ml] (rabbit polyclonals, Novus Biologicals, USA); anti-rabbit p53 [2 µg/ml] and anti-mouse p53pS15 [2 µg/ml] (Cell Signalling Technology, MA); anti-rabbit Chk2 [2 µg/ml],Chk2pT68 [3 µg/ml] (Abcam UK), anti-rabbit ATMpS1981 [2 µg/ml] (Rockland, USA) or anti-ATM [2 µg/ml] (mouse monoclonals, GeneTex, USA) diluted in blocking buffer at the indicated dilutions . Following washing in PBS buffer containing 0.05% Tween20, anti-mouse HRP [1 µg/3ml] (Millipore, USA) and anti-rabbit [1 µg/5ml] (Rockland, USA) secondary antibodies diluted in blocking buffer were used. Secondary antibody reactivity was visualized using ECL (PerkinElmer Life Science).

Irradiation

A Co^{60} source irradiator (GammaCell 220) was used to deliver 2 Gy of IR (ionizing radiation) to the cells (Dose rate 8130 Gy/Hour). Cells were returned to the incubator to recover to the appropriate time point before harvesting/fixation with 4% paraformaldehyde, lysate preparation or processing for FACS.

TUNEL assay

Following IR or mock dose, cells were washed once in PBS and harvested with cell dissociation buffer (GIBCO). The TUNEL assay was employed as per the manufacturer's specifications to determine apoptosis according to the *in situ* cell death detection kit (Roche).

G2M Checkpoint Analysis

Activation of the G2/M checkpoint was determined by histone H3 phosphorylation [149]. Immunohistochemistry for the mitosis-specific marker phosphorylated histone H3 (Serine 10) (P-Histone H3S10) (Cell Signaling) [0.5 µg/ml] was performed two hours after 2Gy ionizing radiation or mock dose. Mitotic index was derived by counting the proportion of immune-positive cells for H3S10 staining divided by the number of nuclei stained by DAPI. General linear models were performed to assess for differences in the proportions for the three different groups (A–T, Control iPSCs and H9) and the irradiated states (irradiated and un- irradiated). Analyses were performed on the mean arcsine square-root proportions, and the results were then back-transformed for presentation. All results presented were backtransformed to the original scale. No significant difference was found between control iPSCs and H9s, so we pooled this data to compare to A–T iPSCs. An average of >650 events were quantified from each condition in 3 independent experiments. Slides were photographed using an OlympusBX61 microscope (4x and 100x magnifications).

Radioresistant DNA synthesis

Radioresistant DNA synthesis was determined by DNA fiber labeling as described [150, 151]. Briefly, A–T and control iPSCs were pulsed for 15 minutes with [50 µM] chlorodeoxyuridine (CldU), washed, followed by exposure to mock/2 Gy of radiation prior to a second pulse for 15 minutes with [50 µM] iododeoxyuridine (IdU). DNA fibres were made following the approach as previously outlined. Ongoing initiations and new replication forks were visualised via immunofluorescent microscopy after staining with rat monoclonal anti-Brdy (Bromodeoxyuridine) (Abcam) [13.3 µg/ml] and mouse monoclonal anti-BrdU (BD) (1/8 concentration not provided by manufacturer). Secondary antibodies were goat anti-rat Alexa488 conjugated secondary (Molecular Probes) [6.7 µg/ml] and donkey anti-mouse Alexa594 conjugated secondary [6.7 µg/ml]. Two-by-two factorial ANOVA were performed to assess for differences in the proportions for the two different genotypes (A–T vs. control) and the irradiated states (irradiated and unirradiated). Analyses were performed on the arcsine square-root proportions, and the results (means and confidence intervals) were then back-transformed for presentation. Analyses showed that there were no differences between the two sub-studies,

and all analyses were performed on the combined dataset, not taking into account the sub-studies. All results presented from analyses were back transformed to the original scale. More than 700 events were quantified from each condition in 2 independent experiments. Slides were photographed using a Zeiss LSM 710 Confocal microscope (63x magnification).

Expression Analysis

RNA was harvested from TRA-1-60 FACS sorted hESCs (MEL1), control iPS (UQ0001i-control1), A–T heterozygote iPS (UQ0001i-ATh47.1) and homozygote iPSCs (UQ0002i-AT34.7), as well as from non-sorted parental fibroblasts, as technical triplicates. Total RNA was isolated from each FACS sorted iPSC cell line and from unsorted fibroblast cell samples using the RNeasy Mini Kit (QIAGEN). The total RNA (and A260/A280 ratio) was then quantified using a NanoDrop 1000. Total RNA (100ng) was subjected to reverse transcription, second-strand cDNA synthesis and *in-vitro* transcription using the TotalPrep RNA Amplification Kit (Illumina). cRNA was hybridized to Illumina HT12 v4 BeadChip microarrays. The raw expression data were normalized using quantile normalisation and without background correction, using the lumi R/Bioconductor package (version 2.4.0) [152]. Only probes passing the Illumina detection threshold were included in the expression analysis; a probe passed the Illumina detection score if it had a detection P-value ≤ 0.01 in at least 75% of cell lines in the same group; these criteria resulted in 20,593 probes being retained. All statistical analyses were performed using R version 2.13.2. All probes were mapped using the annotation package illuminaHumanv4.db (version 1.10.0) available from Bioconductor. The expression data is available for download from Stemformatics and GEO under the accession number GSE35347. Heatmaps were constructed using the gplots R/Bioconductor package (version 2.10.1) where agglomerative hierarchical clustering was used based on a measure of dissimilarity 1 – R, where R represents the Pearson correlation coefficient between any two gene expression profiles and ranges from -1 to 1. Probes mapping to multiple gene symbols were filtered to ensure a one-to-one mapping between probe and gene symbol; the probe with the most significant P-value assessing the significance of differential expression between A–T and control iPSCs, was retained and represented in the resulting heatmap. P-values were generated using the

R/Bioconductor package limma (version 3.8.3), and adjusted for multiple testing using the Benjamini-Hochberg method [153]. The PluriNet gene list as identified by Muller et al. was originally downloaded from http://www.openstemcellwiki.org/ and consisted of 299 gene symbols, listed in appendices [154]. Plurinet genelist is listed in tab 1 of appendices. Pathway analysis was performed using the R/Bioconductor package attract (version 1.4.0) [155] where pathways were defined using the Kyoto Encyclopedia of Genes and Genomes [156]. The comparison of expression between mitochondrial genes in A–T and control iPSCs was based on genes represented in MitoCarta, a curated list of genes known to be involved in mammalian mitochondrial function. We used *attract* to compute a P-value representing the enrichment of genes showing differential expression across the seven cell types for which expression analysis was present. The mitochondrial gene list (shown in tab 3 of appendices) had a statistically significant P-value of 9.47×10^{-19} and we were able to decompose this pathway into four groups of genes showing distinct patterns of correlated expression. Gene lists of groups of mitochondrial genes identified by attract and subdivided on the basis of cell type and/or genotype are listed in tab 4 of appendices.

Imaging of mitochondria (membrane potential, mROS, mitochondrial mass)

To image mitochondria in iPSC colonies, cells were incubated on-plate with TMRM (Tetramethylrhodamine, Methyl Ester, a cell permeant dye which accumulates within the membrane of active mitochondria) at [10 nM] and Mitotracker (a fluorescent mitochondrial stain which binds to mitochondria regardless of membrane potential) (Life technologies) at [100 nM] according to the manufacturer's specifications and visualized on a fluorescent microscope.
For FACs, undifferentiated colonies were washed once in PBS and then harvested with cell dissociation buffer for 10 minutes at 37°C to form single cells. Cells were washed once in PBS before application of TMRM at [10 nM] and NAO (Nonyl Acridine Orange, a dye which selectively binds to cardiolipin within mitochondria in a membrane potential-independent fashion) (Life technologies) at [10 µM] according to the manufacturer's instructions. TMRM was also added to the media during acquisition via FACs. CCCP (Carbonyl cyanide *m*-chlorophenyl hydrazone, an uncoupler of the electron transport gradient within mitochondria)

(Life technologies) (was used at [50 uM] as a control. Mitochondrial ROS (Reactive oxygen species) were quantified by staining with mitoSOX (Life technologies) at [5 μM] according to the manufacturer's specifications.

Generation and characterization of non-viral A–T and control iPSCs

In addition to lentivirally derived iPS lines, we further generated A–T and control iPS lines from fibroblast cultures by transfection with the pCEP4 episomal vectors pEP4EO2SCK2MEN2L and pEP4EO2SET2K (from [36], also using AMAXA nucleofection (free from viral particles). Derived lines were screened similarly to approaches outlined in publications from our laboratory [146, 147] by immunocytochemistry detection of pluripotency markers OCT4, NANOG, SOX2, SSEA-4, TRA-1-81, TRA-1-60 and formation of teratomas comprised of derivatives of all 3 germ layers (data not shown). Standard karyotype analysis confirmed normal or karyotypes in control andA–T iPSCs respectively (data not shown).

Results

ATM protein levels

Family one (ATh47 and AT34) mutation analysis revealed two frameshift deletions (7004delCA and 7886delTATTA) predicted to result in truncated and thus unstable ATM protein. Family two (AT30 and ATh41) mutation analysis revealed compound heterozygous mutations 8368delA and 7570delG (work performed by Professor Richard Gatti, UCLA). As predicted, we failed to detect ATM protein (Figure 3.1A) in western blotting of lysates taken from AT34 fibroblasts or iPS cells (3 clones) (lanes 6, 7, 8&9 respectively). A reduced amount of ATM protein compared to controls was detected in A–T heterozygote ATh47 fibroblasts and iPS cells (lanes 4 and 5). DNA-PK was used as a loading control. Consistent with this, using immunofluorescent microscopy detection we could not visualize ATM in iPS cells from A–T homozygote AT34, while ATM could be detected in both the cytoplasm and nucleus of control iPS cells (Figure 3.1B).

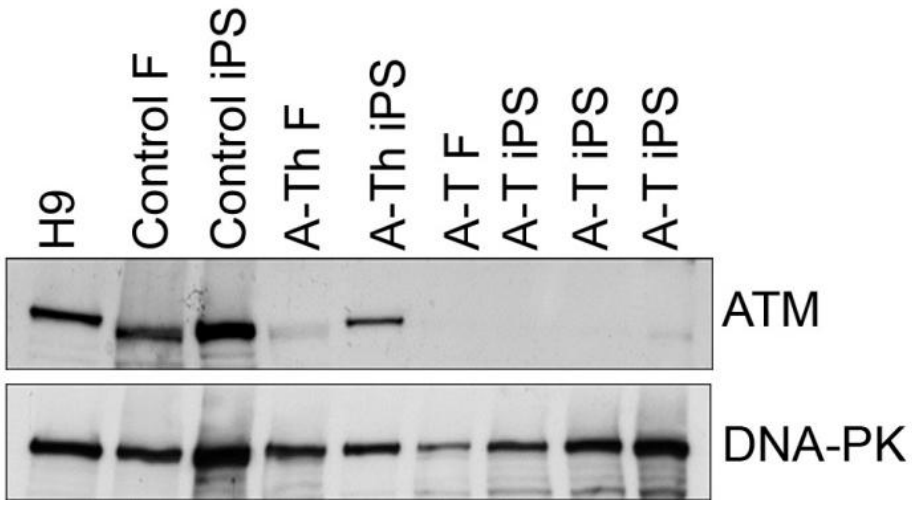

Figure 3.1A – Absence of detectable ATM protein in lysates from A–T patient fibroblasts and iPS cells. Western blot showing expression of ATM in H9 hESCs (lane 1), control fibroblasts (lane 2), control iPSCs (lane 3), heterozygote A–T fibroblasts (lane 4), heterozygote A–T iPSCs (lane 5), A–T homozygote fibroblasts (lane 6), and homozygote A–T iPSCs (lane 7-9). DNA-PK is used as a loading control.

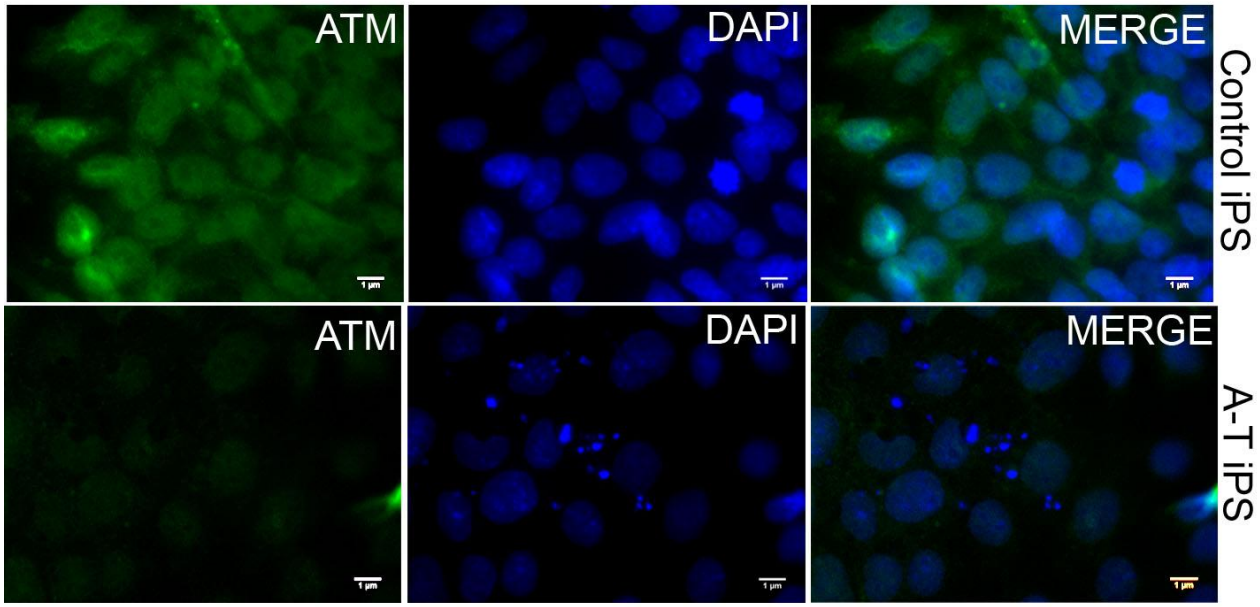

Figure 3.1B – Immunofluorscent microscopy reveals no detectable ATM protein in iPS cells from A–T patient AT34. Immunofluorescent detection of ATM protein in control iPSCs (top) and A–T iPSCs (bottom). DAPI stains the nuclei. Secondary antibody staining alone revealed no cross reactivity (not shown). Scale bars are 1 μm.

ATM Kinase assays

To confirm lack of kinase activity in A–T patient derived iPS cells, we performed irradiation on cultured control/A–T iPS cells and also a human embryonic stem cell line (H9). Lysates were harvested at one and four hours post irradiation, including a mock-irradiated sample (ie 0 hours/no irradiation). After immunoprecipitation (IP) with an antibody for ATM [157]
we observed phosphorylation of ATM at S2996, S367 and S1981 in both control iPS and hESC lines. This however was absent in AT34 indicating a lack of detectable ATM kinase activity (Figure 3.2A). We confirmed this by immunostaining irradiated/mock-irradiated control and A–T iPS cells for autophosphorylation sites on ATM, pS1981 and pS367 (Figure 3.2B). In agreement with western blotting/IP data, immunofluorescent staining failed to detect ionizing-radiation induced foci (which correspond to proteins or protein modifications recruited to sites of DNA damage or repair [158]) in irradiated A–T iPSCs whereas clear nuclear localization of ATM pS367 and ATM pS1981 was detected in irradiated control iPSCs (Fig 3.2B). γH2AX foci

were present in both controls and A–T iPSCs indicating DNA repair was actively proceeding in the absence of ATM protein.

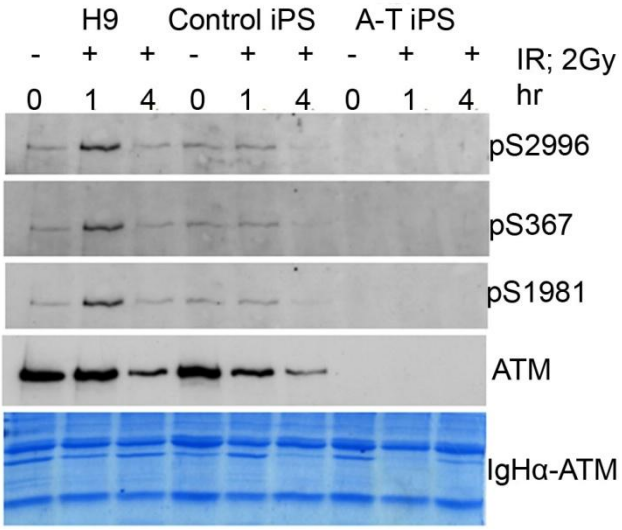

Figure 3.2A - Ionizing radiation fails to activate ATM signaling in A–T iPSCs. Western blot analysis of ATM autophosphorylation sites S2996, S367 and S1981 in immunoprecipitated ATM protein from H9 hESCs, control iPSCs and A–T iPSCs following irradiation with 2 Gy IR for 0, 1 and 4 hours. A Coomassie stained gel of the ATM immunoprecipitate is used as a loading control.

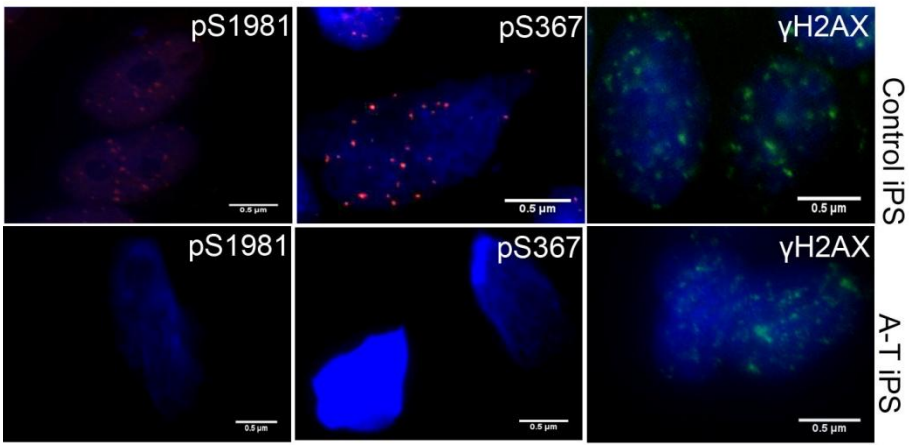

Figure 3.2B - Immunofluorescent detection of ATM autophosphorylation sites S1981 and S367 and γH2AX foci in control iPSCs (top) and A–T iPSCs (bottom) after IR (2Gy, 1hr). Scale bars are 0.5 µm.

Once ATM is activated it phosphorylates a large number of substrates in multiple pathways [148, 159, 160], including proteins involved in cell survival and cell cycle control (eg p53 and Chk2) and maintenance of chromatin structure (Kap1 SMC1). In control iPSCs, all of these substrates were phosphorylated and p53 was stabilized in response to radiation exposure but this did not occur in A–T iPSCs (Fig 3.2C). We conclude from this that ionizing radiation induced ATM-dependent signaling is defective in A–T iPSCs.

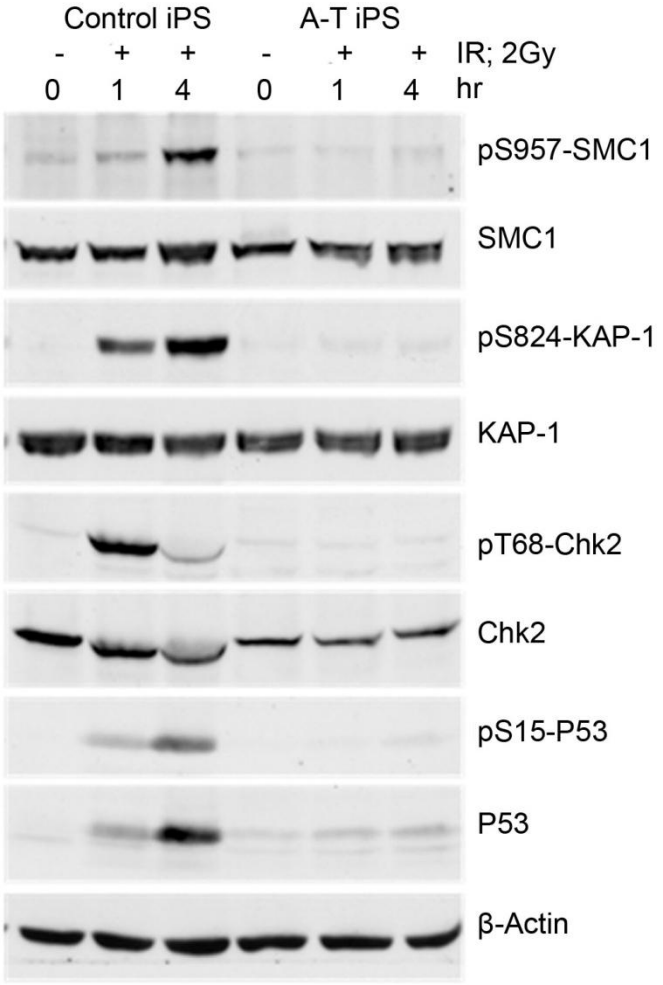

Figure 3.2C – Western blot analysis of phosphorylation of ATM downstream targets SMC1 (S957), KAP1 (S824) and Chk2 (T68) and p53 stabilization in control and A–T iPSCs following 0, 1 and 4 hrs of IR (2 Gy).

Cell cycle response to ionizing radiation

Another cellular hallmark of A–T is defective cell cycle checkpoint activation in response to DNA DSB [74]. We therefore measured G2M delay using histone H3 phosphorylation after exposure to 2 Gy of radiation. Control iPSCs showed characteristic inhibition of entry into mitosis two hours after exposure to 2 Gy similar to H9 hESCs (Fig 3.3A) whereas A–T iPSCs exhibited a greatly reduced inhibition of mitotic entry after the same dose of radiation.

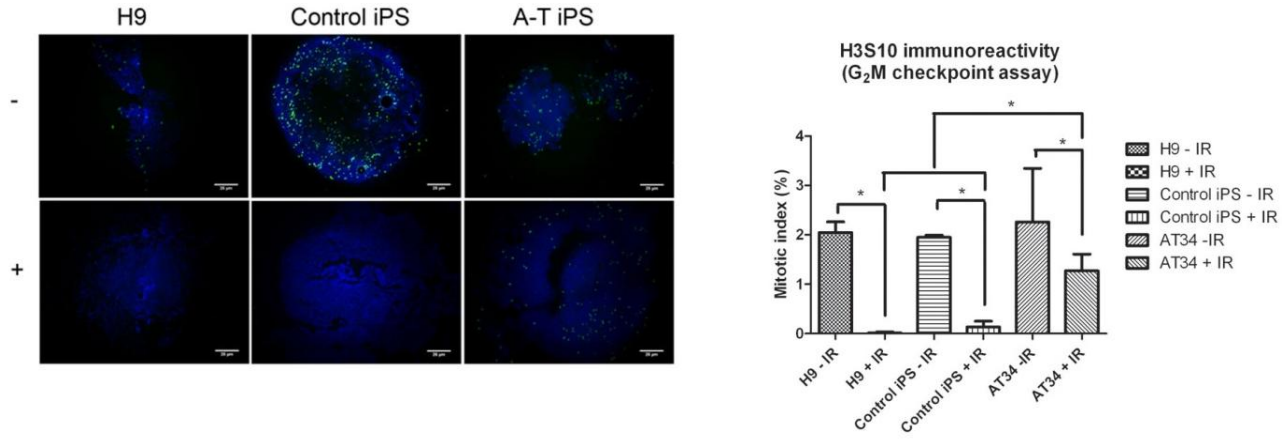

Figure 3.3A - H3S10 immunostaining of cells following 2 Gy IR or mock dose was quantified. A–T iPSCs show persistent staining relative to controls (H9 hESCs and control iPSCs shown in top panel) indicative of a failure to arrest at the G2M checkpoint. (>600 events were quantified from each condition in 3 independent experiments, error bars show SEM, $p < 0.05$). Scale bars are 25 µm.

Exposure of cells to radiation leads to rapid inhibition of DNA synthesis, and this is used to determine the intra-S phase checkpoint. When somatic A–T cells are irradiated they exhibit radioresistant DNA synthesis or a defective S-phase checkpoint [142]. The S-phase checkpoint was determined using a DNA fibre assay where the extent of DNA synthesis is expressed as a percentage of new initiations relative to total elongations in irradiated and non-irradiated cells [151]. DNA synthesis was inhibited by 60% in control iPSCs while in A–T iPSCs DNA synthesis was only inhibited by 20%, demonstrating the presence of radioresistant DNA synthesis in A–T iPSCs (Fig 3.3B).

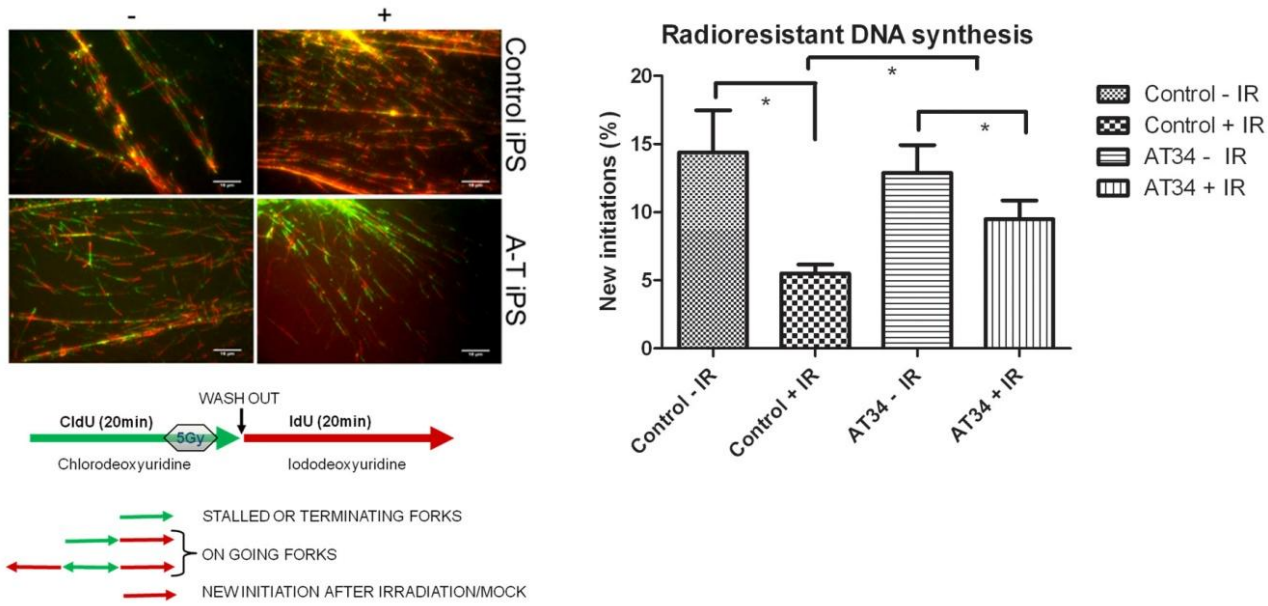

Figure 3.3B - A–T iPSCs exhibit radioresistant DNA synthesis following 2 Gy IR.) (>700 events were quantified from each condition in 2 independent experiments. Error bars show SEM). $p<0.05$). Scale bars are 16 µm.

Radiosensitivity (TUNEL assay)

We next examined the incidence of apoptosis in A–T and control iPSCs 24 h after exposure to 2 Gy of radiation. As shown in Fig 3.3C radiation-induced apotosis was approximately 3-fold higher in A–T iPSCs than in control iPSCs. Fig 3.3C further shows that even under standard culture conditions A–T iPSCs exhibited a two-fold higher load of apoptosis relative to controls.

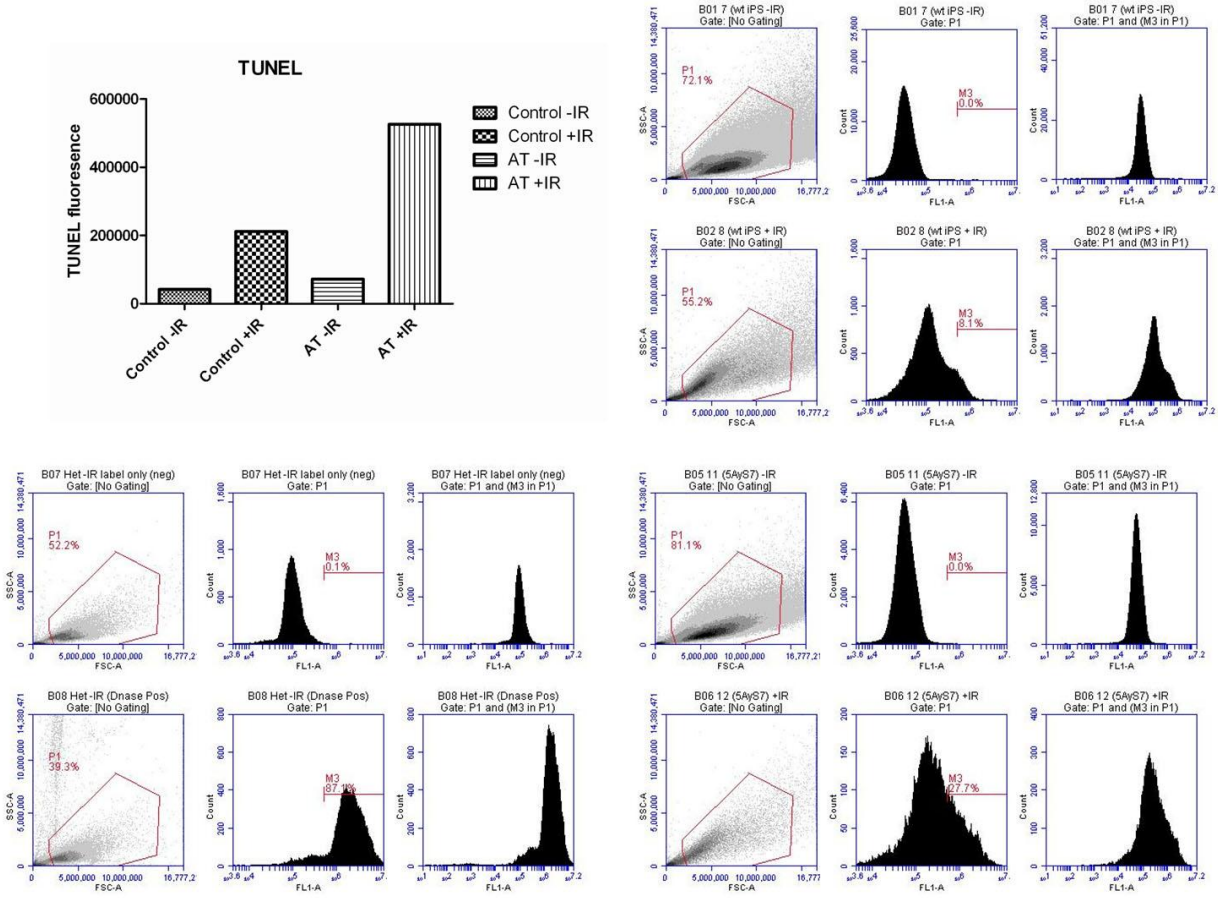

Figure 3.3C - Flow cytometric quantification of TUNEL staining of control and A–T (AT34) iPSCs 24 hrs after mock or 2 Gy IR. Populations were gated to exclude cellular debris and autofluorescence. Positive control was DNase treated iPSCs.

Microarray/Expression analysis

In addition to its role in responding to DNA DSB repair, ATM has also been implicated in a range of other cellular processes and its role in non-irradiated pluripotent cells has remained largely unexplored. We therefore examined in detail the transcriptome of unchallenged A–T iPSCs in culture using a combinatorial approach using the *Genego* and *attract* bioinformatic analysis tools. iPSCs from ATh47, AT34 & CRL2429 were sorted live by flow cytometry for expression of pluripotency surface marker TRA-1-160 to isolate a uniform series of RNA for comparison. Additionally we isolated RNA from hESC line MEL1 as a control for pluripotency

and also RNA from parental fibroblasts from ATh47, AT34 and CRL2429 (Figure 3.4A shows experimental design). Samples were prepared according to materials and methods and hybridized to Illumina HT12 v4 BeadChip microarrays. Samples were harvested as technical triplicates from each line, grown separately. The expression data is available for download from Stemformatics and GEO under the accession number GSE35347.

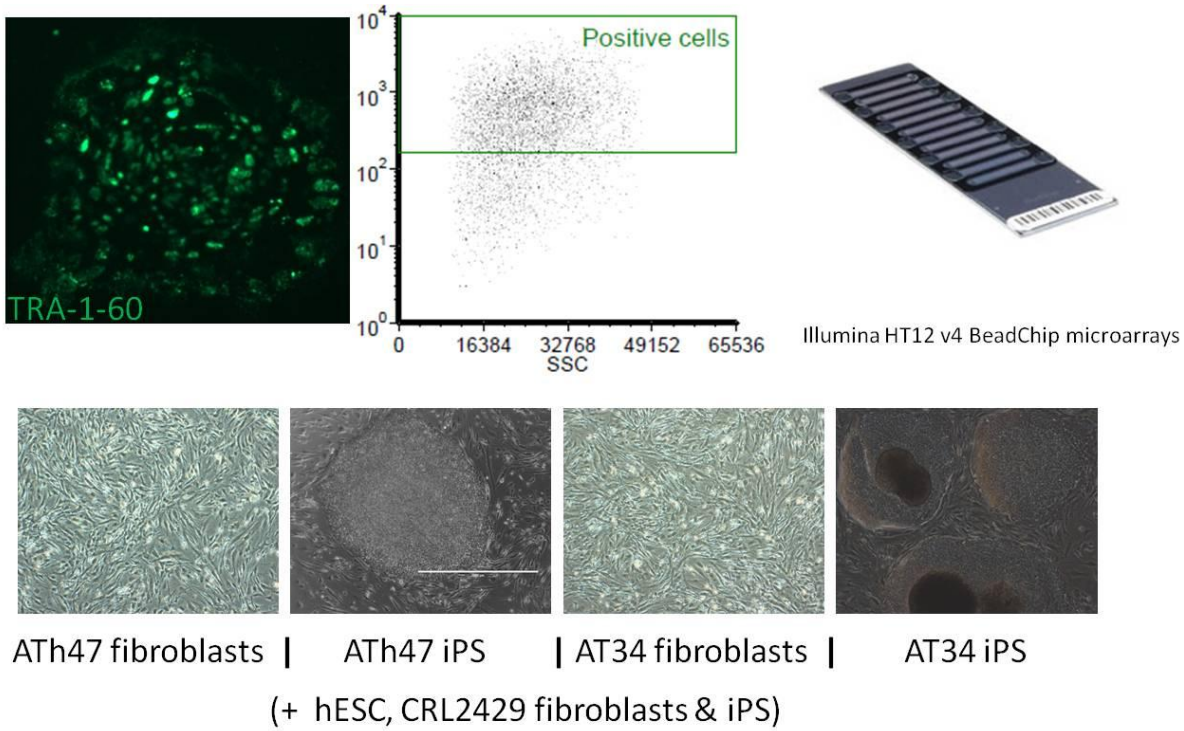

Figure 3.4A – Workflow schema outlining experimental design for expression array study. iPS cells from ATh47, AT34& CRL2429 were sorted live by flow cytometry for expression of the pluripotency surface marker TRA-1-60. Additionally included were parental fibroblasts from each iPS line and also hESC line MEL1.

Principal component analysis (Figure 3.4B) showed tight clustering of all experimental replicates. Separation of cell type (fibroblast vs pluripotent stem cell) based on gene expression could be clearly observed. Immediately apparent was the fact that pluripotent cells clustered more closely together, regardless of genotype. Control fibroblasts, A–T heterozygote fibroblasts and A–T homozygote fibroblasts separated from each other to a greater degree. These data indicate that the large transcriptome differences that exist between A–T fibroblasts and wild type

fibroblasts may largely be resolved after reprogramming. This may reflect the clonal nature of pluripotent stem cells. Additionally, the fact that loss of *ATM* impacts more strongly on fibroblasts than on pluripotent stem cells may provide evidence for redundancy of *ATM* in this setting.

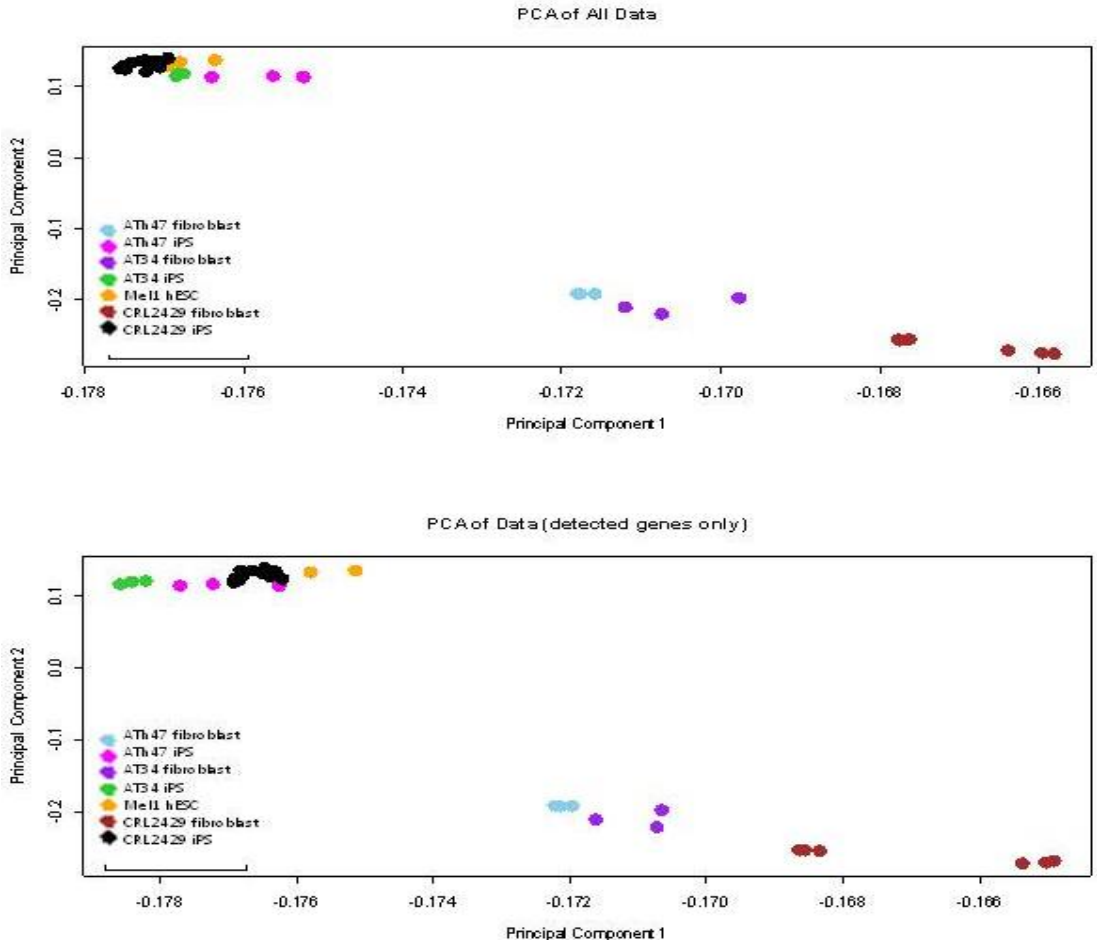

Figure 3.4B – Principal component analysis of all data (top) and detected genes only (bottom). Represented are ATh47 fibroblast (blue), ATh47 iPS (pink), AT34 fibroblast (purple), AT34 iPS (green), MEL1 hESC (yellow), CRL2429 fibroblast (brown) and CRL2429 iPS (black).

We examined principal component analysis plots and performed hierarchical clustering using a genelist of 299 genes assembled by Muller et al. as part of the *PluriNet* - a list of genes critical for self-renewal and pluripotency (Genelist located in appendices tab 1 ‘Plurinet’) [154].

Principal component analysis revealed the similarity in gene expression between A–T iPSCs, control iPSCs and hESCs and this was further reinforced by hierarchical clustering of the 299 pluripotency associated genes of the *PluriNet* (See figure 3.4C). We observed distinct patterns of gene expression between fibroblasts and pluripotent stem cells. iPSCs from ATh47 and AT34 were highly similar (Figure 3.4C) to control iPSCs and hESCs with respect to expression of these genes. We interpreted this to mean loss of *ATM* did not grossly affect pluripotency and that our reprogrammed lines were consistent with a fully reprogrammed iPSC phenotype. Heatmaps were constructed using the gplots R/Bioconductor package (version 2.10.1) where agglomerative hierarchical clustering was used based on a measure of dissimilarity 1 – R, where R represents the Pearson correlation coefficient between any two gene expression profiles and ranges from -1 to 1.

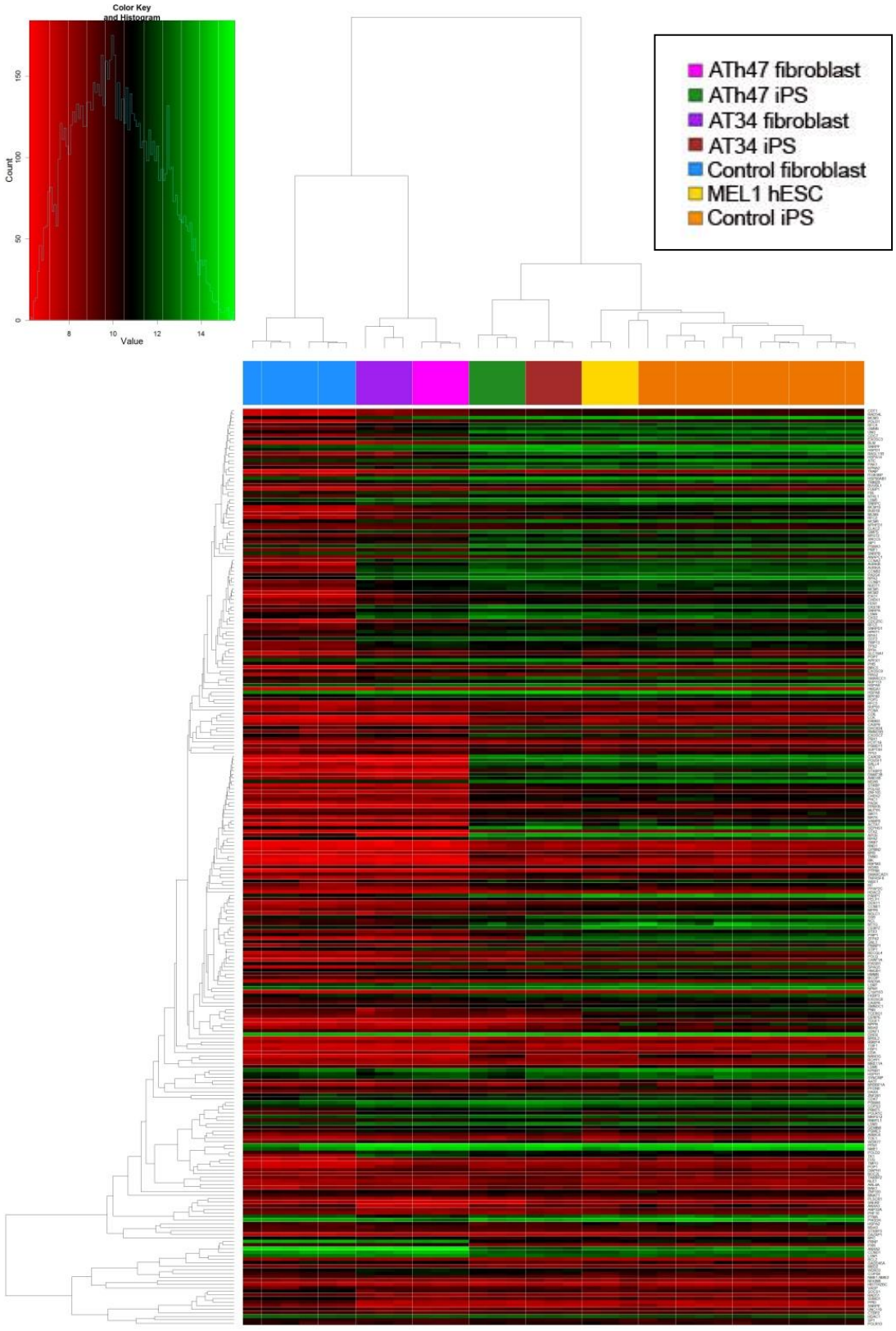

Figure 3.4C – Heatmap generated from *PluriNet* genelist.

Despite the tight clustering of pluripotent cells with regards to expression of genes in the *PluriNet*, 7921 genes were identified by *attract* to exhibit patterns of differential expression ($p<0.05$) (See appendices tab 2 'iPS study genelists' for genelist and log fold change values). A combinatorial approach was employed using both the *Genego* and *attract* bioinformatic analysis tools to analyze these differences. While *Genego* identifies pathways within significantly differentially expressed genes based upon existing knowledge (based on KEGG annotation), the *attract* pathway analysis tool examines the entire data set and identifies and amplifies new coordinately regulated gene sets that are relevant to the mechanisms underlying particular phenotypes [155].

Using a*ttract*, stark expression differences were identified that were largely defined by cell type (ie fibroblast vs. pluripotent stem cell). We focused on differences that were apparent within pluripotent stem cells, focusing on differences between control and *ATM* mutant iPS cells. Four of the significant pathways identified by *attract* are highlighted here to illustrate the expression differences observed between A–T and control iPSC lines. Each panel represents the average expression profile for a subset of genes in the pathway; the subset was selected by grouping together genes with correlated patterns of expression using agglomerative hierarchical clustering. The four main pathways that were identified by *attract* as most significantly altered were; *focal adhesion* (Figure 3.5A), *ECM (Extra-cellular matrix) receptor interaction* (Figure 3.5B), the *pentose phosphate pathway* (Figure 3.5C) and *oxidative phosphorylation* (Figure 3.5D). Genelists are available online through KEGG.

Figure 3.5A depicts heatmap gene expression data from this dataset on a KEGG annotated genelist pertaining to *focal adhesion*, (adjusted p-value 8.40×10^{-5}).

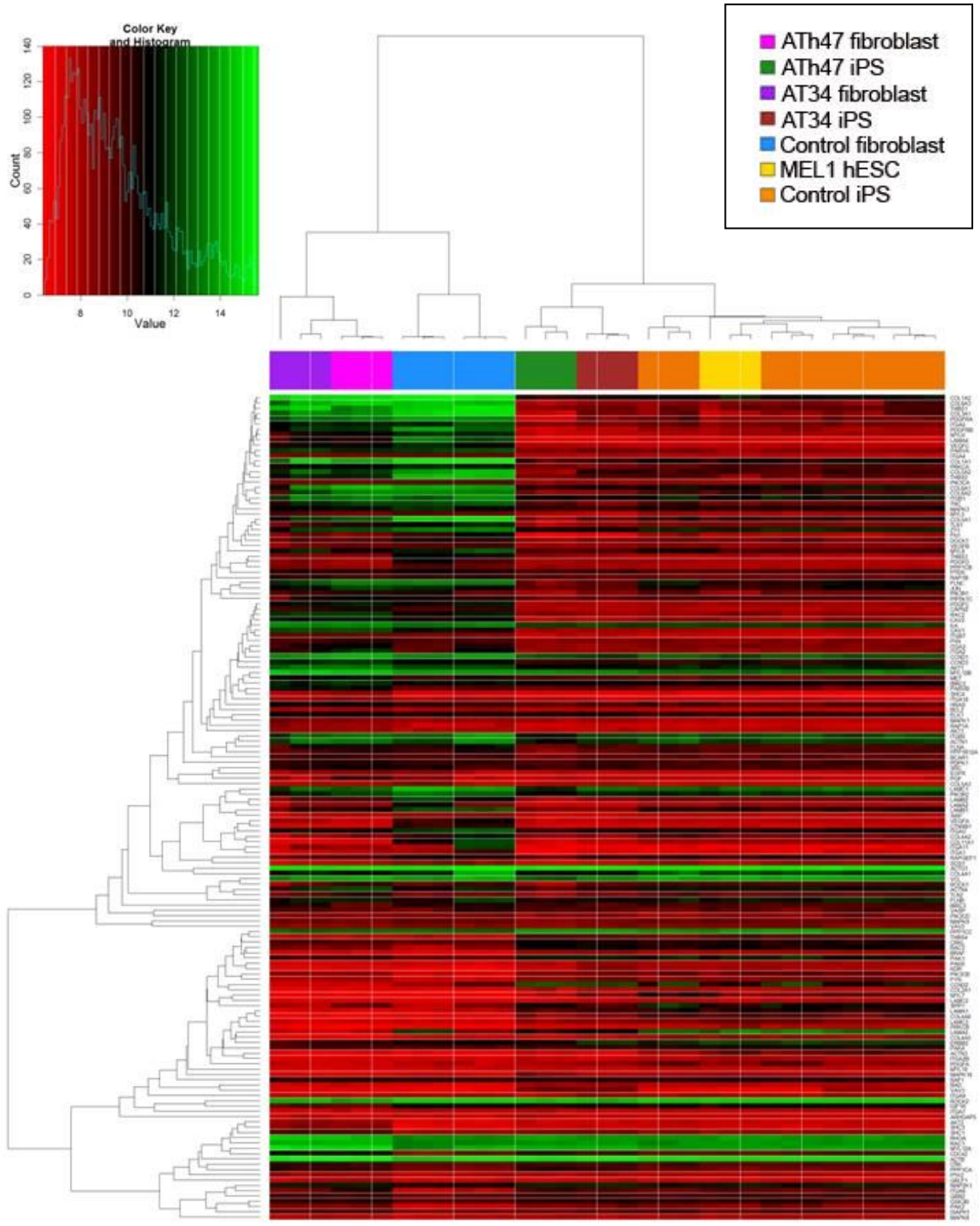

Figure 3.5A – Gene expression data based on *focal adhesion* genelist from KEGG. Adjusted p-value 8.40×10^{-5}.

These data were decompressed into groups based on patterns of correlated gene expression. Figure 3.5B shows one group in which a significant difference is apparent. This group represents 52 unique gene symbols (*BIRC3, COL11A1, COL1A1, COL4A1, COL4A2, COL4A5, COL5A1, COL5A3, COL6A1, COL6A2, CTNNB1, DOCK1, FLNC, FN1, FYN, ITGA1, ITGA11, ITGA7,ITGA9, ITGAV, JUN, LAMA2, LAMB1, LAMB2, LAMC1, CDC42, MYL12A, RAC1, MAPK3 MAPK9 IGF1R, MYLK, PARVB, PDGFD, PIK3R1, PIK3R2, PIP5K1C, PPP1CB, PRKCA, PTK2, RAP1B, RAPGEF1, ROCK1, ROCK2, SOS1, THBS2, THBS3, TLN1, VEGFA, VEGFB, XIAP, ZYX*).

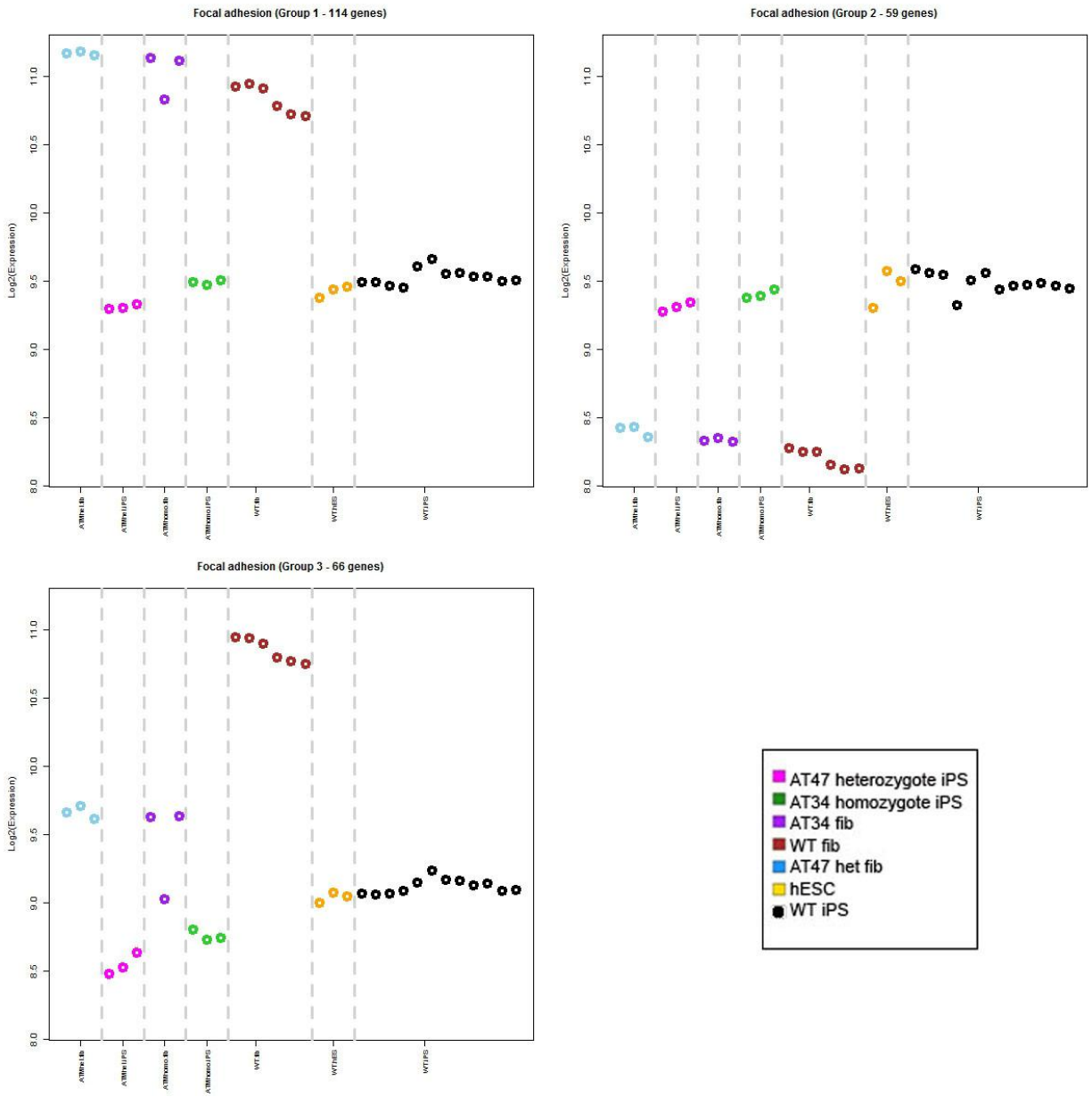

Figure 3.5B – Genelist compressed into groups. Group 3 showed a significant difference between control and ATM mutant iPSCs also apparent in differentiated cells.

Figure 3.5C depicts heatmap gene expression data from this dataset on a KEGG annotated genelist pertaining to *ECM receptor interaction*, Adjusted p-value 0.000165.

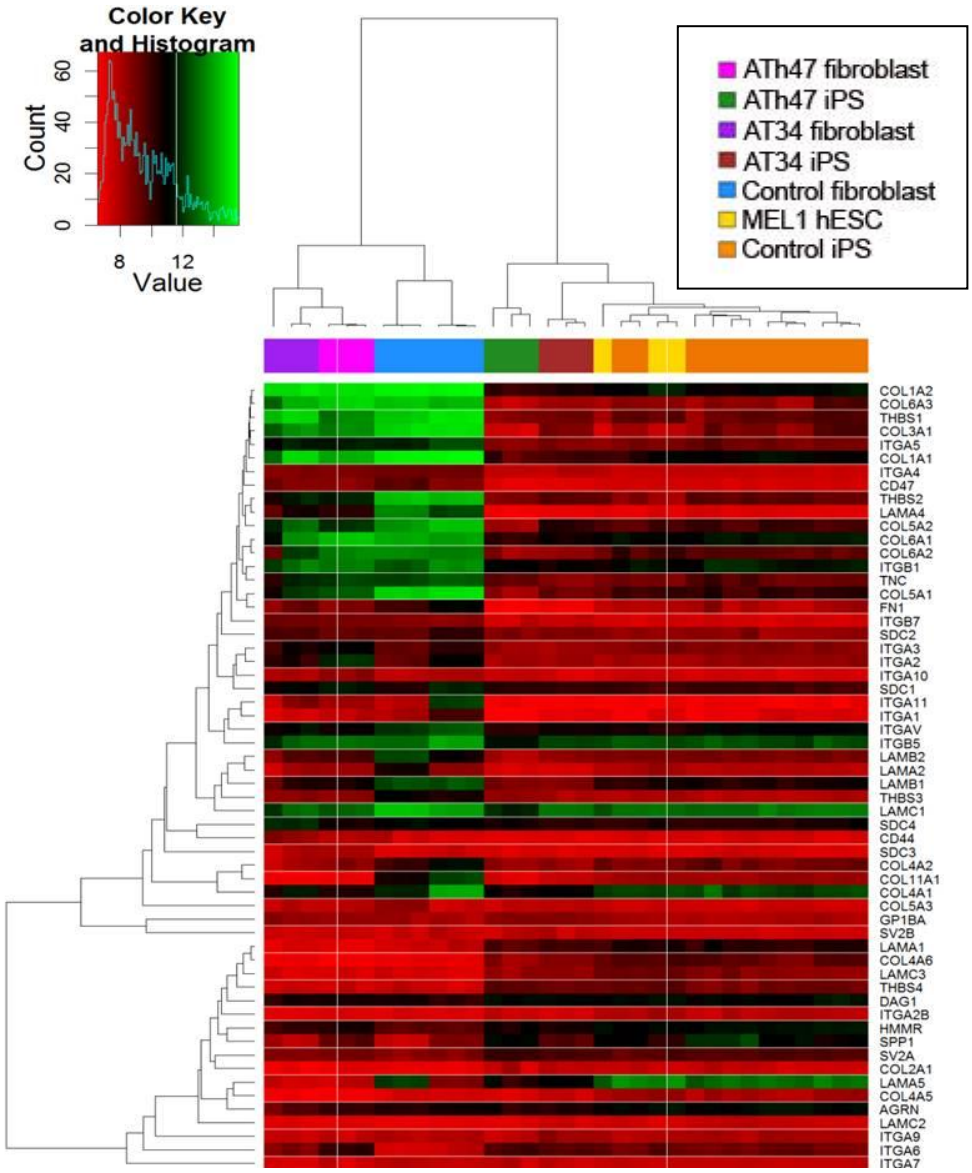

Figure 3.5C - Gene expression data based on *ECM receptor interaction* genelist from KEGG. Adjusted p-value 0.000165.

These data were decompressed into groups based on patterns of correlated gene expression. Figure 3.5D shows one group in which a significant difference is apparent. This group represents 22 unique gene symbols (*COL11A1, COL4A1, COL4A2, FN1, ITGA1, ITGA11, ITGAV, LAMA2, LAMB1, LAMB2, LAMC1, THBS3*).

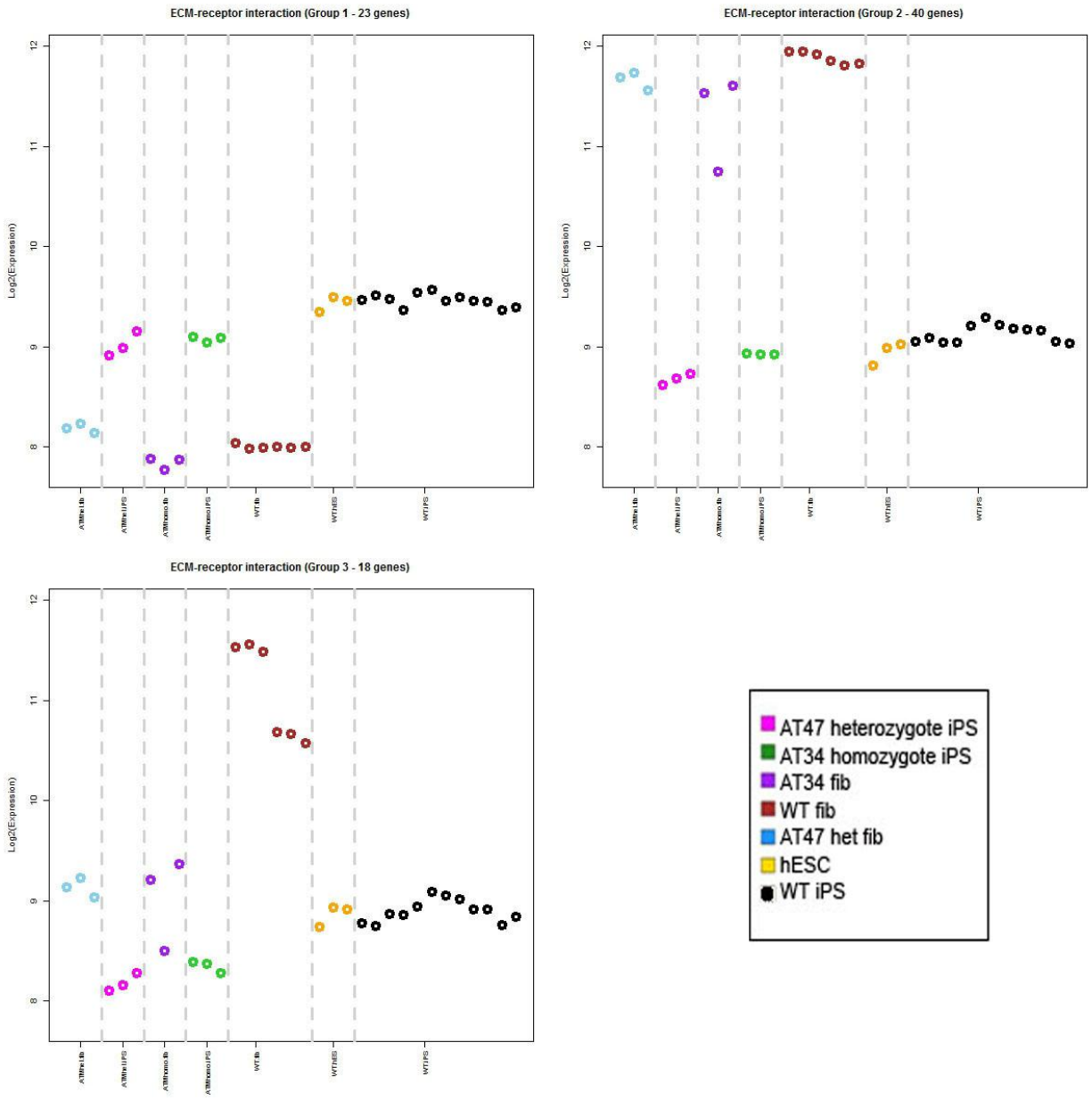

Figure 3.5D - Genelist compressed into groups. Shown is group 3 which showed a significant difference between control and ATM mutant iPSCs that is also apparent in differentiated cells.

Figure 3.5E depicts heatmap gene expression data from this dataset on a KEGG annotated genelist pertaining to the *pentose phosphate pathway*, Adjusted p-value 0.00899.

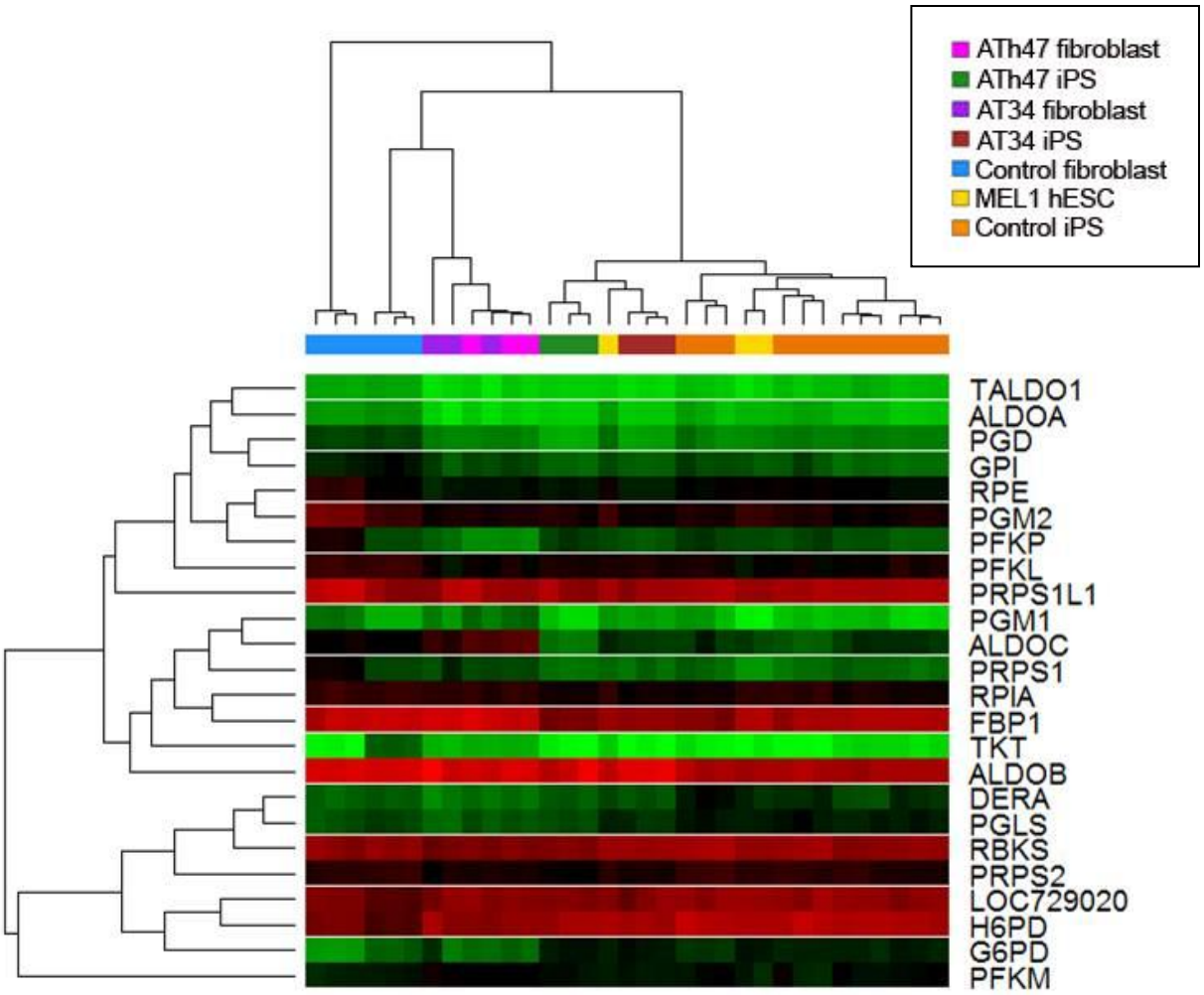

Figure 3.5E - Gene expression data based on *pentose phosphate pathway* genelist from KEGG. Adjusted p-value 0.00899.

These data were decompressed into groups based on patterns of correlated gene expression. Figure 3.5F shows one group in which a significant difference is apparent. This group represents 7 unique gene symbols (*DERA, G6PD, H6PD, LOC729020, PFKM, PGLS, RBKS*).

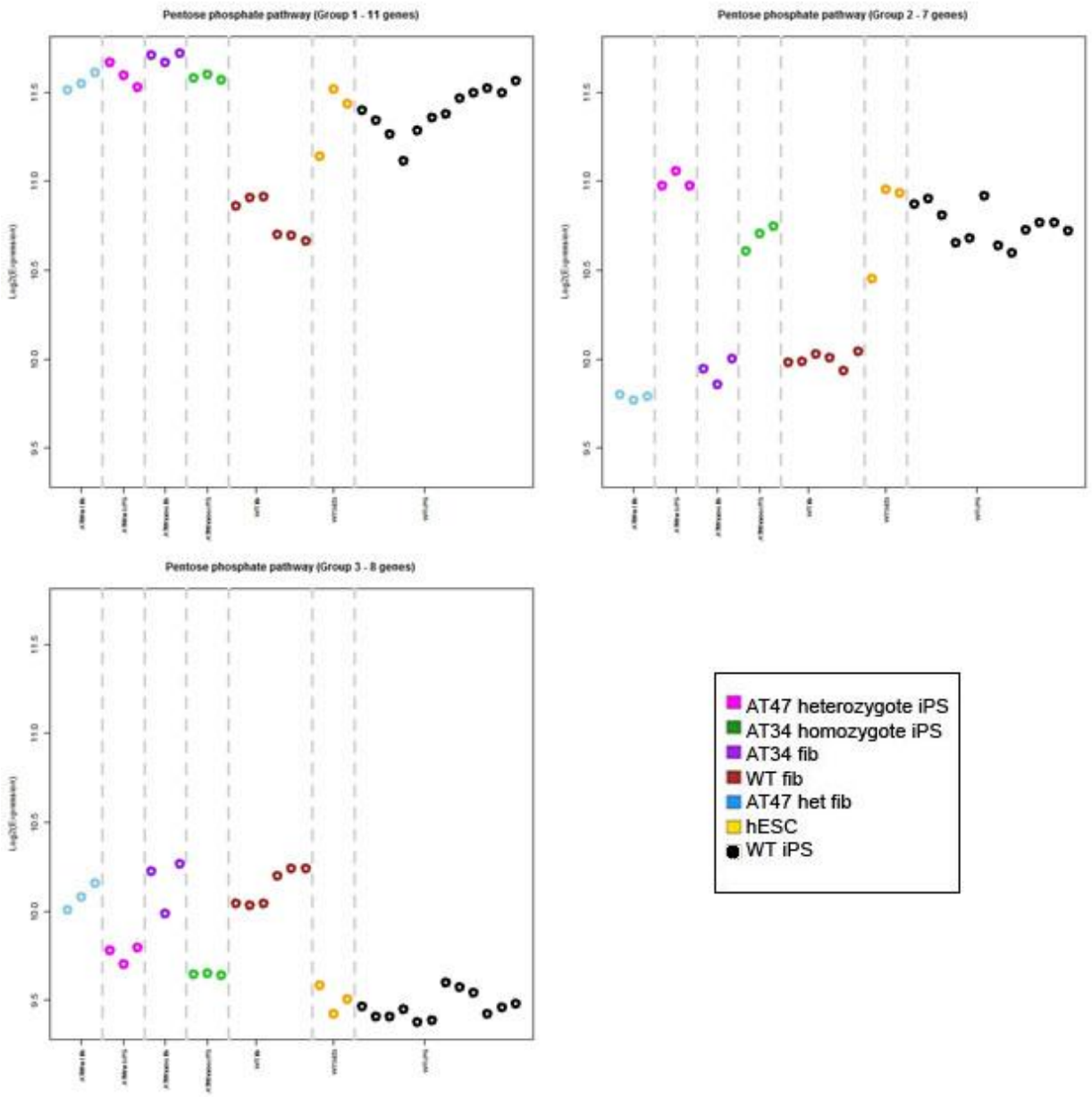

Figure 3.5F – Genelist compressed into groups. Groups 1 showed a significant difference between control and ATM mutant iPSCs.

Figure 3.5G depicts heatmap gene expression data from this dataset on a KEGG annotated genelist pertaining to the *oxidative phosphorylation* pathway, adjusted p-value 0.00336.

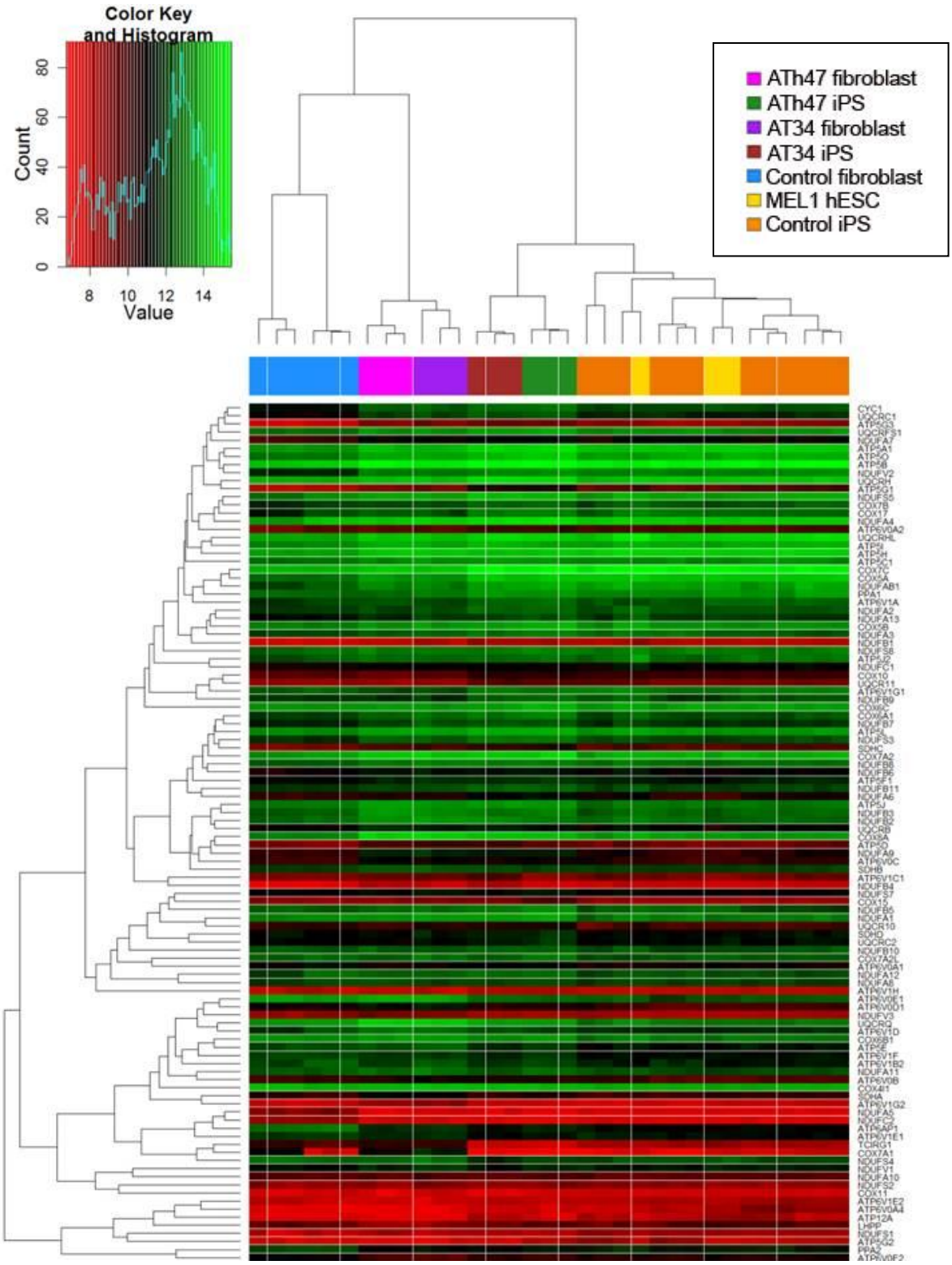

Figure 3.5G - Gene expression data based on *oxidative phosphorylation* genelist from KEGG, adjusted p-value 0.00336.

These data were decompressed into groups based on patterns of correlated gene expression. Figure 3.5G shows one group in which a significant difference is apparent. This group represents 40 unique gene symbols (*ATP5D, ATP5E, ATP5G2, ATP5J, ATP5L, ATP6V0A1, ATP6V0B, ATP6V0C, ATP6V0D1, ATP6V0E1, ATP6V1C1, ATP6V1D, ATP6V1G2, COX15, COX4I1, COX6B1, COX7A2, COX7A2L, COX8A, UQCR10, NDUFA1, NDUFA11, NDUFA12, NDUFA9, NDUFB10, NDUFB2, NDUFB3, NDUFB5, NDUFS7, NDUFV1, NDUFV3, PPA2, SDHA, SDHB, SDHC, SDHD, TCIRG1, UQCRB, UQCRC2, UQCRQ*).

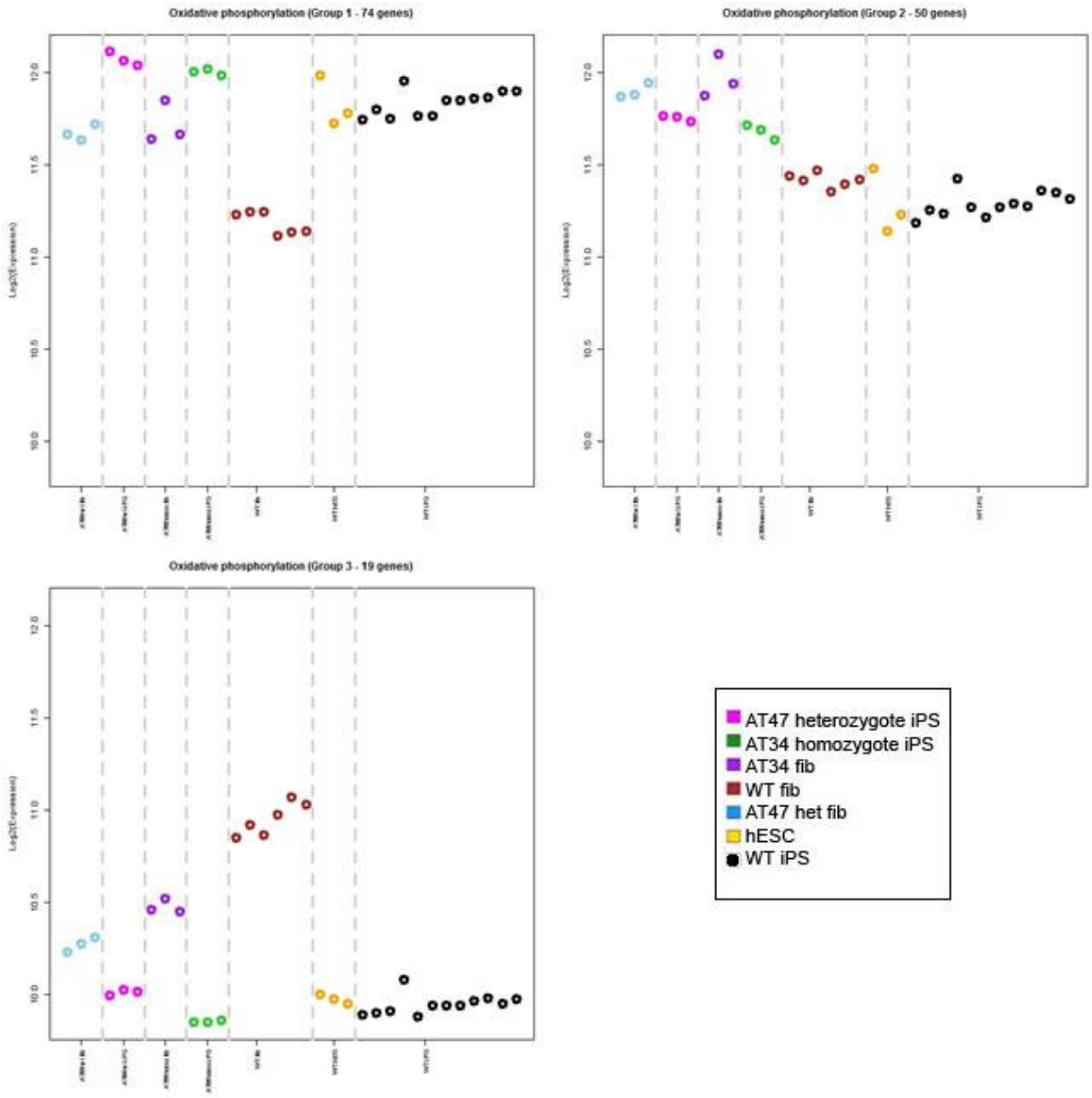

Figure 3.5H – Genelist compressed into groups. Shown is group 2 which showed a significant difference between control and ATM mutant iPSCs.

This led us to analyze the expression of 1080 genes, previously identified in the MitoCarta database [161], that are directly or indirectly associated with mitochondrial function within the 7921 genes that were differentially expressed (P-value < 0.05). Remarkably 464/1080 of these mitochondria associated genes were identified within the A–T iPSCs differentially expressed gene list (heatmap shown in Fig 3.5I), suggesting that mitochondrial function was a significantly

altered pathway in AT34. (Appendices shows list of up- and down-regulated genes). Using *attract* we were further able to attribute these mitochondrial gene expression differences to either cell state (i.e. iPS + ES vs fibroblasts) or genotype (i.e. A–T homozygous + heterozygous vs wild type), identifying four groups of mitochondrial activity. In two of these groups (group 2 and 3) *ATM* deficiency showed no difference, whereas Group 1 consisted of conserved ATM-centric changes that were apparent in both fibroblasts and pluripotent cells (Fig 3.5J). Most interestingly, Group 4 identified 212 mitochondria associated genes that appeared to be cell-type specific (See Appendices for gene lists of all four groups).

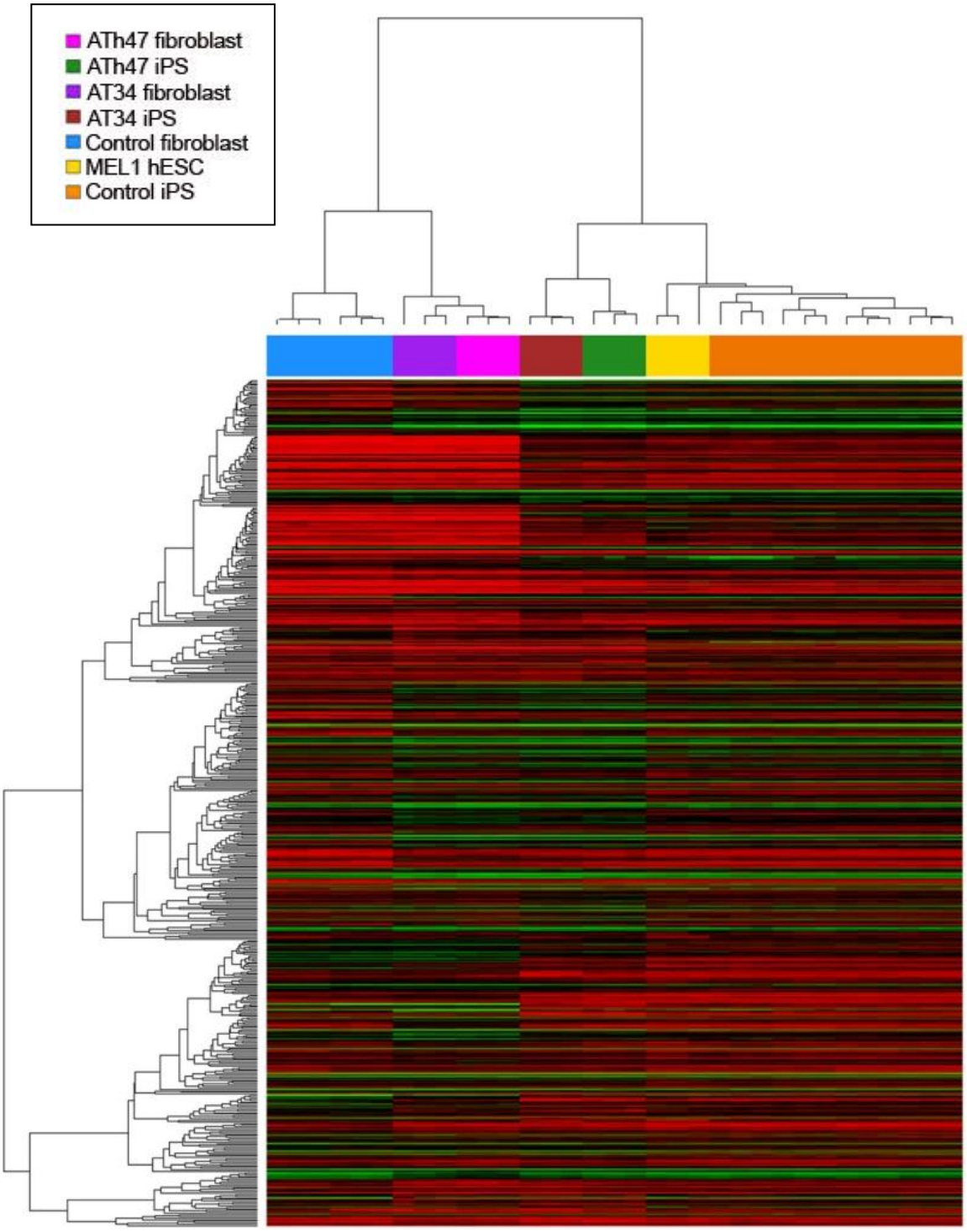

Figure 3.5I - Heatmap comparison of mitochondria associated genes (Mitocarta) between A–T heterozyogote fibroblasts and iPSCs, A–T homozygote fibroblasts and iPSCs, control fibroblasts and iPSCs and MEL1 hESCs.

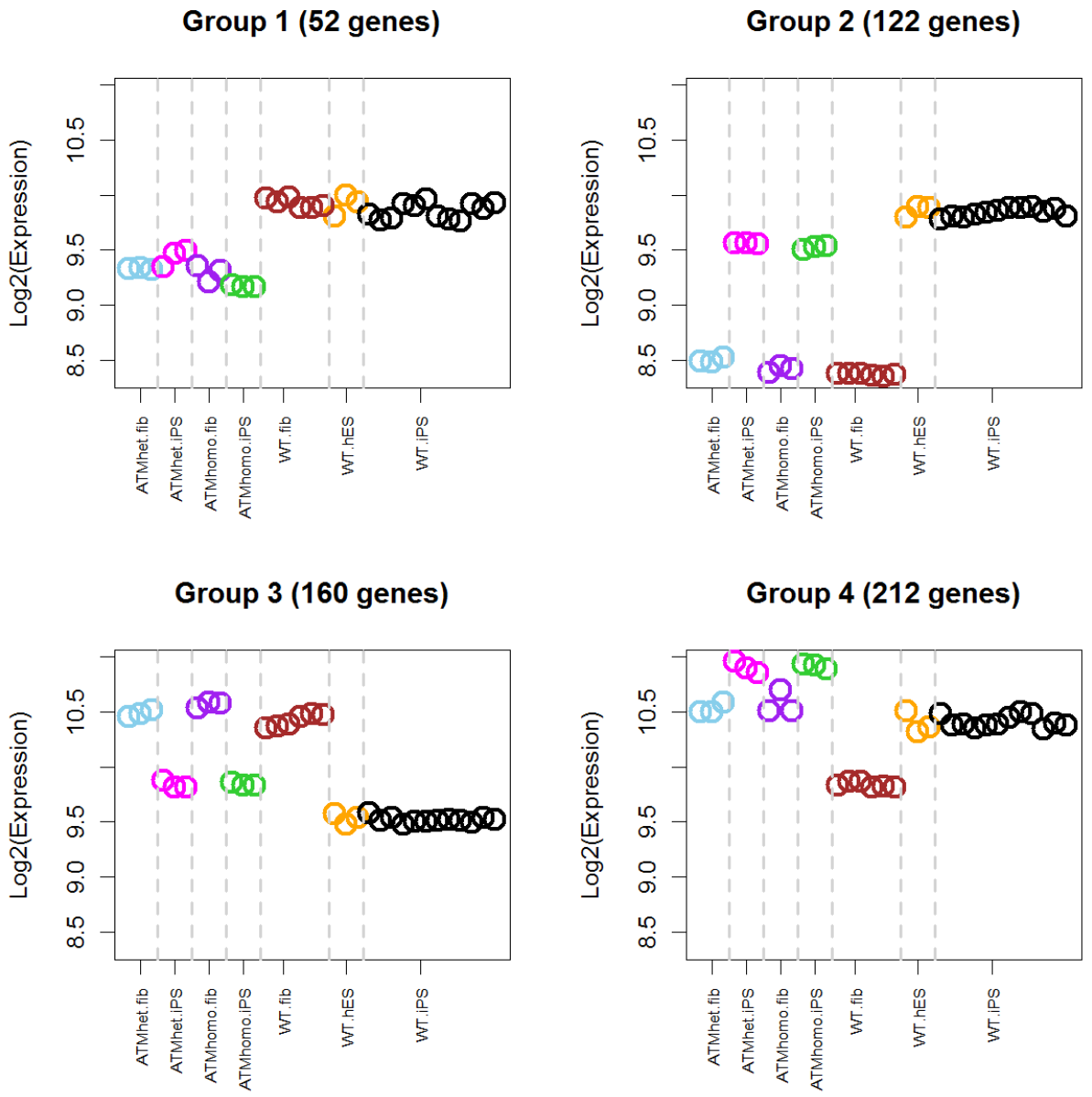

Figure 3.5J - Based on a genelist of mitochondria associated genes (Mitocarta) *attract* analysis identifies four groups of mitochondria associated gene expression showing distinct patterns of correlated expression depending on cell type or genotype.

Further curation of this list selecting for genes either encoded by mtDNA (mitochondrial DNA) or imported into mitochondria shows that 140/143 truly mitochondrial genes were upregulated in

AT34 (Fig 3.5K). The majority of these 143 genes are either components of the respiratory chain, involved in assembly and import of respiratory chain complexes, mitochondrial metabolite transporters and mitochondrial ribosomal proteins and tRNA-synthetases (transfer RNA-synthetases) (see Appendices for annotated gene list). These gene expression changes are consistent with an upregulation of mitochondrial biogenesis in human pluripotent cells in the absence of *ATM*. (Fig 3.5L for statistical analyses).

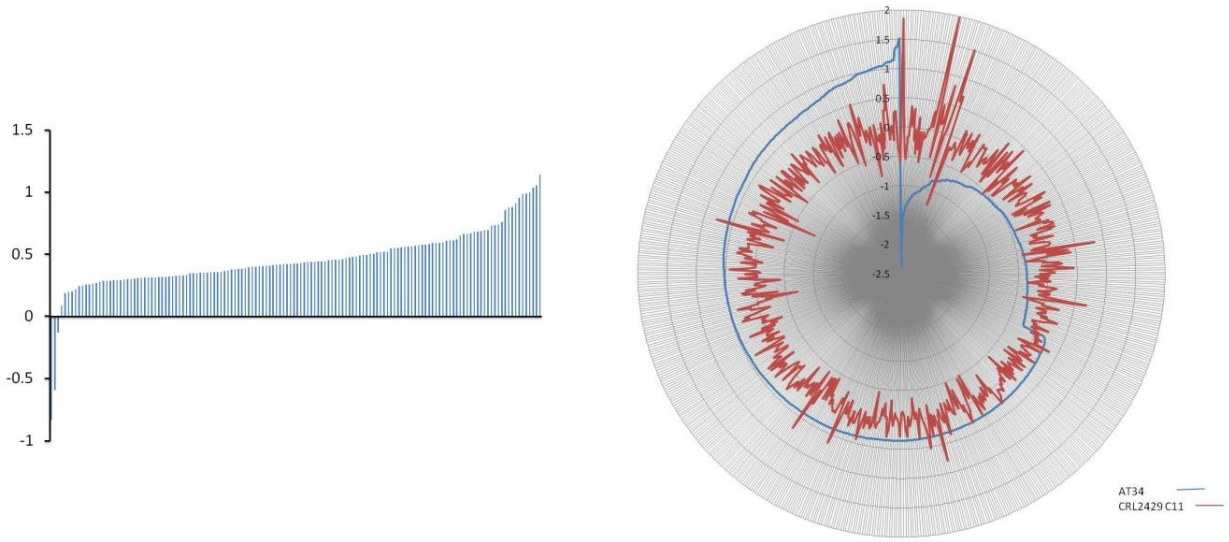

Figure 3.5K - Expression of 141 genes expressed in mitochondria derived from Group 4 (iPS cell specific changes in A–T iPSCs from Fig 3B). Graphs (bar and radial) indicate log fold change of group 4 genes compared to control iPSCs and MEL1 hESCs.

In addition to this agnostic/explorative approach to test for functional enrichment in mapped pathways, we speculated on processes that we hypothesized to be perturbed given the extensive number of roles of ATM. We examined a range of pathways using *attract*.

Interestingly we observed no significant difference in *p53 signaling* pathways (p val 0.336142616536926) (Figure 3.6A). Similarly, we did not uncover a difference in mapped *Apoptosis* pathways (p val 0.901958279328076) (Figure 3.6B), *Insulin* pathways (p val

0.882166731302835) (Figure 3.6C) or pathways in *Cancer* (p val 0.00699368907618373) (Figure 3.6D). We additionally examined *Nucleotide excision repair* pathways and found no significant difference (p val 0.590619722289039) (Figure 3.6E). *Mismatch repair* pathways (p val 0.00699368907618373) (Figure 3.6F) showed no significant differences nor did *Base excision repair* pathways (p val 0.0541797877745253) (Figure 3.6G). No differences were apparent upon examination of *Non-homologous end joining* pathways (p val 0.577862061713731) (Figure 3.6H) or *Homologous recombination* (p val 0.369396388402474) (Figure 3.6I). It was interesting to note that in general, expression of genes encapsulated by the homologous recombination KEGG pathway tended towards greater levels of expression in pluripotent cells rather than fibroblasts. Further to this, there appeared consistent differences in expression levels in fibroblasts between control and mutants that were not apparent in pluripotent cells, indicating a potential redundancy for ATM related homologous recombination. We did observe a significant disruption in *Cell cycle* pathways (p val 0.000175757287476981) (Figure 3.6J). When we decomposed these differences into groups (Figure 3.6K) we observed differences mainly to occur in fibroblasts and not in iPS cells. (See Appendices for gene lists from all heatmaps).

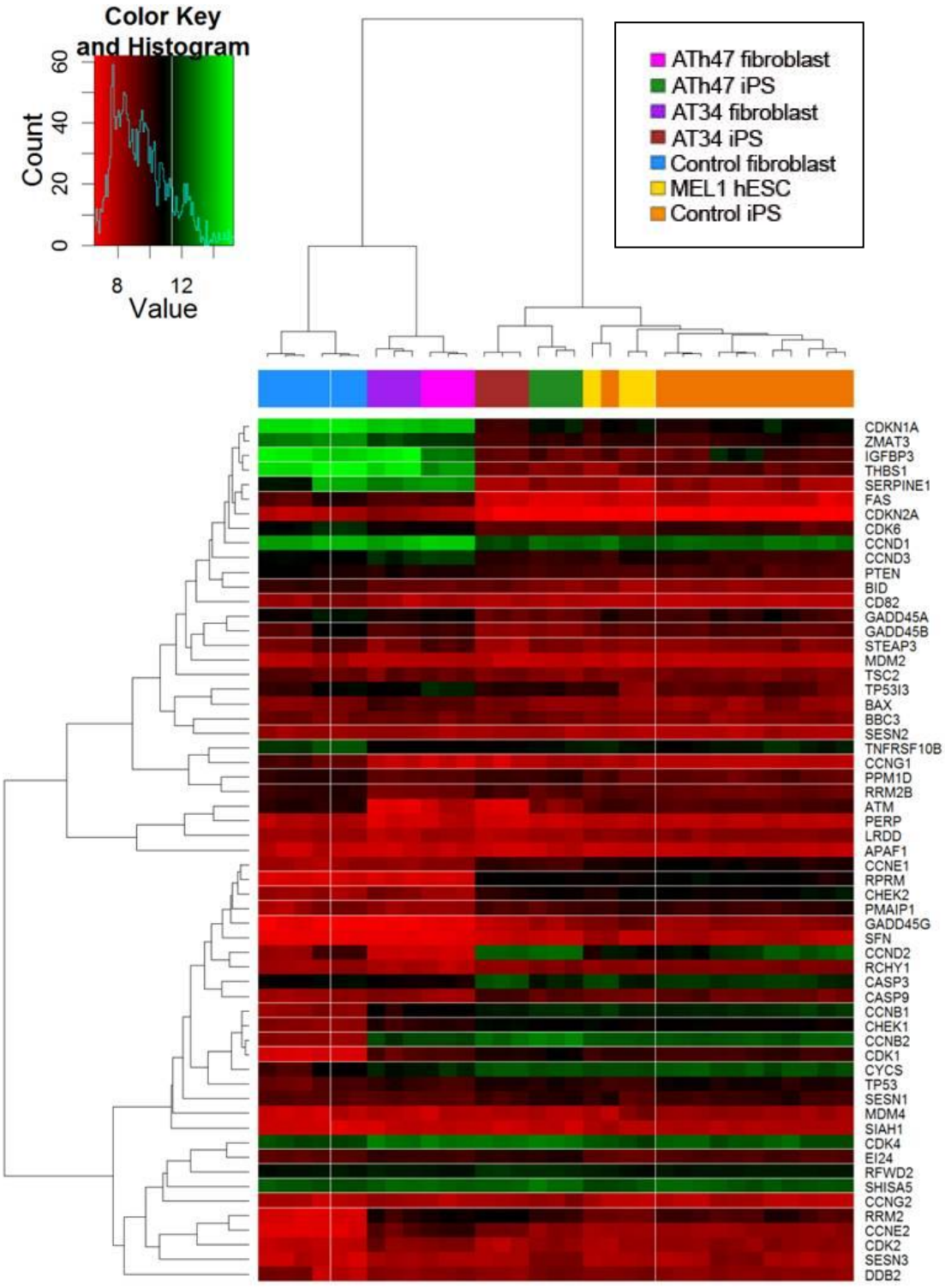

Figure 3.6A – Heatmap of expression dataset depicting known *p53 signalling* pathways. Adjusted p val = 0.336142616536926.

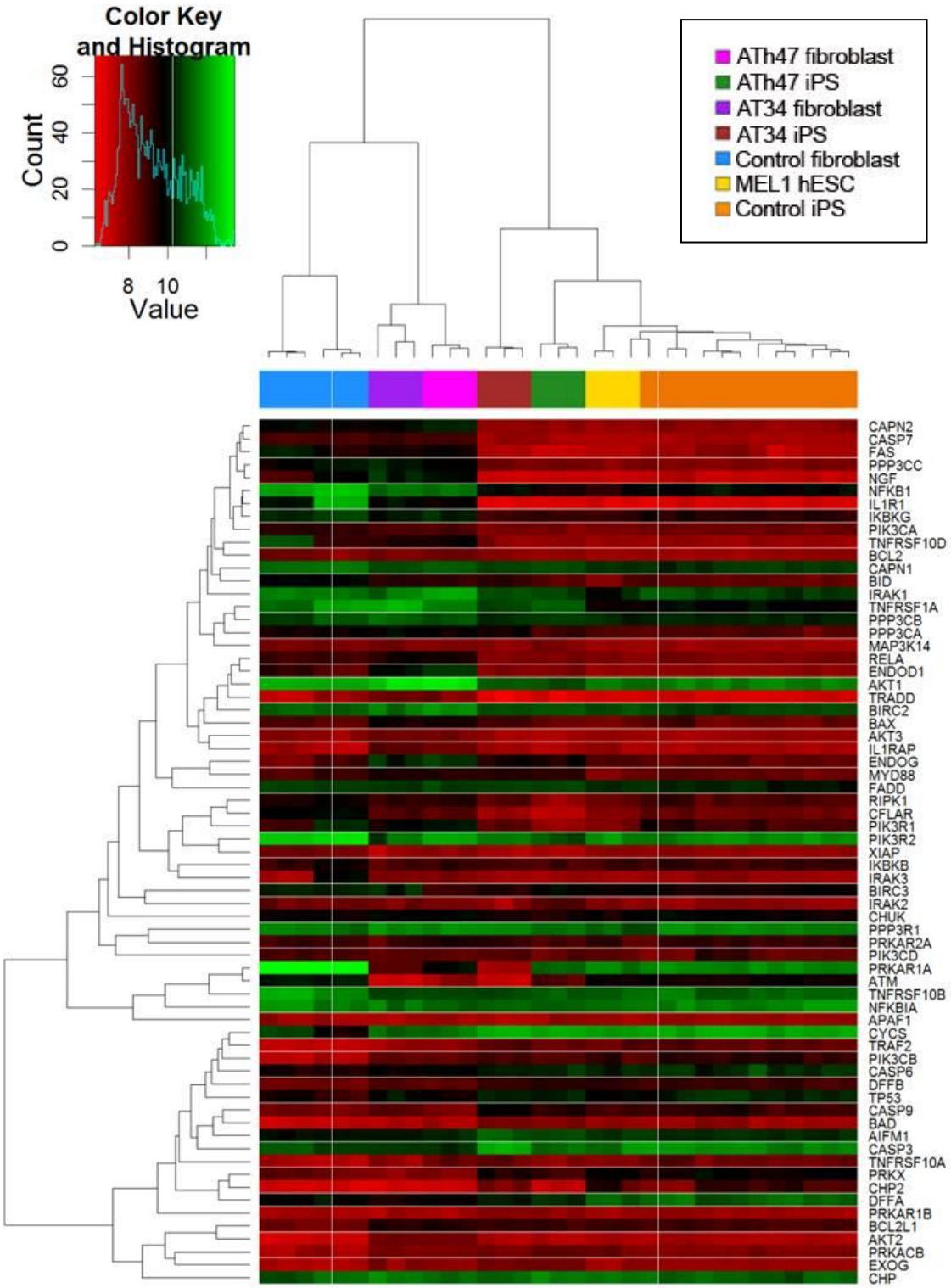

Figure 3.6B – Heatmap of expression dataset depicting known *Apoptosis* signalling pathways. Adjusted p-val 0.901958279328076.

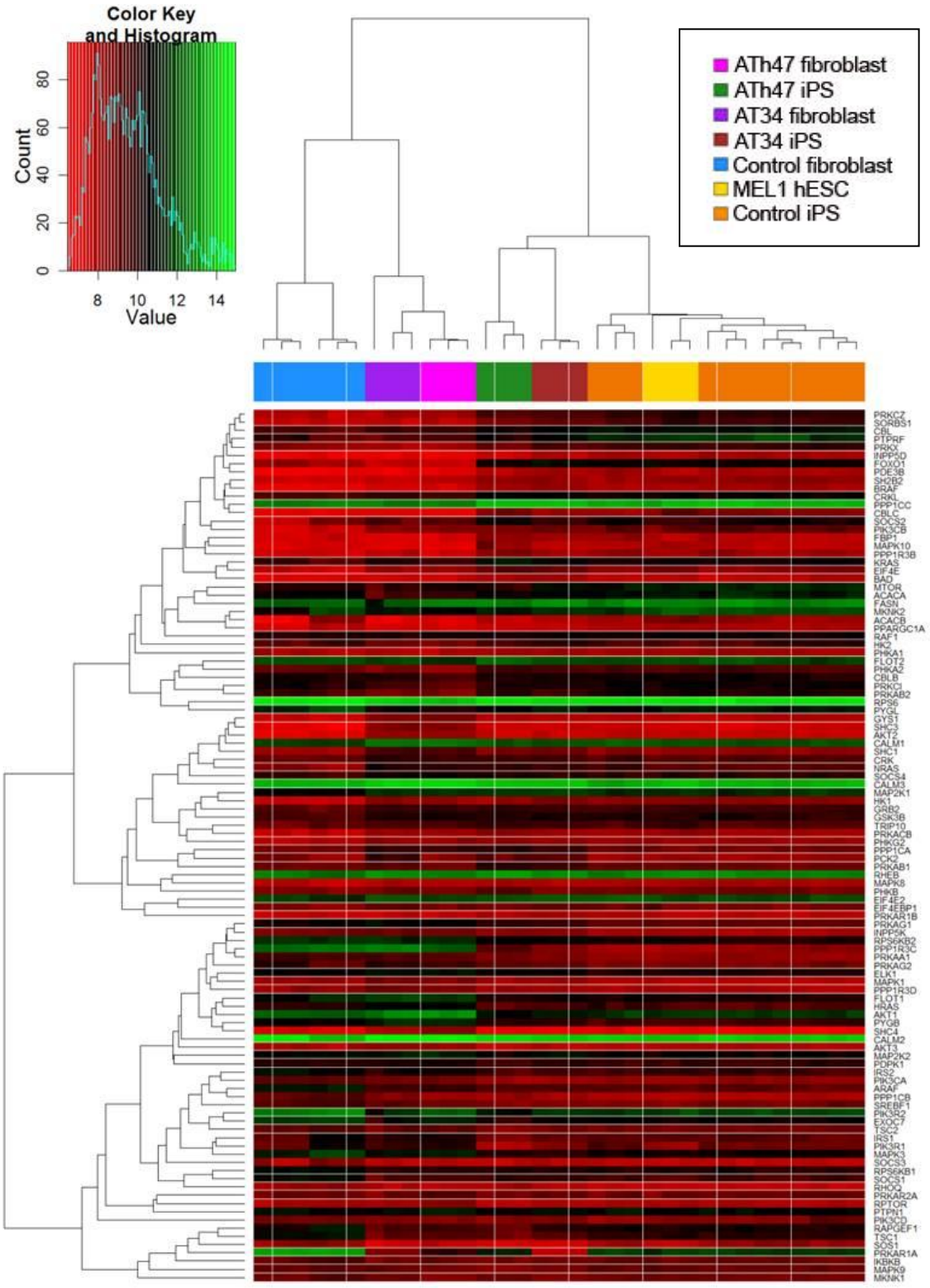

Figure 3.6C – Heatmap of expression dataset depicting known *Insulin* signalling pathways. Adjusted p-val 0.882166731302835.

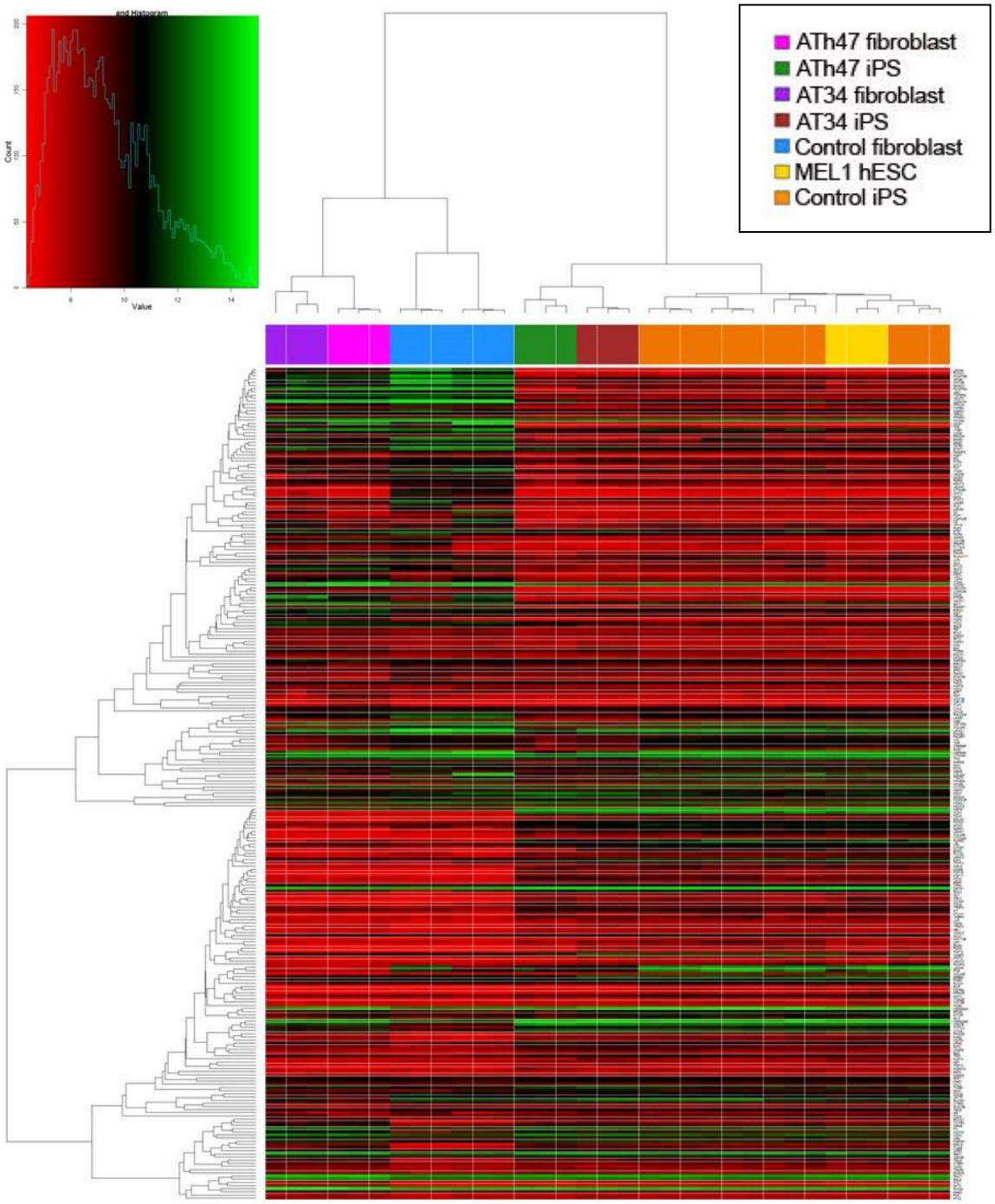

Figure 3.6D – Heatmap of expression dataset depicting known *Pathways in cancer* signalling pathways. Adjusted p-val 0.00699368907618373.

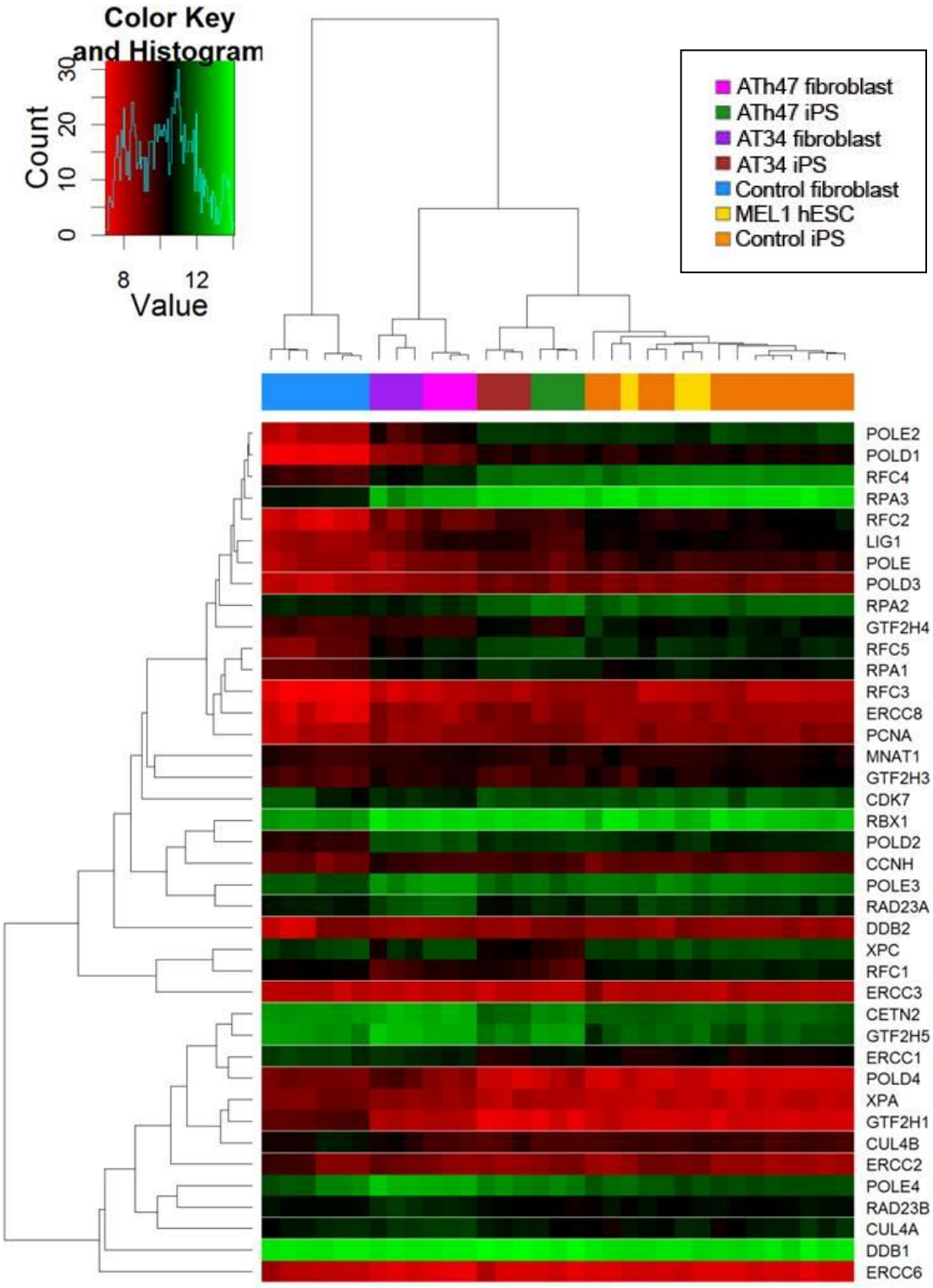

Figure 3.6E – Heatmap of expression dataset depicting known *Nucleotide excision repair* (NER) signalling pathways. Adjusted p-val 0.590619722289039.

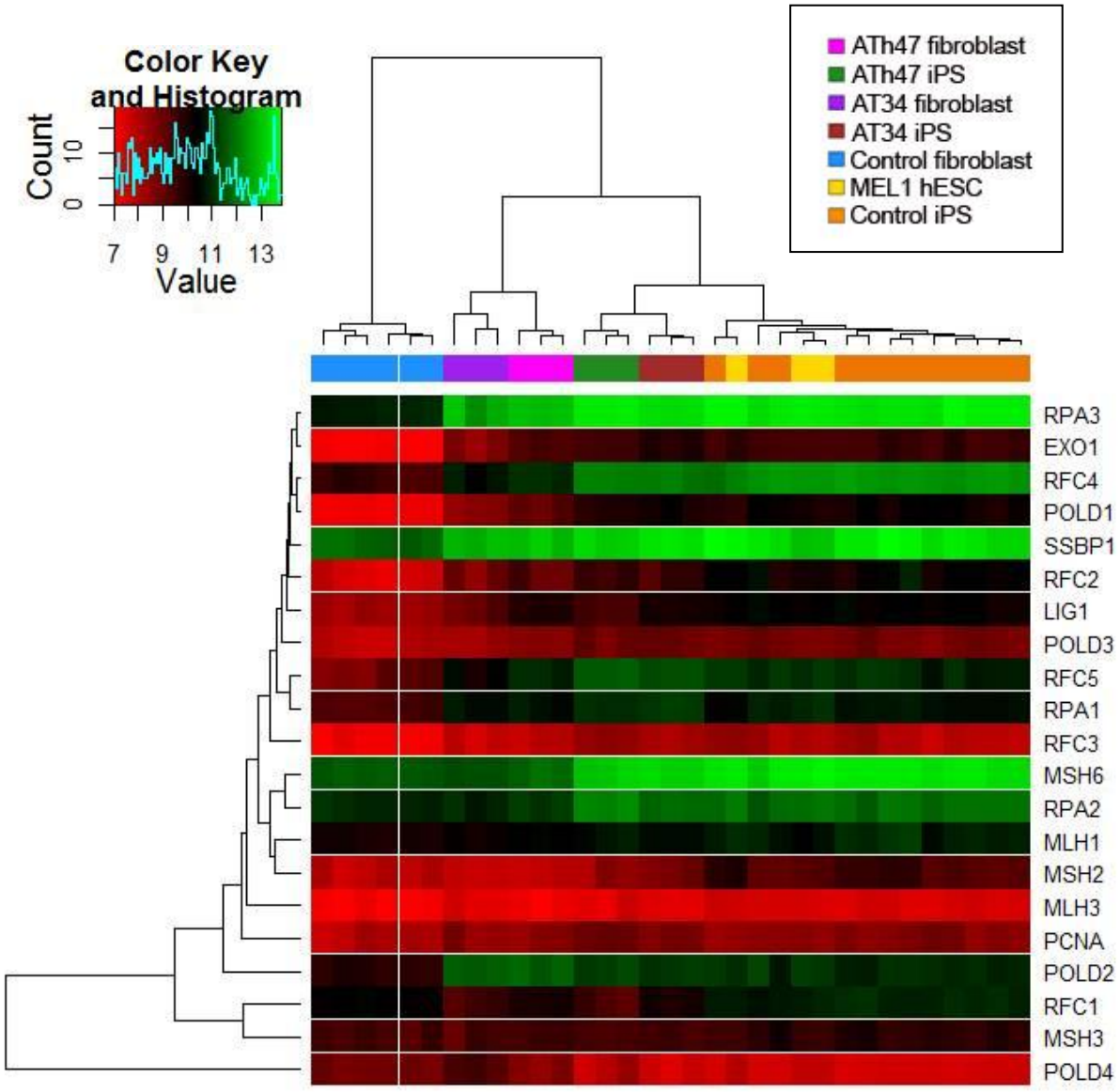

Figure 3.6F – Heatmap of expression dataset depicting known *Mismatch repair* (MR) signalling pathways. Adjusted p val 0.00699368907618373.

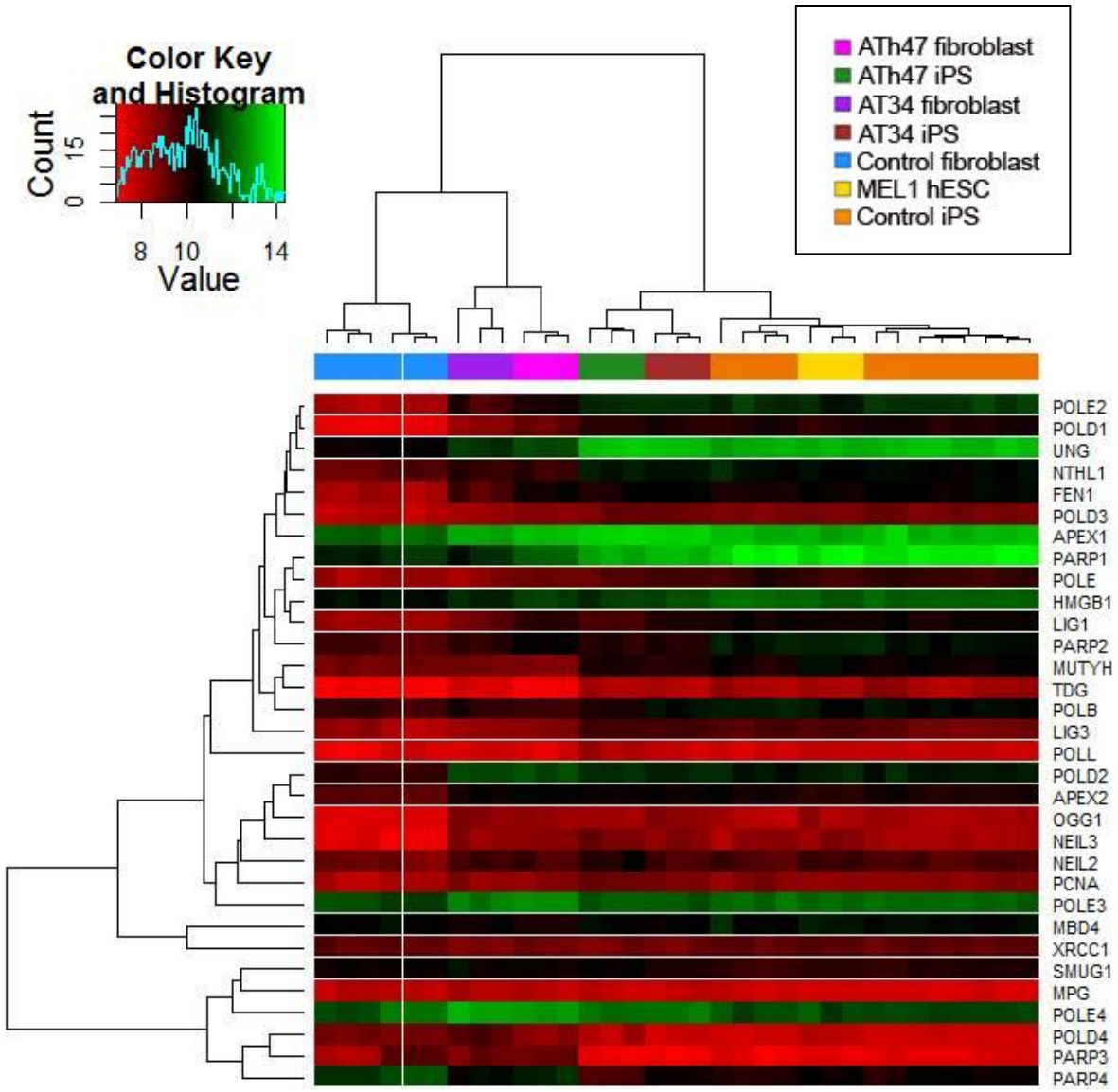

Figure 3.6G – Heatmap of expression dataset depicting known *Base excision repair* (BER) signalling pathways. Adjusted p-val 0.0541797877745253.

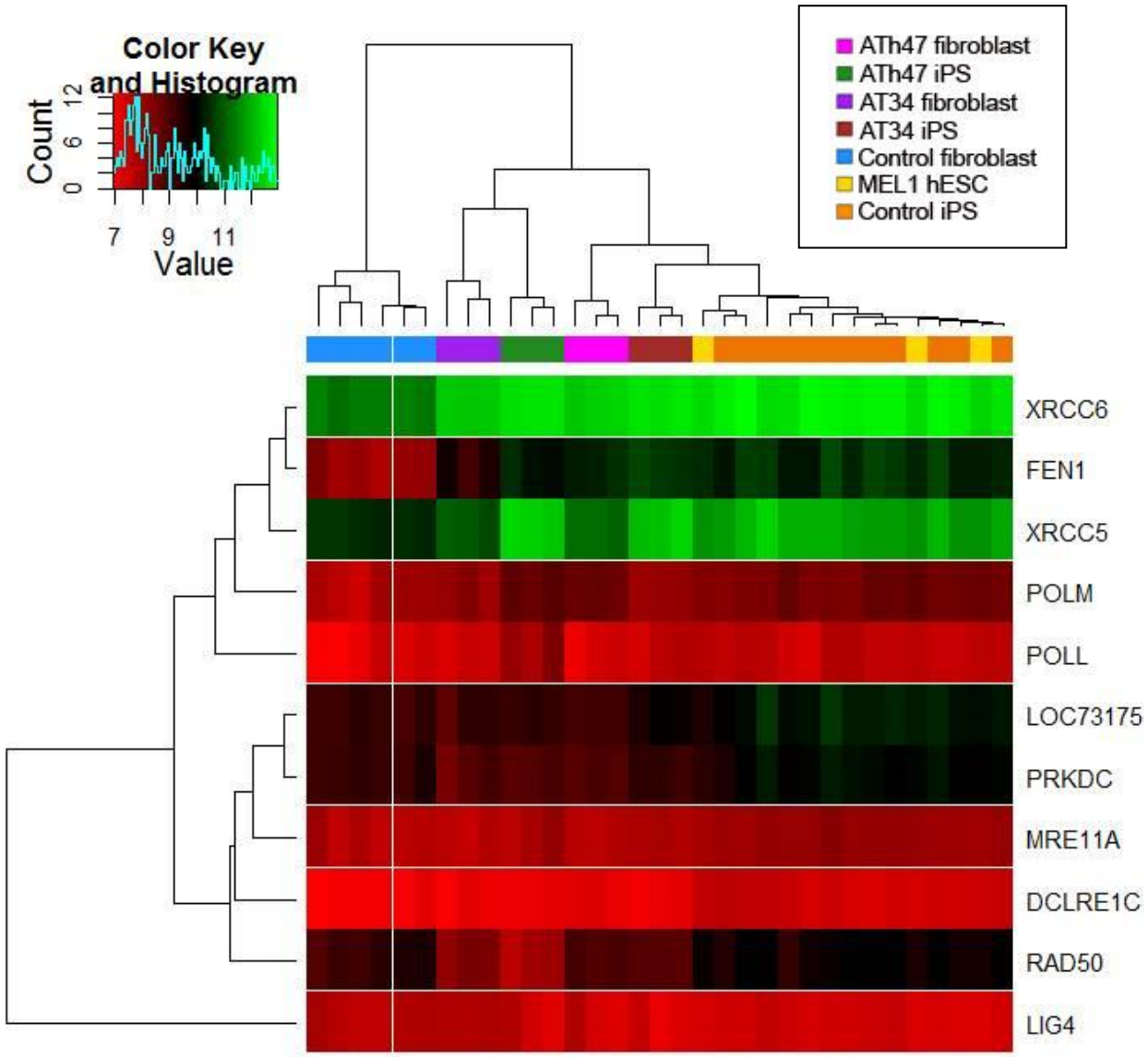

Figure 3.6H – Heatmap of expression dataset depicting known *Non-homologous end joining* (NHEJ) signalling pathways. Adjusted p-val 0.577862061713731.

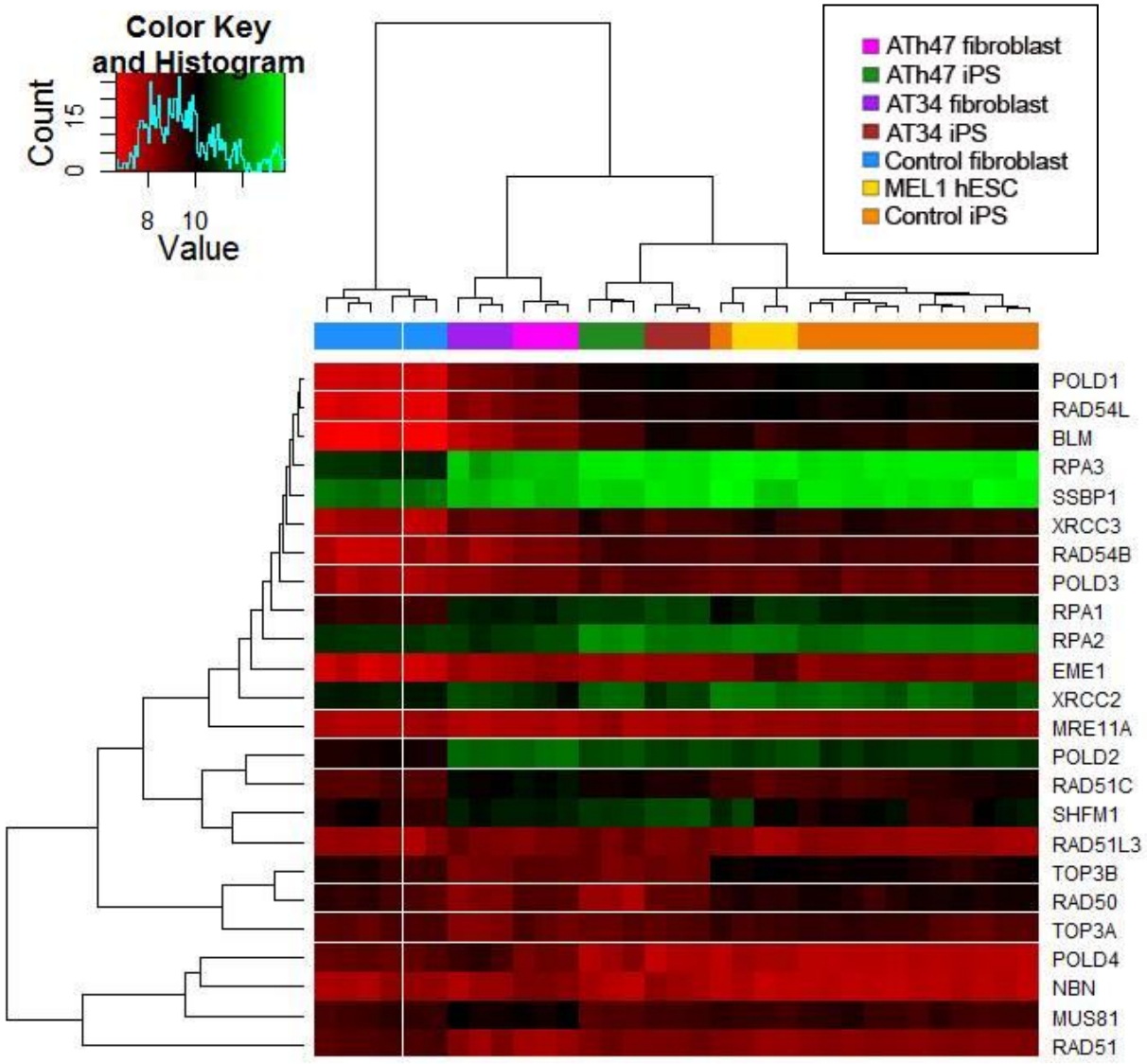

Figure 3.6I – Heatmap of expression dataset depicting known *Homologous repair and recombination* (HRR) signalling pathways. Adjusted p-val 0.369396388402474.

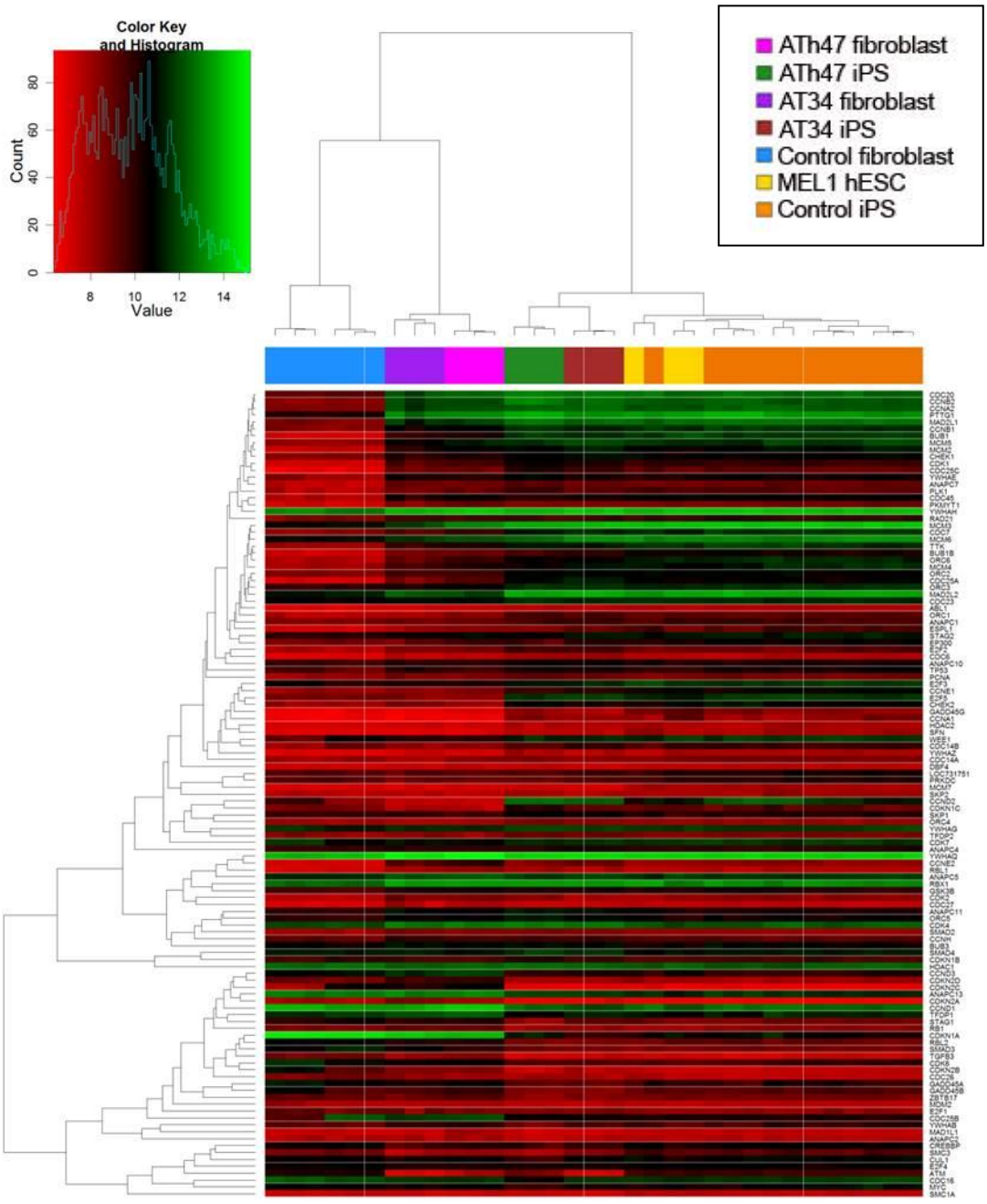

Figure 3.6J - Heatmap of expression dataset depicting known *Cell cycle* pathways. Adjusted p-val 0.000175757287476981.

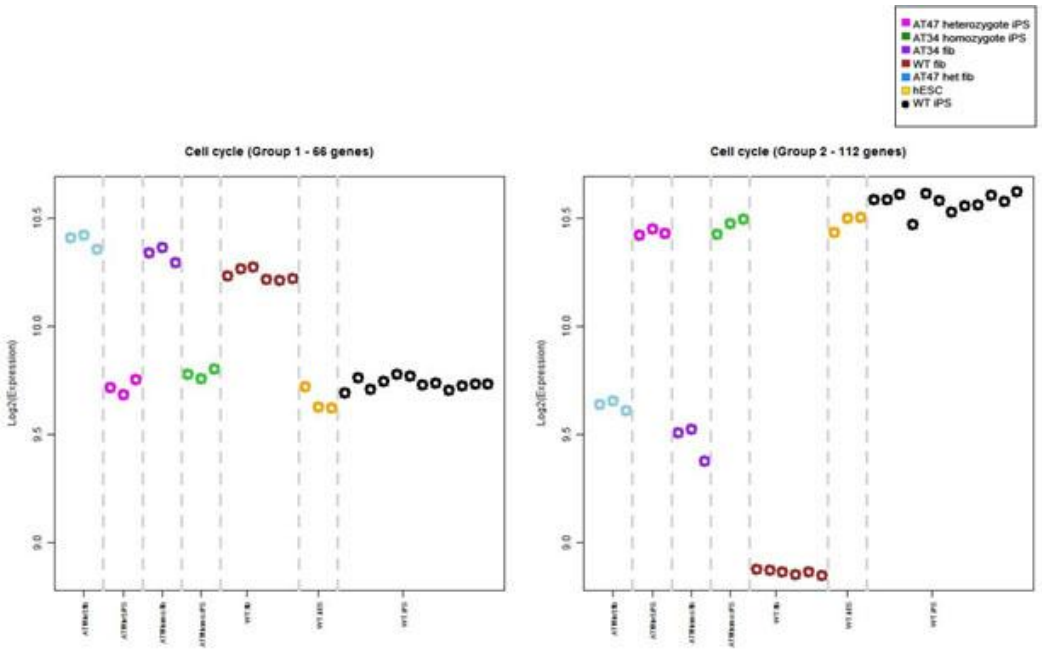

Figure 3.6K - Based on a genelist of Cell cycle associated genes *attract* analysis identifies two groups of Cell cycle associated gene expression showing distinct patterns of correlated expression depending on cell type or genotype.

We next assessed the role of mitochondrial function by testing the expression differences for the mitochondrial-associated genes across phenotype groups using *attract*. The *attract* algorithm computes an F-statistic for each gene and enrichment of a pathway is assessed by performing a two sample T-test between the F-statistics associated with mitochondrial function (yellow curve) with all detected genes (blue curve). Genes informative of phenotype-specific expression have larger F values. The panel (Figure 3.5L) outlines the distribution of the two sets of F-statistics, and shows how the mitochondrial function pathway has F-statistics that are in general elevated with respect to the distribution of all detected genes, implying mitochondrial function is a differentially expressed pathway (P-value < 10^{-18}). (Figure 3.5M) We used the informativeness metric [155] to determine the number of distinct correlated patterns displayed by mitochondrial associated genes; the informativeness metric is a criterion to be maximized, we evaluated different numbers of clusters ranging from one to eleven, and four groups was found to be the optimal number. The expression patterns for the four groups are shown in Figure 3.5J.

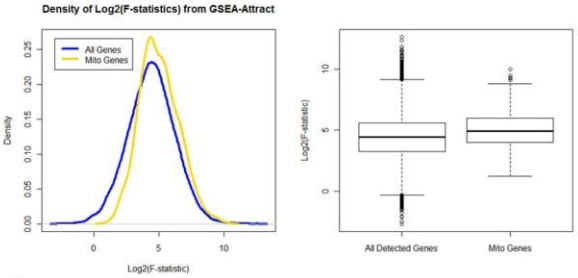

L

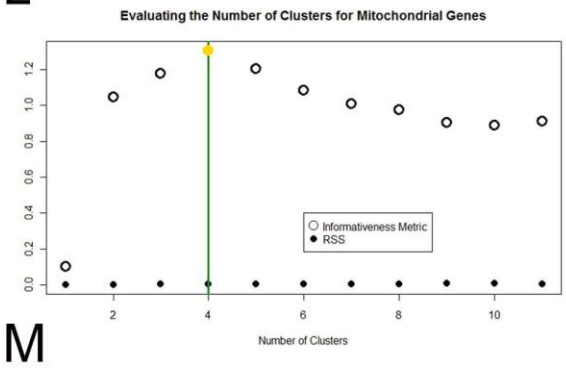

M

Figure 3.5L - F-statistics and mitochondrial pathway differences as significantly altered.

Figure 3.5M - Informativeness metrics show the number of distinct correlated patterns exhibited by mitochondrial associated genes.

We next assembled an *ad* hoc genelist comprising several already available genelists from *GeneGo* featuring genes involved with reactive oxygen species (See appendices for genelist) (Figure 3.6N). *Attract* did not identify significant differences between A–T and controls.

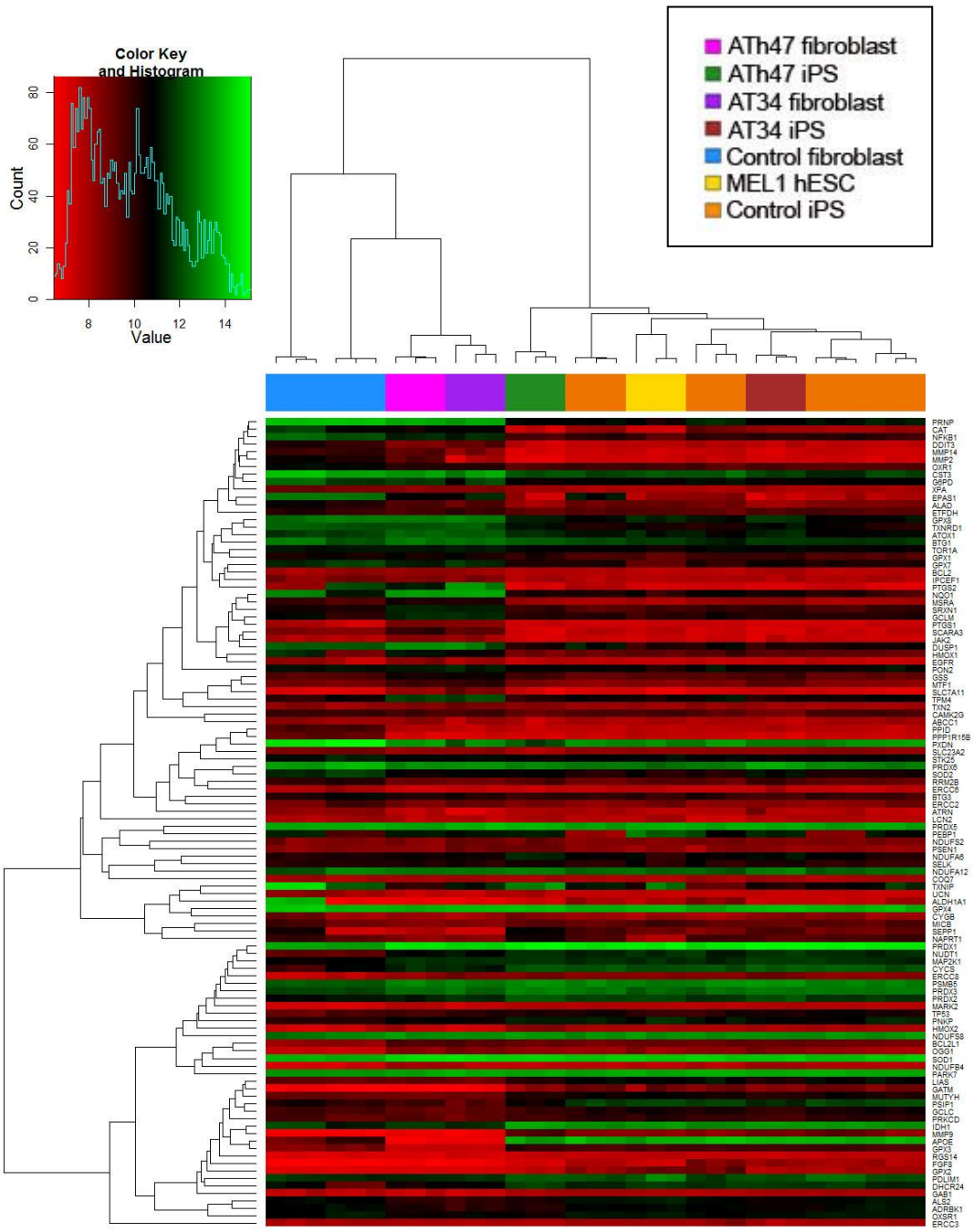

Figure 3.6N - Attract did not identify evidence for significant differences between A–T and controls in *ROS* related pathway analysis.

Microarray data analysis has limitations in the sense that it deals in subjective measures and arbitrary cutoffs. This was made evident by the fact that with manual curation we uncovered significant upregulation of at least 20 additional genes encoding mitochondrial subunits that *attract* did not uncover, presumably because of their absence from KEGG pathways (Table 3.7A). Similarly we uncovered a pattern of downregulation of fourteen of the fifteen calcium channel subunits present on the microarray (Table 3.7B). Of additional but separate interest we also observed downregulation of PRKAR1A and AKT1 in both AT34 and ATh47. An interesting candidate, USMG5 displayed a fourfold logarithmic reduction in AT34 relative to controls – this protein was recently implicated in an ataxia protein interaction network [162].

Symbol	Log fold change (AT34vs Control iPS)	Log fold change (ATh47 vs Control iPS)	Log fold change (Control iPS vs hESC)
ATP5G1	0.879697747	1.005706404	0.040068516
ATP5D	0.808888661	0.305364676	-0.037015153
ATPIF1	0.772782542	0.395881527	-0.276939929
ATP5J	0.586485205	0.556881899	0.055372155
ATP5J	0.582163227	0.681494553	0.000403128
ATP5G3	0.559820711	0.514100551	0.154488698
ATP5G2	0.552364632	0.772560084	0.322428895
ATP5S	0.526482787	0.528431104	-0.093293718
ATP5SL	0.48314288	0.61127372	0.008340032
ATP5EP2	0.415975049	0.590469529	0.058106787
ATP5E	0.404733121	0.792942441	0.025797113
ATP5L	0.40031937	0.524885896	0.055296864
ATPAF2	0.358323384	0.405847178	-0.029555362
ATP5G2	0.335844459	0.766074004	0.190547207
ATP5S	0.333281638	0.461165977	-0.215473278
ATP5L	0.330950889	0.370221967	-0.019457518
ATPBD4	0.315184184	0.657552259	-0.185593351

ATP5I	0.310226785	0.043968871	0.072011023
ATP5J	0.302399925	0.252747201	-0.023577465
ATP5O	0.259069258	0.54817956	0.082716635
ATP5C1	0.242824677	0.063586125	-0.009348865
ATP5A1	0.238097299	0.372145838	-0.118572547
ATP5C1	0.228728672	0.089595633	0.097053251
ATP5I	0.203871589	-0.121502466	0.056571071
ATP5D	0.19339542	0.100848767	-0.228252914
ATPAF1	0.158262357	0.586663787	-0.108477873
ATP5J2	-0.003966432	0.001872947	-0.041567632
ATP5J2	-0.087100137	-0.007233056	-0.234234751
ATP5H	-0.130968333	-0.07396789	-0.041035925
ATP5H	-0.2922839	-0.163063531	0.068335249
ATPIF1	-0.33092393	-0.162238268	0.057887325
ATP5G2	-0.82926336	-0.155006678	0.700133159

Table 3.7A – Genelist and log fold-change values for mitochondrial subunits uncovered additional to list from *attract.*

SYMBOL	Log fold change (AT34vsControl)	Gene
CACNG7	-0.4272	CACNG7 calcium channel, voltage-dependent, gamma subunit 7
CACNA1G	-0.32034	calcium channel, voltage-dependent, T type, alpha 1G subunit
CACNA1A	-0.22678	calcium channel, voltage-dependent, P/Q type, alpha 1A subun
CACNG6	-0.14929	calcium channel, voltage-dependent, gamma subunit 6
CACNG6	-0.07283	calcium channel, voltage-dependent, gamma subunit 6
CACNB2	-0.13284	calcium channel, voltage-dependent, beta 2 subunit
CACNA1C	-0.11747	calcium channel, voltage-dependent, L type, alpha 1C subunit
CACNB3	-0.06833	calcium channel, voltage-dependent, beta 3 subuni
CACNA1S	-0.03287	calcium channel, voltage-dependent, L type, alpha 1S subunit
CACNB4	0.16541	calcium channel, voltage-dependent, beta 4 subunit
CACNA1H	-1.06409	calcium channel, voltage-dependent, T type, alpha 1H subunit
CACNA1H	-0.70808	calcium channel, voltage-dependent, T type, alpha 1H subunit
CACNA2D2	-0.70487	calcium channel, voltage-dependent, alpha 2/delta subunit 2
CACNA1F	-0.60717	calcium channel, voltage-dependent, L type, alpha 1F subunit
CACNA1I	-0.53881	calcium channel, voltage-dependent, T type, alpha 1I subunit

Table 3.7B – Manually curated list of calcium channel subunits shows a consistent trend for downregulation in A–T iPS compared to controls.

While our analysis using *attract* goes some lengths to address these concerns we kept an open mind with respect to analysis of this dataset and instigated an independent analysis using *GeneGo*. We uploaded our dataset to *GeneGo* and examined representation of pathways featuring transcripts that were significantly up or down regulated. Table 3.7C below details the top 50 pathways based on the 7921 genes differentially expressed as deemed by attract ($p<0.05$).

#	Maps	pValue	Ratio	
1	Cytoskeleton remodeling_TGF, WNT and cytoskeletal remodeling	1.264E-15	54	111
2	Cytoskeleton remodeling_Cytoskeleton remodeling	5.000E-14	49	102
3	DNA damage_ATM/ATR regulation of G1/S checkpoint	3.698E-12	23	32
4	Development_TGF-beta receptor signaling	5.363E-09	26	50

5	DNA damage_Role of Brca1 and Brca2 in DNA repair	7.937E-09	19	30
6	Apoptosis and survival_Granzyme B signaling	3.632E-08	19	32
7	Reproduction_GnRH signaling	5.843E-08	31	72
8	Protein folding and maturation_POMC processing	6.676E-08	18	30
9	Cell cycle_The metaphase checkpoint	7.438E-08	20	36
10	DNA damage_Role of NFBD1 in DNA damage response	1.127E-07	11	13
11	Apoptosis and survival_FAS signaling cascades	1.191E-07	22	43
12	Transport_Clathrin-coated vesicle cycle	1.587E-07	30	71
13	DNA damage_ATM / ATR regulation of G2 / M checkpoint	2.229E-07	16	26
14	Cell cycle_Regulation of G1/S transition (part 1)	2.459E-07	20	38
15	Cell cycle_Role of SCF complex in cell cycle regulation	2.509E-07	17	29
16	Cell adhesion_Histamine H1 receptor signaling in the interruption of cell barrier integrity	3.349E-07	22	45
17	Cell cycle_Nucleocytoplasmic transport of CDK/Cyclins	4.486E-07	11	14
18	Development_Slit-Robo signaling	4.916E-07	17	30
19	Immune response_MIF - the neuroendocrine-macrophage connector	5.442E-07	22	46
20	Development_ACM2 and ACM4 activation of ERK	6.346E-07	21	43
21	Development_A2A receptor signaling	6.346E-07	21	43
22	Apoptosis and survival_Role of IAP-proteins in apoptosis	9.246E-07	17	31
23	Development_Activation of Erk by ACM1, ACM3 and ACM5	1.030E-06	21	44
24	DNA damage_Mismatch repair	1.293E-06	13	20
25	Cell adhesion_Integrin-mediated cell adhesion and migration	1.358E-06	22	48
26	Apoptosis and survival_DNA-damage-induced apoptosis	1.434E-06	11	15
27	Apoptosis and survival_p53-dependent apoptosis	1.747E-06	16	29
28	Immune response_Neurotensin-induced activation of IL-8 in colonocytes	1.949E-06	20	42
29	Transport_RAN regulation pathway	2.272E-06	12	18
30	Development_G-Proteins mediated regulation MAPK-ERK signaling	2.556E-06	21	46
31	Muscle contraction_Regulation of eNOS activity in endothelial cells	2.600E-06	26	64
32	Signal transduction_Activin A signaling regulation	2.935E-06	17	33

33	Apoptosis and survival_TNFR1 signaling pathway	3.092E-06	20	43
34	Apoptosis and survival_HTR1A signaling	3.165E-06	22	50
35	Development_GM-CSF signaling	3.165E-06	22	50
36	Cell adhesion_Chemokines and adhesion	3.293E-06	35	100
37	Development_VEGF signaling via VEGFR2 - generic cascades	3.355E-06	31	84
38	Immune response_CD16 signaling in NK cells	3.946E-06	27	69
39	Regulation of CFTR activity (norm and CF)	4.279E-06	24	58
40	Cell adhesion_Role of tetraspanins in the integrin-mediated cell adhesion	4.335E-06	18	37
41	Apoptosis and survival_Role of CDK5 in neuronal death and survival	4.987E-06	17	34
42	DNA damage_NHEJ mechanisms of DSBs repair	5.255E-06	12	19
43	Immune response_ETV3 affect on CSF1-promoted macrophage differentiation	5.587E-06	16	31
44	Apoptosis and survival_Endoplasmic reticulum stress response pathway	1.007E-05	22	53
45	Cytoskeleton remodeling_Regulation of actin cytoskeleton by Rho GTPases	1.179E-05	13	23
46	Development_Angiotensin signaling via PYK2	1.377E-05	19	43
47	Development_VEGF signaling and activation	1.377E-05	19	43
48	Development_Angiotensin activation of ERK	1.568E-05	16	33
49	Apoptosis and survival_Caspase cascade	1.568E-05	16	33
50	Cell cycle_Spindle assembly and chromosome separation	1.568E-05	16	33

Table 3.7C – List of top 50 pathways featuring significantly different gene expression signatures based on Genego pathway analysis of 7921 genes differentially expressed between A–T iPSCs and control iPSCs ($p<0.05$).

The first statistically significantly pathway was '*TGF, WNT and cytoskeletal remodeling*'. 54 out of the 111 genes annotated to this pathway were significantly dysregulated in our dataset. A second entry '*Cytoskeleton remodeling*' exhibited 49 out of 102 mapped genes as being

differentially regulated. Interestingly and in support of this data, there is evidence for altered cellular morphology and microfilament arrays arising from A–T patient fibroblasts [163].

Unsurprisingly, the next pathway in this list was '*DNA damage ATM/ATR regulation of G1/S checkpoint*' that showed 23 out of 32 pathway constituents dysregulated in which ATM ia a central transducer of signaling.

The fourth entry to occur was '*Development TGF beta receptor signaling*' which showed twenty-six out of fifty pathway members to be significantly dysregulated. Disruption of this pathway is particularly interesting given TGF-β has downstream effects on development including neuronal differentiation which involves signaling through SMAD proteins [164]. Interestingly disruption of TGF-β signaling has been shown to contribute towards neurodegeneration in Alzheimer's pathology [165, 166].

We next observed thirty out of seventy-one members of the '*Transport Clathrin-coated vesicle cycle*' to be differentially regulated which was interesting given the report showing that ATM binds to β-ADAPTIN in cytoplasmic vesicles [8]. β-ADAPTIN is part of the AP-2 adaptor complex, which is involved in clathrin-mediated endocytosis of receptors. *AP-2* was significantly downregulated in this dataset.

Validation of microarray results

It was interesting to note that both analysis methods (*attract* and *GeneGo)* yielded slightly different results, however this is not surprising given that they operate within different parameters for analysis. In our opinion, the major finding of our microarray analysis was the extensive and consistent upregulation of mitochondrial genes. We validated our microarray analysis by performing qPCR for a number of mitochondrially-expressed genes. We noticed significant (unpaired t-test) increases in transcript abundance in seven out of ten mitochondrial associated genes (Figure 3.7A).

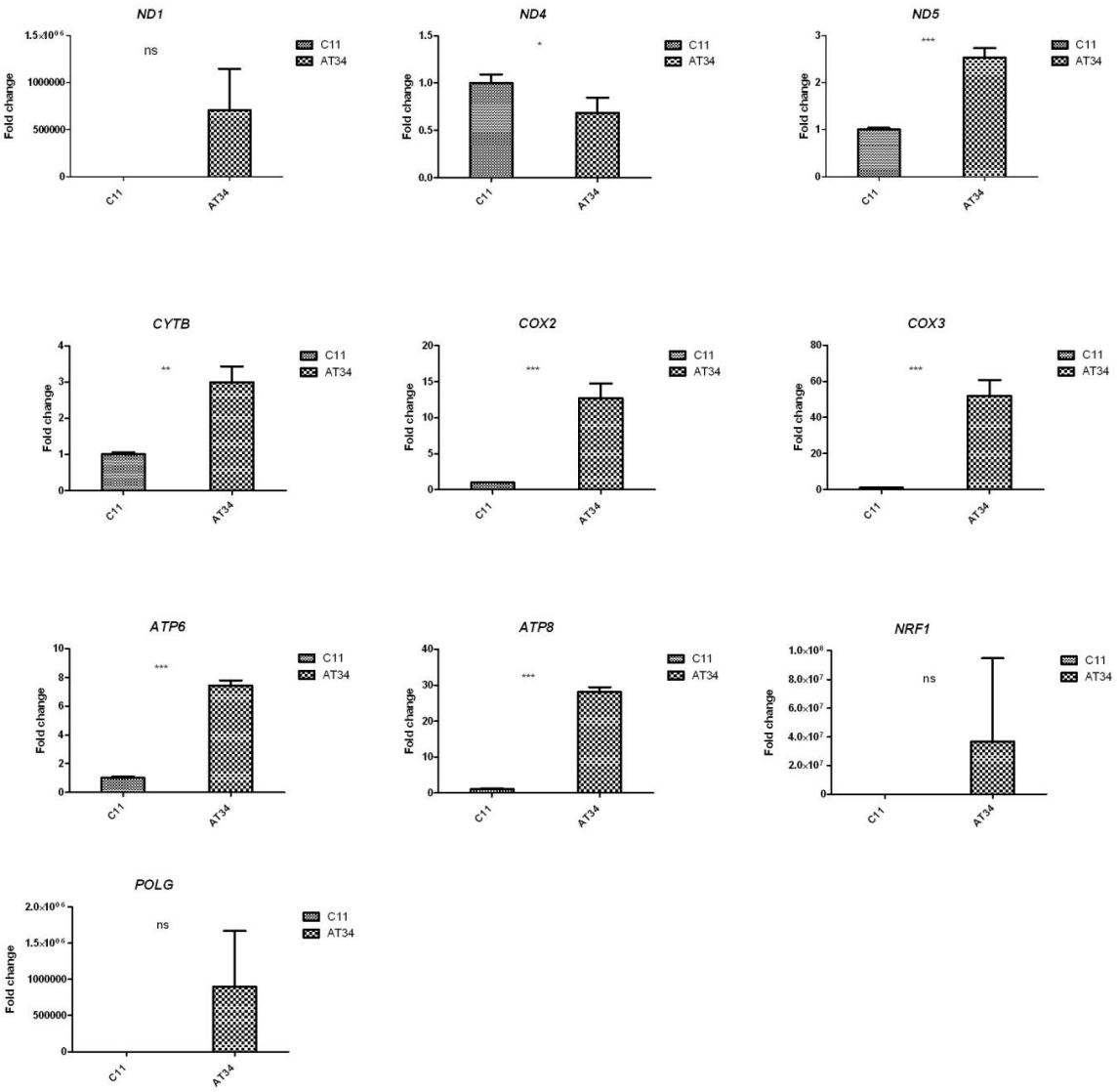

Figure 3.7A – qPCR shows upregulation of nine of ten mitochondrial genes (between C11 control iPSCs and AT34 A–T iPSCs), six of which were statistically significant - *ND1* (ns), *ND4*(*), *ND6* (***), *CYTB* (**), *COX2* (***), *COX3* (***), *ATP6* (***), *ATP8* (***), *NRF1* (ns) and*POLG* (ns). Unpaired t-tests were performed to ascertain statistical significance. Expression was normalized to *B-Actin*.

We sought to ascertain whether this overt and extensive upregulation of mitochondrial genes was conserved in a second A–T iPS cell line and performed qPCR for a similar panel of mitochondrial genes in three control and three A–T clones, live sorted for surface marker TRA-1-60.

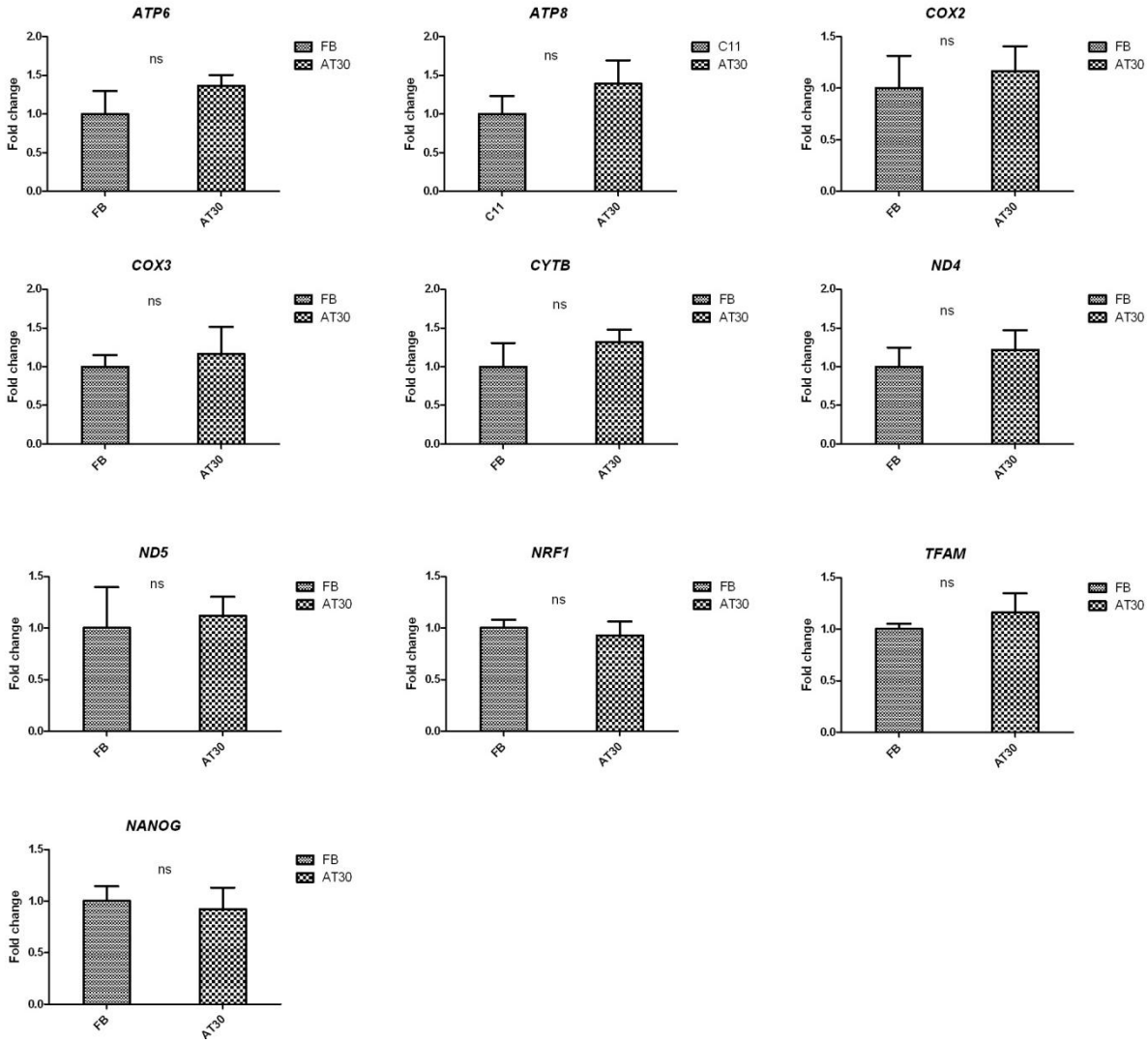

Figure 3.7B – qPCR shows slight upregulation of mitochondrial genes (between second control line FB and second A–T line AT30 - three control and three mutant clones), however results fail to achieve significance by unpaired t-tests. Expression was normalized to *B-Actin*.

Although we observed a statistically significant upregulation of mitochondrial genes *ND4* (*), *ND6* (***), *CYTB* (**), *COX2* (***), *COX3* (***), *ATP6* (***), *ATP8* (***) (Figure 3.7A), in AT34 compared to controls, this phenomena was not apparent to the same extent when we examined a second A-T line (AT30 – Figure 3.7B), indicating that these changes may have been mutation or cell-line specific.

Mitochondria in iPS cells

We investigated whether there were any functional manifestations of this disruption of mitochondrial gene expression by examining a range of mitochondrial parameters including membrane potential (through the use of TMRM), mitochondrial localization/morphology (Mitotracker Green) and mitochondrial mass by staining with N-acridine-orange (NAO). Through incubation of iPS cells with Mitotracker Green and TMRM, we were able to visualize mitochondrial localization and also membrane potential (Figure 3.8A). We observed consistent Mitotracker Green and TMRM staining within iPS cell colonies although we noted marked fluctuations in intensity at the periphery of colonies that we took to correspond with increased mitochondrial biogenesis as a result of cellular differentiation.

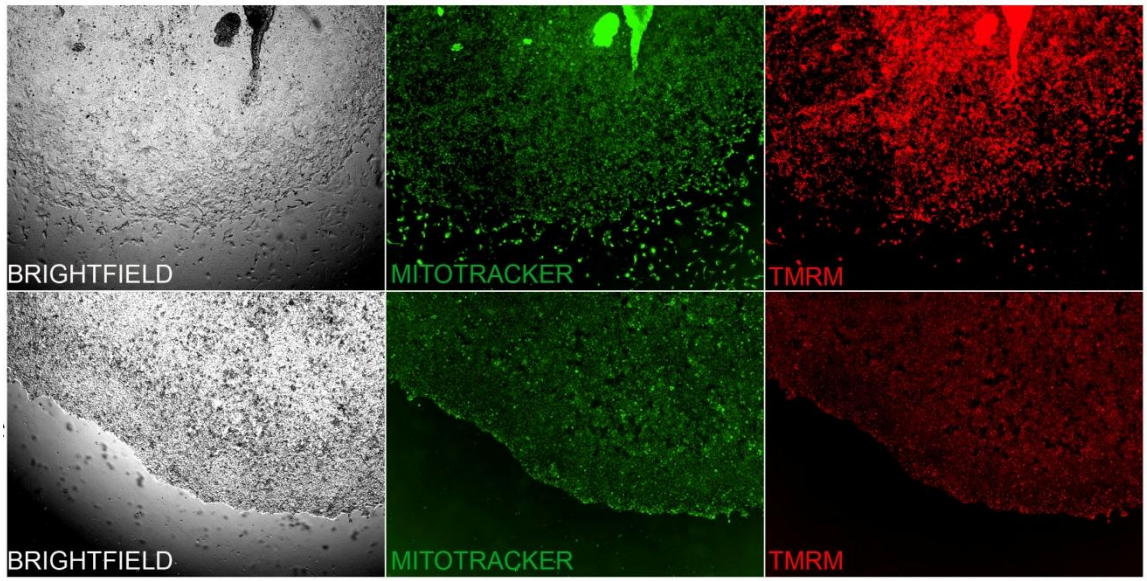

Figure 3.8A – iPS cells were incubated with TMRM to visualize mitochondrial membrane potential and Mitotracker Green to visualize mitochondria. Top panels show representative images from control iPS and lower panels show A–T iPS (AT34).

We did not observe any apparent differences in staining intensity by fluorescent microscopy and decided to use a more quantitative approach by flow cytometry. iPS cells were harvested for

flow cytometry as outlined and incubated with TMRM and NAO in the presence and absence of ATP synthase inhibitor Oligomycin and electron chain uncoupler CCCP as controls for specificity (Figure 3.8B).

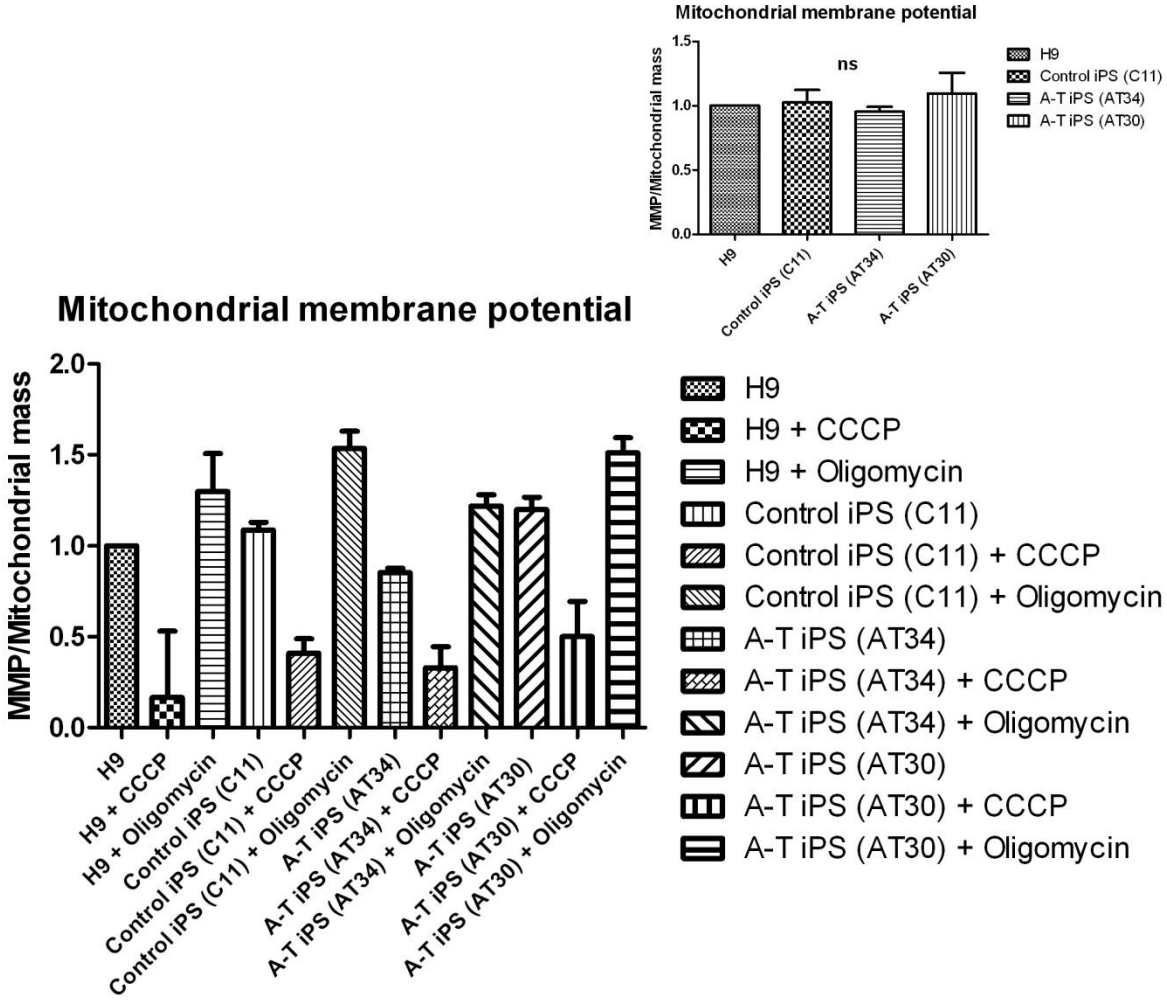

Figure 3.8B – iPS cells were incubated with TMRM in the presence and absence of CCCP and Oligomycin. Inlay in upper right-hand corner shows normalized mitochondrial membrane potentials (TMRM signal/NAO signal) for ease of viewing. One-way ANOVA reveals no significant differences between mitochondrial membrane potential. Graph shows mean results from 3 individual sets of flow cytometry experiments.

Additionally we examined levels of mitochondrial ROS using mitoSOX. Although we did not observe statistically significant elevation of mitochondrial ROS between A–T and controls it was

interesting to note that in all iPS cell lines staining was almost two-fold higher than that in H9 hESC (Figure 3.8C).

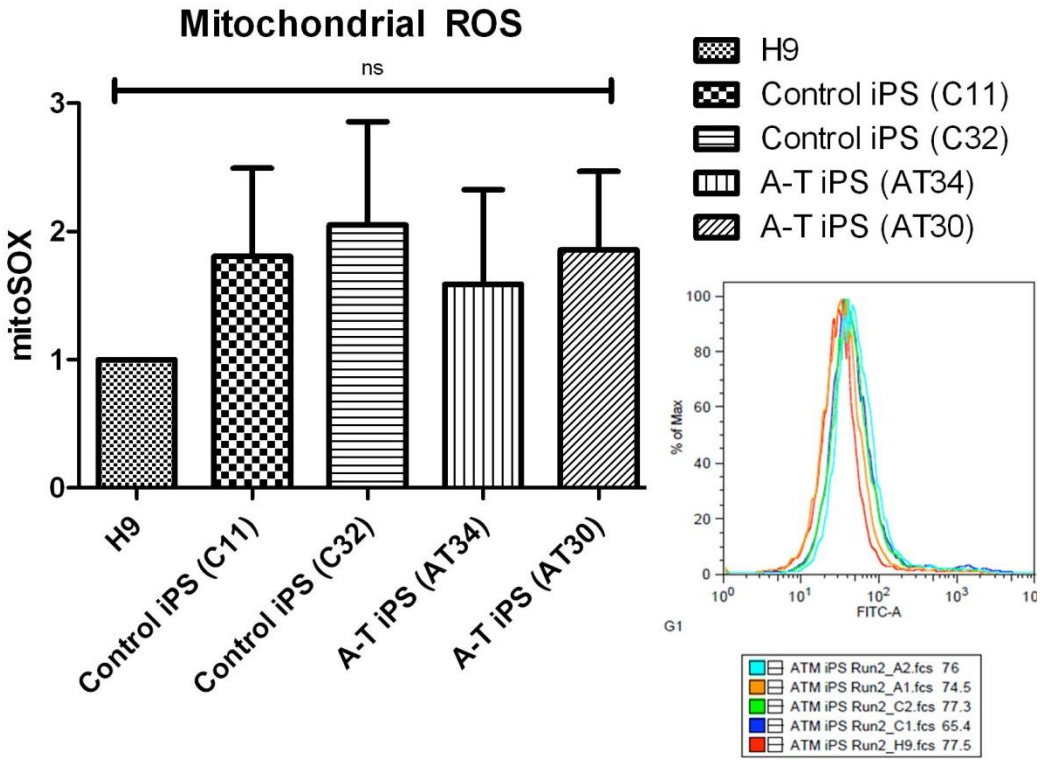

Figure 3.8C – iPS cells incubated with mitoSOX reveal levels of mitochondrial reactive oxygen species. Graph shows mean results from 3 individual sets of flow cytometry experiments. No significant difference was apparent after a One-way ANOVA. Lower panel shows flow cytometry plot (FITC).

Discussion

Several recent findings highlight the phenomena of elevated levels of DNA damage signaling and repair gene expression in ESCs and iPSCs in comparison to somatic cells, which has been attributed to the elevated need for protection of the genome [79, 82]. ATM has been demonstrated to activate signaling pathways in ESCs and iPSCs in response to DNA damage [79-81] and to be vital for G2M arrest in hESCs after introduction of DNA damage by low doses of IR [15, 80], however IR may not accurately represent the normal levels and type of DNA damage which occur within the cellular environment.

Maintaining a stable genome within the developing embryo is an important requirement for the survival and viability of an organism – similarly, the stability of ESCs and iPSCs relate directly to their applicability as clinical entities and disease models. Recent work outlines the high degree of similarity in response to DNA damage between ESCs and iPSCs with respect to cell cycle arrest, double strand break repair and gene expression [79]. Further to this, it was illustrated that pluripotent and somatic cells utilize DNA damage repair pathways via distinctly [84] different methods, which makes sense given the different nature of these cells and their requirements for growth. It has been suggested that ESCs primarily utilize HRR (homologous repair and recombination) rather than error prone NHEJ (non-homologous end joining), which is supported by the observation of 10-fold higher formation of RAD51 foci in ESCs when compared to differentiated astrocytes [84]. Our microarray data support this concept by showing a general trend for the upregulation of DNA repair pathway genes in pluripotent cells compared to fibroblasts. HRR is dependent on sister chromatids for repair templates - as ESCs spend 70% of their time in S and G2M phase, they are able to initiate this more stringent form of repair [79]. ESCs have a doubling time of approximately 20-30 hours [85] and cycle rapidly due to an abbreviated G1 phase and facilitated G1 to S transition [86]. Due to this accelerated rate of DNA replication and also mitotic division, ESCs and iPSCs may be at a greater risk of replication errors, especially in the context of genomic instability syndromes, such as A–T. In somatic cells, ATM phosphorylates p53 to arrest G1/S cell cycle transition in the presence of DNA damage [87] however this mechanism exists differently in ESCs because they lack a conventional restriction point in late G1 [88]. Interestingly we observed no marked disruptions to basal p53 signaling between *ATM* deficient iPS cells and controls, consistent with this notion. Filion et al. showed that ESCs lack this G1 checkpoint in response to IR [81]. This group and others [15, 80] show supporting data and demonstrate that ESCs arrest in the G2phase after IR in an ATM dependent manner.

Although we provide evidence showing that gene expression of members of the major DNA repair pathways are minimally disrupted, we have clearly illustrated that IR-induced ATM signaling is absent in A–T iPS cells and as a result cell cycle aberrations are present. After IR,

we observed classical signs of damage induced inhibition of entry into mitosis in control iPS cells. In contrast to this A–T iPSCs displayed greatly reduced inhibition of mitotic entry, indicating that damage induced cell cycle control was compromised. It is not unreasonable to speculate that this method of action could foster the accumulation of compromised progenitors that would normally be targeted by repair or removal from the pool by cell death. In support of this we measured S-phase DNA synthesis and this checkpoint was found to be compromised also.

Numerous papers report that ESCs are hypersensitive to environmental insult, resulting in elevated levels of apoptosis [90, 91]. Filion et al. demonstrated that ESCs undergo caspase-related mitochondrial apoptosis, demonstrating a mechanism for the removal of irreparably damaged cells [81]. Because hypersensitivity to ionizing radiation is a well established characteristic of somatic A–T cells [167, 168] we examined the incidence of apoptosis in A–T and control iPSCs 24 hours after exposure to 2Gy of radiation. As shown in Figure 3.3C radiation-induced apoptosis was approximately 3-fold higher in A–T iPSCs than in control iPSCs. Figure 3.3C further shows that even under standard culture conditions A–T iPSCs exhibited a two-fold higher load of apoptosis relative to controls. In somatic cells ATM activation by DNA DSB and subsequent signaling through p53 represents a major pathway for induction of apoptosis [169], implying that loss of ATM activity may confer resistance to apoptosis. In contrast our data show an increased sensitivity to spontaneous and radiation induced apoptosis.

Due to the highly stringent need for faithful repair and fidelity within the embryo, there may be several levels of inbuilt redundancy that exist to take over in the absence of ATM. This is evidenced by findings that a BAC recombineered *ATM* knockout hESC line maintained normal karyotype for extended periods of culture. This is speculated to be because ATM independent pathways were sufficient to maintain genomic fidelity in normal culture conditions [15]. Biton et al. used hESCs to demonstrate that ATM is nuclear and that it responds to DNA DSB [170]. More recently, ATM was shown to be vital for the coordination of cell cycle control of pluripotent stem cells after ionizing radiation (IR) in G2 but not G1 [80]. Interestingly,

interference with ATM activity in hESCs using the specific ATM inhibitor KU55933 [84] or BAC mediated gene knockout [15] suggested that ATM may be dispensable for repair of DSB and genomic stability in hESCs. Adams et al. provide evidence showing that repair pathways that dominate in the pluripotent state are ATR-driven HRR in comparison to ATM-driven NHEJ in differentiated cells [78] The apparent contrast between the necessity for ATM in maintaining genomic integrity between somatic and pluripotent stem cells demonstrates that ATM related and unrelated DNA repair pathways behave in contextually dependent manners depending on cell state. In support of this, and despite the fact we observed aberrant post-damage induced control of cell cycle, we were able to generate and maintain karyotypically normal cultures of A–T iPS cells for extended periods. Methodologies capable of detecting genomic abberations at higher resolution such as array CGH may be optimal for increasing the understanding of genomic fidelity, however these can be cost-prohibitive. Our microarray data also support the observations that ATM may be redundant in pluripotent cells. Interestingly, in pluripotent A–T cells we observed little disruption to pathways including p53 signaling, apoptosis, pathways in cancer, insulin signaling base excision repair, non-homologous end joining, mismatch repair or nucleotide excision repair, though many of these processes were disturbed in *ATM* deficient fibroblasts, supporting our theory for ATM redundancy in pluripotency.

ATM was recently shown to act in a chromatin-state dependent manner, with respect to repair of DNA DSBs. It was found that ATM signaling increased proportionally to the heterochromatic state of the genome [92]. ESCs are primarily euchromatic [93], and as Adams et al. pointed out, this may explain why ATM dependent signaling pathways appear to be dispensable to hESCs in some regards [78].

In pluripotent A–T cells we observed differences in focal adhesion and ECM interaction pathways. Although there is some evidence to suggest cytoskeletal arrangement defects in cells from A–T patients [163], these pathways are reported to be highly variable in pluripotent stem cell lines (Personal communication: Professor Christine Wells), and our small sample size may have affected this. It is interesting to note however the recurrent appearance in these pathways of a number of genes linked to ATM including BIRC3 (Baculoviral IAP repeat-containing 3) [171].

ATM has been demonstrated to signal to BIRC3 through NFκB in response to IR in murine lymphoid tissue. We also noticed dysregulation of *C-Jun*, previously shown to have a role in ATM related oxidative stress-mediated response [172]. PDGF (Platelet-derived growth factor-beta was included in this list and has previously shown to activate ATM kinase in response to p53 induced oxidative stress [173]. We noted dysregulation of *XIAP*, previously shown to be part of the ATR/ATM related DNA damage response [174] and also dysregulation of *IGF1R* (Type 1 insulin –like growth factor receptor) which has previously been shown to modulate ATM function [175].

Gene expression profiling revealed that the pattern of expression in A–T fibroblasts was markedly different from that in control fibroblasts. Surprisingly, this was not the case for the control and A–T iPSC, where the majority of pathways were similarly regulated despite the absence of ATM. Nevertheless, our pathway analysis uncovered extensive differences in the regulation of oxidative phosphorylation genes supporting a defect at the level of the mitochondrion. It is not clear how ATM might be involved in the regulation of mitochondrial respiration, however, there have been several reports that illustrate mitochondrial abnormalities in these cells (Ambrose et al., 2007; Fu et al., 2008). Ambrose et al. (2007) described abnormal structural organization of mitochondria in A–T cells. They also observed reduced mitochondrial membrane potential and diminished respiratory activity in A–T cells that is consistent with the results obtained here. Fu et al. (2008) showed that ATM functions through AMPK in mitochondrial biogenesis and thus in its absence, defective biogenesis could be contributing to the disease phenotype. An extensive list of ataxias and other syndromes have been linked with mitochondrial dysfunction including NARP (neuropathy and retinis pigmentosa)[176], MELAS (mitochondrial encelphalomyopathy, lactic acidosis with stroke-like episodes) [177] and MERRF (Myoclonus epilepsy with ragged red fibres)[178]. These mitochondrial pathway defects may become evident when the mechanism or demand for energy production is altered, such as during differentiation induced mitochondrial biogenesis. An imbalance of mitochondrial enzyme activity could lead to overproduction of ROS, which has been associated with pathology in A–T [98, 179, 180]. It is not impossible that differences observed in mitochondrial gene expression stemmed from subtle differences in reprogramming state between control and A–T

cells as comparison of iPS cells remains a major challenge for the field. We also observed that *G6PD* was downregulated in A–T iPSC compared to controls. This is consistent with a recent report (Consentino et al. 2011) that showed that ATM activates the pentose phosphate pathway (PPP) by stimulating complex formation between heat shock protein 27 and G6PD to increase G6PD activity. In response to oxidative stress, carbohydrate metabolism is rerouted from glycolysis through the PPP and it is well established that oxidative stress activates ATM (Guo et al. 2009) and A–T cells show evidence of oxidative stress. The downregulation of *G6PD* in A–T iPSC fits with these observations. Despite extensive disruption of gene expression in mitochondrial related pathways we did not uncover any gross differences in mitochondrial membrane potential or levels of mitochondrial reactive oxygen species between A–T and control iPS cells. We speculate that as tissues differentiate and specialize, driving the demand for ATP, subtle differences may manifest more obviously. We cannot however discount the possibility that this expression signature could have arisen through other mechanisms, for example the process of live-sorting cells by flow cytometry which was used to obtain cells for RNA extraction is known to induce stress [181]. It is known that reprogramming causes drastic remodeling of a number of aspects relating to mitochondrial activity [182]. It is possible that our reprogrammed cells exist along a continuum with respect to their mitochondrial dynamics. Although we noted tight clustering of gene expression of members of the *PluriNet*, suggesting our cells were similarly pluripotent, we cannot discount changes that may be present as a result of this.

The great majority of studies on the characterisation of A–T cells and on the functioning of ATM have been carried out in lymphoblastoid cells and fibroblasts and to a lesser extent on lymphocytes (Bensimon et al. 2011). Mouse models recapitulate a great deal of the A–T phenotype but do not exhibit neurodegeneration (Frappart and McKinnon 2006). It is becoming apparent that the DNA damage response is a dynamic process that is differentially regulated in response to ontological requirements. This study and others suggest that ATM is not vitally required for the maintenance of pluripotent genomic integrity. We suggest that manifestation of A–T symptoms may present during or downstream from differentiation events when cells

become more reliant on ATM dependent signaling for DNA repair or ATM in non-canonical contexts, such as protection against ROS or developmentally related apoptosis.

Although we have shown that ATM is required for the coordination of DNA repair and cell cycle control initiatives after DNA damage (Figures 3.2C, 3.3A&B), our pathway analysis data support the theory that in an unchallenged state ATM is redundant for protection of the genome in pluripotent cells, being either not required or having compensatory mechanisms in place to fulfill its role in this context. We note marked disruption of DNA damage surveillance and repair processes in A–T fibroblasts that are not evident in A–T iPSCs that supports this idea. A limited number of studies have been carried out with ESCs in which ATM has been abrogated by disruption of the gene, siRNA knockdown or by treatment with the ATM inhibitor KU55933 (Biton et al. 2007; Song et al. 2010). Momcilovic et al. (2009) showed that KU55933 had variable effects in ESCs at concentrations used in somatic cells and that a 10-fold increase was required to effectively inhibit ATM activity in this cell type. For this reason, A–T iPSCs may provide more stringent model systems to examine ATM involvement in the embryonic setting.

While *Atm*-deficient mice recapitulate some of the cellular defects observed in A–T, including radiosensitivity, immunodeficiency, high incidence of cancer, and defective germ cell development [73, 99] other A–T-related defects, such as neuronal degeneration are not evident in *Atm*-deficient mice, highlighting the need for a human A–T model system. iPSCs from individuals with A–T therefore present an opportunity to elucidate the role of *ATM* in the pluripotent context, to study A–T pathogenesis and to create relevant patient-specific cell platforms for drug screening. Pluripotent stem cells provide a model system to differentiate cells of interest to study. It is possible to some degree to recreate the process of neurogenesis to obtain neurons of various regional identities. This technology may hold the secret to unlocking the complexities of ATM and its role in neurodegeneration.

4.0 A basic model for neurogenesis in A–T derived iPS cells

Introduction

The major debilitating symptom of A–T (crippling ataxia and loss of movement control) is thought to arise due to loss of granule and Purkinje cells from the cerebellum [183], however there is a wide array of evidence to support the pathological involvement of other cell types within the brain. These include anterior horn cells, which are present in the ventral grey matter section of the spinal cord. There is additional evidence implicating spinal motor neurons, and also cells in the Substantia nigra (located in the midbrain, consisting of a high level of dopaminergic neurons), Oculomotor nuclei (midbrain), inferior olivary nucleus (medulla oblongata) and the Dentate nucleus (deep within cerebellar white matter)[184-186].

A number of models, including both mouse and human [14, 108, 187-190], have been put forward over the years to explore the function of ATM including its roles in neurodegeneration, yet little consensus exists regarding a common unifying role for ATM which sufficiently explains the neurodegeneration prominent in this condition.

Possibly due to the fact that the first and major role for ATM revolves around its involvement in the maintenance of genomic stability, the central paradigm of DNA damage regulation by ATM is often used to explain the neurodegeneration in A–T. Popular theories assert that ATM is involved with DNA damage surveillance and removal of compromised progenitors during or after development. Other theories extend to postulate that ATM is involved in dynamically regulating brain-specific aneuploidy [106] or regulation of long interspersed element-1 (L1) retrotransposition (shuffling and expansion of repetitive DNA sequence elements) throughout the nuclear genome [191]. Although there is certainly evidence for these theories, it seems unlikely that they alone are responsible for the symptoms of A–T, given the myriad of other roles for ATM and pleiotropic nature of the disease.

There is solid evidence that ATM is involved with developmental processing including regulation of cell death [107]. Dynamic patterns of ATM expression within the developing mouse CNS were observed following *in situ* hybridization experiments, showing high levels

throughout early development which later taper off suggesting that problems with neural development might happen early as a consequence of ATM deficiency [108]. This finding was supported by the observation that ATM was upregulated during *Xenopus* brain development also [109]. A similar study confirmed this in humans and provided evidence for a role of cytoplasmic ATM in developing cerebellar neurons [13]. Allen et al. showed that ATM was required for normal development and differentiation of adult neural progenitor cells and suggested other physiological roles for this protein [110]. Despite these findings, it is clear that a major question remains about whether A–T is a developmental or degenerative disease.

A recent paper implicates ATM in neural activity by showing that in its absence, cultured neurons lacking ATM exhibited defective Long Term Potentiation, while also showing slower rates of spontaneous vesicular dye release [7]. This group showed that ATM could be isolated from synaptosomal preparations, postulating that the ATM protein physically associated with phosphorylated versions of VAMP2 and SYNAPSIN-1 in the pre-synaptic nerve terminal. Interestingly this group demonstrated a physical association between ATM and its close homologue ATR, predominantly occurring in the cytoplasm of neuronal cells. Another group showed that knockout of ATR in mouse models gave rise to animals grossly devoid of proper cerebellar development [192].

Historically, ROS have often been cited as a contributor to the pathology in A–T [104]. At least two publications [98, 101] show evidence that links ROS with specific degeneration of PCs in the cerebellum in A–T models. Chen et al. speculate that ATM acts outside of its canonical role as a DNA damage regulator in participating in the defense against ROS. Only recently was the mechanism behind this explained [12] in which ATM was shown to be involved in a specific and distinct form of ROS surveillance and response through disulfide bond formation. Imbalance of ROS is a commonly recurring phenomena in many other diseases, especially neurological disorders, including Parkinson's and Alzheimer's [103] which is not surprising given imbalance of physiological processes can give rise to ROS with relative ease. It was shown that p38 MAPK acts as a negative regulator to control neural stem cell (NSC) proliferation in response to oxidative stress that may offer some insight into the mechanism behind the neurodegeneration in

A–T [105]. Given the large metabolic requirements and the fact that a large proportion of the neurons in the brain are post mitotic, the role of ATM in neuronal cells may be chiefly in response to ROS, rather than solely orchestrating DNA damage related cell cycle regulation.

An area which is receiving increasing amounts of attention with respect to a range of neuropathologies is the mitochondrion. Mitochondria at their most basic provide energy for cellular metabolism in the form of ATP (Adenosine Triphosphate). The reality is that mitochondria are incredibly dynamic and complex organelles that orchestrate and are involved with almost every aspect of cell biology. Mitochondria are also the major source of ROS within the cell. Dysfunction of the mitochondria is increasingly being associated with diseased states. A recent publication describes a mechanism to explain the neurological dysfunction in ARSACS syndrome whereby mutations in the *sacsin* gene give rise to mislocalisation of mitochondria within the somites and proximal dendrites of Purkinje cells [193]. This in turn affected the ability of these neurons to properly synapse with each other. It is becoming harder to ignore the accumulating evidence implicating mitochondria in a myriad of different neurological syndromes and ataxias [176, 178]. A handful of papers provide evidence that ATM may be involved in regulating mitochondrial homeostasis [113, 194-196], however none propose a mechanism that may explain the involvement of mitochondria with the neurodegeneration in A–T. In addition to the role of mitochondria in providing energy for cellular respiration and balance of ROS, the mitochondria are also the second largest source of calcium buffering within the cell [197].

Calcium levels are important in regulating processes such as cell death and migration during the development of the CNS. Calcium is a versatile second messenger which co-ordinates a range of cellular processes, particularly in neurons where it is involved with activity and signaling, development (including control of CNS migration [198]), mitochondrial function [199], kinase signaling [200], communication [201], homeostasis and survival (including regulated cell death) [202]. Dysregulation of calcium handling is implicated in a range of neuropathologies including stroke/cerebral ischemia (whereby impaired influx/egress of calcium across the plasma membrane affects calcium homeostasis) [203], certain variants of Alzheimer's disease (in which

lipid peroxidation and resulting generation of toxic byproducts may impair membrane ion-motive ATPases and glucose/glutamate receptors, altering calcium influx and also synaptic or endoplasmic reticulum calcium homeostasis) [204]. Unregulated accumulation of calcium is also a major component of excitotoxic cell death in the CNS. There is an increasing body of literature implicating calcium and mitochondrial aberrations in a range of neurological and metabolic conditions, including a study which demonstrates via patch-clamp-recording of murine Purkinje cells, an electrophysiological deficit caused by a significant decrease in calcium currents. Weaver syndrome presents an interesting case –mutations in the *Girk2 (Kcnj6)* a gene that encodes a G-protein-coupled inward rectifier potassium channel, results in a loss of ion selectivity and constitutive activation [205]. As a result calcium levels are perturbed resulting in defects in neurite extension, cell migration and aberrantly regulated cell death in cerebellar granule cells.

It seems likely that rather than any one of the popular and isolated ATM theories being correct, there may be an over-arching connection between them that incorporates the role of ATM in development, responding to and repairing DNA damage, sensing ROS, metabolic signaling, mitochondrial homeostasis, apoptosis regulation and the possibility of unknown functions. To elucidate precisely what drives the neurodegenerative changes in A–T and why Purkinje cells within the cerebellum are predominantly affected remains the challenge. Therefore, we explored the concept of differentiating iPS cells into neuronal progenitors to investigate whether we could model various aspects of A–T with a view to better understanding this disease.

Using a modified version to that published recently [206], we produced a highly pure population of neuronal progenitors which could be differentiated into electrophysiologically active neuronal cells. We investigated a range of parameters using this model including differentiation bias/potential, growth and proliferation in culture, gene expression and calcium trafficking kinetics after induction of neuronal activity by depolarization, HDAC4 localisation, mitochondrial morphology, localization and membrane potential. We showed that genetic manipulation of these neurons was possible by introducing copies of mCherry-tagged ATM,

which restored a functional DNA damage response. Additionally we delivered a real-time genetically encoded fluorescent calcium reporter gCaMP5 to further examine calcium kinetics.

This chapter illustrates a proof of principle that patient-specific neurons can be made from iPS cells and that these neurons offer a robust and reproducible model system to investigate the neuropathology in ATM. Additionally we show a phenotype which may contribute to the understanding of this disease and highlight the fact that *in vitro* manipulation of neural stem cells, a technique which will be vital for use of stem cells in a clinical setting, is possible.

Materials and methods

Neuronal Differentiation

iPSC cultures were grown for 5 days after passage prior to commencement of differentiation and changed directly into KSR hESC media supplemented with 5 μM Dorsomorphin (Stemgent) and 10 μM SB431542 for the first 6 and 12 days of differentiation, respectively, with media changes every 2 days. KSR hESC media was gradually substituted with Neurobasal medium (GIBCO) (with N2&B27 supplements used at the manufacturer's specifications) (GIBCO) with 25%, 50%, 75% and 100% N2B27 Neurobasal medium in KSR hESC media on days 4, 6, 8 and 10 respectively. Neurospheres were formed on day 6 of differentiation by 10 minute incubation in 1 mg/ml Collagenase IV (GIBCO) at 37°C and dislodging of large pieces of colonies by use of a cell scraper and P1000 pipette. Neuralized colony fragments were seeded into Ultra-low Cluster plates (Costar) where they aggregated into tight spheres. On day 12 of differentiation neurospheres were seeded onto Matrigel™ (BD) coated plates and N2B27 Neurobasal media was subsequently changed every 3-4 days as neurons grew out from the sphere borders. Cultures were passaged every week by cell dissociation buffer (Sigma) at a 1:2 – 1:3 ratio, eventually leading to the complete dissociation of neurosphere aggregates. 4-6 week old cultures were subsequently matured by the addition of 20 ng/mL brain-derived neurotrophic factor (BDNF) and 20 ng/mL glial-cell-line-derived neurotrophic factor (GDNF) (R&D), 200

nM ascorbic acid, and 0.5 mM dibutyryl-cAMP (Sigma) for 2 weeks with media changes every 2 days to replenish growth factors.

Immunostaining

For immunostaining cells were washed once gently, so as not to disturb large spheroid colonies or fragile cell extensions, in PBS and fixed in 4% paraformaldehyde for 15 minutes at room temperature. For nuclear staining samples were permeabilized in 0.1% TritonX100 at room temperature for 10 minutes or ice cold methanol for 15 minutes at -20^{o}C, before blocking with 10% goat serum and incubation with the relevant antibodies overnight at 4°C. Antibodies and dilutions used were β-III-TUBULIN (Millipore) [1:1000], GFAP (Dako) [1:1000], MAP2 (Millipore) [1:1000], PAX6 (Developmental Studies Hybridoma Bank)[1:500], OTX5f5 [1:000] (Developmental Studies Hybridoma Bank), Synapsin (Calbiochem) [1:500]. Following washing with PBS (3 times 5 minutes at room temperature) secondary antibodies goat anti-mouse IgG_1, goat anti-mouse IgG_{2B}, goat anti-mouse IgM and Donkey anti-rabbit IgG (Alexa fluor) [2 µg/ml] were used to reveal reactivity. Nuclei were stained with DAPI or Hoechst. This preparation minus the addition of primary antibody was used to confirm specificity of staining.

FACS

Neurons were harvested by washing once in PBS and using either Cell dissociation buffer (Life technologies) or TrypLE (Invitrogen) to generate a single cell suspension. Cells were fixed in 4% paraformaldehyde for 15 minutes at room temperature and blocked for 10 minutes in 1% BSA/PBS before application of primary pre-conjugated antibodies. Antibodies were CD44, CD24, CD184, CD271, CD15, B-III-TUBULIN (Millipore) [1:1000] & GFAP (Dako) [1;1000]. Cells were strained through a cell strainer to remove clumps and ensure a single cell suspension suitable for FACs.

Irradiation

A Co^{60} source (GammaCell 220) irradiator was used to deliver 5 Gy of IR (Dose rate 8130 Gy/Hour) to the cells. Cells were returned to the incubator to recover to the appropriate time point before harvesting/fixation with 4% paraformaldehyde.

Imaging of mitochondria (mitochondria and mitochondrial membrane potential)

For neurons a plate-based assay was employed. Mitochondria in live neurons were labeled using Mitotracker green at 100 nM and TMRM at 10nM. Hoescht was applied [1:15000] for 5 minutes to visualize nuclei. Autofocus functionality was employed to image a large number of fields across multiple wells in a black-walled 96 well plate using an InCell Analyzer 2000 automated microscope. Images were analyzed using software to delineate the borders of individual cells and quantify the fluorescent intensities in separate channels. Cells were imaged in phenol-red free HEPES containing media containing N2&B27 supplements.

Neurosphere growth assay

40 single neurospheres (2x10 control, 2x10 A–T) were individually seeded in suspension into wells of a 96-welled plate in N2B27 medium. Neurospheres were photographed every other day using an OlympusIX51 microscope for two weeks. Images were compressed to 8-bit files and appropriate thresholds were set to define the borders of each individual neurosphere before applying an area measurement algorithm using ImageJ. Sample identity was blinded to analyser.

Neurite extension assay

Neurospheres were seeded onto Matrigel (BD) coated tissue culture plastic dishes and allowed to attach for several hours. Time-lapse microscopy was employed over 17 hours to visualize the migration of neurons from the border of the spheres and extension of projections was quantified manually using ImageJ. Sample identity was blinded to analyser.

Calcium imaging (FLIPR) in neuronal cultures

Calcium imaging was performed using the FLIPR Tetra High Throughput Cellular Screening System, essentially as described by Vetter and Lewis [207]. Neurons were seeded in a black walled 386 well plate, loaded with a calcium-sensitive fluorescent dye (5M Fluo-4-AM) in physiological salt solution (PSS; composition 140 mM NaCl, 11.5 mM glucose, 5.9 mM KCl, 1.4 mM MgCl2, 1.2 mM NaH2PO4, 5 mM NaHCO3, 1.8 mM CaCl2, 10 mM HEPES) containing in addition 0.3% BSA for 30 minutes at 37 °C. Neurons were depolarized with microinjection of KCl to a final concentration of 50 mM. A FLIPR Tetra (Molecular Devices) fluorescent plate reader was used to measure response to activation with using a cooled CCD camera with excitation at 470 – 495nM and emission at 515–575nM. Camera gain and intensity were adjusted for each plate to yield a minimum of 1000 arbitrary fluorescence units (AFU) baseline fluorescence. Prior to addition of KCl, 10 baseline fluorescence readings were taken, followed by fluorescent readings every second for 300 seconds. Delta F/F was calculated for each time point as (fluorescence at time t – avg. baseline fluorescence)/(avg. baseline fluorescence) to give a normalized measure of fluorescence. Negative control consisted of neurons incubated with PSS buffer only. For the third FLIPR experiment, after depolarization a subsequent microinjection of Inomycin was performed to lyse cells and measure resulting fluorescence to normalize samples for cell numbers.

Statistical analysis was performed on calcium transients data through application of a MATLAB algorithim designed to extract parameters from individual transients including max peak, slope of the curve and area underneath the curve. To exclude outliers from interfering with statistical analysis a threshold approach was adopted to identify and exclude traces from neurons that did not ‘fire’ in a given condition. This was also retained and recorded as a quantitave output. Images below depict four typical traces showing fluorescent signals from individual wells of neurons that (A) did not illicit a response to stimulus, (B) illicited some response but not sufficient to meet threshold critera and (C & D), illicited responses that met criteria and were used for subsequent downstream feature extraction and statistical analysis. Student’s t-tests were applied to the data (with or without Welch’s correction, based on patterns of variance – a

boxed p-value represents tests with Welch's correction). One way ANOVAs with multiple comparison post-tests were utilized where applicable.

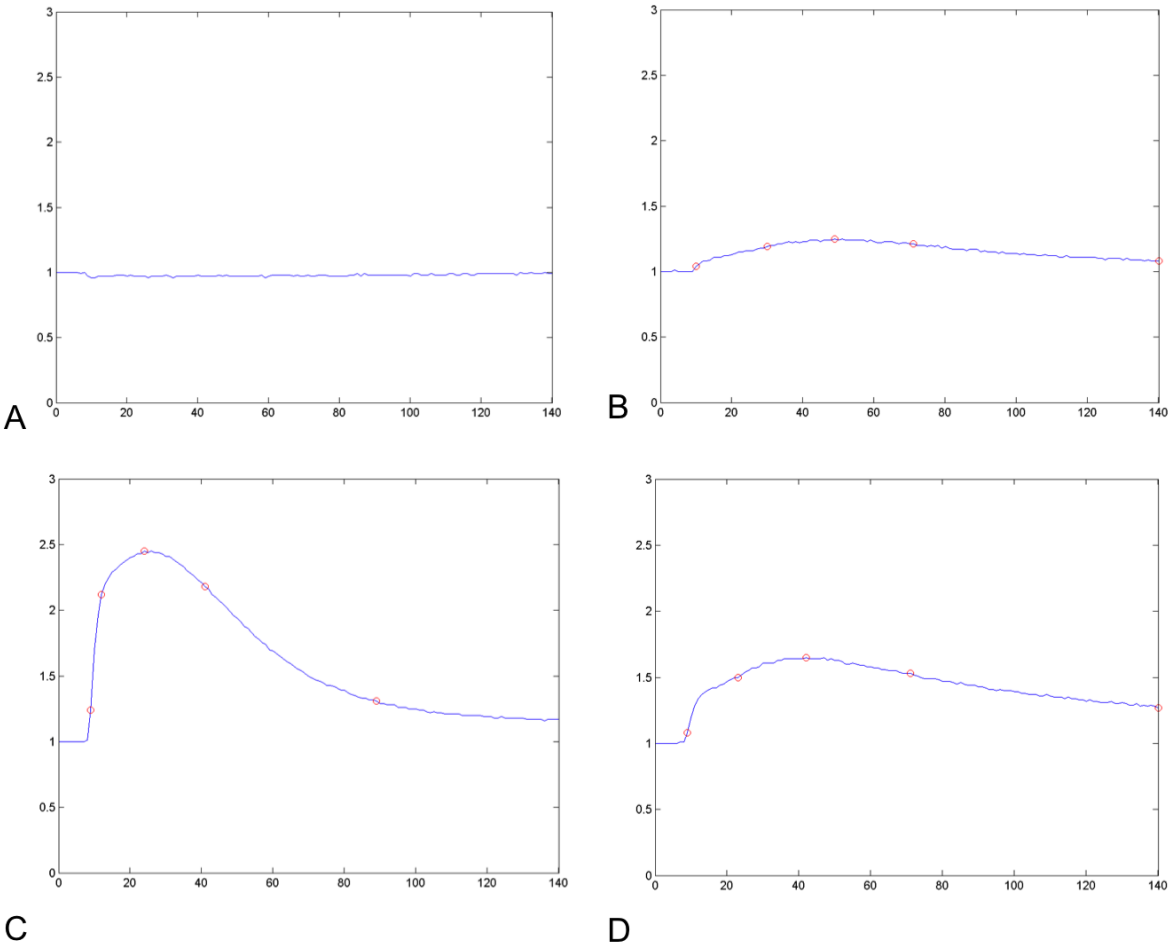

Amaxa nucleofection of neurons with gCaMP5 and ATMmCherry constructs

Briefly, Amaxa AD1 buffer was equilibrated to room temperature containing 5 µg gCaMP5 and or ATM-mCherry plasmids (a kind gift from Dr Sergei Kozlov) per reaction. Plasmids were delivered to Matrigel coated 24 well plates (Nunc) containing neurons at approximately 70-80% confluency using the Amaxa Nucleofector 4D EH215 electroporation program. Fresh buffer was applied and cells were allowed to recover at 37°C in an incubator.

Single cell calcium imaging using gCaMP5

Single cell calcium imaging was performed on neurons transfected with the real-time fluorescent calcium reporter gCaMP5. Cells were imaged in phenol-red free HEPES containing media with N2&B27 supplements. Neurons were selected on the basis of their morphology (multiple lengthy dendrites), which were also positive for gCaMP5 and imaged for 30 seconds of baseline fluorescence before the application of media to a final concentration of 50 mM KCl to induce depolarization. One image per second was taken. ImageJ was used to perform background fluorescent subtraction, application of Gaussian blur and define a region of interest before applying a stack-measuring algorithm to quantify change in fluorescence. Samples were blinded to the analyzer.

Patch clamping of iPSC derived neurons

Neurospheres were grown in N2B27 Neurobasal medium and were seeded on glass coverslips coated in Matrigel for several days until neurons migrated from the borders of the sphere. For electrophysiological recordings neurons were perfused with artificial cerebrospinal fluid containing 119 mM NaCl, 2.5 mM KCl, 1.3 mM $MgCl_2$, 2.5 mM $CaCl_2$, 1 mM $Na_2H_2PO_4$, 26.2 mM $NaHCO_3$, and 11 mM glucose (equilibrated with 95% O2, 5% CO2). Recording pipettes (3¬5 M‡) fabricated from borosilicate glass were filled with a solution 135 mM $KMeSO_4$, 8 mM NaCl, 10 mM HEPES, 2 mM Mg_2ATP, 0.3 mM Na_3GTP, 0.1 mM spermine, 7 mM phosphocreatine, and 0.3 mM EGTA. Visualization of the neurons was achieved using an upright microscope (BX50WI; Olympus) with 400x magnification. Whole-cell recordings were made using MultiClamp 700A (Molecular Devices), filtered at 4 kHz, and digitized at 8 kHz using an ITC-16 board (Instru-Tech). Analysis was performed using Axograph X. Individual neurons were voltage clamped at -70 mV and showed classical signs of voltage-gated sodium and potassium channel activity after depolarization (voltage steps from -80 mV to +40 mV). To verify that the inward and outward currents were driven by sodium and potassium, respectively, the inward currents were blocked by 1 mM Tetrodotoxin and the outward currents were blocked by replacing potassium with cesium in the pipette solution.

Quantification of γH2AX foci

Neurons were treated in chamber slides with 50 mM KCl in N2B27 neurobasal media either singly (1x5 min) or triply (3x 5minutes with 5 minutes in between). Singly depolarized cells were fixed at two, six, twelve and twenty-four hours post depolarization including a mock depolarized control. Cells receiving repeated KCl stimuli were fixed at two and twenty-four hours post depolarization. Cells were washed once gently, so as not to disturb fragile cell extensions, in PBS and fixed in 4% paraformaldehyde for 15 minutes at room temperature. Samples were permeabilized in 0.1% TritonX100 at room temperature for 10 minutes, before blocking with 1% BSA and incubation with γH2AX antibody (Millipore) (1:1000) overnight at 4°C. Following washing with PBS (3 times 5 min at room temperature) secondary antibody goat anti-mouse IgG_1, (1:1000) was used to reveal reactivity. Slides were mounted in Prolong Gold Antifade reagent with DAPI. This preparation minus the addition of primary antibody was used to confirm specificity of staining.

Nuclei were chosen at random and foci were photographed using an OlympusBX61 fluorescent microscope. Images were blinded and subjected to analysis using the software TRI2 to quantify the mean number of foci per cell. Briefly, images were modified using the 'smart-sharpen' filter in Photoshop followed by conversion to an 8-bit format where TRI2 software applied a Hough transform based algorithm (CHARM). This approach was confirmed using a matlab algorithim to quantifty foci based on uniform parameters.

Results

Neuronal differentiation and validation

We differentiated A–T and control iPSCs into neuronal progenitors using a modified version of the dual SMAD inhibition protocol previously described [208] (Figure 4.1A depicts in schematic form the protocol used). Through application of SB431542 (TGF-β inhibitor) and Dorsomorphin (BMP inhibitor) SMAD related control of pluripotency is disrupted. The result is interruption of normal pluripotentcy mechanisms and subsequent restriction of lineage commitment generating

a suspension of highly pure neuronal progenitors which grow as neurospheres. These spheres can be plated down upon which migration of cells with a neuronal morphology and reactivity for markers β-III-TUBULIN and MAP-2 are observed (Figure 4.1A). This protocol was optimized within our lab by James Briggs. PAX6 could be detected in paraffin embedded serially sectioned neurosphere aggregates by day 8 (Figure 4.1B). It should be noted that images show pelleted neurosphere aggregates from early during the induction protocol. As such there are cells present that are not yet expressing PAX6. Sample homogeneity is addressed in subsequent figures.

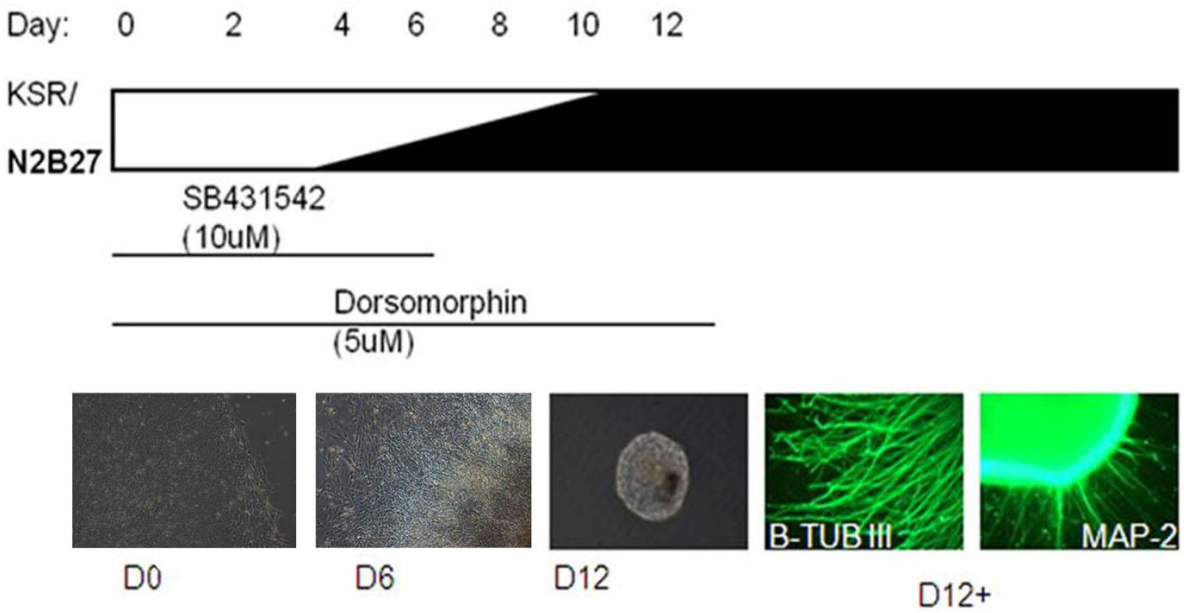

Figure 4.1A - Schematic representation of neural induction protocol involving stepwise addition of N2B27 neurobasal medium and small molecules SB431542 and Dorsomorphin for the first 6 and 12 days respectively. Neurospheres were generated on day 6 of induction and plated after 12, giving rise to colonies with neuronal projections and morphologies and were β-III-TUBULIN and MAP-2 positive.

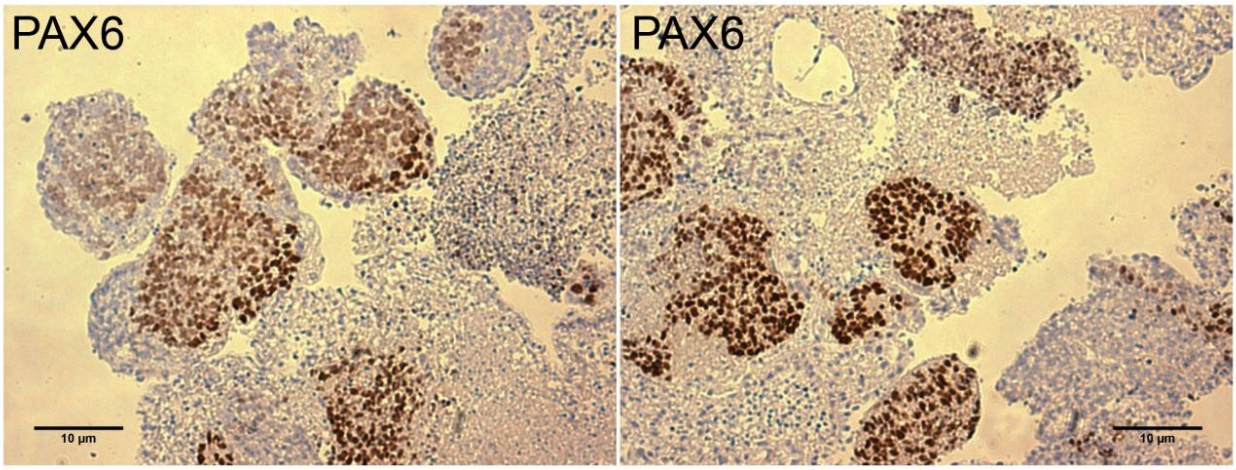

Figure 4.1B – Early neural progenitor marker PAX6 is detected by day 8 in serially sectioned neurosphere aggregates. Scale bars are 10 µm.

Immunostaning for lineage specific transcription factors PAX6, OTX1 & OTX2 after 35 days of neuronal induction revealed the central region of these neurospheres (marked in Figure 4.1C) were largely reactive for these markers and as such resembled neuronal cells with an anterior neuronal phenotype (Figure 4.1C).

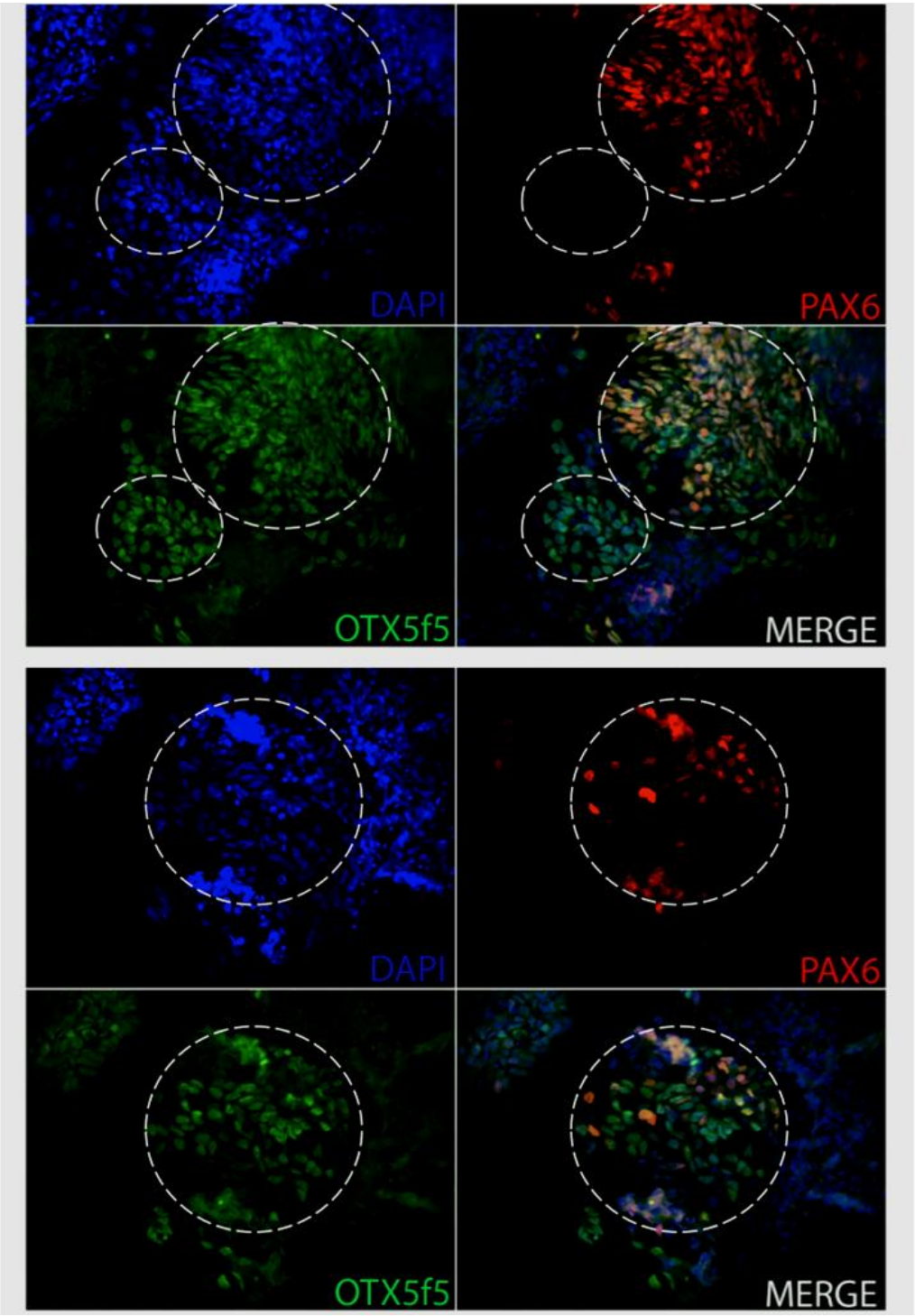

Figure 4.1C – Neuronal progenitors exhibit widespread expression of OTX1 & OTX2 (FITC), as well as PAX6 (TRITC).

After the initial neural induction, neurospheres can be dissociated and passaged for prolonged periods of time resulting in a more pliable population of cells partly comprised of single neuronal cells and also smaller spheres still containing progenitor cells. qPCR analysis (Figure 4.2A) revealed robust induction of core neurogenic genes in differentiated cultures over the course of the induction protocol. Stark upregulation of *DCX, Pax6, Sox9* and *Mash1* transcript was observed - all corresponding to the appearance of a neural progenitor progenitor shown to appear by day 8 (See figure 4.1B). We also noted increases in *Sox1 & Sox2* transcript however these were to a lesser magnitude. Large error bars here may be indicative of a spread in the timing and magnitude of appearance of this transcript, suggestive of inter-line variation with respect to neural induction kinetics.

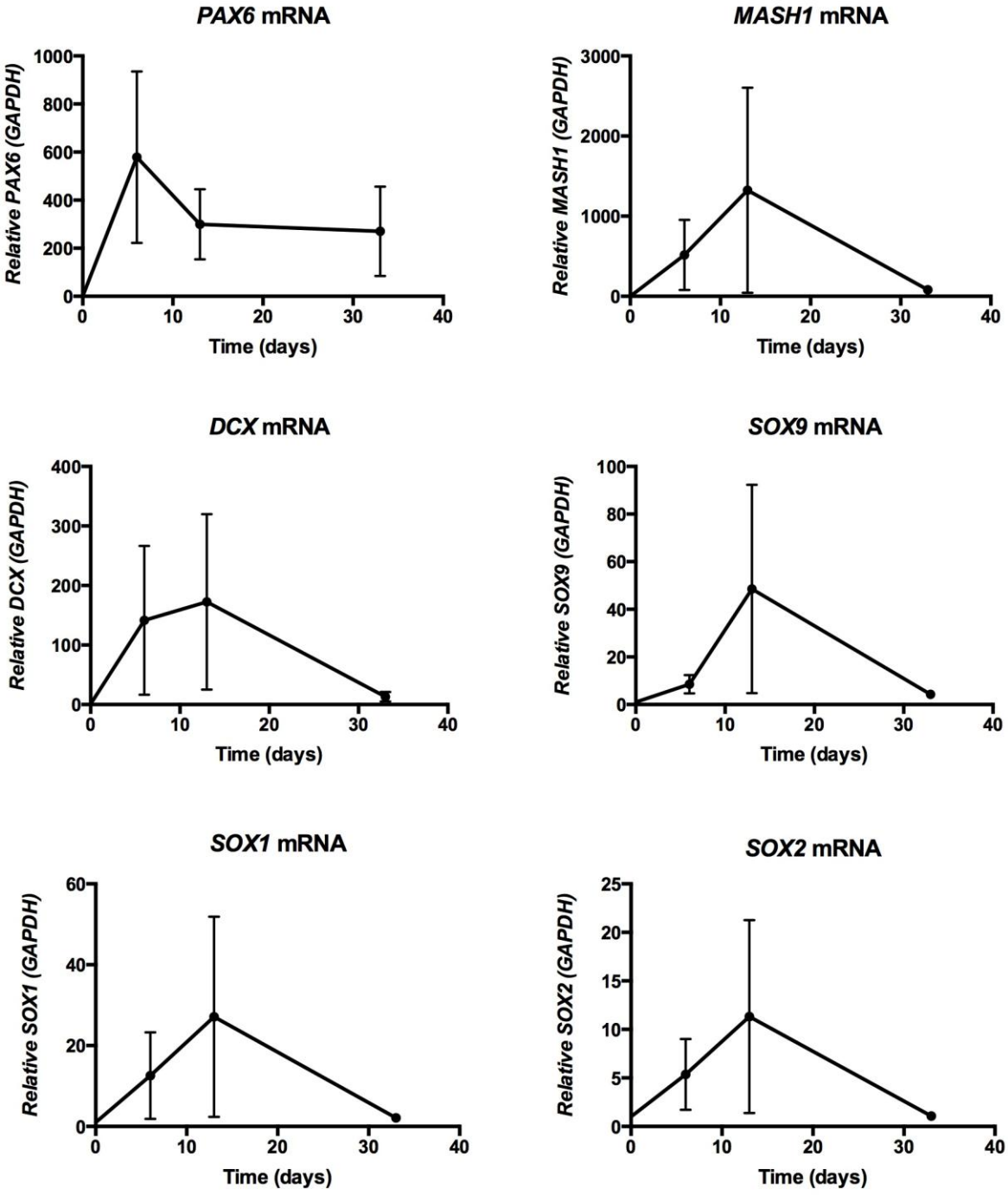

Figure 4.2A – qPCR analysis of neural induction at day 0 (undifferentiated iPS cells), day 6 (intermediate neural progenitors), day 13 (neurospheres) and day 33 (committed neurons).

To ensure inter-line comparisons and subsequent downstream analyses were viable we examined the population composition of our neuronal inductions. The two major species of cells present (PAX6 expressing progenitors and β-III-TUBULIN positive immature neurons) were quantified and no differentiation bias was apparent between controls and A–T neurons as measured by an unpaired t-test (Figure 4.2B). Quantitative assessment of the proportions of cells present totaled ~90-100% (65-85% PAX6 + neural progenitors and 15-20% B-III-TUBULIN + neurons). After 60 days in culture we analyzed the expression of a combination of cell surface markers shown to identify neuronal populations [209]. We could detect CD15, CD24, CD44, CD184 by flow cytometry but not CD271. This expression profile is consistent with a mixed population of glia, neurons and neural stem cells (Figure 4.2C). Figure 4.2D shows phase contrast images before dissociation for FACs. Cells with overtly neuronal, glial or progenitor morphologies were easily distinguishable by light microscopy.

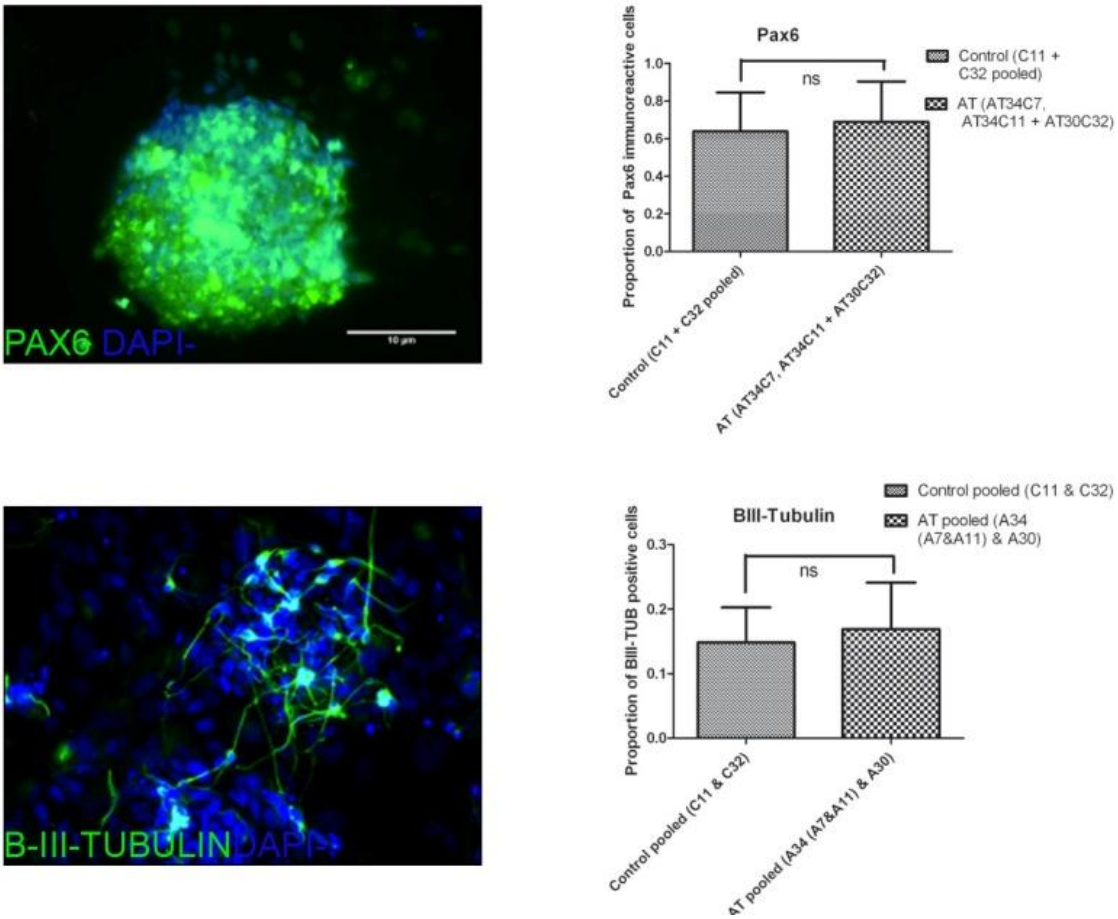

Figure 4.2B – PAX6 and β-III-TUBULIN immunoreactivity was quantified in A–T and control neurons showing comparably represented populations of progenitors/committed neurons by an unpaired t-test. Scale bar is 20 µm.

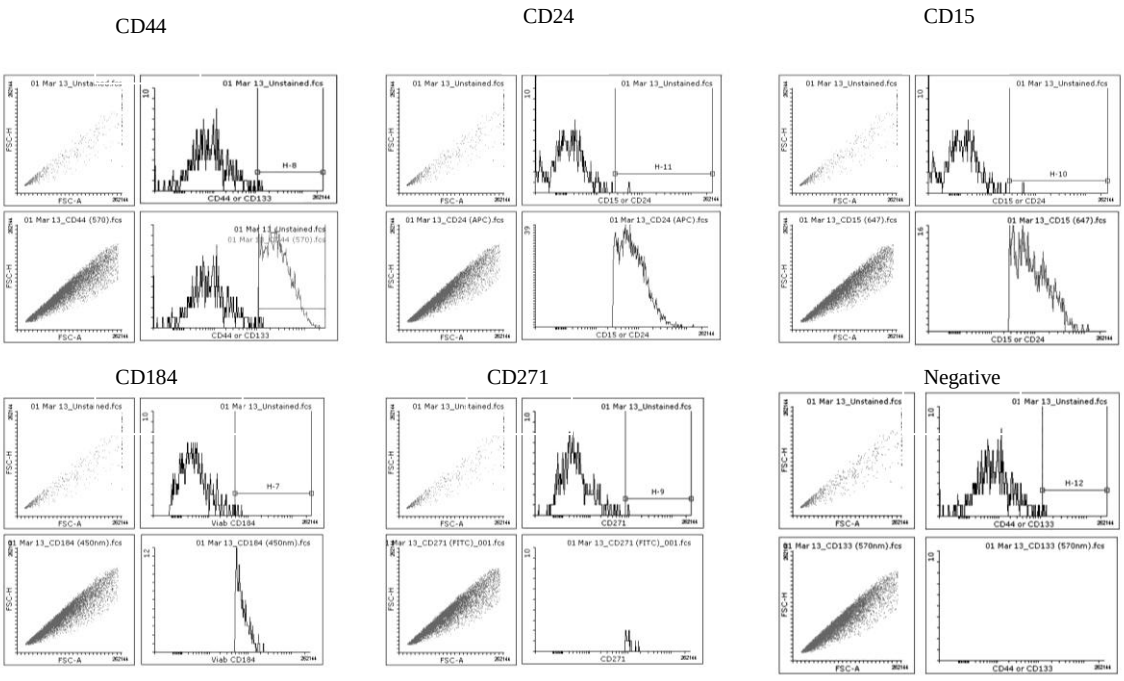

Figure 4.2C – Flow cytometry reveals reactivity with markers for CD15, CD24, CD44 and CD184 but negligible reactivity with an antibody to CD271 indicating surface profiles consistent with a mixed population of glia, neurons and neural stem cells.

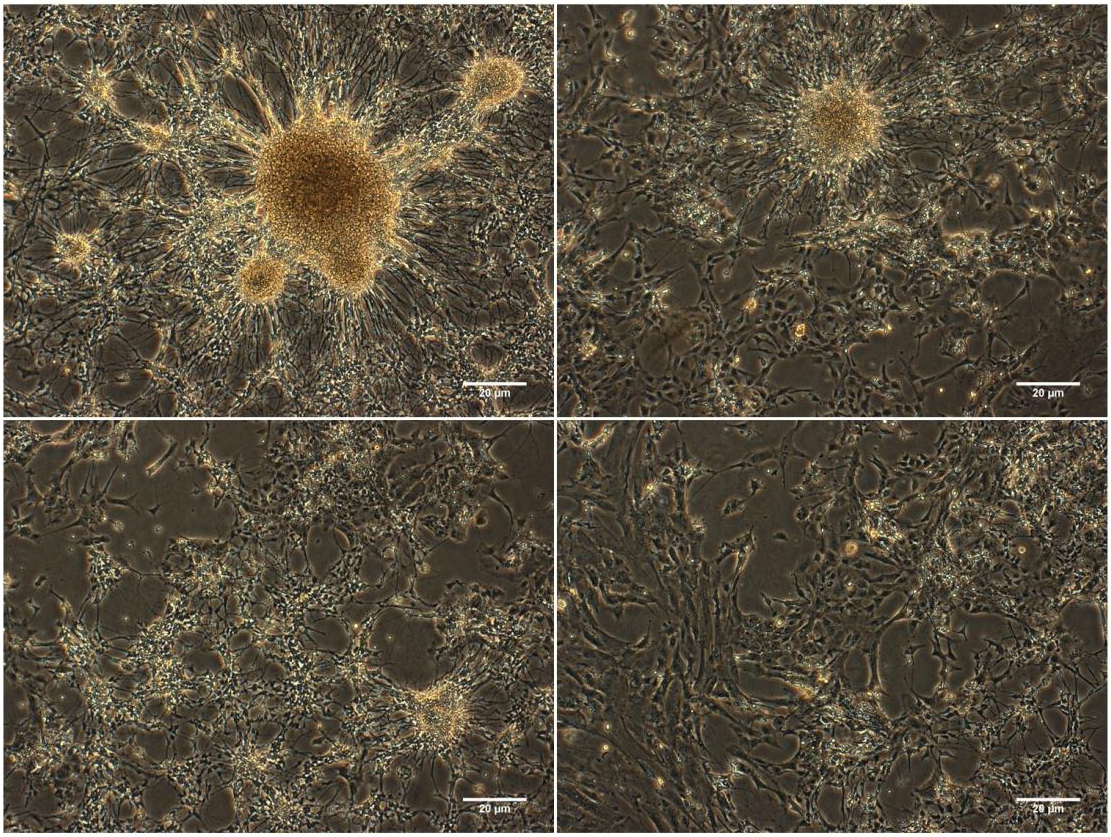

Figure 4.2D – Phase contrast images of neuronal cultures at day 60. Scale bars are 20 µm.

Neurosphere growth assay

After 12 days of neural induction, proliferation of neurospheres was profiled over the course of two weeks by monitoring of growth size in culture. No significant difference was observed between two control and two A–T (AT30 and AT34) cell lines (n=10 for each cell line). A Two-way ANOVA was applied with a Bonferonni post-test ($P > 0.05$). These data suggest that there is no detectable difference in neural commitment or neural stem cell expansion rate between control and A–T iPSC derived neurons.

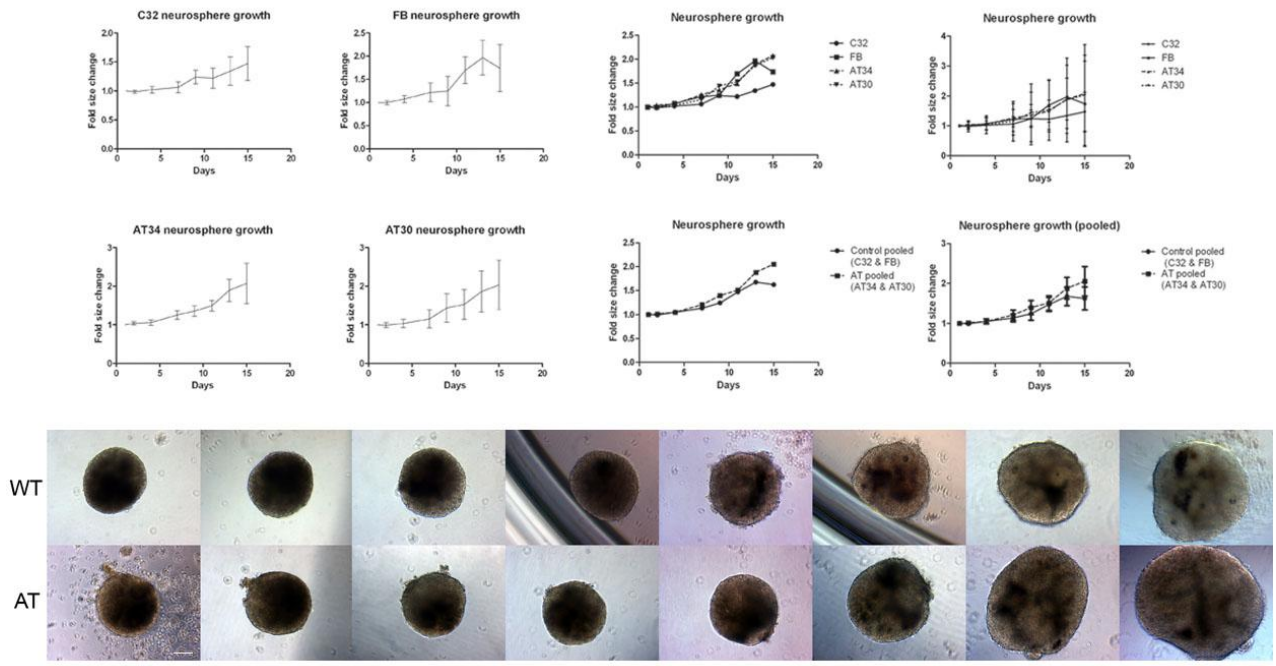

Figure 4.3A – Neurosphere growth was profiled over 2 weeks. Control lines C11 & FB (Top row far left) showed a commensurate pattern of growth and expansion in comparison to A–T neurospheres AT34 & AT30 (lower row far left). Error bars indicate SEM. When pooled there was no significant difference in growth rate between A–T and controls (Two-way ANOVA with Bonferoni correction) (far right show graphs with SEM). Scale bar in lower left panel is 20 µm.

Neurite extension assay

Similarly when we observed neurite extension from neurons by time-lapse microscopy we observed no statistically significant difference between A–T and control derived neurons (unpaired t-test). Administration of an antioxidant 5-carboxy-1.1.3.3-tetramethylisoindolin-2-yloxyl (CTMIO), previously shown to increase complex dendritogensis of ATM deficient murine Purkinje neurons [101], resulted in a reduction in neurite extension rate in both A–T and control derived neurons presumably due to the toxicity of the solvent.

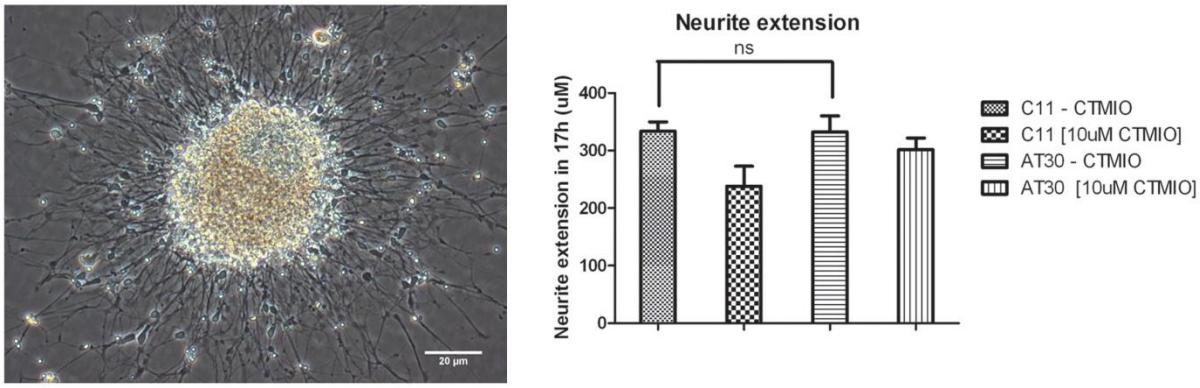

Figure 4.3B – Neurite extension was measured over 17 hours using time-lapse microscopy in A–T and control iPS cell derived neurons with and without antioxidant CTMIO [10 µM]. Scale bar is 20 µm. An unpaired t-test shows no significant difference in mean neurite extension length between A–T and controls. Error bars show SEM.

Gliogenesis

We noticed after 60 days the onset of glia in our neuronal induction preparations (Figure 4.3C). We manually quantified the proportion of β-III-TUBULIN positive neurons to GFAP positive glial cells from two controls and two A–T neuronal cell lines (Figure 4.3D).

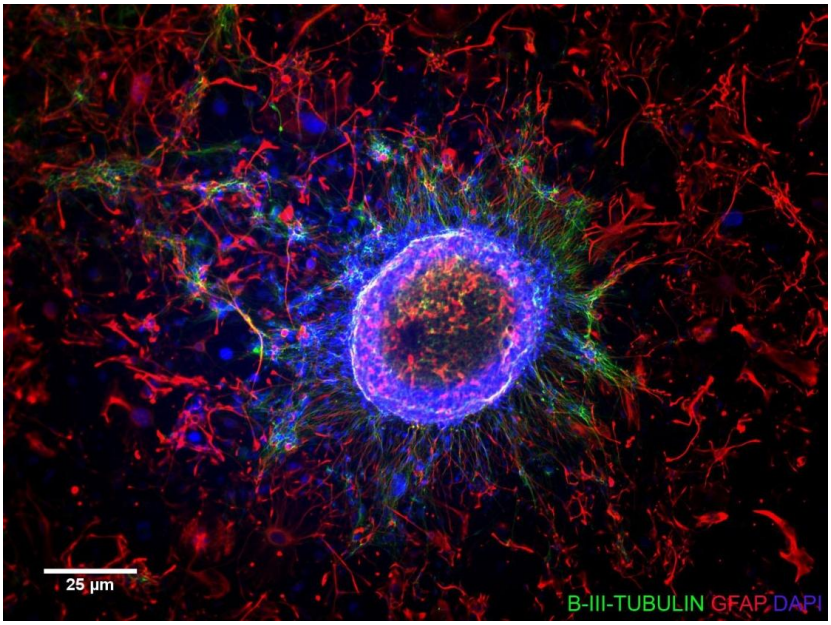

Figure 4.3C – Neurons (FITC channel marked by β -III-TUBULIN staining) and Glia (Deep red channel marked by GFAP marker) arose after 60 days of neural induction protocol. Scale bar is 25 µm.

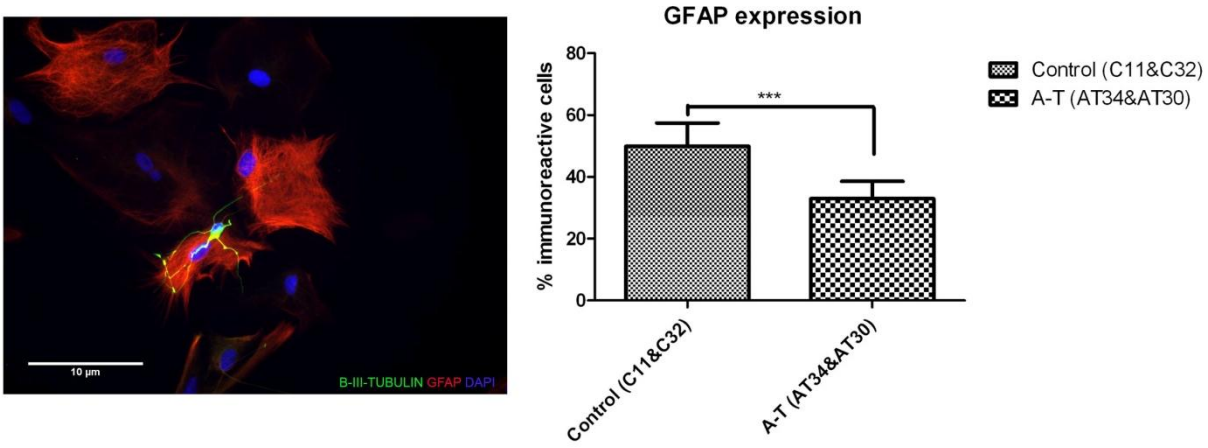

Figure 4.3D – The proportion of glial cells present was manually quantified in control and A–T cultures. Scale bar is 10 µm.

We observed a statistically significant reduction in glial cells arising from A–T cultures. To confirm this phenomenon, we performed a second neural induction and used a more sensitive FACS based approach (Figure 4.3E). FACS plots are shown in Figure 4.3F.

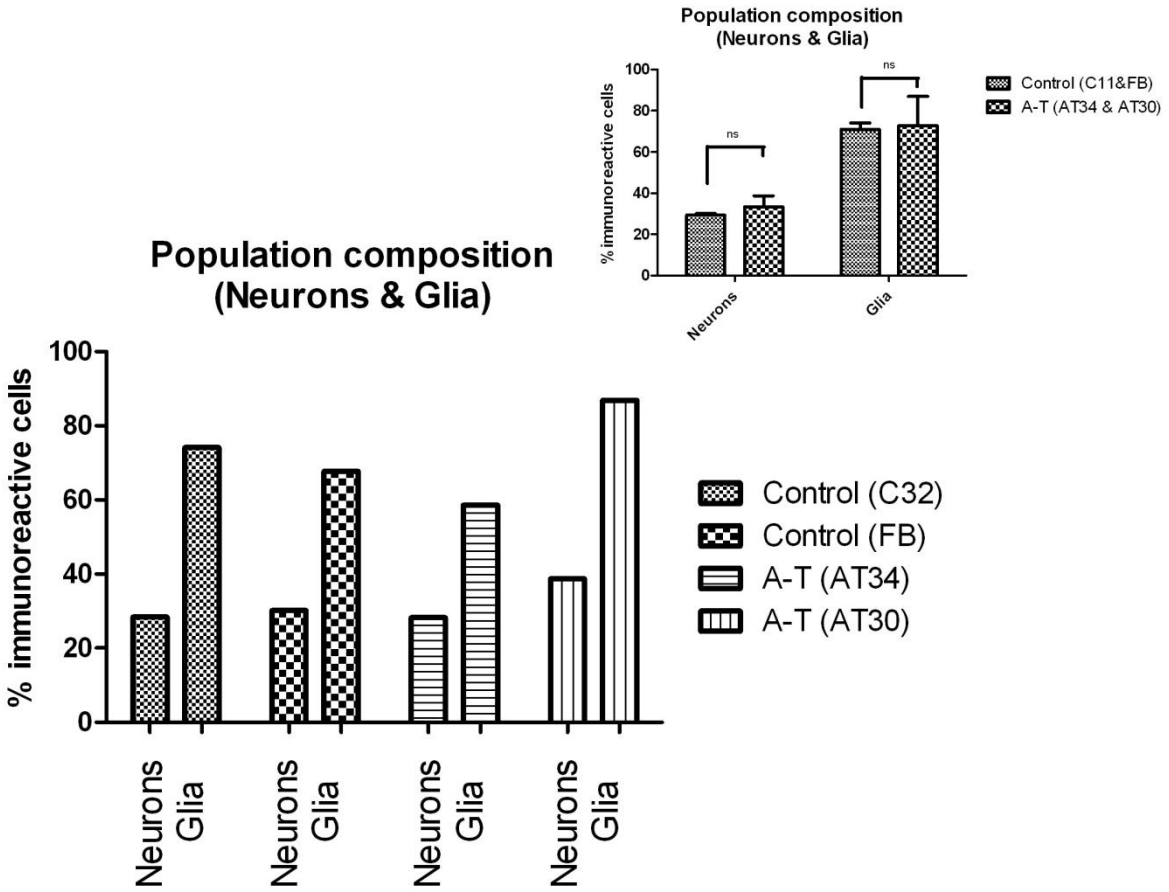

Figure 4.3E – Population composition (neurons and glia) was examined by FACS and revealed no statistically significant difference between A–T and control populations.

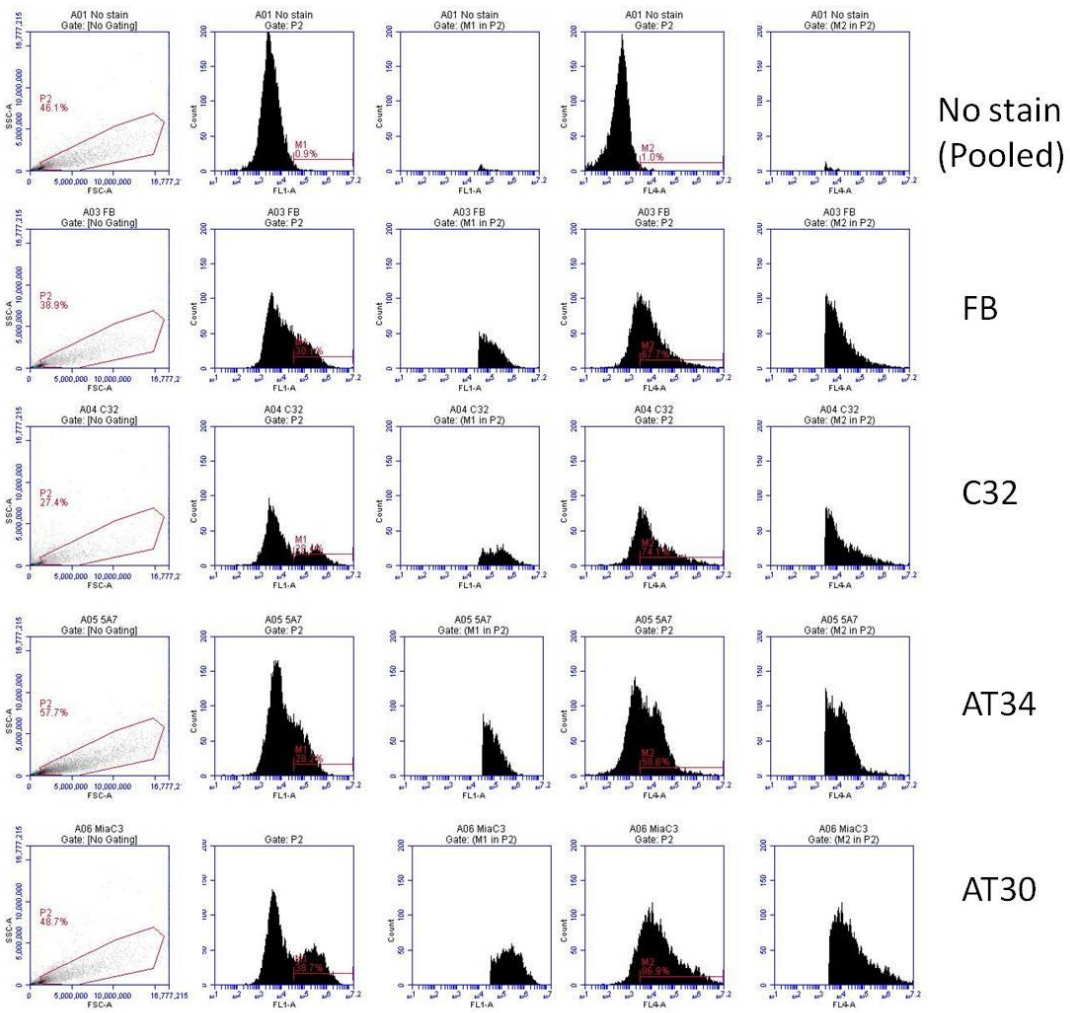

Figure 4.3F – FACS plots show FSC/SSC and gating of neurons & glia to exclude debris (far left columns), gating to exclude autofluorescence in FL-1 (488 nm) (second column) and FL-4 (633 nm) (fourth column). Third column shows double-gated population of interest positive for β-III-TUBULIN. Fifth and final column shows reactivity with GFAP antibody using a similar gating strategy.

In a second neural induction and by using the more sensitive methodology of FACS we could not reproduce evidence for differences in the proportion of glia that were present between control and A–T neural populations (Figure 4.3E lower panel shows raw data and inlay in upper right shows pooled data with unpaired t-test results). Staining intensity for GFAP appeared

consistently more intense in both A–T lines in comparison to controls, possibly suggestive of Glial activiation.

Neuronal activity

To validate our neuronal differentiation protocol was producing neurons that were physiologically relevant we tested several parameters to assay for a stimulus-based response. When stimulus was applied (KCl 50 mM depolarization), these cultured neurons displayed electrophysiological activity in the form of calcium transients, as shown by Ca2+ imaging performed using the FLIPR (Fluorometric imaging plate reader) Tetra High Throughput Cellular Screening System (Figure 4.4 – Panel A). Additionally we isolated RNA from stimulated neurons and examined transcription of Immediate early genes (IEGs) which are known to be transcribed after neuronal activation [210]. We observed between 1.5 to 5-fold change in gene expression four hours after depolarization (Figure 4.4 - Panel B). Using an unpaired t-test (with Welch's correction) we observed no statistically significant difference in transcription of any IEGs between control and A–T derived neurons. As an added measure we performed whole cell recordings by patch clamping neurons (Figure 4.4 - Panel C). To verify that the inward and outward currents were driven by sodium, and respectively potassium, the inward currents were blocked by 1 mM Tetrodotoxin and the outward currents were blocked by replacing potassium with cesium in the pipette solution. Immunostaining with an antibody to SYNAPSIN (a protein involved with neurotransmitter release and an indirect marker of functional neurons, revealed robust expression of this marker (Figure 4.4D).

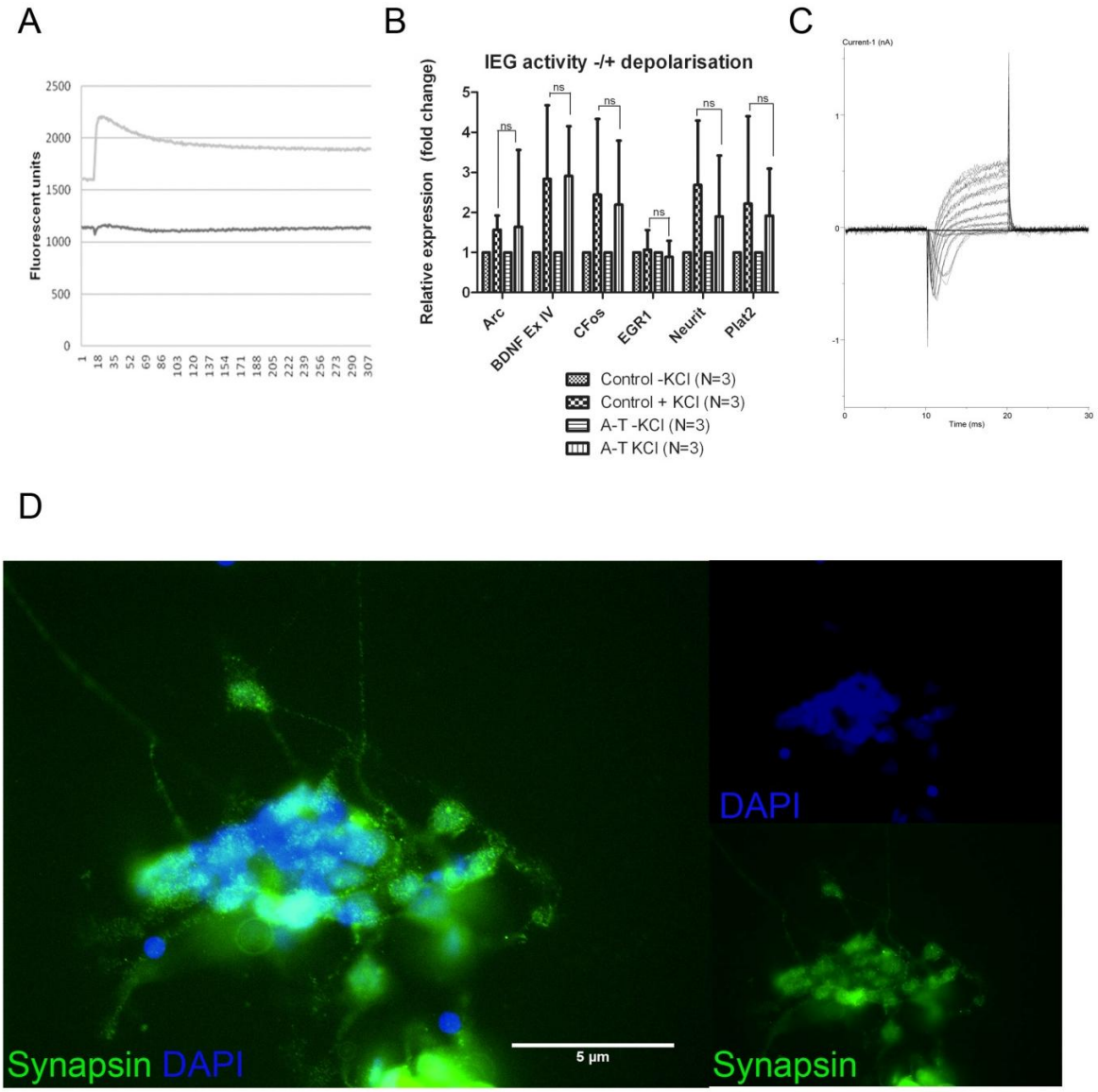

Figure 4.4 – Neuronal activity in neurons (A) Depolarization induced calcium transients in iPSCs derived neuronal cultures following *in vitro* maturation. A representative experiment is shown. Buffer only control is shown in dark grey. (B) Four hours post depolarization IEG activity is measured by qPCR for *Arc, BDNF Ex IV, CFos, EGR1, Neurit* and *Plat2.*An unpaired t-test (with Welch's correction) revealed no significant differences between A–T and controls. (C) Whole cell recording by patch clamping of iPS cell derived neurons display activity of voltage-gated sodium and potassium channel activity after depolarization (voltage steps from -80mV to +40mV). (D) Immunoreactivity with antibody to Synapsin was observed. Scale bar is 5 µm.

Having established that our protocol generated SYNAPSIN positive neurons that display both induction of IEGs aswell as Na/K transients following patch clamping, we next interrogated KCl induced neuronal calcium trafficking. Routine validation of neurons across separate neural differentiation experiments was done by assaying for presence of neuronal activity as shown by calcium trafficking after application of stimulus. Through loading of neurons with a calcium sensitive dye (Fluo-4-AM), equivalent numbers of neuronal cells were seeded into 384 well plates and imaged using a high throughput fluorescent plate reader setup (FLIPR Tetra) that was used to observe intracellular calcium transient kinetics after stimulation of neurons by microinjection of depolarizing agent. We subjected calcium transients to feature extraction (max peak/amplitude, area under the curve and slope) and statistical analysis, highlighting differences in kinetics between individual cell lines/clones. We initially tested a variety of conditions in two validated neuronal cell lines (one control C32, and one A–T AT34) to elucidate the mechanisms driving this, which are outlined below (Figure 4.5A).

Neurons derived from control iPS (C32) exhibited classic entry and release of calcium after microinjection of 50 mM KCl. After measuring 10 seconds of baseline fluorescence we observed a sharp rise (2.5 fold) in fluorescence indicating calcium influx into the cell via voltage-gated ion channels (Figure 4.5A; panels C&D). In contrast we observed markedly less robust entry of calcium into the A–T cells after depolarization with an approximate 1.25 fold increase in fluorescent intensity (Figure 4.5A; panels C&D). Comparison of max amplitude between A-T and control neurons revealed a statistically significant difference ($p = <0.0001$). Along with this we noticed a change in the shape of the curve, in which calcium egress seemed constant and protracted rather than a steep slope as seen in controls (Figure 4.5A, panels C&D). To explore this we examined the area under the curve and slope of the curve between control and A-T neurons. Differences in both parameters were statistically significant ($p = 0.0002$ and $p = <0.0001$ respectively). 16 replicate wells of each cell line were imaged simultaneously and data pooled. Error bars showing SEM are shown on the right-hand panels. Statistical data was taken only from replicate wells that met threshold criteria considered as ‘firing’ (criteria shown in

materials and methods) – comparable firing rates were generated (87.5 & 81.25% for control and A-T respectively).

To test whether ATM may be having an acute effect on calcium trafficking within the cell, we incubated both control and A–T neurons with ATM inhibitor Ku55993 at a concentration of 10 μM for 24 hours. Incubation with Ku55993 in controls (Figure 4.5A, panels E&F) resulted in not only a reduction in amplitude but modification of the shape of the curve indicating that this treatment was having some effect on calcium trafficking within the cells. It should be noted that we also observed this effect in A–T neurons (Figure 4.5A, panels G&H) that was pronounced. Interestingly, when control neurons were incubated for an identical period of time with a DMSO only control at the same concentration to that used in application of inhibitor there was no difference in calcium efflux (Figure 4.5A, panels I&J). We did however observe a difference when A–T neurons were imaged in the presence of DMSO only control (Figure 4.5A, panels K&L) in the form again of a change in amplitude and slope of the curve. Statistical analyses support these findings by showing that a significant change in amplitude of the curve was present in A-T neurons ($p<0.0001$), but not controls ($p = 0.3070$). Taken together these data suggest that treatment with ATM inhibitor is having some effect on calcium trafficking but it becomes difficult to define the precise degree amongst the background of having a population of cells (A–T) seemingly more sensitive to treatment with the inhibitor vehicle. It is also possible that this inhibitor is having an off-target effect on a target other than ATM that is influencing calcium trafficking or generally impacting on cell viability.

We previously noted the consistent down-regulation of mRNA coding for calcium channel subunits in A–T iPSC microarray data (Table 3.7B) and speculated that if this was conserved in neurons, this may affect calcium uptake and release. We used two calcium channel inhibitors (Nifedipine, an L-type calcium channel blocker and CVID, an N-type calcium channel blocker) to examine whether we could reproduce the difference in calcium activity observed between A–T neurons and controls. Application of 10 μM Nifedipine almost completely ameliorated calcium efflux in control cells, drastically changing the amplitude ($p = <0.0001$), area under the curve ($p = <0.0001$) and slope of the curve ($p = <0.0001$) (Figure 4.5A, panels M&N). We

noticed a similar trend in A–T neurons (Figure 4.5A, panels O&P) ($p = <0.0001$, $p = 0.0072$ and $p = 0.0055$ respectively). Interestingly, application of CVID at 10 µM resulted in almost no change to the amplitude ($p = 0.3685$), area under the curve ($p = 0.9758$) or slope of the curve ($p = 0.1791$) in control neurons (Figure 4.5A, panels Q&R) but a reduction in the amplitude ($p = <0.0001$) of the curve in A–T neurons (Figure 4.5A, panels S&T). Additionally a change could be observed in the slope of the curve however this failed to meet statistical significance ($p = 0.1202$). All experimental conditions were performed to include four to sixteen replicates that were pooled. SEM is presented on the right hand side panels in each case.

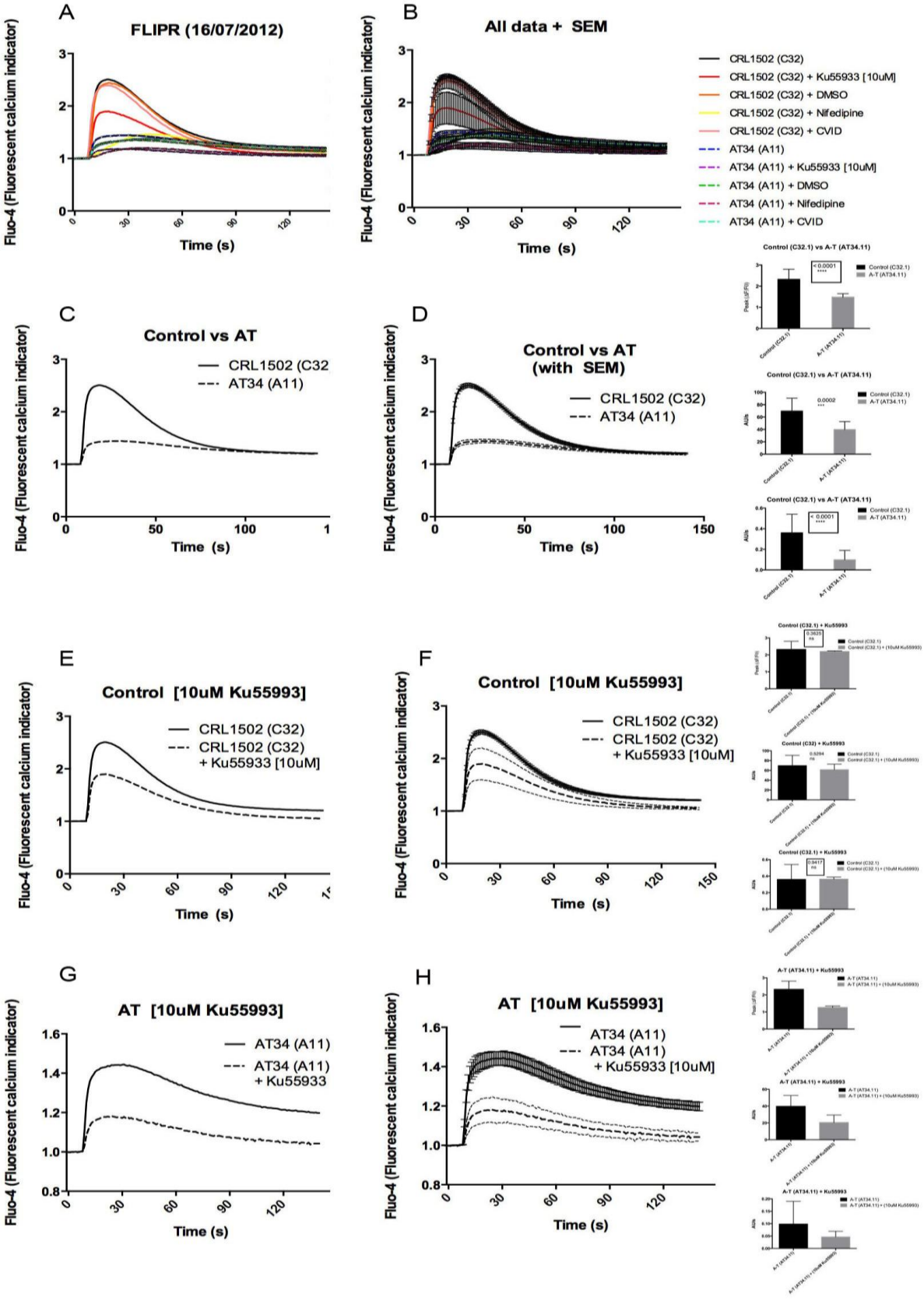
A
FLIPR (16/07/2012)
Fluo-4 (Fluorescent calcium indicator)
Time (s)
B
All data + SEM
Fluo-4 (Fluorescent calcium indicator)
Time (s)
CRL1502 (C32)
CRL1502 (C32) + Ku55933 [10uM]
CRL1502 (C32) + DMSO
CRL1502 (C32) + Nifedipine
CRL1502 (C32) + CVID
AT34 (A11)
AT34 (A11) + Ku55933 [10uM]
AT34 (A11) + DMSO
AT34 (A11) + Nifedipine
AT34 (A11) + CVID
C
Control vs AT
CRL1502 (C32
AT34 (A11)
Fluo-4 (Fluorescent calcium indicator)
Time (s)
D
Control vs AT
(with SEM)
CRL1502 (C32)
AT34 (A11)
Fluo-4 (Fluorescent calcium indicator)
Time (s)
Control (C32.1) vs A-T (AT34.11)
Control (C32.1) vs A-T (AT34.11)
Control (C32.1) vs A-T (AT34.11)
E
Control [10uM Ku55993]
CRL1502 (C32)
CRL1502 (C32)
+ Ku55933 [10uM]
Fluo-4 (Fluorescent calcium indicator)
Time (s)
F
Control [10uM Ku55993]
CRL1502 (C32)
CRL1502 (C32)
+ Ku55933 [10uM]
Fluo-4 (Fluorescent calcium indicator)
Time (s)
Control (C32.1) + Ku55993
Control (C32) + Ku55993
Control (C32.1) + Ku55993
G
AT [10uM Ku55993]
AT34 (A11)
AT34 (A11)
+ Ku55933
Fluo-4 (Fluorescent calcium indicator)
Time (s)
H
AT [10uM Ku55993]
AT34 (A11)
AT34 (A11)
+ Ku55933 [10uM]
Fluo-4 (Fluorescent calcium indicator)
Time (s)
A-T (AT34.11) + Ku55993
A-T (AT34.11) + Ku55993
A-T (AT34.11) + Ku55993

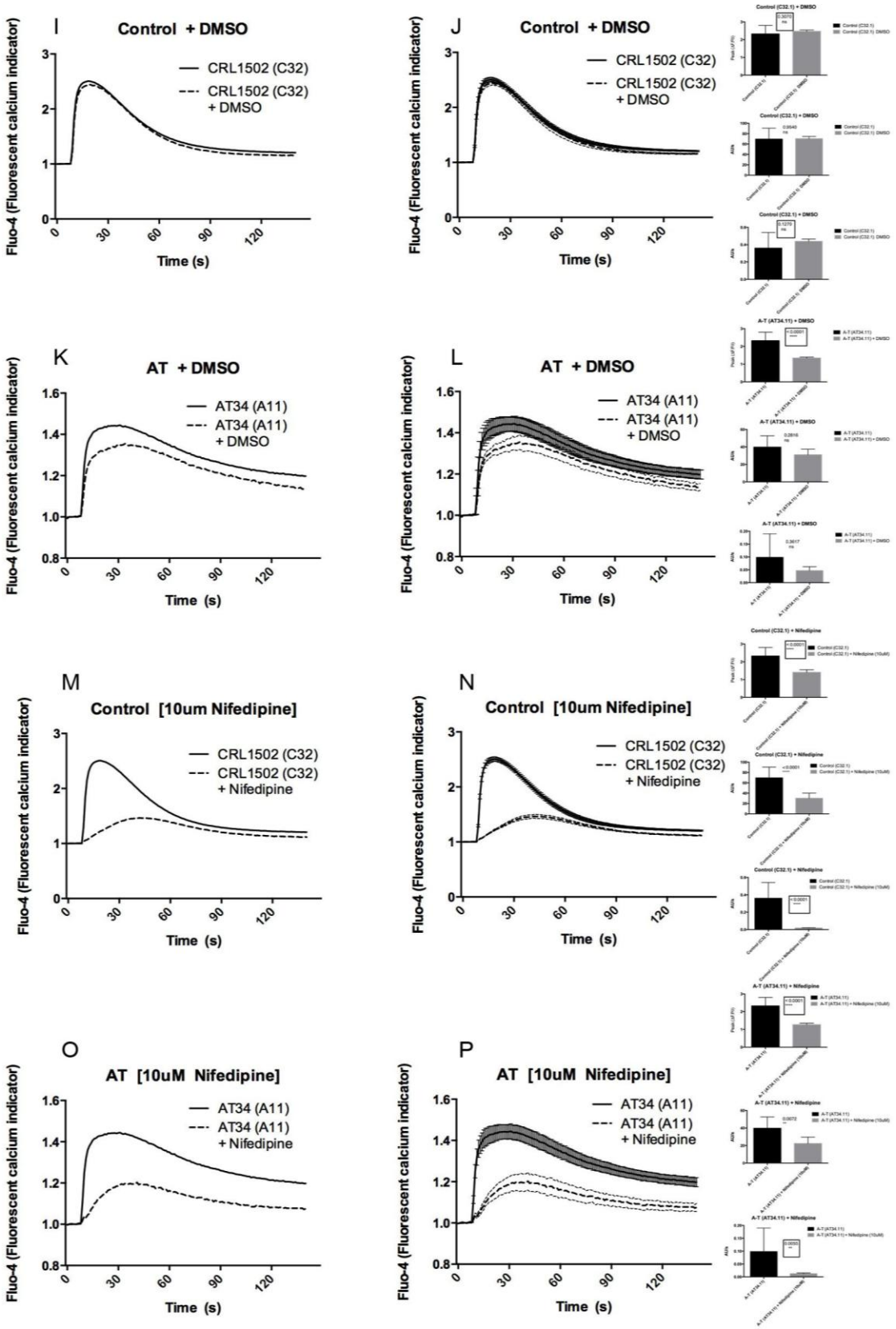
I
Control + DMSO
CRL1502 (C32)
CRL1502 (C32) + DMSO
Fluo-4 (Fluorescent calcium indicator)
Time (s)
J
Control + DMSO
CRL1502 (C32)
CRL1502 (C32) + DMSO
Fluo-4 (Fluorescent calcium indicator)
Time (s)
K
AT + DMSO
AT34 (A11)
AT34 (A11) + DMSO
Fluo-4 (Fluorescent calcium indicator)
Time (s)
L
AT + DMSO
AT34 (A11)
AT34 (A11) + DMSO
Fluo-4 (Fluorescent calcium indicator)
Time (s)
M
Control [10um Nifedipine]
CRL1502 (C32)
CRL1502 (C32) + Nifedipine
Fluo-4 (Fluorescent calcium indicator)
Time (s)
N
Control [10um Nifedipine]
CRL1502 (C32)
CRL1502 (C32) + Nifedipine
Fluo-4 (Fluorescent calcium indicator)
Time (s)
O
AT [10uM Nifedipine]
AT34 (A11)
AT34 (A11) + Nifedipine
Fluo-4 (Fluorescent calcium indicator)
Time (s)
P
AT [10uM Nifedipine]
AT34 (A11)
AT34 (A11) + Nifedipine
Fluo-4 (Fluorescent calcium indicator)
Time (s)

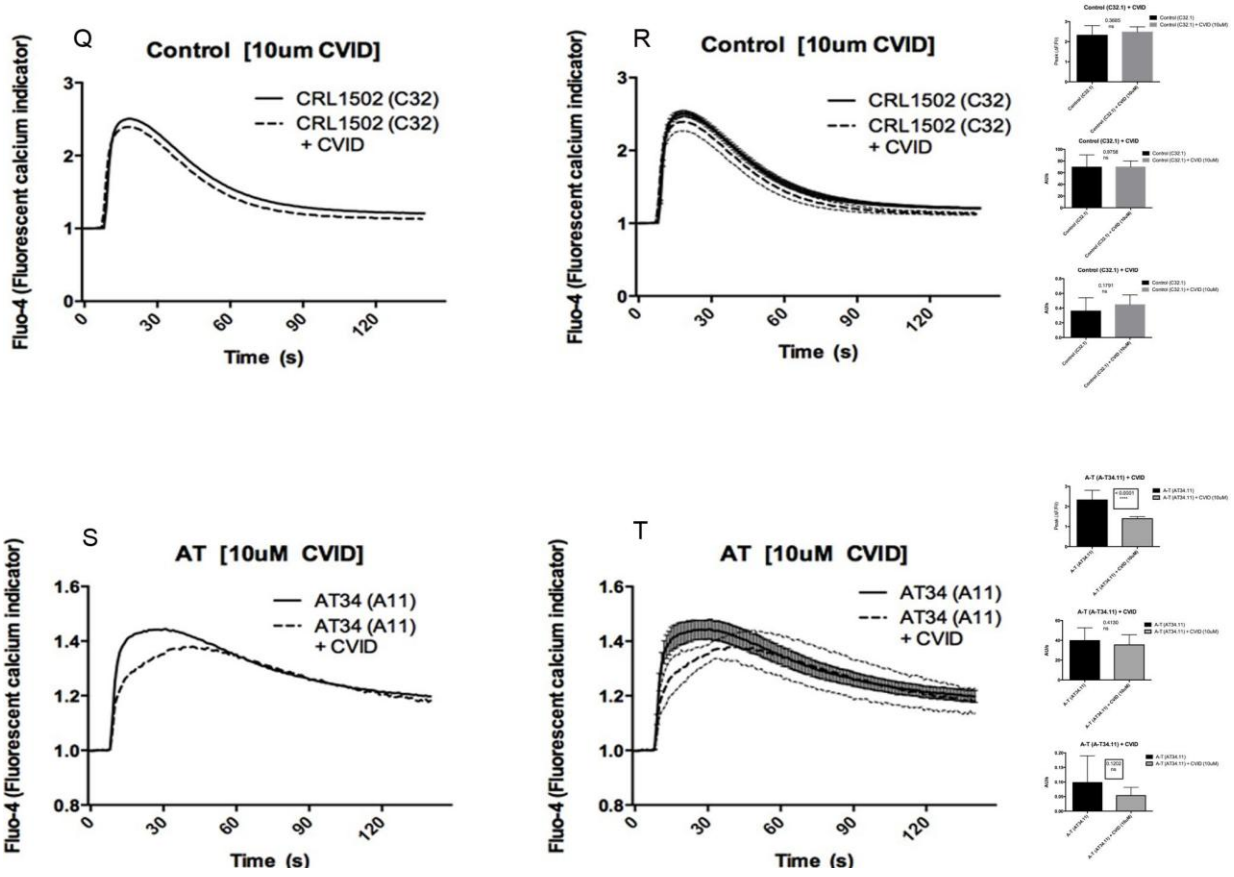

Figure 4.5A – Calcium dynamics after depolarization. Traces are presented on the left hand side without error bars for ease of viewing. In all cases panels to the right display identical trace graphs with error bars showing SEM. Graphs depicting statistical analyses are present to the right of each trace showing max peak (top), area under the curve (middle) and slope of the curve (bottom). P-values were generated by performing unpaired t-test with or without Welch's correction depending on distribution of variance. (A & B) Experimental design and overview (C&D) Control (C11 solid line) and A–T (AT34 dotted line) neurons loaded with Fluo-4-AM and depolarized with 50 mM KCl. A–T neurons (dotted line) show reduced amplitude and latency in rate of calcium release after depolarization.16 replicate wells of each cell line were imaged simultaneously and data pooled. Error bars are shown on the right-hand panels. Control and A–T neurons incubated with ATM inhibitor Ku55993 at a concentration of 10 μM for 24 hours (E,F,G&H). DMSO only control at the same concentration to that used in application of

inhibitor there was no difference in calcium efflux (panels I,J,K&L). Control and A–T neurons treated with 10 µM. Nifedipine (M,N, panelsO&P). Control and A–T neurons treated with CVID at 10 µM (panels Q,R,S&T). All experimental conditions were performed to include four replicates which were pooled. SEM is presented on the right hand side traces in each case. Dotted lines mark treated sample for comparison.

To investigate whether this phenomena was reproducible we performed this experiment a second time on an independent set of differentiated control and A–T neurons (Figure 4.5B). To test this was a legitimate effect not arising from an accumulated karyotypic artefact we included a second control (C11) and A–T (AT30) line. Feature extraction from calcium transients through a MATLAB algorithim showed comparable rates of firing in controls (100% & 83.66%) and A-T neurons (100% & 57.14%). A student's t-test confirmed the absence of a statistically significant difference (p= 0.6264, Figure 4.5B, panel ZL). We again observed an effect whereby calcium egress in A-T neurons appeared latent and protracted in comparison to those of controls (Figure 4.5B, panels B&C) however this was not as apparent as the initial experiment. For simplification of viewing, these results were pooled by genotype to present the remaining analysis. Statistical analyses were performed on unpooled (by genotype) data that met the threshold considered to constitute a successful 'firing' event (Student's t-test to compare firing rate and One way ANOVA with multiple comparisons to examine peak, area and slope parameters (Figure 4.5B, panels ZL-ZO). Statistically significant differences in peak height were apparent between samples, however this extended beyond the control vs A-T genotype comparison (ie. significant differences could be observed between control lines). This was also observed for both the area under and slope of the curve. We consider this to constitute evidence that factors outside of ATM status contribute the differences observed in these data and as a result additional controls/modifications to this technique may be necessary.

Control (Figure 4.5B, panels F&G) and A–T (Figure 4.5B, panels H&I) treatments incubated with DMSO only showed minimal changes. To test whether the previous observations with ATM inhibitor Ku55993 were specific and reproducible we incubated cells again with Ku55993 for 24 hours at two different concentrations, 1 µM and 10 µM. Surprisingly we saw little effect

at either condition in controls (Figure 4.5B panels J&K/N&O) or A–T neurons (Figure 4.5B panels L&M/P&Q). We observed consistent effects to the previous experiment when N-type calcium channel blocker Nifedipine was applied at 10 µM (Figure 4.5B panels R&S/T&U respectively). In contrast to the previous experiment we witnessed consistent shifts in the shape of the curves in both control (Figure 4.5B panels V&W) and A–T (Figure 4.5B panels X&Y) after application of CVID at 10 µM.

We explored the notion that the mitochondria may be contributing to the dynamics of calcium efflux by attempting to disrupt mitochondria via the electron transport chain using CCCP. Acute (two hour) treatment of control (Figure 4.5B panels Z&ZA) neurons resulted in a slight shift in the slope of the curve indicating the possibility that mitochondrial calcium stores might be contributing to the calcium transients. Interestingly we did not observe this shift in A–T neurons (Figure 4.5B, panels ZB&ZC). We did however observe a consistent trend for an increase of calcium entry into A–T neurons when CCCP was applied for sustained periods of time (15 hours) at 10 µM (Figure 4.5B, panels ZF&ZG) and 1 µM. 11 and 13 replicate wells were analyzed respectively for each experimental condition.

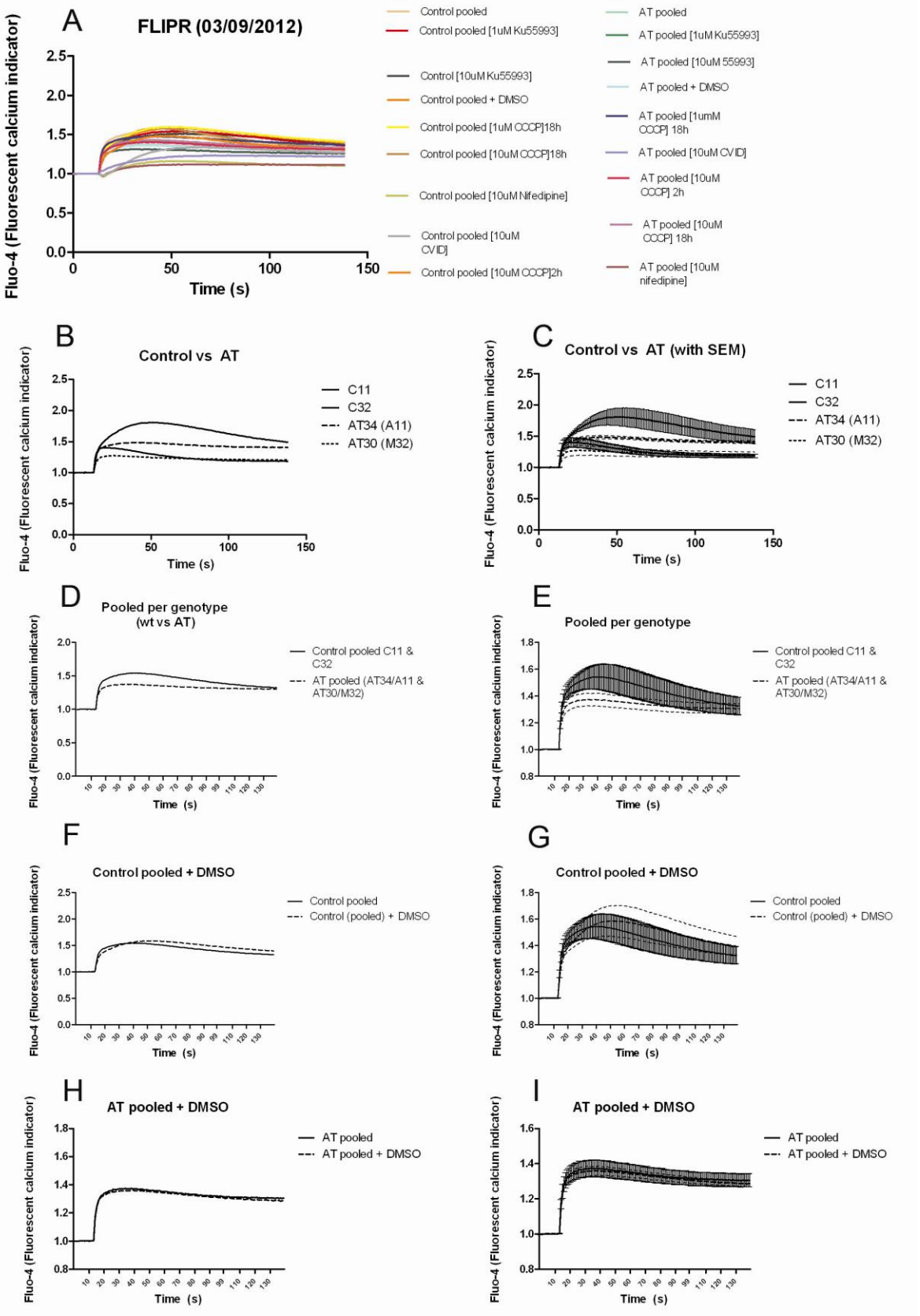
A
FLIPR (03/09/2012)
Fluo-4 (Fluorescent calcium indicator)
Time (s)
Control pooled
Control pooled [1uM Ku55993]
Control [10uM Ku55993]
Control pooled + DMSO
Control pooled [1uM CCCP]18h
Control pooled [10uM CCCP]18h
Control pooled [10uM Nifedipine]
Control pooled [10uM CVID]
Control pooled [10uM CCCP]2h
AT pooled
AT pooled [1uM Ku55993]
AT pooled [10uM 55993]
AT pooled + DMSO
AT pooled [1umM CCCP] 18h
AT pooled [10uM CVID]
AT pooled [10uM CCCP] 2h
AT pooled [10uM CCCP] 18h
AT pooled [10uM nifedipine]
B
Control vs AT
C11
C32
AT34 (A11)
AT30 (M32)
C
Control vs AT (with SEM)
D
Pooled per genotype (wt vs AT)
Control pooled C11 & C32
AT pooled (AT34/A11 & AT30/M32)
E
Pooled per genotype
F
Control pooled + DMSO
Control pooled
Control (pooled) + DMSO
G
H
AT pooled + DMSO
AT pooled
AT pooled + DMSO
I

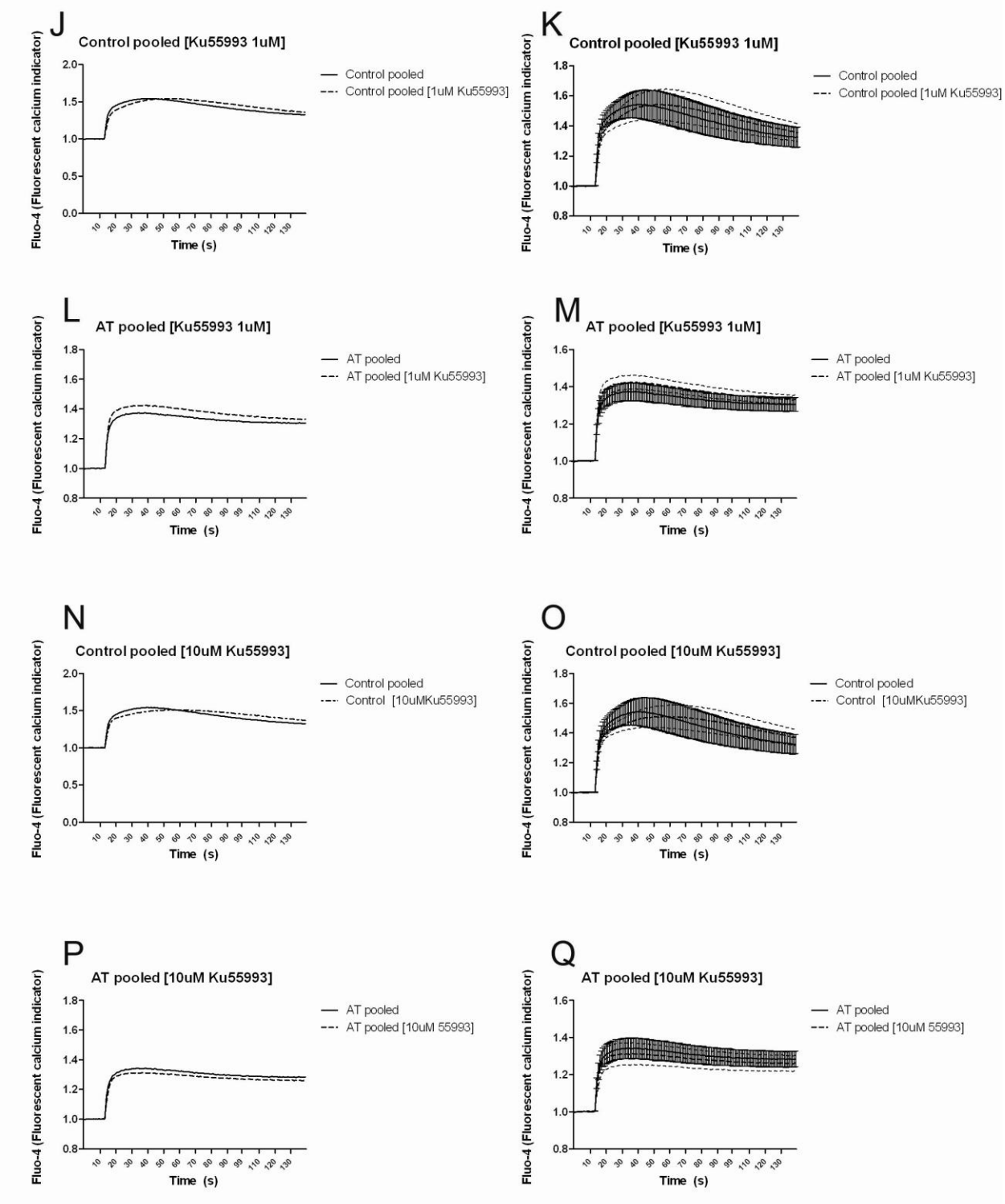
J
Control pooled [Ku55993 1uM]
Fluo-4 (Fluorescent calcium indicator)
Time (s)
Control pooled
Control pooled [1uM Ku55993]
K
Control pooled [Ku55993 1uM]
Fluo-4 (Fluorescent calcium indicator)
Time (s)
Control pooled
Control pooled [1uM Ku55993]
L
AT pooled [Ku55993 1uM]
Fluo-4 (Fluorescent calcium indicator)
Time (s)
AT pooled
AT pooled [1uM Ku55993]
M
AT pooled [Ku55993 1uM]
Fluo-4 (Fluorescent calcium indicator)
Time (s)
AT pooled
AT pooled [1uM Ku55993]
N
Control pooled [10uM Ku55993]
Fluo-4 (Fluorescent calcium indicator)
Time (s)
Control pooled
Control [10uMKu55993]
O
Control pooled [10uM Ku55993]
Fluo-4 (Fluorescent calcium indicator)
Time (s)
Control pooled
Control [10uMKu55993]
P
AT pooled [10uM Ku55993]
Fluo-4 (Fluorescent calcium indicator)
Time (s)
AT pooled
AT pooled [10uM 55993]
Q
AT pooled [10uM Ku55993]
Fluo-4 (Fluorescent calcium indicator)
Time (s)
AT pooled
AT pooled [10uM 55993]

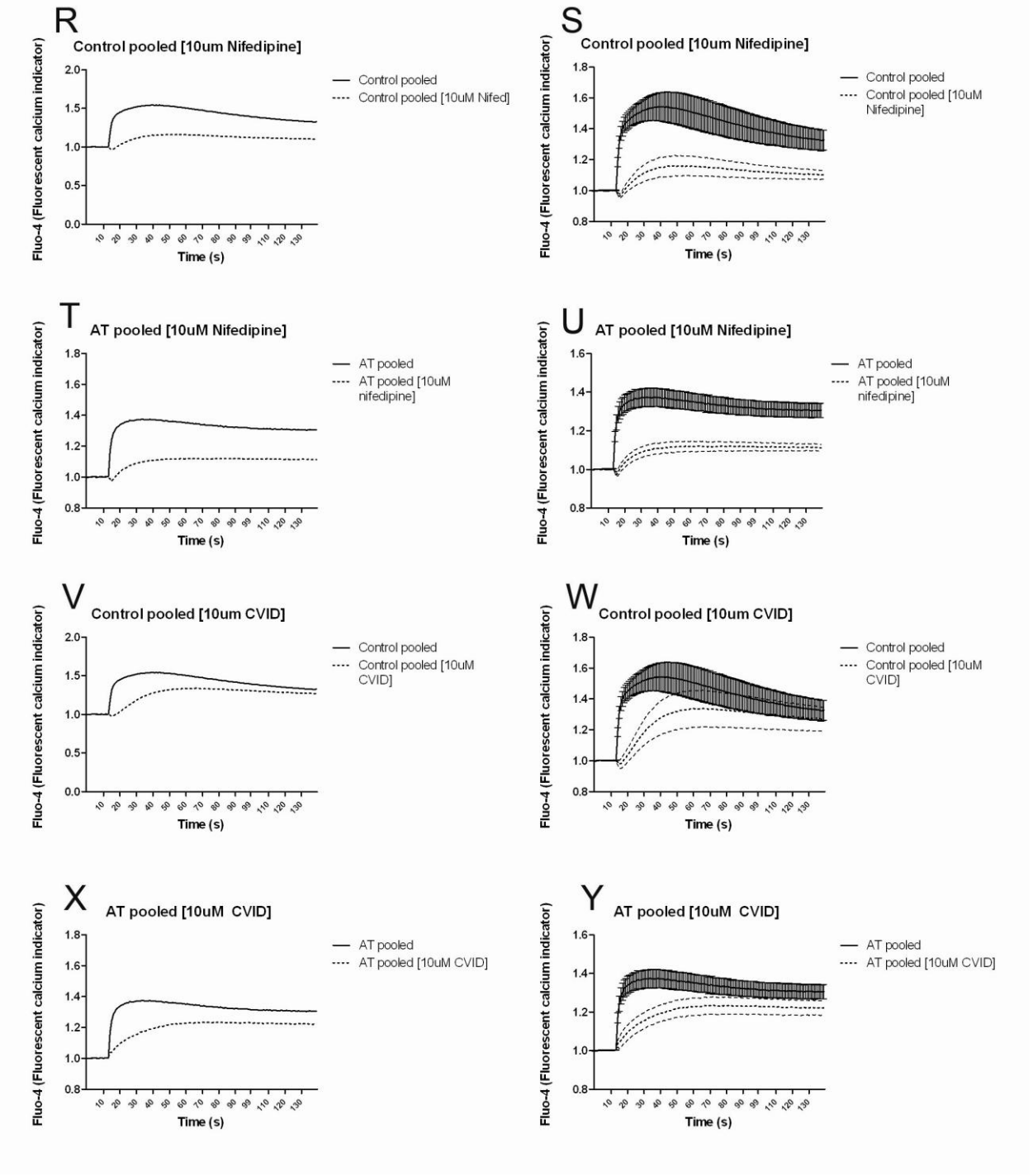
R
Control pooled [10um Nifedipine]
Fluo-4 (Fluorescent calcium indicator)
Time (s)
Control pooled
Control pooled [10uM Nifed]
S
Control pooled [10um Nifedipine]
Fluo-4 (Fluorescent calcium indicator)
Time (s)
Control pooled
Control pooled [10uM Nifedipine]
T
AT pooled [10uM Nifedipine]
Fluo-4 (Fluorescent calcium indicator)
Time (s)
AT pooled
AT pooled [10uM nifedipine]
U
AT pooled [10uM Nifedipine]
Fluo-4 (Fluorescent calcium indicator)
Time (s)
AT pooled
AT pooled [10uM nifedipine]
V
Control pooled [10um CVID]
Fluo-4 (Fluorescent calcium indicator)
Time (s)
Control pooled
Control pooled [10uM CVID]
W
Control pooled [10um CVID]
Fluo-4 (Fluorescent calcium indicator)
Time (s)
Control pooled
Control pooled [10uM CVID]
X
AT pooled [10uM CVID]
Fluo-4 (Fluorescent calcium indicator)
Time (s)
AT pooled
AT pooled [10uM CVID]
Y
AT pooled [10uM CVID]
Fluo-4 (Fluorescent calcium indicator)
Time (s)
AT pooled
AT pooled [10uM CVID]

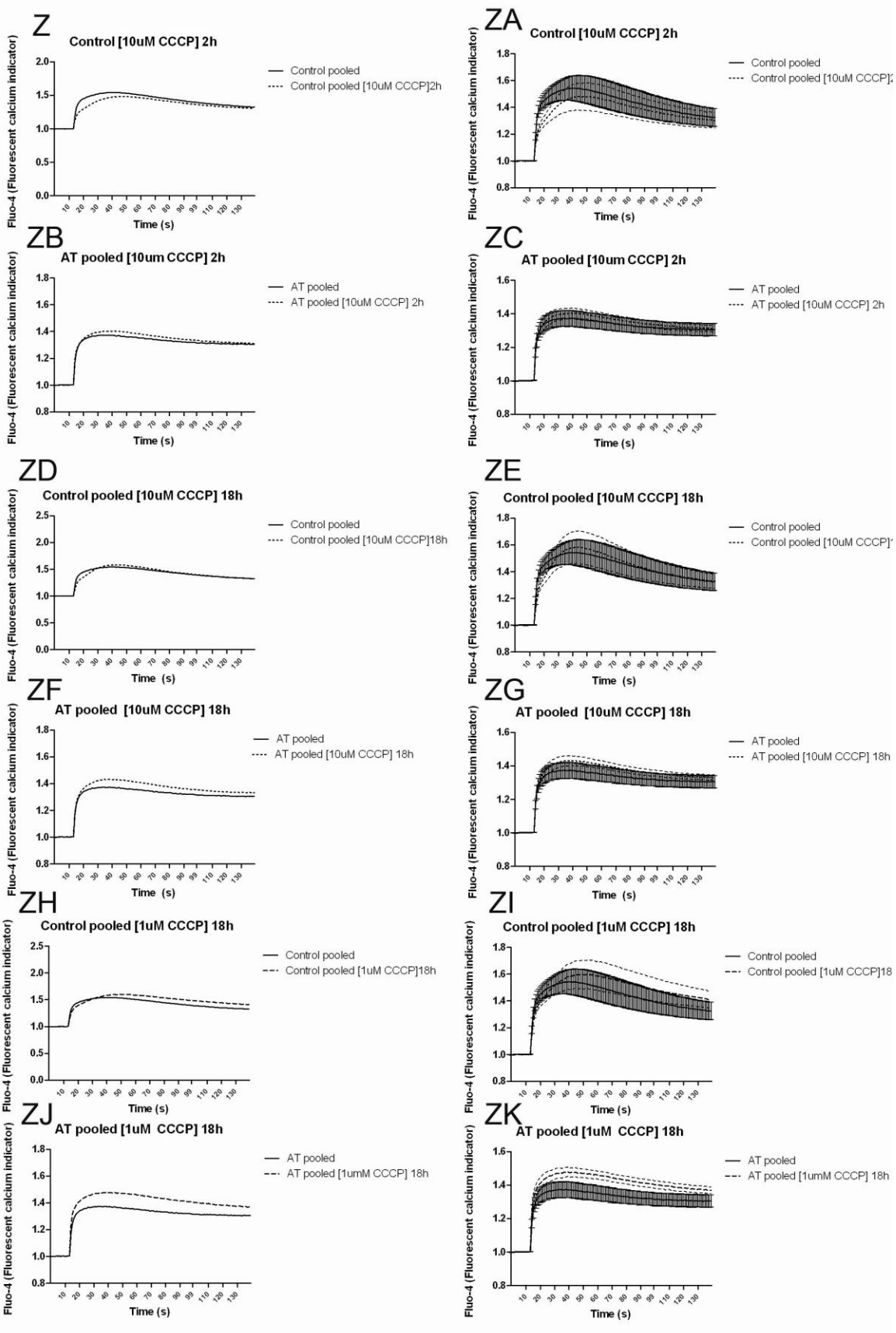
Z
Control [10uM CCCP] 2h
Control pooled
Control pooled [10uM CCCP]2h
ZA
Control [10uM CCCP] 2h
Control pooled
ZB
AT pooled [10um CCCP] 2h
AT pooled
AT pooled [10uM CCCP] 2h
ZC
AT pooled [10um CCCP] 2h
AT pooled
AT pooled [10uM CCCP] 2h
ZD
Control pooled [10uM CCCP] 18h
Control pooled
Control pooled [10uM CCCP]18h
ZE
Control pooled [10uM CCCP] 18h
Control pooled
ZF
AT pooled [10uM CCCP] 18h
AT pooled
AT pooled [10uM CCCP] 18h
ZG
AT pooled [10uM CCCP] 18h
AT pooled
AT pooled [10uM CCCP] 18h
ZH
Control pooled [1uM CCCP] 18h
Control pooled
Control pooled [1uM CCCP]18h
ZI
Control pooled [1uM CCCP] 18h
Control pooled
ZJ
AT pooled [1uM CCCP] 18h
AT pooled
AT pooled [1umM CCCP] 18h
ZK
AT pooled [1uM CCCP] 18h
AT pooled
AT pooled [1umM CCCP] 18h
Fluo-4 (Fluorescent calcium indicator)
Time (s)

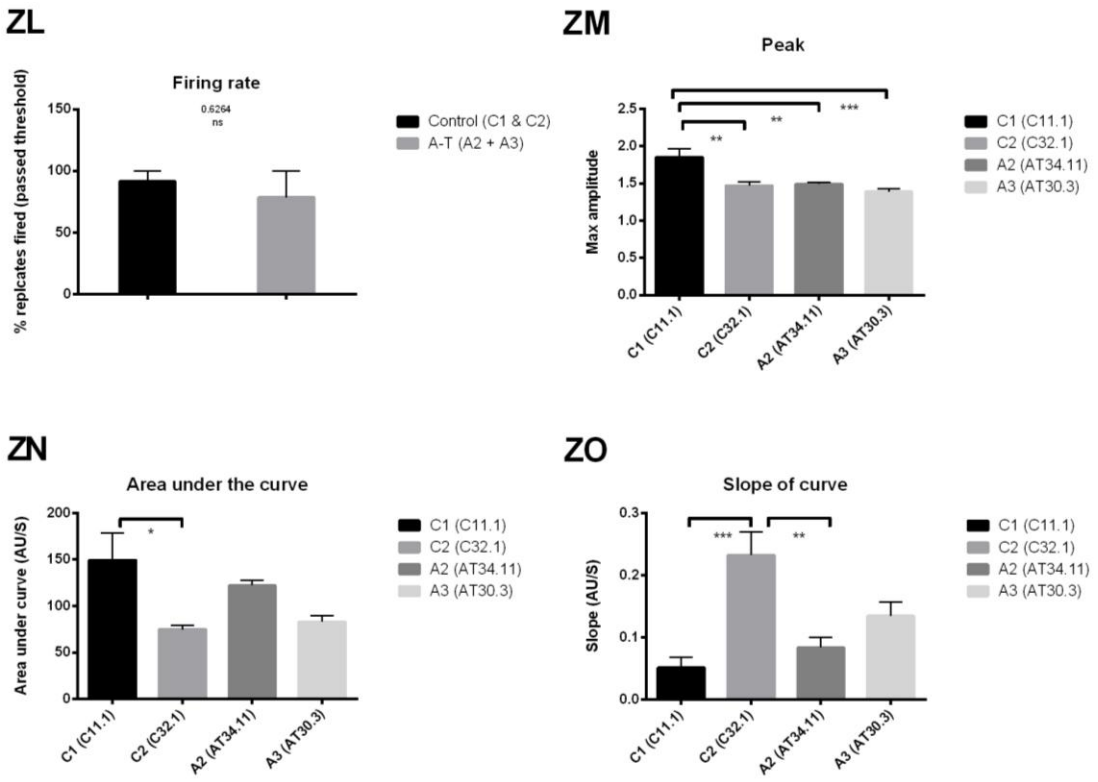

Figure 4.5B – Calcium dynamics after depolarization. In all cases (except panel A & ZL-ZO) panels to the right display identical trace graphs with error bars showing SEM. (Figure 4.5B panel A) Experimental design and overview (Figure 4.5B, panels B&C). Control neurons (C11 & C32 marked by solid lines) and A–T (AT34 & AT30 marked by dotted lines) neurons loaded with Fluo-4-AM and depolarized with 50 mM KCl. 11 and 13 replicate wells were analyzed respectively for each experimental condition to establish baseline depolarization kinetics. (Figure 4.5B, panels D&E) Data pooled per genotype. A–T neurons (dotted line) show consistent latency in rate of calcium release after depolarization. Control (Figure 4.5B, panels F&G) and A–T (Figure 4.5B, panels H&I) treatments incubated with DMSO only. Control (Figure 4.5B, panels J&K/N&O) or A–T neurons (Figure 4.5B, panels L&M/P&Q) treated with 1 µM or 10 µM Ku55993 respectively. Nifedipine was applied at 10 µM to controls and A–T neurons (Figure 4.5B, panels R&S/T&U respectively). Control (Figure 4.5B, panels V&W) and A–T (Figure 4.5B, panels X&Y) after application of CVID at 10 µM. Acute (two hour) treatment with decoupler of mitochondrial electron transport chain CCCP at 10 µM of control (Figure

4.5B, panels Z&ZA) and A–T (Figure 4.5B, panels ZB&ZC) neurons. CCCP was applied for 15 hours at 10 μM in control (Figure 4.5B panels ZD&ZE) and A–T (Figure 4.5B panels ZF&ZG) and also at 1 μM (Figure 4.5B panels ZH&ZI/ZJ&ZK). 11 and 13 replicate wells were analyzed respectively for each experimental condition. Dotted lines mark treated sample for comparison. (ZL) Statistical analysis of firing rate between control and A-T neurons shows no statistically significant difference (Student's t-test). (ZM, ZN & ZO) Statistical analyses (One-way ANOVA with multiple comparisons) of slope peak, area under the curve and slope of the curve, respectively. P-values for significant interactions only are shown (with exception of t-test in panel ZL).

In an attempt to ascertain whether there was a legitamate effect caused by ATM deficiency we performed a third neural induction using two existing previously validated lines, control (C32) and A–T (AT34) in addition to two new episomally derived iPS cells (Control – FB and A–T AT30) (Figure 4.5C). To confirm that the change in calcium transient kinetics we observed was not due to fluctuation in plating density or survival rate we used Inomycin as a loading control to normalize traces for cell number. Additionally, we included a vastly increased number of technical replicates (>90). Comparable firing rates were observed between two control lines (95.75 & 96.875%) and two A-T lines (90.625 & 85.4%), respectively. A student's t-test revealed no significant difference in this regard (Figure 4.5C, panel C). We again observed AT34 (Figure 4.5C, panels A & B) (light dotted line) to show a characteristically slow egress of calcium after depolarization. We did not witness this phenomenon in AT30 (heavily dotted line; non-virally generated), despite previously having seen this in AT30 (virally generated line from same patient– Figure 4.5B, panels B &C), which resembled transients from control neurons. Statistical analyses supported the notion that there were differences between control and A-T lines – a one-way ANOVA shows statiscally significant differences between amplitude in control and A-T lines. (Figure 4.5C, panel D) There was however a significant difference (albeit to a lesser degree) between the two control lines (C2 & C3). Similarly, there were significant differences in both the area under the curve (Figure 4.5C panel E) and slope of the curve (Figure 4.5C panel F). Again these differences were not limited to A-T vs control comparisons with

differences present between C2 & C3 indicating that the effect observed might have been due to intrinsic variabilities of the cell lines, rather than ATM deficiency.

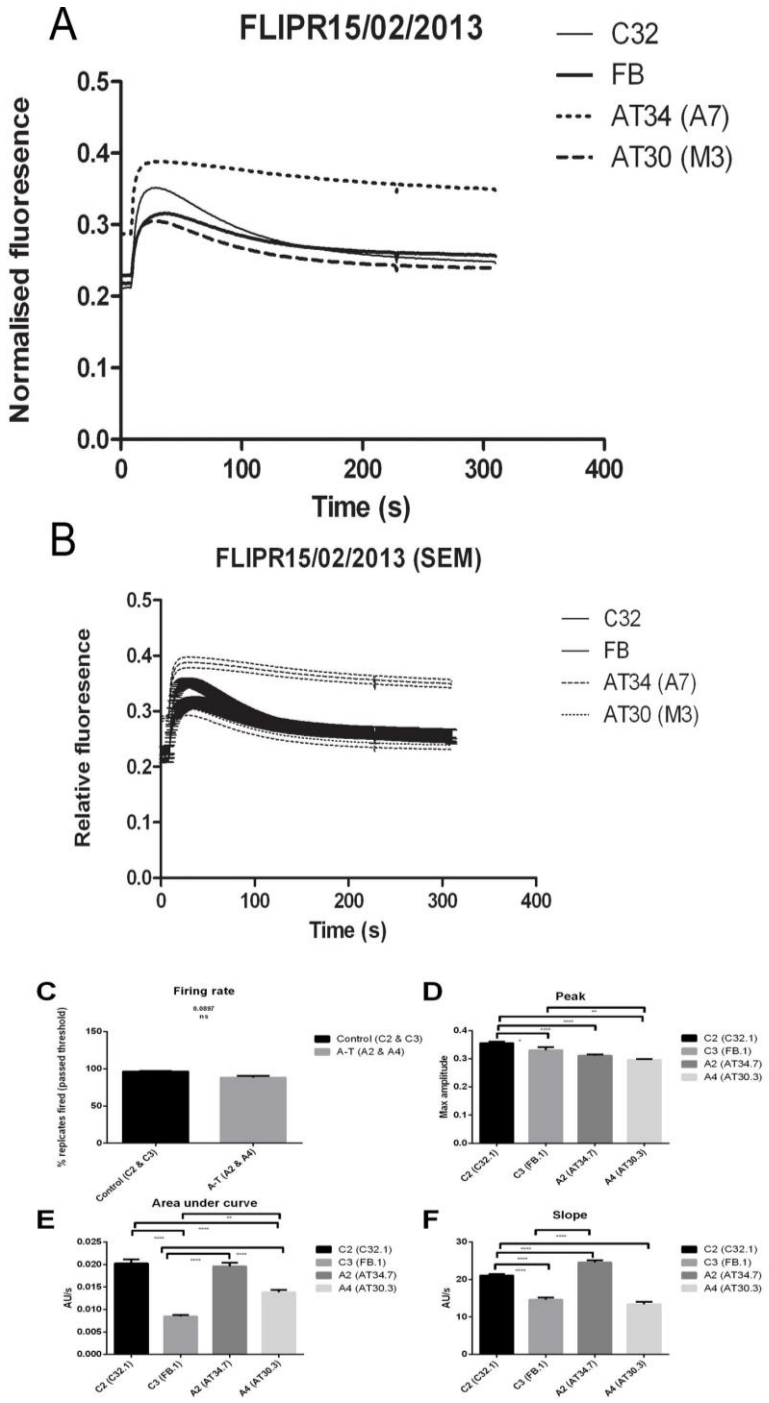

Figure 4.5C – (A) Normalized traces after correction for cell number as marked by Inomycin fluorescence. Top panel shows data without error bars for ease of viewing. (B) Lower panel shows data with SEM. (C) Statistical analyses on firing rate (Student's t-test) and one way ANOVAs pertaining to peak height (D), area under the curve (E) and slope of the curve (F).

This data shows evidence for calcium handling errors in certain A–T neuronal cell lines but not others. Statistical analysis supports this assertion to a degree, but also highlights the distinct possibility that factors outside of ATM deficiency may contribute towards calcium trafficking ability. We believe the strongest possibility is that differences in population composition beyond our limit of detection (ie particular sub-sets of neuronal or glial cell types) may have contributed to this effect and that the cumulative signal of a population of cells may not be the most suitable method for interrogating cellular handling deficits, which may only manifest in a small subset of neuronal cells. To ascertain whether this phenomenon was manifested through differences at the cellular level of calcium traficking or whether it represented a shift in the population makeup of excitable neurons, we approached the problem by imaging of single neuronal cells transiently transfected with a genetically encoded real-time calcium reporter, gCaMP5.

Cells transfected with gCaMP5 were visualized in phenol-red free media on an Olympus inverted fluorescent time-lapse microscope (Figures 4.5D&E). A field of view containing at least one gCaMP5 positive neuron was located and 30 seconds of baseline fluorescence recorded before application of KCl to a final concentration of 50 mM.

After LUT (look-up-table) inversion, subtraction of background fluorescence, application of a gaussian blur filter, regions of interest could be defined and fluorescence from individually imaged time points could be converted to numerical data corresponding to a fluorescent value representative of calcium intensity.

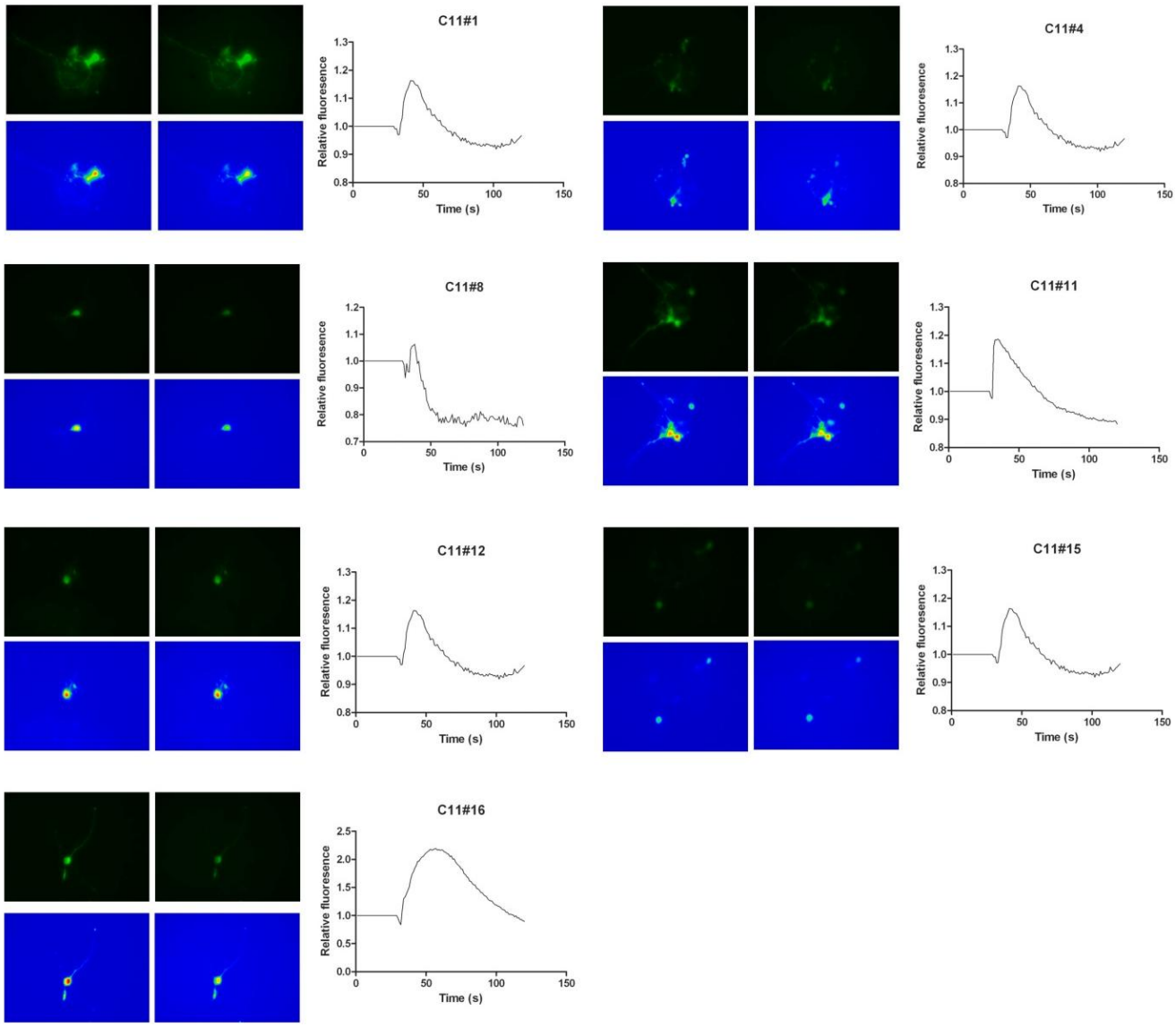

Figure 4.5D - Fluorescent time-lapse imaging of gCaMP5 positive control neurons.

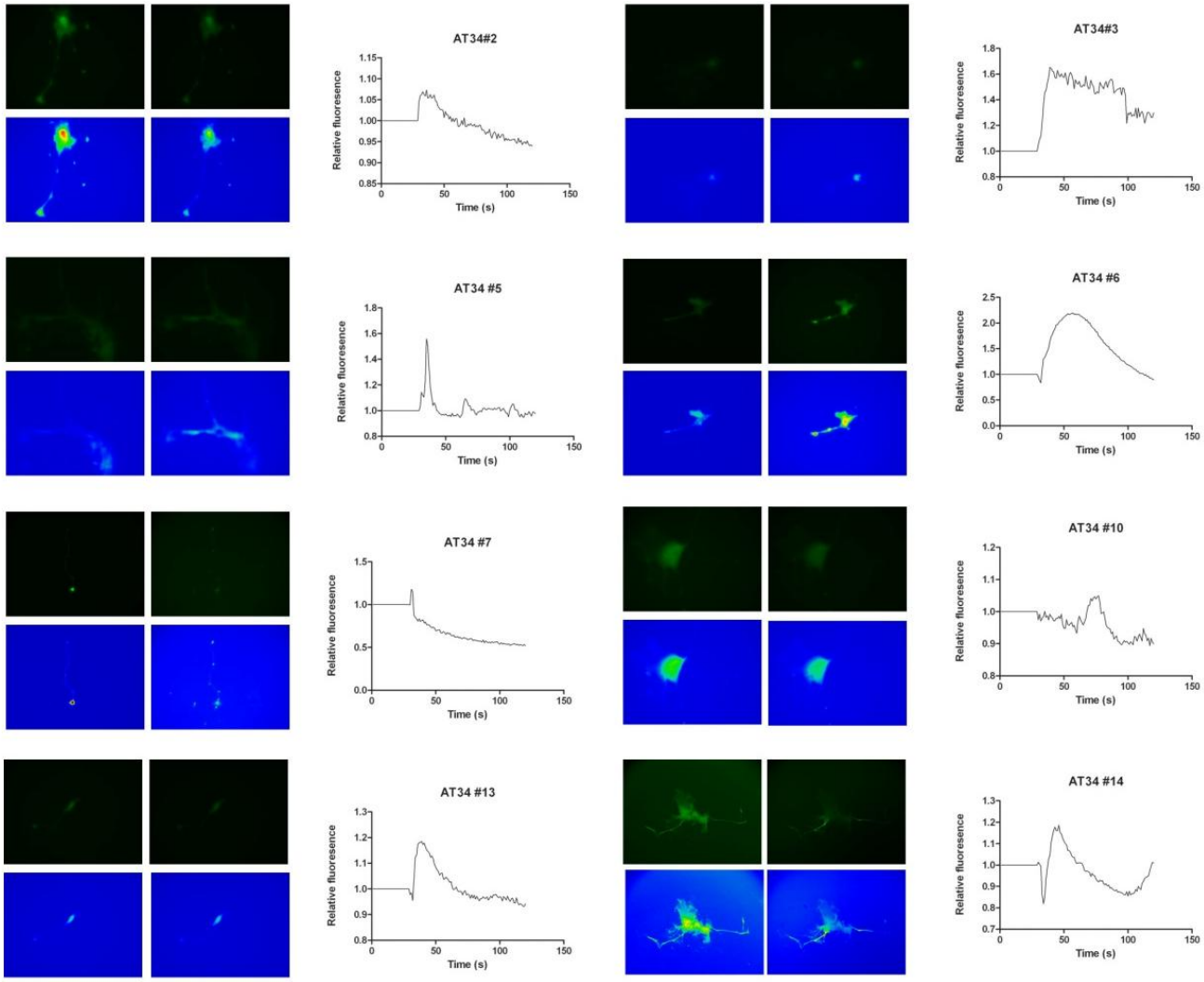

Figure 4.5E - Fluorescent time-lapse imaging of gCaMP5 positive A-T neurons.

We were able to isolate consistent calcium transients by analyzing time-lapse imagestacks as outlined above. Analysis of images taken of depolarized control neurons revealed classical uptake and release of calcium. Images in figures depict before/after treatment with KCl in FITC channels and also false-colour heatmap. In contrast we noticed A–T neurons (AT34) to show a higher incidence of aberrant calcium flux (5 out of 8 A–T neurons showing traces vastly different patterns from classical uptake and release dynamics). When pooled, these traces revealed a very minor shift in the curve, possibly consistent with a calcium handling abnormality (Figure 4.5F). Statistical analyses (Figure 4.5F, panels A-C) of extracted data showed comparable rates of firing (75% & 75% respectively) and also no significant differences in

amplitude ($p = 0.6154$) or slope of the curve ($p = 0.8124$). As opposed to the high throughput imaging studies in Figures 4.5A, B & C, statistical analyses of calcium transients from gCaMP5 imaging experiments were limited to feature extraction reporting peak and slope curve metrics. We could not fit a model which reliably captured the area under the curve, given the profiles of individual neurons showed a spread in activity-types (as opposed to whole-plate pooled signal), see individual traces in Figure 4.5E.

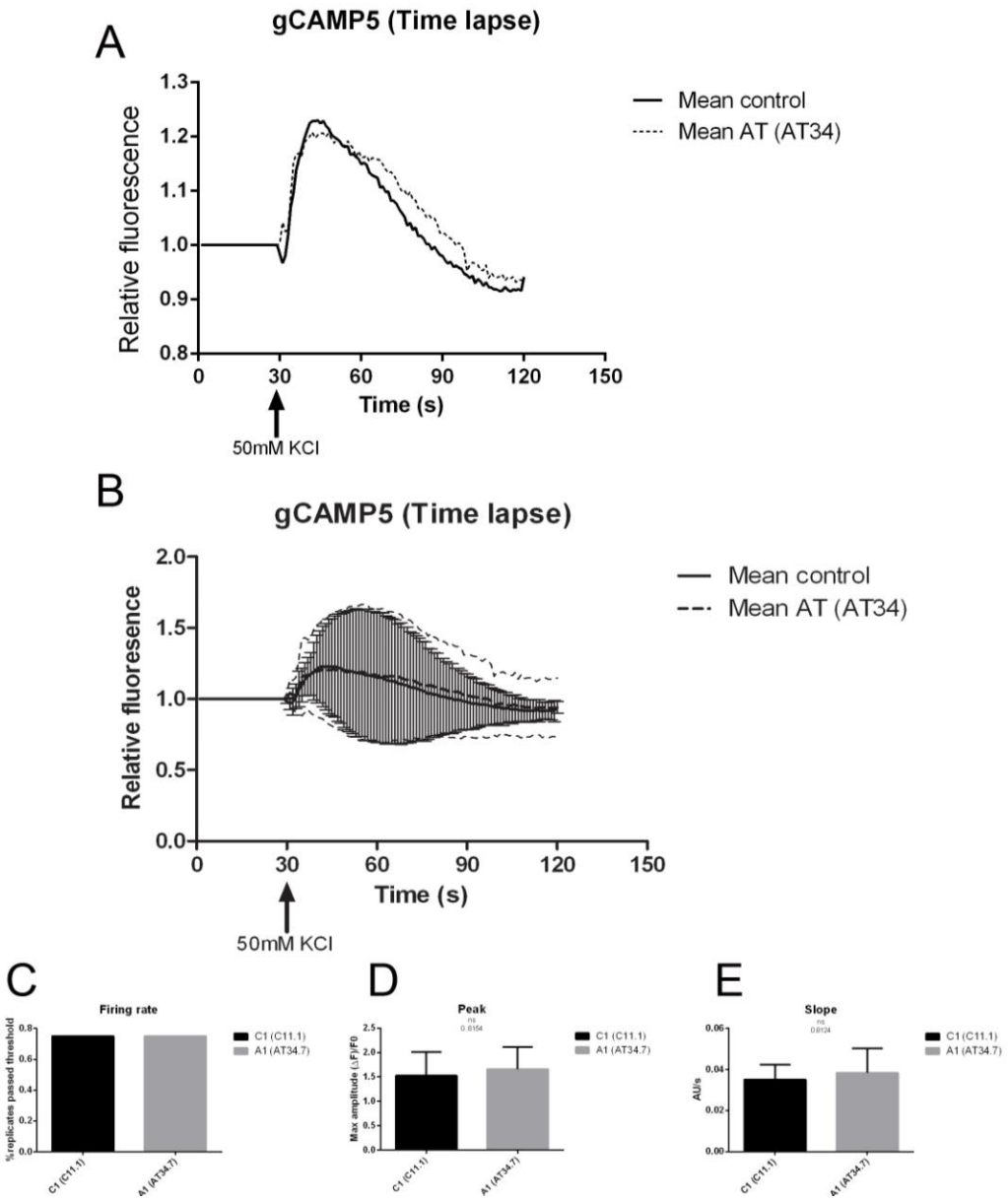

Figure 4.5F – Pooled data from timelapse gCaMP5 imaging (B) Middle panel shows SEM, top panel is without for viewing ease. (C) Firing rate was comparable between A-T and control, as was amplitude (D) and slope of curve (E). No significant differences were found between control and A-T neurons.

We expanded the single cell imaging experiment to include two A–T and two control lines to examine whether this effect was reproducible (Figure 4.5G). Neuronal firing rates as determined by our data extraction protocol revealed no significant differences ($p = 0.6419$). Comparison of curve peaks displayed no significant difference ($p = 0.1124$). Similarly the slopes of the curves were not significantly different ($p = 0.6302$), however it was apparent that there were differences in calcium efflux post-depolarisation. A statistical test to demonstrate this could not be performed.

We observed data consistent with Figures 4.5A,B & C– while we noticed a similar trend towards latent calcium flux after depolarization in AT34, this evident but not as apparent in our second A–T line (AT30) supporting observations from the final FLIPR experiment. Differences in calcium transients did not reach statistical significance on the parameters tested, indicating that additional experimental/analysis methods need require development or that a larger number of clones might be required to demonstrate whether this phenotype was truly a result of ATM deficiency.

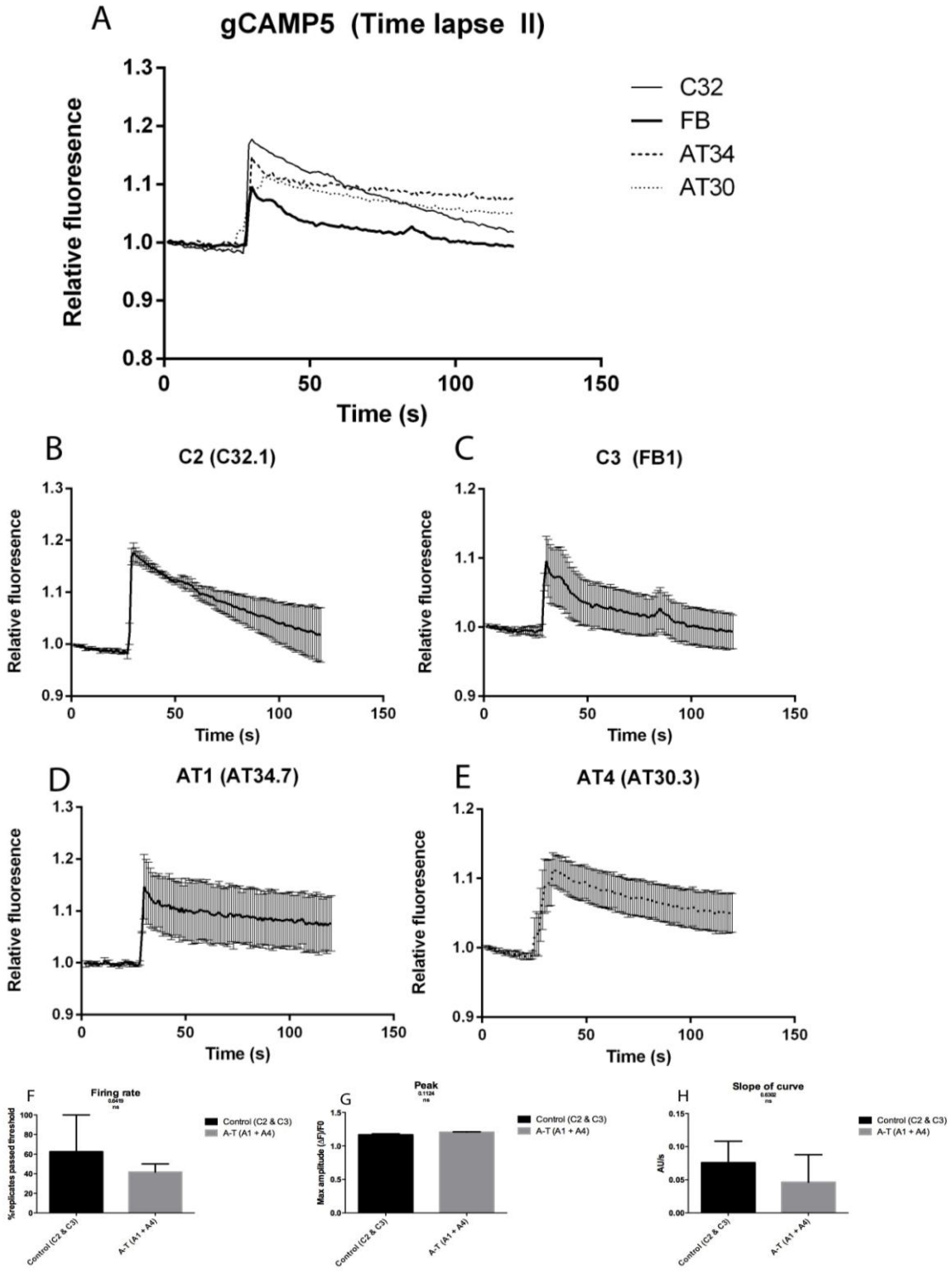

Figure 4.5G – Data from timelapse fluorescence microscopy of gCaMP5 positive neurons (bottom panels shows replicate traces from each cell line with SEM, top panel is without for viewing ease). Panels F-H show statistical analyses.

Transfection of neurons with ATM-mCherry

We sought to test whether reintroduction of ATM caused modulation of calcium handling by first testing for presence of a well known phenotype of ATM deficiency; a defective DNA damage response. We were able to transfect neuronal preparations with a mCherry tagged version of ATM at low efficiency (see Figure 4.5H main panel for phase contrast/TRITC fluorescence merged live image). Interestingly we noted fluorescence emanating from both the nucleus alone (bottom right panel) and nucleus/cytoplasm combined (upper panel).

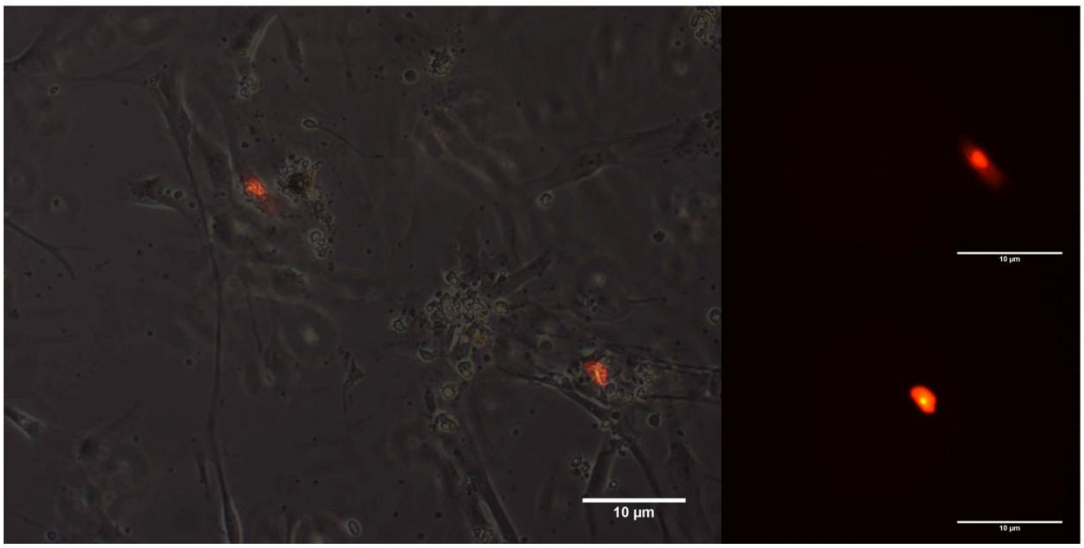

Figure 4.5H - Neurons transfected with ATMmCherry after 60 hours.

We irradiated/mock-irradiated control and A–T neurons with 5 Gy ionizing radiation (Figure 4.6A). After one hour, reactivity with antibodies to ATMpS1981 and SMC1pS957 was observed in controls, but not in A–T derived neurons.

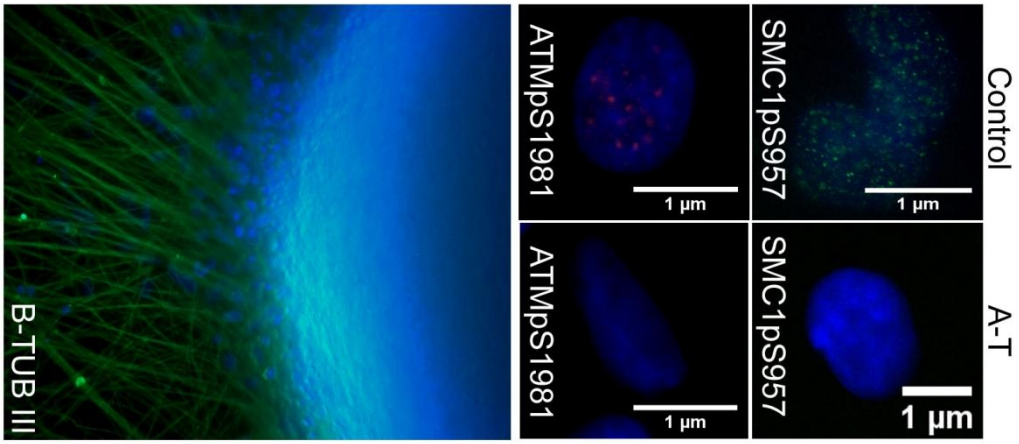

Figure 4.6A – Control and A–T neurons (AT34) were mock/irradiated with 5 Gy ionizing radiation. Immunostaining shows reactivity with ATMpS1981 and SMC1pS957 following one hour indicating ATM autoactivation and phosphorylation of DNA damage substrate SMC1. Scale bars are 1 µm.

We then mock/irradiated neurons transfected with ATM-mCherry. Following one hour and immunostaining with an antibody to ATMpS1981 we observed foci in control neurons that were also present in mCherry positive A–T neurons (Figure 4.6B).

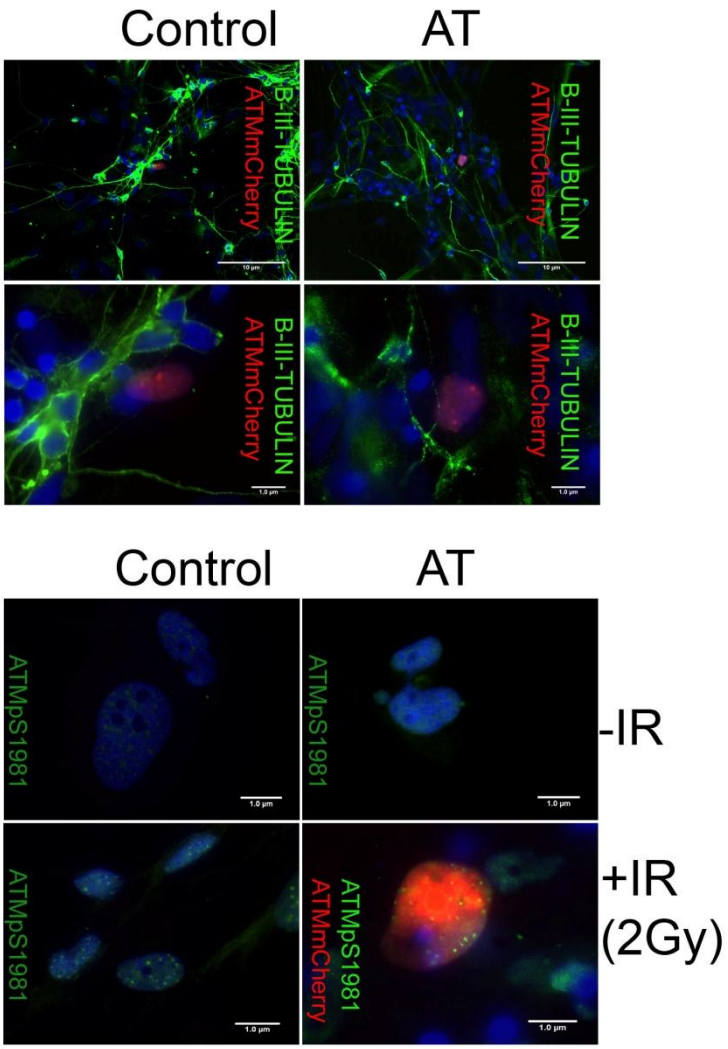

Figure 4.6B – Introduction of ATM-mCherry restores a functional DNA damage response. Top panels show staining for pan-neuronal marker β-III-TUBULIN and mCherry positive control and A–T cells. Scale bars are 10 and 1 μm respectively. Lower panels show restoration of ATMpS1981 foci in ATM-mCherry expressing cells.

We next sought to ascertain whether delivery of ATM-mCherry had an effect on calcium transients after depolarization. We were able to generate a small number of cells doubly transfected with both gCaMP5 (FITC channel) and ATM- mCherry (TRITC channel) (Figure 4.6C). Imaging took place as described above.

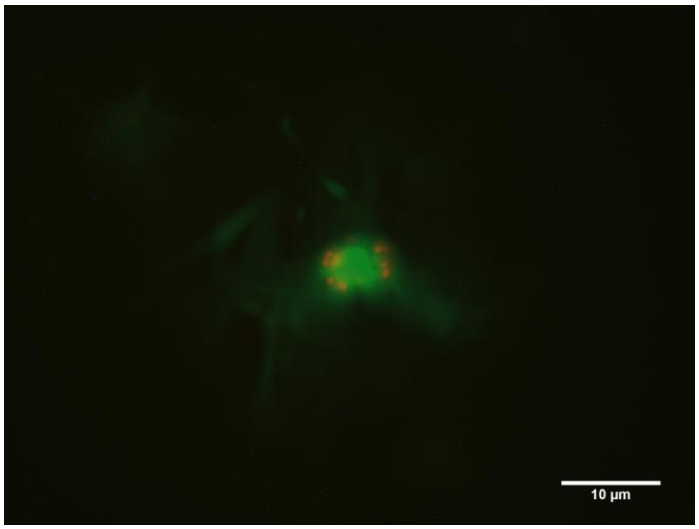

Figure 4.6C – Neurons transfected with gCaMP5 (FITC) and ATM mCherry (TRITC)

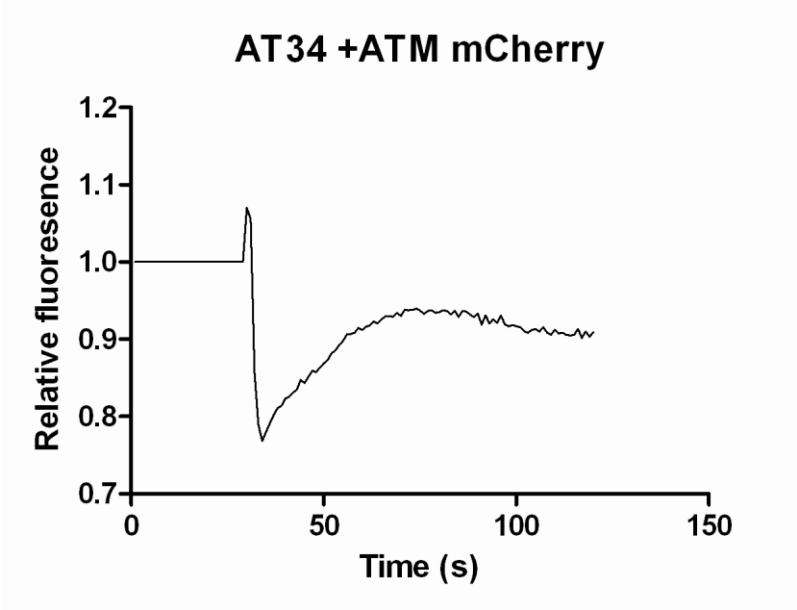

Figure 4.6D – gCaMP5/ATM mCherry neurons were depolarized using 50 mM KCl and fluorescent intensity monitored.

Despite successful complementation of ATM and restoration of DNA damage response, imaging of neurons positive for gCaMP5 and ATM mCherry did not reach efficiency where we could compare calcium trafficking kinetics.

While we showed a robust and reproducible difference in calcium trafficking kinetics in one A–T neuronal cell line (multiple experiments by FLIPR and single cell imaging), we could not reproduce this change in all other A–T cell lines, suggesting the possibility that this effect may have been attributable to a factor other than ATM. It is feasible that this defect arose from a karyotypic abnormality, residual transgene reactivation or some other accumulated culture artefact. We were not able to definitively prove this defect was due to ATM deficiency using ATM inhibitor due to irreproducibility of its action and off-target effects. Although we showed restoration of a functional DNA damage response through complementation of A–T neurons with ATM-mCherry, this was at too low of an efficiency to be useful for illucidating population-wide calcium trafficking dynamics and suitable controls could not be derived. It is plausible also that a shift in population composition may have given this effect ie. it is possible that the presence of sub-populations of responding neurons were differently represented across experiments and cell lines. Evidence supporting this includes the fact that differing responses were observed with independent treatments with Nifedifine and CVID.

Mitochondria in iPSC derived neurons

Given our iPS cell expression data and the accumulating evidence for the role of ATM in mitochondrial homeostasis we explored several parameters of mitochondrial activity in iPS derived neuronal cells from A–T and controls. Despite extensively disrupted mitochondrial gene expression patterns, we previously noted that iPS cells from A–T fibroblasts displayed comparable mitochondrial membrane potential relative to controls (Chaper three – Figure 3.8D). We speculated that the shift of metabolic pathways from pluripotency (largely glycolytic) to neuronal cells (more reliant on oxidative phosphorylation) would drive the demand for ATP generation by oxidative phosporylation upwards and may reveal differences between A–T and controls.

Mitotracker green was employed to visualize mitochondrial localization and morphology in live neurons, whilst TMRM was used to examine mitochondrial membrane potential (Figure 4.7A).

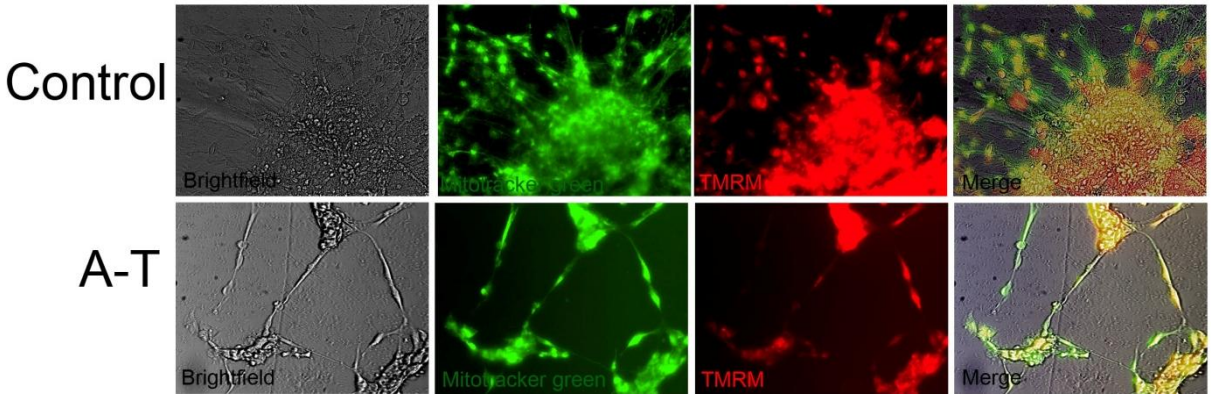

Figure 4.7A – Mitochondria in live neurons. Shown from left to right are brighfield images, FITC channel showing mitochondria stained with Mitotracker green, deep red channel showing mitochondrial membrane potential via TMRM and finally merged channels.

We saw no evidence for aberrant mitochondrial morphology or localization, especially noting the distribution of mitochondria throughout the length of the dendrites in both control (top row) and A–T (bottom row) (Figure 4.7B).

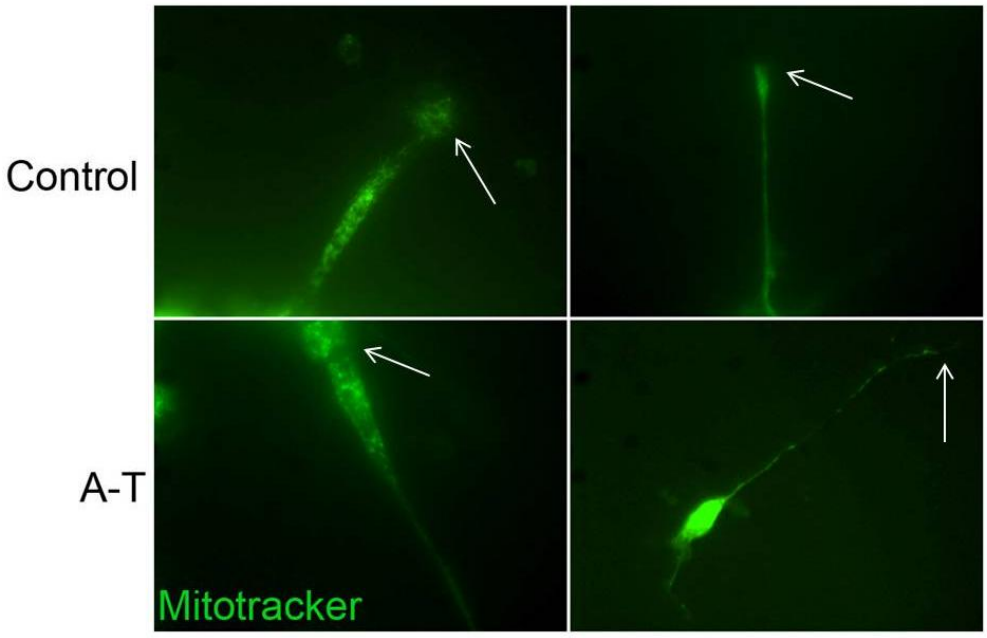

Figure 4.7B – Mitochondrial localisation in live neurons. FITC channel showing mitochondria stained with Mitotracker green are located to proximal ends of neuronal dendrites in both control and A–T neurons.

To quantify mitochondrial characteristics we employed a high-throughput plate-based assay using an InCell Analyzer automated microscope to photograph a large number of replicate wells. Mitochondria were labeled using Mitotracker green and TMRM to visualize fluorescent signal according to accumulation within the mitochondria relative to membrane potential. Hoechst was used to visualize nuclei. InCell analyzer software was used to identify cells based on positive staining in the ultraviolet/Hoechst region (Figure 4.7C see upper left panel). Intensity segmentation was used in the FITC (Mitotracker green – Figure 4.7C see upper right panel) and deep red (TMRM – Figure 4.7C see lower left panel) channels to define the peripheries of the cells.

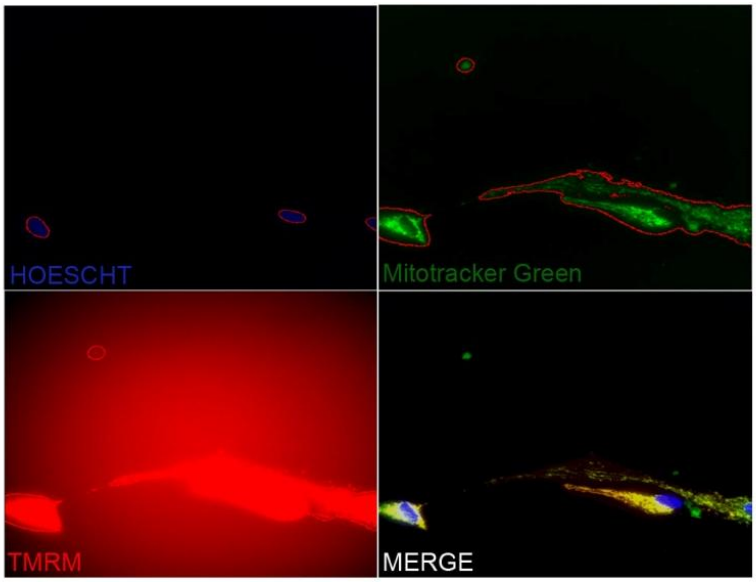

Figure 4.7C – Mitochondria in live neurons identified by InCell analysis software. Shown are nuclei stained by Hoechst (upper left), FITC channel showing mitochondria stained with Mitotracker green (upper right), deep red channel showing mitochondrial membrane potential via TMRM intensity (lower left) and finally merged channels (lower right). Red borders indicate the peripheries of single objects identified by InCell Analyzer automated analysis software.

Fluorescent intensity in each channel was ascribed a numerical value by InCell analysis software. 25 randomly assigned fields of view were automatically photographed for each

channel (Hoechst/FITC/Deep red/Brightfield) from each well of a 96 well plate. Six technical replicate wells were imaged from each cell line (two control - C11&C32 and two A–T - AT34C11 &AT30C32), making for a total of 150 merged channel images each consisting of between zero and ten neurons. Three technical replicates for each cell line were imaged in the presence of electron transport chain uncoupler CCCP. An unpaired t-test showed no significant differences in intensity from Mitotracker staining between A–T and controls (Figure 4.7D top row, right panel). We did however detect significant differences in mitochondrial membrane potential between control and A–T lines (Figure 4.7D bottom row, right panel). We observed consistent but small decreases in mitochondrial membrane potential in the presence of CCCP, possibly due to the polarized nature of the neurons. Interestingly, these differences were even less apparent in both A–T lines, suggesting a possible defect of the electron transport chain mechanism.

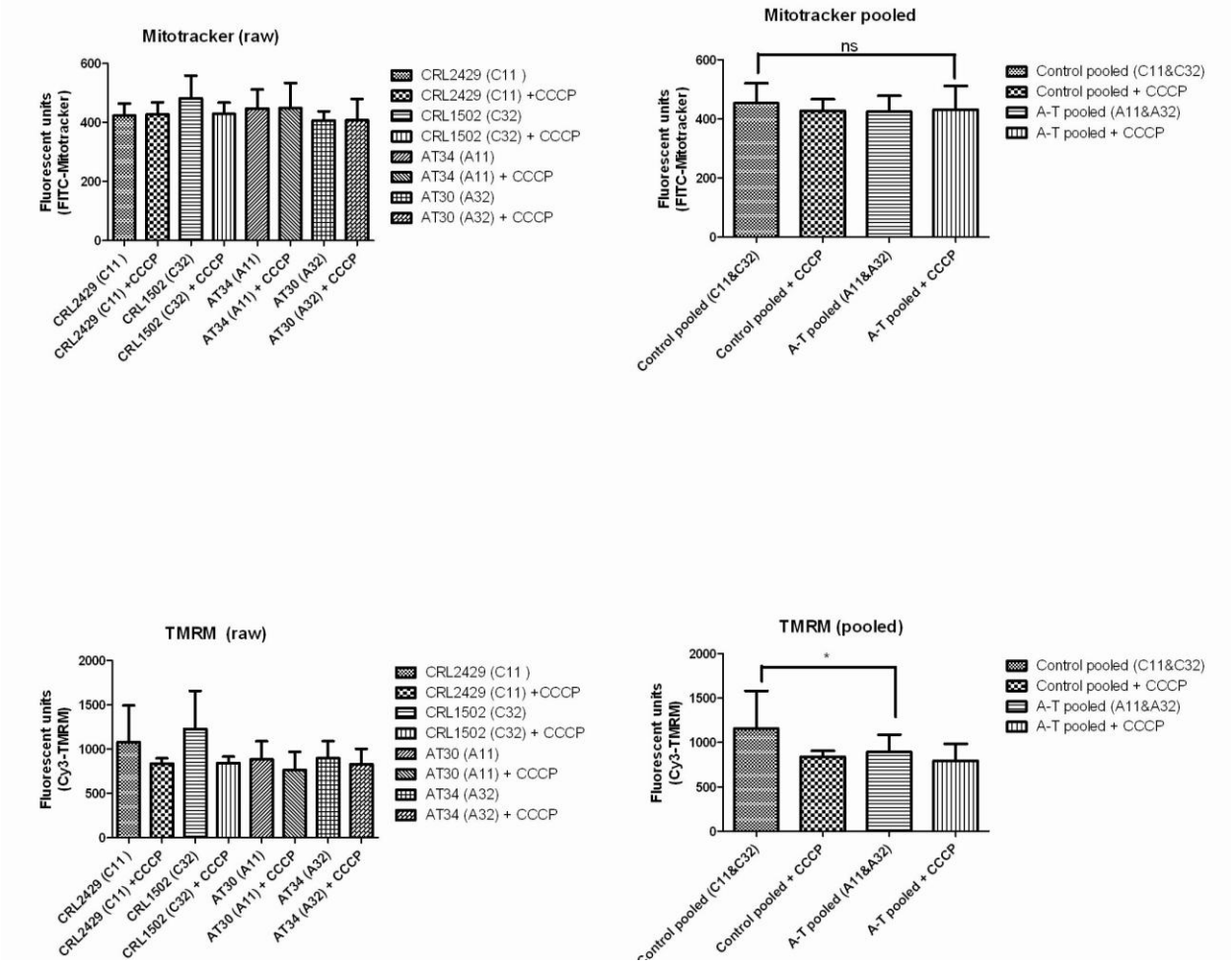

Figure 4.7D – Top left panel shows raw readout for mitotracker values. Top right shows normalized numbers for mitotracker green fluorescence. Lower left panel shows raw values for TMRM/mitochondrial membrane potential values. Lower right shows normalized values. Error bars show SEM.

Given the evidence for altered calcium handling and mitochondrial aberrations, we sought to ascertain whether A–T neurons might exhibit elevated levels of excitotoxic cell death in response to depolarization with increasing concentrations of KCl after 24 hours. We seeded equivalent numbers of control (C11&C32) and A–T (AT34&AT30) derived neurons into wells of a 384 well black-walled plate and treated these with a concentration gradient of KCl (from 0-100 mM) for 24 hours. Survival was ascertained by quantifying the number of adherent neuronal cells after this period (See figure 4.7E) via high-throughput microscopy using the InCell

Analyzer as described above. Two control and two A–T lines were used. 25 fields of view were imaged for each fluorescent channel from biological triplicates. No difference was apparent between control and A–T cells after a Two-way ANOVA statistical test was applied.

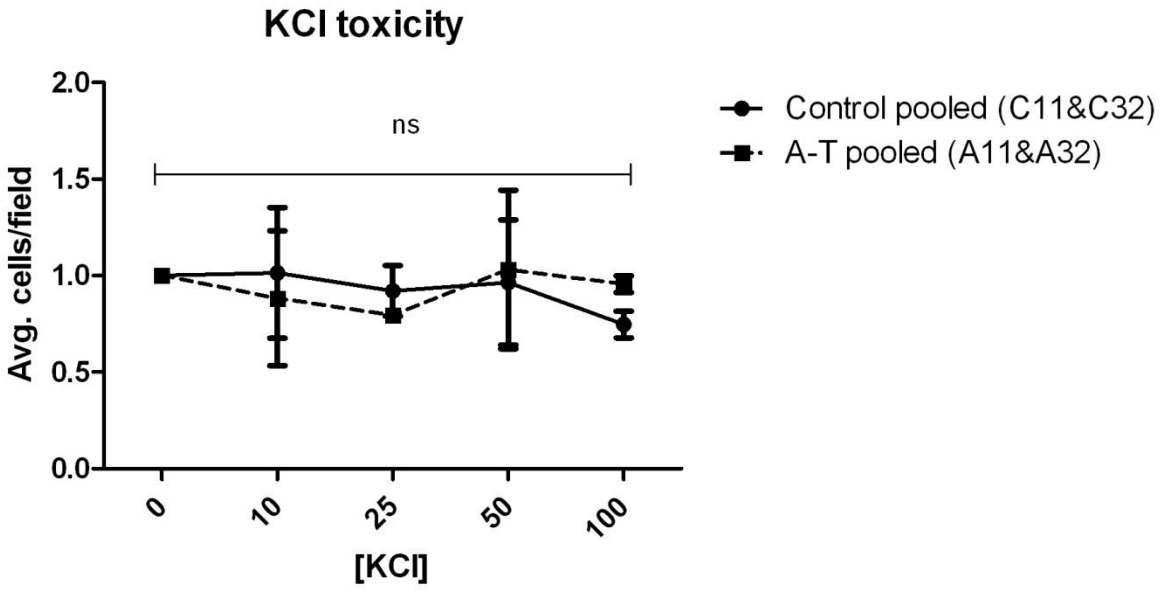

Figure 4.7E – Toxicity to a concentration gradient of [0-100 mM] KCl was assessed by surviving fraction of adherent cells after 24hours. A Two-way ANOVA reveals no significant difference between control and mutant neurons.

HDAC4 localisation in neurons

A recent publication details the mislocalization of HDAC4 in *Atm* deficient neurons [10]; we speculated that since HDAC4 is a substrate for mitochondrial caspase, such a mislocalisation of HDAC4 in A–T neurons may underlie the reduction in mitochondrial membrane potential observed in A–T iPS derived neuronal cultures. We therefore examined the localization of HDAC4 within our neuronal population using a MATLAB based algorithm to plot the ratio of nuclear to cytoplasmic HDAC4 intensity. We defined the borders and intensity of neuronal cultures fluorescently stained with antibodies to β-III-TUBULIN (pan-neuronal marker - FITC), HDAC4 (Cy3/Deep red) and DAPI (DNA/nucleus). β-III-TUBULIN identified and delineated the cellular borders of neurons. Using MATLAB we identified single neuronal cells and

quantified the ratio of fluorescent intensity emanating from both nucleus alone (borders defined by DAPI in the ultraviolet fluorescent channel) and from the entirety of the cell in the deep red channel (See Figure 4.8A for segmentation and Figure 4.8B for merged photographs).

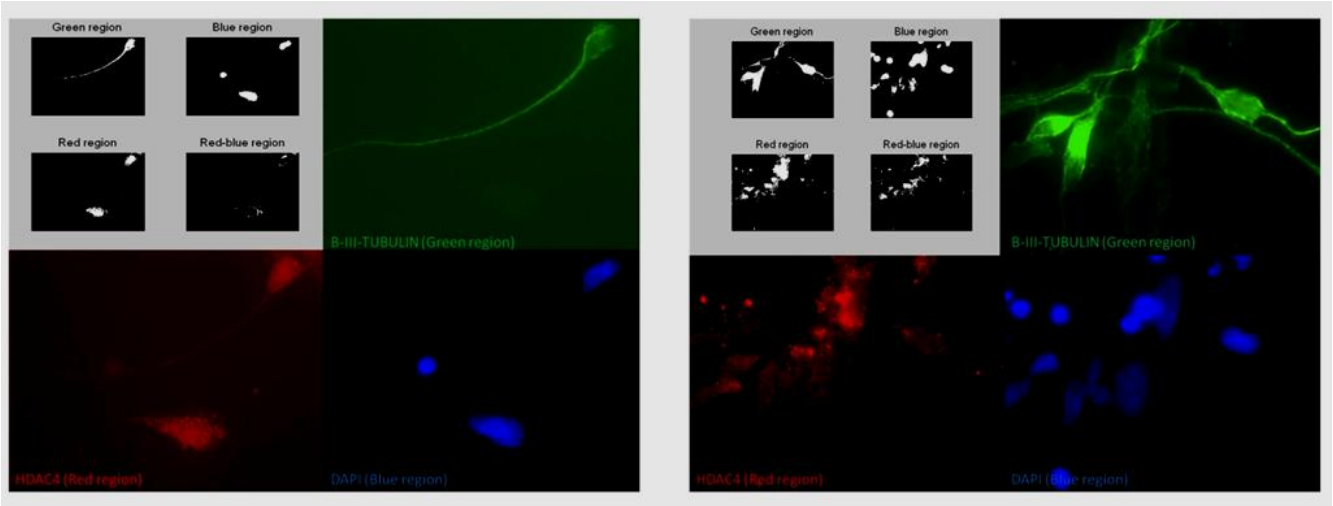

Figure 4.8A – Upper left panels show output of image segmentation by MATLAB algorithim. β-III-TUBULIN (pan-neuronal marker - FITC) shown in upper right panels, HDAC4 (Cy3/Deep red) shown in lower left panels and DAPI (DNA/nucleus) shown in lower right panels.

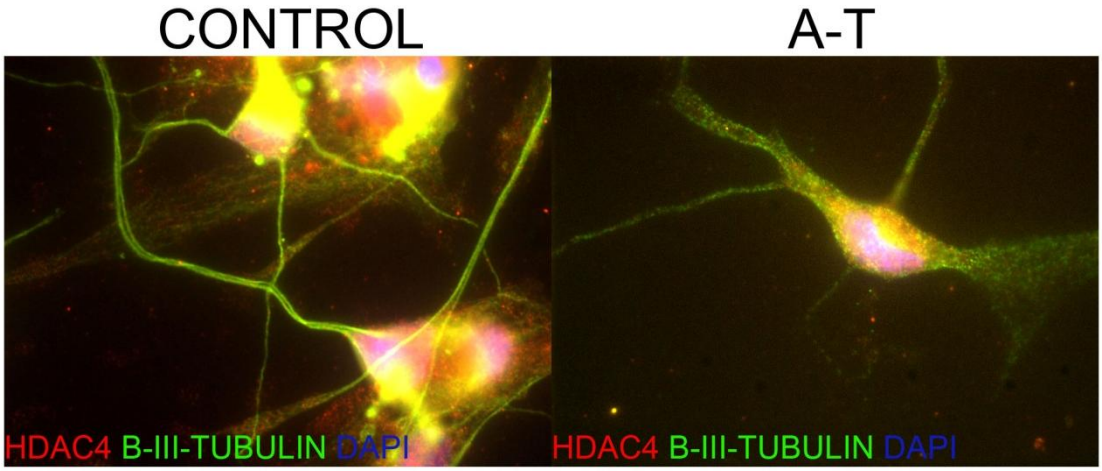

Figure 4.8B – HDAC4 in neurons. Merged channels from HDAC4 (Cy3/Deep red) and β-III-TUBULIN (pan-neuronal marker - FITC). DAPI stains the nucleus.

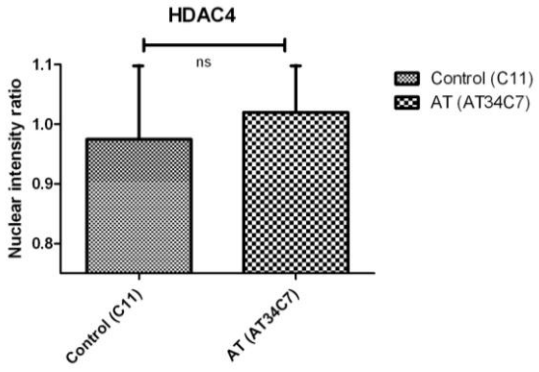

Figure 4.8C – HDAC4 nuclear intensity does not differ significantly between control and A–T neurons as indicated by an unpaired t-test.

These values were used to derive a mean nuclear intensity ratio. In contrast to recent findings [10] we did not uncover evidence for a statistically significant difference in cellular localization of HDAC4 in A–T neurons (Figure 4.8C), suggesting that this effect may be specific to certain neuronal sub-types and also suggesting that differences in mitochondrial membrane potential were HDAC4 localization independent. This difference in observation may also be due to discrepancies between antibody specificity and would require further testing to prove definitively. Interestingly we observed evidence of punctuate pockets of HDAC4 localized to the dendrites of neurons from both control and A–T (Figure 4.8D), suggesting possible additional roles for HDAC4, for example in vesicle trafficking.

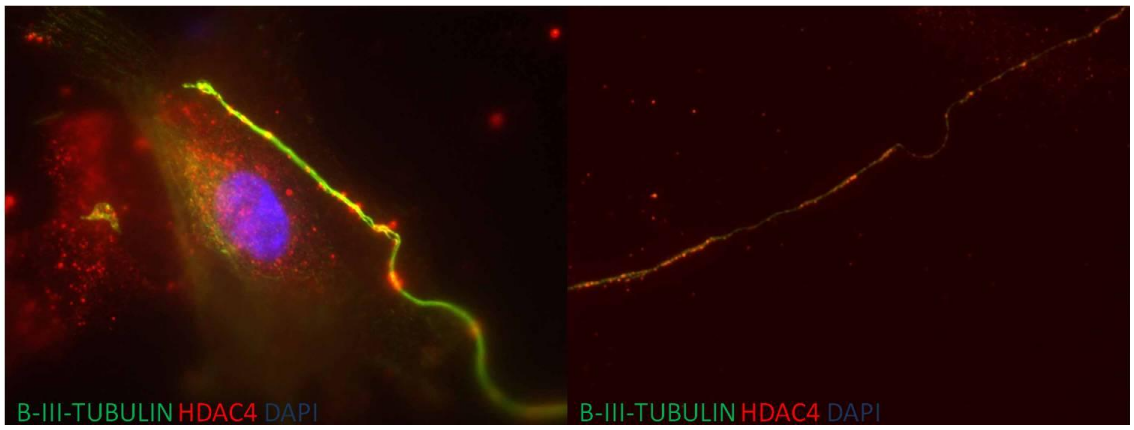

Figure 4.8D – HDAC4 localization in neuronal dendrites. Merged channels from HDAC4 (Cy3/Deep red) and β-III-TUBULIN (pan-neuronal marker - FITC). DAPI stains the nucleus.

Activity induced DNA damage

Given the recent finding that physiological brain activity caused DNA double-strand breaks in murine neurons [211], and the accepted role for ATM in resolving these breaks [92], we examined the response of neurons in culture in response to KCl induced depolarization by examining γH2AX foci formation kinetics.

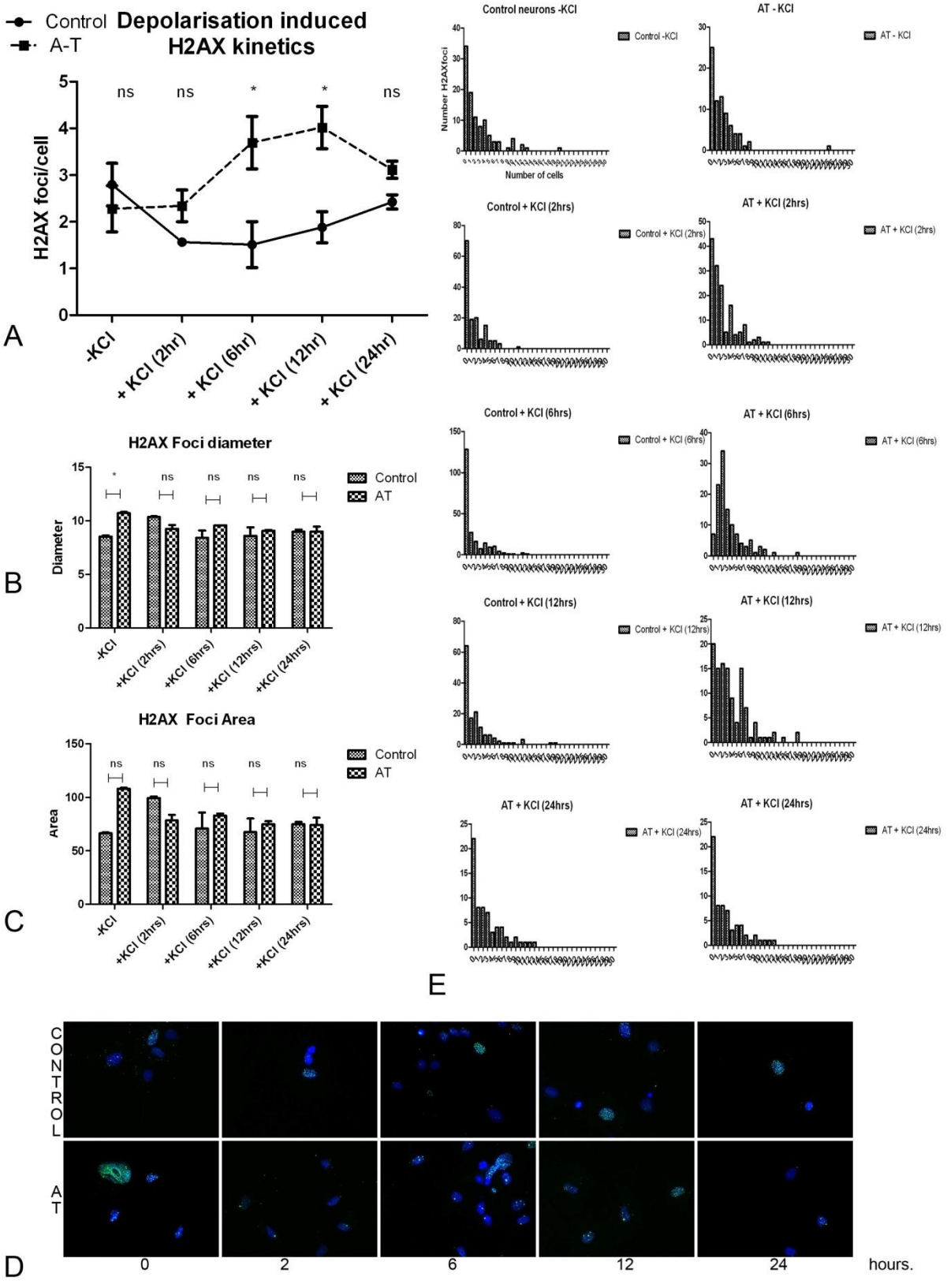
Control
A-T
Depolarisation induced
H2AX kinetics
H2AX foci/cell
ns
ns
*
*
ns
-KCl
+ KCl (2hr)
+ KCl (6hr)
+ KCl (12hr)
+ KCl (24hr)
A
H2AX Foci diameter
Diameter
Control
AT
-KCl
+KCl (2hrs)
+KCl (6hrs)
+KCl (12hrs)
+KCl (24hrs)
B
H2AX Foci Area
Area
C
Control neurons -KCl
AT - KCl
Number H2AXfoci
Number of cells
Control + KCl (2hrs)
AT + KCl (2hrs)
Control + KCl (6hrs)
AT + KCl (6hrs)
Control + KCl (12hrs)
AT + KCl (12hrs)
AT + KCl (24hrs)
E
CONTROL
AT
0
2
6
12
24
hours.
D

Figure 4.9 – (A) γH2AX kinetics after depolarization with [50mM] KCl. Two-way ANOVA with Bonferonni post-test reveals a statistically significant difference between A–T and control neurons in γH2AX foci numbers six & twelve hours after stimulus. (B) Foci diameter size showed no statistically significant differences between control and A–T neurons at all time points with the exception of the mock-treated control. (C) Foci area size showed no statistically significant differences between control and A–T neurons at all time points. (D) Representative photos of nuclei (DAPI) and γH2AX foci (FITC). (E) Breakdown of depolarization kinetics by number of foci per cell.

A baseline reading of between 2 and 3 foci per cell was detected from both A–T neurons and controls. Two hours after stimulation with KCl we detected neither a robust induction of γH2AX foci nor a significant difference between A–T and control neurons. Interestingly, six hours after stimulus we detected an approximately two-fold induction of γH2AX foci in A–T neurons that continued to increase until 12 hours before beginning to decrease to levels approaching baseline. This same induction of foci was not apparent in control neurons suggesting that in the absence of ATM neuronal activity induced DNA strand break repair is impaired. There were no statistically significant differences in foci size by diameter or area (Figure 4.9 B&C) between A–T and controls or any of the time points, indicating that foci measuring parameters were adequate across all conditions. When broken down to examine foci numbers cell by cell (4.9E), the A–T neurons were more predisposed to forming γH2AX foci but commensurate with controls in their ability to resolve them by 24 hours.

We performed this experiment a second time (Figure 4.9B) and observed a consistent induction of γH2AX foci after treatment with KCl. Again kinetics of foci repair were different between A–T and controls. We did not detect evidence for induction of DNA strand breaks using treatment with neurotransmitter GABA (Figure 4.9B).

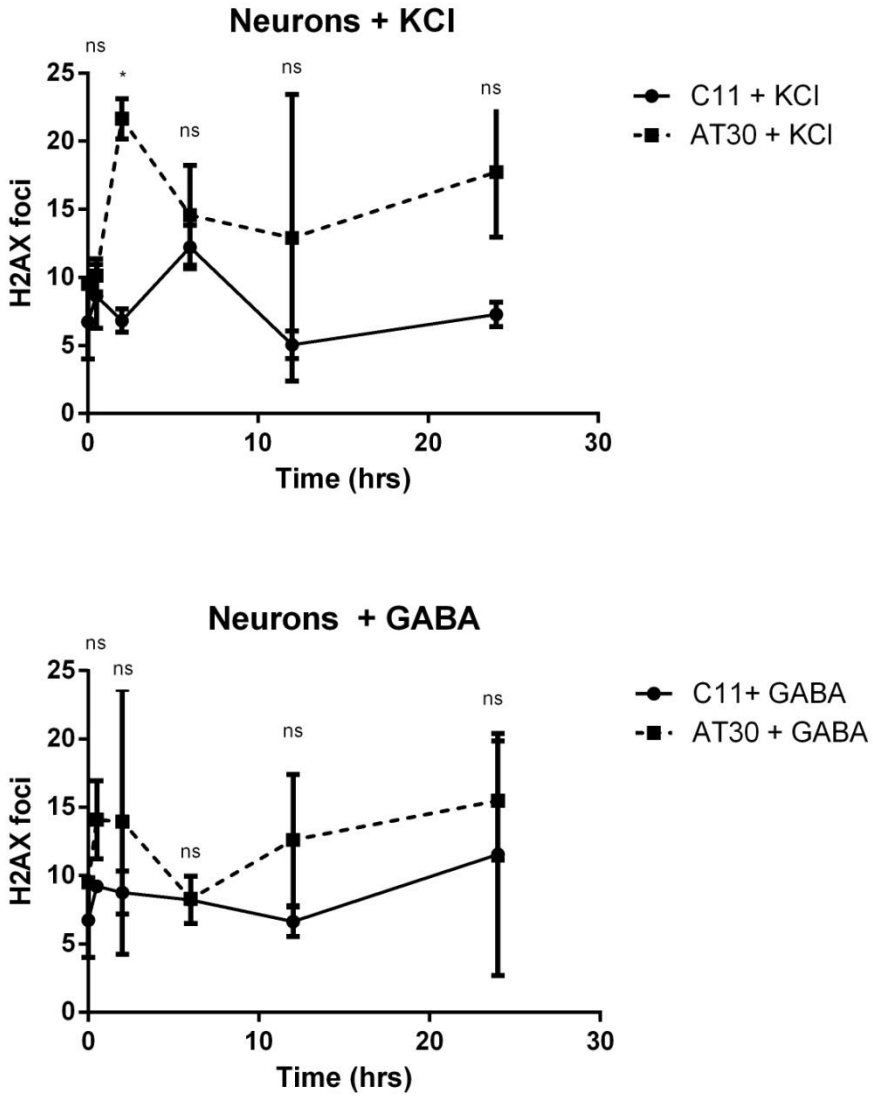

Figure 4.9F - γH2AX kinetics after depolarization with [50mM] KCl and GABA. Two-way ANOVA with Bonferonni post-test reveals a statistically significant difference between A–T and control neurons in γH2AX foci numbers two hours after KCl stimulus. We did not observe statistically significant differences in γH2AX foci after treatment with GABA.

Discussion

Using a modified version of a published protocol [206], we generated an homogenous population of neuronal progenitors that are capable of differentiating into electrophysiologically active committed neurons. This was, to the best of our knowledge and at the time of writing the first exemplification of an iPS cell derived neuronal model of A–T. However this has recently changed [196, 212].

We profiled a range of parameters including differentiation propensity, proliferation & neurite extension rate, and found no evidence for defects arising from ATM deficiency. This was surprising given reports suggesting that ATM is required for neurogenesis [110] and also the fact that we had previously observed ATM deficiency to cause dysregulation of *TGF beta receptor signaling* gene networks, which govern differentiation (chapter 3).

These neurons displayed classical signs of voltage-gated sodium and potassium channel activity after depolarization and also trafficking of calcium. We noticed a recurrent trend for the aberrant and latent egress of calcium after depolarization from certain A–T neuronal cell lines. A relatively unexplored notion is that of defective calcium handling contributing towards the symptoms in A–T. Of particular interest has been the elucidation of calcium related deficiencies underlying a range of neuropathologies with striking similarities to those in A–T. Amongst others, these include defective calcium channel currents in Purkinje cells of mutant *leaner* mice [213] and also altered calcium signaling in spinocerebellar ataxia type 2 [214]. Khanna et al. showed defective calcium trafficking in lymphoblastoid cells isolated from A–T patients [111]. Of additional interest, Chiesa et al. showed that A*TM* deficient mice exhibited age-dependent defects in calcium spike bursts and calcium currents in patch clamping of Purkinje cells slices [112]. Interestingly, through stimulation and high-throughput imaging we observed differences in calcium trafficking kinetics after depolarization in neurons derived from A–T iPS cells that is consistent with a number of these reports. We extended this study to show that this effect was reproduced at the single cell level by transfecting neurons with a genetically encoded real-time

fluorescent calcium reporter gCaMP5. This calcium handling deficit was not reproducible through the administration of ATM inhibitor *Ku55933*, nor did it extend to all cell lines tested, presenting the possibility that it is the complex culmination of genetic background, neuronal cell-type specific or artefactual in nature. Interestingly, when we depolarized A–T neurons generated from episomally derived iPS cells we did not observe the same trend effect on calcium trafficking, suggesting that either generational background affects neuronal activity (possibly by reactivation of transgene) or by affecting population dynamics by skewing the presence of cell types featuring a calcium handling deficit. A recent finding from Barzili et al. showed reduced phase synchronization of cultured mouse A–T cortical neurons using a multi-electrode array [215]. Barzilai et al. suggest that astrocytes are compromised in the absence of ATM and as a result prevent calcium wave propagation is disturbed, which is consistent with our results (Personal communication, Ari Barzilai). It is possible that this defective glial contribution may have contributed to the effect we observed when monitoring calcium trafficking dynamics in our neuronal cultures. Also of interest, is the fact that ATM and it's close homolog ATR were recently shown to localize to dendrites and dendritic spines where they were shown to undergo bicuculline activiation to phosphorylate target substrates [216]. This may explain the observed deficits with calcium trafficking and also the inability to reproduce this apparent defect through application of an ATM inhibitor (which is known to affect ATR also and may have confounded interpretation). Prolonged imaging whereby time until calcium levels reach baseline may be an informative set of follow-up experiments to these.

We were able to deliver an mCherry-tagged ATM construct into these neurons and showed that it restored a functional DNA damage response. We could not generate sufficient numbers of doubly transfected cells to ascertain the effect of ATM restoration on calcium trafficking.

Several publications [5, 113, 116, 194, 195] detail the association of ATM and impaired mitochondrial homeostasis in a range of cell types other than neurons, leading us to study aspects of mitochondrial health in iPS cell derived neurons. We did not detect evidence for mislocalisation of mitochondria within the neural cell bodies or axons of these cells, but noticed a consistent and small decrease in the mitochondrial membrane potential. This result was

recently confirmed by Lee et al., [196] in a paper which details the generation of iPS cells from patients with A–T and their subsequent use for neuronal differentiation and drug screening.

We explored a recent development to emerge from the field that the mislocalization of HDAC4 is causative to the neurodegenerative phenotype in A–T by examining localization of HDAC4 in iPS cell derived neurons, speculating that a similar subset of cells may show aberrant HDAC4 localization in addition to differences in MMP, however we showed this not to be the case, suggesting that HDAC4 localization may be highly cell-type specific.

A very recent paper demonstrates that physiologic brain activity causes DNA double-strand breaks in neurons [211]. Given the role of ATM in responding to double-strand breaks we examined the possibility that this process may be perturbed in A–T by studying the kinetics of γH2AX foci after stimulation of neurons with KCl. Suberbielle et al., showed that exploration of novel environments caused double strand breaks in neurons of mice but they did not directly induce neuronal activity in cultured cells from these mice. Although this was shown to occur via the NMDA (n-methyl-d-aspartate) receptor, little insight into the mechanism driving these phenomena was apparent. This raises an interesting question as to the purpose of these induced double strand breaks, regarding whether their existence may be due in fact to metabolic damage or a more precisely controlled mechanism to regulate transcription in activated neurons.

We observed stark differences in kinetics between control and A–T neurons. While baseline levels of γH2AX foci were comparable, drastically more foci were formed following depolarization in A–T neurons compared to controls indicating a potential mechanism for accumulation of DNA damage in neuronal cells. This may help explain semi-recent findings of increased chromosome instability in the A–T brain [106] and excess aneuploidy in an A–T mouse model of the adult cerebral cortex.

We have established a model system that allows for investigation into the role of ATM in the developing human nervous system. Given the suggestions in the literature and also our previous findings we chose to focus on several areas of interest to study – calcium handling, the

mitochondria and neuronal activity. Provided in this chapter is evidence that both the mitochondria and the ability of A–T neurons in calcium handling are compromised, adding to the theory that A–T is a disease of the mitochondria. We speculate that given the close connection between the mitochondria and calcium buffering, that this is not an unrelated defect.

Importantly we have shown that *in vitro* manipulation of neural stem cells, a technique that will be vital for use of stem cells in a clinical setting, is possible by restoring ATM and thus a functional DNA damage response. Emerging techniques including use of TALENs and CRISPRs to perform high fidelity genome editing (eg. correction of mutations) may be more suitable to utilization in this setting [217, 218]. We show a novel mechanism whereby activity-induced neuronal double-strand breaks occur more readily in A–T derived neurons than in controls – a mechanism which could shed important light onto this disorder.

This chapter also serves to illustrate the proof of principle that patient-specific neurons can be made from iPS cells and that these neurons offer a robust and reproducible model system to investigate the neuropathology in ATM. We showed a proof of concept that this system could be used to test drugs (CTMIO and the effect on neurite extension). Although in this case we cannot report useful findings in this regard, iPS cells and their derivatives are likely to be highly useful as a tool for patient-specific drug screening in the future. A major challenge remains to establish a developmentally relevant model system with which to understand the progression and pathogenesis of A–T. Namely, a model that closely recreates the developmental cascade of events which unfold during the formation of the cerebellum may be more informative about the nature of the defect involved in A–T. Additionally this model would give the most relevant drug-screening platform possible, with the idea that cells from within the cerebellar cortex, such as Purkinje and granule cells could be generated in large numbers and used for i*n vitro* drug testing purposes.

5.0 A developmentally relevant model system for Neurogenesis in A–T

Introduction

Degeneration of the cerebellum is largely understood to underlie the ataxic component of A–T, however the mechanism by which this occurs is unclear. Circuitry within the cerebellum controls motor and sensory learning as well as the vestibular ocular reflex. There is little consensus in the field regarding whether A–T is a developmental or progressive disease. The role of ATM within the developing cerebellum also remains largely unclear although there are reports of temporal ATM upregulation, which are consistent with a specific purpose during development [13]. Given the extensive body of evidence that ATM is responsible for orchestrating a wide array of developmental, metabolic and protective processes, it seems unlikely that it is the perturbation of one particular process that leads to to the devastating defects seen in A–T. We therefore hypothesize that defects in a combination of interrelated processes that involve ATM may instigate particular pathologies at different stages of development and that the full spectrum of neurodegeneration in A–T is the compounded effect of one or more of these processes. To deconvolute the role of ATM in developmental, cell autonomous and cell to cell interaction based processes in the cerebellum requires a systematic temporal analysis of the development of the various cell types of the cerebellum.

Development of the early nervous system is controlled *in vivo* by strict spatial and temporal gradients of morphogen expression. While these are well studied in animals and evolutionarily conserved to a degree, large knowledge gaps exist with respect to human development. Through understanding of these processes and the networks which govern these developmental events, it is possible to recreate them, to a certain extent, *in vitro* [206, 219]. Early during embryonic development, neurogenesis occurs in which the developing embryonic brain begins to organize into three distinct compartments or regions, namely the prosencephalon (forebrain), mesencephalon (midbrain) and rhombencephalon (hindbrain) (shown in figure 5.1A). A distinct border forms between the mid and hindbrain territories – the isthmic organizer, a prominent signaling center which is involved with secretion of inductive cues in the form of growth factors

involved with patterning. Development of the isthmic organizer is controlled by the region-specific transcription factors, *En1*&*2, Pax2,5*& *8, Otx2* and *Gbx2* [220]. The cerebellum arises from the caudal-most region (the rhombencephalon) of the neural tube. Individual regions called rhombomeres form within the rhombencephalic segment — the cerebellum arises from two rhombomeres located in the alar plate of the neural tube [221].

Formation of the cerebellum can be thought of to occur via discrete steps. Firstly the characterization of the cerebellar territory at the mid–hindbrain (MHB) boundary (dictated by the isthmic organizer) occurs. Following this, formation of two compartments for cell proliferation occurs. Firstly, the Purkinje cells and the deep cerebellar nuclei arise from the ventricular zone of the metencephlaic alar plate (during mouse embryonic development Purkinje cells are born between E11 and E13 as their progenitors exit the cell cycle and start to migrate out of the ventricular zone). Secondly, the second germinal zone (also known as the rhombic lip) produces granule neurons where they eventually migrate to form the internal granule layer of the cerebellar cortex. Subsequent formation of cerebellar circuitry and maturation takes place post-natally [222].

Insight from developmental studies shows that enforced expression of *Fgf8* is sufficient to induce ectopic midbrain and cerebellar tissue formation [223]. Insulin has been shown to have caudalizing activity, suppressing expression of forebrain markers *Six3, Rx* & *Otx2* during neuronal differentiation [220]. FGF2 has been demonstrated to have rhombomere-1 inducing activity in an embryonic neural explant assay [224] and to increase expression of *Wnt1* and *Fgf8* [220]. During development of the mouse cerebellum, both BDNF (Brain derived neurotrophic factor) and NT-3 (Neurotrophin-3) are required (Released by granule cells; maximal levels occur during post-natal development at weeks 1-2 for NT-3 and week 2 for BDNF). Knockout studies in mice demonstrate that both NT-3 and BDNF are required for survival and differentiation of Purkinje and granule cells, as well as functioning of the cerebellar circuit and development of cerebellar foliation [225]. CAPS2 (Ca2+-dependent activator protein for secretion) facilitates formation of vesicles that contain catecholamines and neuropeptides [226]. CAPS2 knockout mice show a decrease in BDNF and NT-3 release resulting in aberrant cerebellar development

and function (delayed development/increased cell death of Purkinje and granule cells, defective migration, atrophic arbors of PCs). RA (retinoic acid) influences the expression of the *Hox* homeotic genes with neuronal stem cells of the hindbrain/branchial regions being especially responsive [227]. RARβ (retinoic acid receptor Beta) has been shown to mediate the response to RA treatment in controlling *Hox* gene expression, with the finding that RA controls anterior posterior polarization in mouse embryos [228]. SHH and JAG1 (NOTCH2 ligand) induce expansion of granule cell progenitors during the development of the cerebellar cortex [229].

Several research groups have attempted to take advantage of these insights into signaling events that occur during early development to achieve specification of hindbrain neurons including Purkinje and granule cells, albeit with varying success.

In 2006, a Japanese group reported the first generation of cerebellar neurons from murine ES cells, reporting induction of $MATH1^{+}$ cerebellar granule cell precursors and Purkinje cell progenitors (that give rise to the two main constituents of the cerebellar cortex) [130]. This was achieved via timed application of soluble patterning signals FGF8, BMP4 and WNT3a to serum-free cultured embryoid bodies. Shortly after this initial observation, an American group [229] published a similar protocol using secreted factors WNT1, FGF8 and Retinoic acid, recapitulating patterning events in the cerebellar region of the neural tube, followed by application of factors that induce early granule cell marker expression (BMP6, BMP7 & GDF7) and finally treatment with mitogens (JAG1, SHH) which are involved with proliferation. More recently a publication followed that outlined a protocol attempting to more closely recreate the self-inductive signaling microenvironment of the early murine cerebellum. In this study, timed prospective selection of Purkinje cell progenitors using the cell-surface marker NEPH3 was performed [220]. A modified version of work performed by Salero et al., [229] was shown to produce a population of functional cerebellar-like cells from hESCs [131].

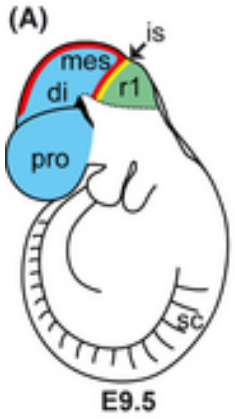

Figure 5.1A - Diagramatic representation of the developing mouse (E9.5) with a focus on the neural tube (coloured). Depicted are the prosencephalon (pro) & diencephalon (di) -structures that give rise to the forebrain, and also the mesencephalon (midbrain, mes) and rhombomere 1 (r1, which forms the cerebellum). Also depicted is the isthmic organizer (is) that separates the mesencephalon and r1 by a border of gene expression (blue marks *Otx2* positive territory, while red shows *Wnt1*, Yellow is *Fgf8* and Green is *Gbx2*). Figure adapted from [230].

In this chapter, are reproduction and optimizisation of the protocol of Erceg et al. (2010) to ascertain whether it is possible to generate neurons resembling those of the cerebellum. We successfully induced expression of mid–hindbrain markers EN1, HOXB4 & GBX2 and also transcription factors demarcating the two main cerebellar progenitor types, MATH1 (rhombic lip/granule cell progenitors) and PTF1α (ventricular zone/Purkinje, Golgi, Stellate cell progenitors). Further, it is shown that it is possible to expand these progenitors to produce cells that express markers consistent with, and are morphologically similar to, developing granule cells. Although we noticed the sporadic appearance of neuronal cells with a Purkinje cell-like morphology (large distinctive soma, multiple, branching, elaborate dendrites), it was not possible to isolate or propagate these cells, pointing towards a knowledge gap regarding the correct supportive trophic microenvironment required for culture and expansion of these cells. To gain insight into the early events which occur during the formation of the cerebellum and

how this may be affected in the absence of ATM, RNA sequencing of neuronal progenitors after 34 days of differentiation was performed.

Materials and methods

Differentiation of cerebellar-like cells

Embryoid bodies (EBs) were formed by detachment of undifferentiated iPS cells from the MEF monolayer (12,000/cm^2) using a P200 pipette. EBs were transferred to a low-attachment plate (Costar) in Knock-Out Serum (KSR) replacement hESC culture medium (80% DMEM -F12 (GIBCO), 20% KnockOut-Serum replacement (GIBCO), 2 mM L-glutamine (GIBCO), 1% non-essential amino acids (NEAA) (GIBCO), 0.1 mM 2-mercaptoethanol at 37°C at 5% CO_2 at high humidity. EBs were cultured in the absence of basic fibroblast growth factor (to promote differentiation towards neurectodermal lineage). Medium was changed each day. After four days EBs were resuspended in neural induction medium (DMEM F-12with Glutamax (GIBCO), N2 supplement (GIBCO) and heparin sulfate (R&D)) and supplemented with human FGF8 (Sigma Aldrich) (100 ng/mL) and RA (Retinoic acid) (10 µM) (Sigma Aldrich). After 7 days of incubation in this medium EBs were deposited in plates coated with laminin (Sigma) (2 µg/mL) and fibronectin (BD) (5 µg/mL) in basal medium eagle (BME) media (Invitrogen) supplemented with ITS (Insulin, Transferrin, Selenite) (GIBCO), human FGF8 (100 ng/mL), human FGF4 (Life technologies) (100 ng/mL) and human basic fibroblast growth factor (Invitrogen) (20 ng/mL) and allowed to grow for four days. Medium was changed to DMEM-F12 with human FGF8 (100 ng/mL), WNT1 (Peprotech/Abacus) (50 ng/mL) and WNT3A (50 ng/mL) (R&D) for five days. The next stage of differentiation involved culturing the cells in BME media supplemented with N2, B27 (GIBCO), human BMP4 (R&D), (50 ng/mL), human BMP6 (R&D) (20 ng/mL), human BMP7 (Peprotech/Abacus) (100 ng/mL) and human growth differentiation factor 7 (GDF7) (R&D) (100 ng/mL) for a further eight days. Attached cells were then disaggregated and replated on laminin/fibronectin for another 8 days of growth in BME supplemented with N2, B27, human BMP4 (50 ng/mL), human BMP6 (20 ng/mL), human BMP7 (100 ng/mL), human GDF7 (100 ng/mL), human Sonic hedgehog (R&D) (100 ng/mL),

human neurotrophin 3 (R&D), (NT3) (100 ng/mL), jagged1 (JAG1) (R&D) (20 ng/mL) and human brain derived neutrotrophic factor (BDNF) (100 ng/mL) (R&D).

Immunostaining

For immunostaining cells were gently washed once with PBS+ so as not to disturb large spheroid colonies or fragile cell extensions in PBS and fixed in 4% paraformaldehyde for 15 minutes at room temperature. For nuclear staining samples were permeabilized in 0.1% TritonX100 at room temperature for 10 minutes or ice cold methanol for 15 minutes at -20^{o}C, before blocking with 10% goat serum and incubation with the relevant antibodies overnight at 4°C in blocking medium. Antibodies and dilutions used were ZIC1 (Saphire bioscience) (1:1000), ZIC3 (Millipore) (1:1000), ENGRAILED1 (Millipore) (1:500), GBX2 (Abnova) (1:500), β-III-TUBULIN (Millipore) (1:1000), MATH1 (Developmental hybridoma studies bank) (1:1000). Following washing with PBS (3 times 5 minutes at room temperature) secondary antibodies goat anti-mouse IgG_1, goat anti-mouse IgG_{2B}, goat anti-mouse IgM and Donkey anti-rabbit IgG (Alexa fluor) (2 µg/ml) were used to reveal reactivity. Nuclei were stained with DAPI or Hoechst. This preparation minus the addition of primary antibody was used to confirm specificity of staining.

Paraffin embedded tissue sectioning and immunostaining

Neurospheres were harvested by centrifugation at room temperature (500g) and fixed in 4% paraformaldehyde at room temperature as a loose cell pellet before making into a cell pellet by adding molten agarose, spinning down again then allowing solidification. Once solidified, pellets were processed into paraffin, embedded and sectioned. Sections were mounted on Menzel Superfrost Plus adhesive slides and air dried overnight at 37^{o}C. Sections were next dewaxed and rehydrated through descending graded alcohols to water before transfer to Tris buffered saline (TBS) pH 7.6. Endogenous peroxidase activity was blocked by incubating the sections in 2.0% H_2O_2 in TBS for 10 minutes. Sections were washed in three changes of water before transfer of slides to EDTA antigen retrieval buffer pH8.8 for 15 minutes at 100^{o}C to heat unmask the antigen from the aldehyde bonds. Slides were allowed to cool for 20 minutes in the retrieval solution then were washed in 3 changes of TBS. Nonspecific antibody binding was inhibited by incubating the sections in Biocare Medical Background Sniper for 15 minutes.

The following primary antibodies: PAX6 (Developmental studies hybridoma bank) (1:100), PTF1α (Abnova) (1:100), ZIC3 (Millipore) (1:100) and ENGRAILED1 (Millipore) (1:100) were diluted with TBS, applied to the slides and were incubated at room temperature for 60 minutes. Sections were washed in three changes of TBS before MACH1 Mouse Probe was applied for 15 minutes at room temperature. Sections were washed in three changes of TBS and MACH1 Universal Polymer HRP was applied for 30 minutes at room temperature. Sections were washed in three changes of TBS before the signal was developed in betazoid DAB chromogen, MACH1 Kit for 5 minutes. Sections were then washed in water three times to remove excess chromogen. Sections were lightly counterstained in Haematoxylin, washed in water, dehydrated through ascending graded alcohols, cleared in xylene, and coverslipped. Antibodies were tested against a panel of known controls including tissue from pancreas, kidney, placenta, colon, uterus, lung and melanoma skin, as well as mouse whole brain and human embryonic cerebellum.

Neurosphere growth assay

Twenty single neurospheres (10 control, 10 A–T) were seeded in suspension individually into wells of a 96-well low attachment plate (Costar) in N2B27 Neurobasal media. Neurospheres were photographed every other day using an Olympus IX51 microscope for two weeks. Images were compressed to 8-bit files and appropriate thresholds were set to define the borders of each individual neurosphere before applying an area measurement algorithm using ImageJ.

Sequencing library preparation

Total RNA was extracted using *RNA Spin II* isolation columns (*Machery Nagel*). On column digestion of DNA with RNase free *DNase* was performed according to the manufacturer's specifications (*Ambion*, Austin, TX). RNA samples were subject to RNA integrity analysis using the RNA 6000 Nano total RNA kit (*Agilent*). All samples recorded a RIN (RNA integrity number) in excess of 8.5 out of 10. Samples were processed according to the TruSeq Stranded Total RNA Sample preparation LS protocol kit (*Illumina)* as per the manufacturer's specifications. In short, and according to best practices for RNA handling, rRNA was depleted from 1 µg total RNA samples using rRNA removal beads and a magnetic stand, before

purification, fragmentation and cDNA synthesis. Samples were adenylated at the 3' end before ligation of specific adapters. DNA fragments were enriched by PCR specific for adapter sequences. Libraries were cleaned up and validated by resolution on DNA 1000 Bioanalyzer chips (*Agilent)*. Libraries were sequenced across two lanes of a HighSeq 2500, using the rapid run protocol to obtain 100bp paired-end reads.

Differential gene expression analysis

After read quality control using FastQC [231], primary alignment to the reference human genome (hg19) was carried out using the Burrows-Wheeler Aligner [232] version 0.6.2 with default mapping parameters. Output data was converted to bam format using SAMtools [233]. The exon_utils.py module of the MISO framework [234] was used to extract constitutive exons longer than 1000 nucleotides, and pe_utils.py was used to determine the mate inner distance and mate standard deviation parameters for each dataset. Tophat [235] version 2.0.8 was then used to map reads to the genome and reference transcriptome (GENCODE v. 17 [236]) simultaneously, with the parameters --b2-very-sensitive --read-mismatches 3 --read-gap-length 2 --read-edit-dist 3 --read-realign-edit-dist 0. All subsequent analyses were conducted using the results of this mapping. Count tables were obtained using the HTSeq [237] framework in union mode, with GENCODE v. 17 as a reference. Differential gene expression analysis was conducted using the R package for statistical computing [238] using the edgeR [239] and DESeq [240] libraries. Genes were tested for differential expression if they displayed one count per million in at least three of the libraries (edgeR) or at least 10 counts across all of the datasets (DESeq). Genes were considered differentially expressed if found to be significant by both tools with a Benjamini-Hochberg adjusted p-value < 0.01 and a greater than twofold change in expression between the replicate samples.

Comparison with Illumina Human Body Map and Developmental Brain Transcriptome Data

Developmental brain transcriptome RNA-seq RPKM data was downloaded from http://www.brainspan.org/. Illumina Human Body Map 2.0 RNA-seq data for 16 tissues (1 paired end and 1 single end library per tissue) from the sequence read archive (Accession

number ERA022994) was mapped to the human genome/transcriptome as described above. Gene-level RPKMs for the data generated in this study and the Illumina Human Body Map were calculated based on counts determined by htseq to GENCODE17 genes. Due to challenges in unambiguously assigning reads to transcripts and to enable accurate data comparison, an approach similar to that taken by the developmental brain transcriptome project was used: composite models of genes were generated, with each gene annotated as the union of all exonic nucleotides across all of its transcripts in GENCODE17, and the length of each of these was used as the "gene length" for the RPKM calculation. Hierarchical clustering of ranked RPKM with average agglomeration of euclidean distance was then performed in R using the pvclust [241] package.

Gene ontology and pathway analysis

Pathway analysis was carried out using Ingenuity Pathway Analysis [242].
Gene ontology analysis was also carried out using the DAVID software suite [243]. Biological process, cellular component and molecular function were annotated using GO level 1, which contain annotations for the largest number of genes; using all annotation levels for these analyses did not significantly alter the results. PANTHER phylogeny-aware ontologies at all levels are also presented. Tissue similarity analysis was carried out using DAVID using the UP_tissue module. DAVID Results are included in appendices tabs 9-18.

Results

Induction of the Isthmic organizer

Given the recurrent trend amongst published works detailing differentiation of cerebellar neurons to reproduce self-inductive developmental signaling cues, I examined whether evidence that delivery of factors involved in early isthmocerebellar development (FGF8 and RA) were sufficient to instigate this program in our culture setting. To do this I differentiated the hESC line H9 using a shortened version of the above protocol and assayed for the presence of the hindbrain-specific transcription *Gbx2*, which marks the isthmic organizer and thus the mid-hindbrain barrier. I also examined the synergistic co-repression and *Otx2 (*which competes with *Gbx2* to define the mid-hind brain barrier*)* and the expression of caudal neural cell marker *Hoxb4*.

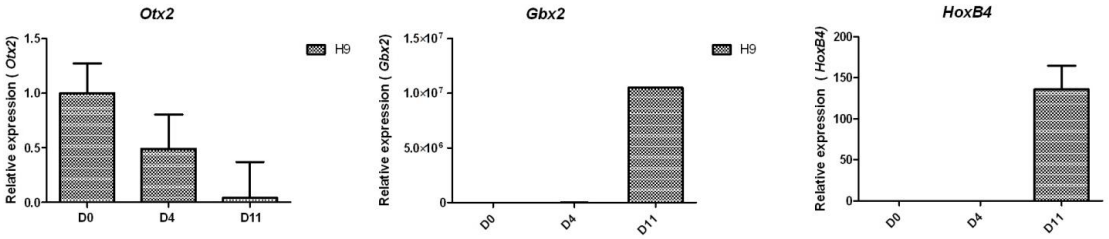

Figure 5.2A – Pooled data from from four* independent qPCR experiments (technical triplicates run in each) amplifying *Otx2, Gbx2* and *HoxB4* transcript from day zero (undifferentiated iPS), day four (after four days of EB formation) and day 11 (treatment of EBs with retinoic acid and FGF8). Whole brain lysate cDNA (a kind gift from the Queensland Brain Bank) was used as a positive control from which *Otx2*, *Gbx2* and *HoxB4* expression could be detected robustly (not shown). Transcript expression was normalized to *B-Actin*. NTC were included and did not approach threshold levels. Error bars show SEM. *Fewer than four replicates performed for *HoxB4* due to limited material.

Similar to the data reported by [131] we observed a gradual decline in *Otx2* transcript with a concordant upregulation of *Gbx2* transcript (Figure 5.2A). This is in keeping with the downregulation of *Otx2* by *Gbx2* which takes place in the first rhombomere *in vivo* in an antagonistic relationship that serves to define and control cerebellar development from the MHB junction [244]. Expression of *HoxB4, a* marker for caudal neural cells [245] could be detected after 11 days of differentiation indicating specification of hindbrain cells had commenced by this stage.

We next confirmed the robustness of this protocol in a further two iPSC lines (C11&C32) and again performed qPCR for *Otx2* and *Gbx2* (Figure 5.2B). A vehicle only (mixture of solvents used for dilution of small molecules and growth factors) was used as a control.

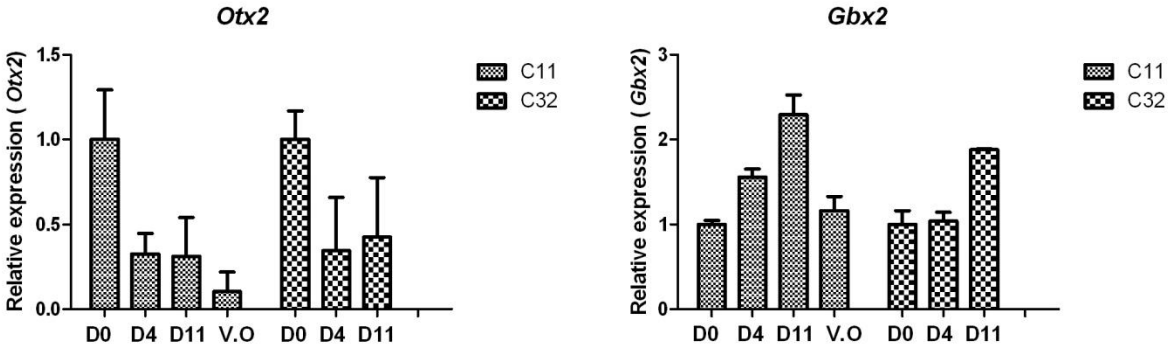

Figure 5.2B – qPCR data amplifying *Gbx2* and *Otx2* transcript from day zero (undifferentiated iPSCs), day four (after four days of EB formation) and day 11 (treatment of EBs with retinoic acid and FGF8). Expression levels from vehicle only control are included. NTC were run and did not approach threshold levels. Transcript expression was normalized to *GAPDH*. Error bars show SEM.

Similar kinetics were observed to those in Figure 5.2A, as *Otx2* transcript declined during the induction protocol with a concordant upregulation of *Gbx2*. We did notice stark differences in induction efficiency in *Gbx2* between differentiation experiments that could indicate a high degree of intrinsic variability in a particular cell line's ability to respond to FGF8 and or retinoic

acid. Detectable levels of both transcripts were evident in vehicle only controls, although at reduced levels indicating that the vehicle and or undirected differentiation process alone was sufficient to induce some neural commitment.

We next examined whether pre-patterning of EBs with two small molecules previously shown to induce neuronal differentiation (SB431542 and Dorsomorphin) would more efficiently induce neuroectodermal differentiation than incubation in hESC media (without bFGF) alone (Figure 5.2C).

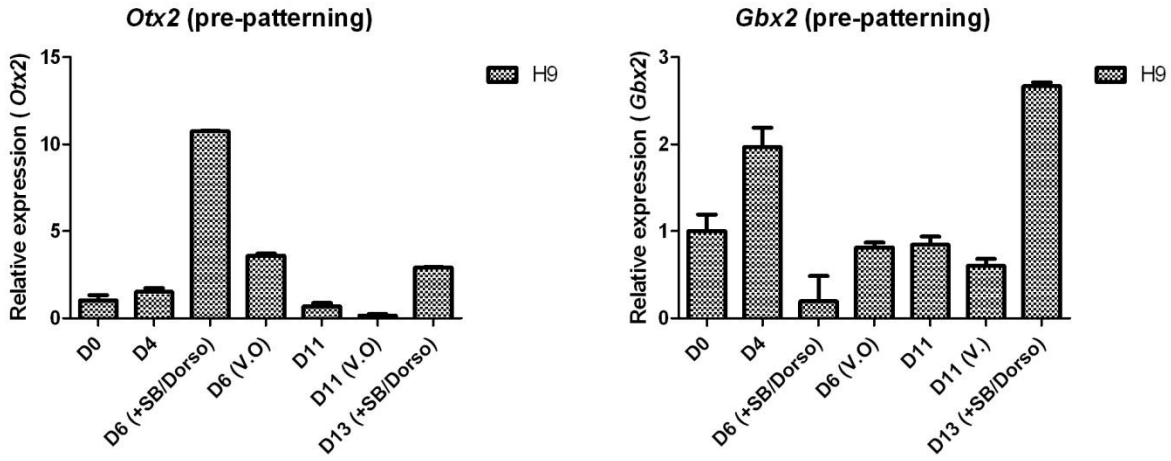

Figure 5.2C - qPCR data amplifying *Gbx2 and Otx2* transcript from day zero (undifferentiated iPSCs), day four (after four days of EB formation), day six (after 6 days' incubation with SB431542 & Dorsomorphin), day six (vehicle only), day 11 (treatment of EBs with retinoic acid and FGF8), day 11 (vehicle only) and finally day 13 (after 6 days of treatment with SB421542 and Dorsomorphin as well as subsequent incubation with FGF8 and retinoic acid). NTC were run and did not approach threshold levels. Transcript expression was normalized to *GAPDH*. Error bars show SEM.

We observed similar differentiation kinetics to previous experiments. It was however clear that pre-patterning by addition of an additional six-day window of treatment of adherent cultures with SB431542 (10 µM) and Dorsomorphin (5 µM) induced robust expression of *Otx2*. As

expected, we saw concordant downregulation of *Otx2* and upregulation of *Gbx2* by day 13, which was markedly higher than samples induced with FGF8 and retinoic acid alone.

We observed by qPCR a characteristic pattern of increasing *Gbx2* expression coupled with dwindling abundance of *Otx2* mRNA, a process known to occur to delineate the border of the first rhombomere. Collectively we interpret these data to mean that application of factors involved with early patterning of the mid–hindbrain *in* vivo are capable of giving rise to similar events *in vitro* and that this process can be used to generate neuronal precursor cells with a gene expression signature characteristic of the developing hindbrain.

Generation of a population of cerebellar-like cells

We extended our differentiation protocol using the approach outlined in [131]. Briefly, we maintained and expanded undifferentiated control and A–T iPS cells on MEFs (12,000/cm^2) for four days before generating embryoid bodies. These embryoid bodies were cultured in hESC KOSR media without bFGF for four days before application of neural induction media containing FGF8 and retinoic acid. We then plated these neuralized EBs onto tissue-culture plates previously coated with laminin and fibronectin and in the presence of FGF8, FGF4 and bFGF for seven days. Subsequent to this, we changed media to include WNT1, WNT3a and FGF8 for a further five days before harvesting and replating these cells in the presence of media containing BMP4, BMP6, BMP7 and GDF7 for eight days. Further to this, we incubated these cells in media containing BMP4, BMP6, BMP7 and GDF7, SHH, JAG1, BDNF and NT3 for an additional 8 days (full protocol is described in materials and methods section and outline showed in Figure 5.3A). We noticed the appearance of neuroepithelial type cells by day 14, and subsequent formation of polarized rosette type structures by day 16, which could be isolated and replated to produce a population of rapidly proliferating neural cells by day 24 onwards (see Figure 5.3A).

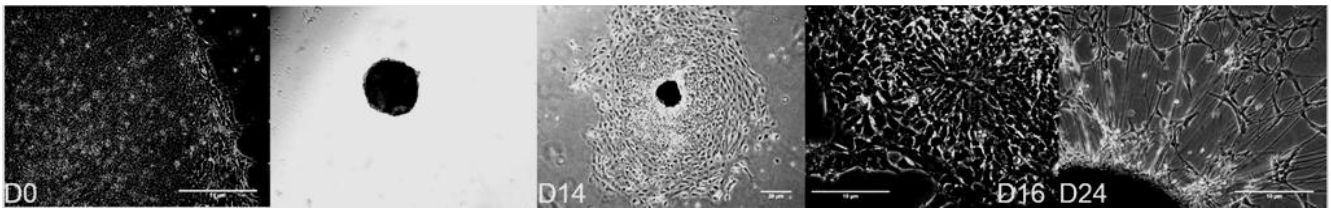

Figure 5.3A – Representative phase contrast images at time points detailing the differentiation process starting with undifferentiated iPS cell colonies (D0) and subsequent generation of embryoid bodies (D4), plating down of neuralized EBs gives rise to neuroepithelia (D14) forming rosettes (D16) and finally a population of proliferating neurons with heterogenous morphology (D24). Scale bars are 10 μm with the exception of D14 that is 20 μm to exhibit detail and extent of neuroepithelial colony.

Neurosphere growth assay

We monitored growth and expansion of control and A–T neurospheres in culture by capturing brightfield images of neurospheres and applying an ImageJ threshold based algorithm to calculate growth by change in area (Figure 5.3B). No differences between control and A–T iPSC derived neurospheres were apparent as measured by a Two-way ANOVA (with Bonferoni post-test) at the initial three time points. Growth rates did appear to diverge at day 10 onwards, with A–T neurospheres proliferating more rapidly ($P<0.05$ and $P<0.01$ respectively) indicating that the internal growth program may change subtly over this period.

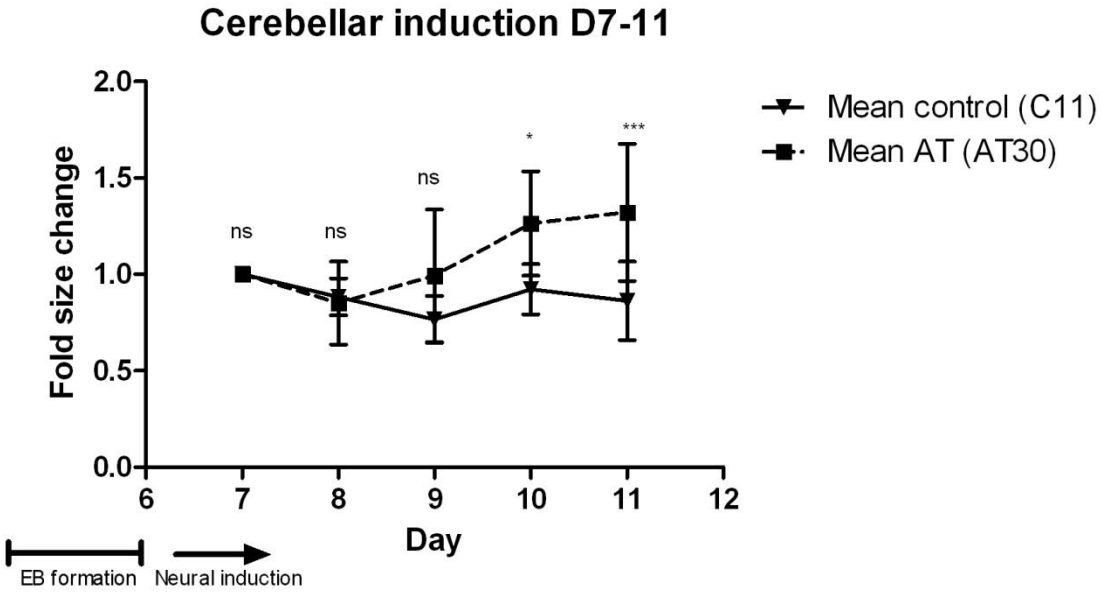

Figure 5.3B – Neurosphere growth measurements during 5 days in neural induction media (FGF8 & Retinoic acid) reveal no significant differences at initial 3 time points measured but statistically significant differences ($P<0.05$ and $P<0.01$ respectively) as measured by Two-way ANOVA with Bonferoni post-test.

Serial sectioning of paraffin embedded neurospheres

To confirm the presence of cerebellar specific proteins we obtained human embryonic cerebellum and adopted a protocol to paraffin embed and stain serially sectioned material from both control tissue and neurospheres. We detected expression of mid-hind brain marker ENGRAILED 1 in controls and also neurospheres cultured beyond 34 days. By day 50 robust expression of ventricular zone progenitor marker PTF1α was observed. Reactivity with ZIC3 and PAX6 was noted in a subset of cells suggesting granule cell differentiation had begun to occur. It was interesting to note the appearance of foliation at the periphery of the neurospheres (Figure 5.3C, lower 3 right hand side panels), reminiscent of the arrangement of the cerebellar cortex.

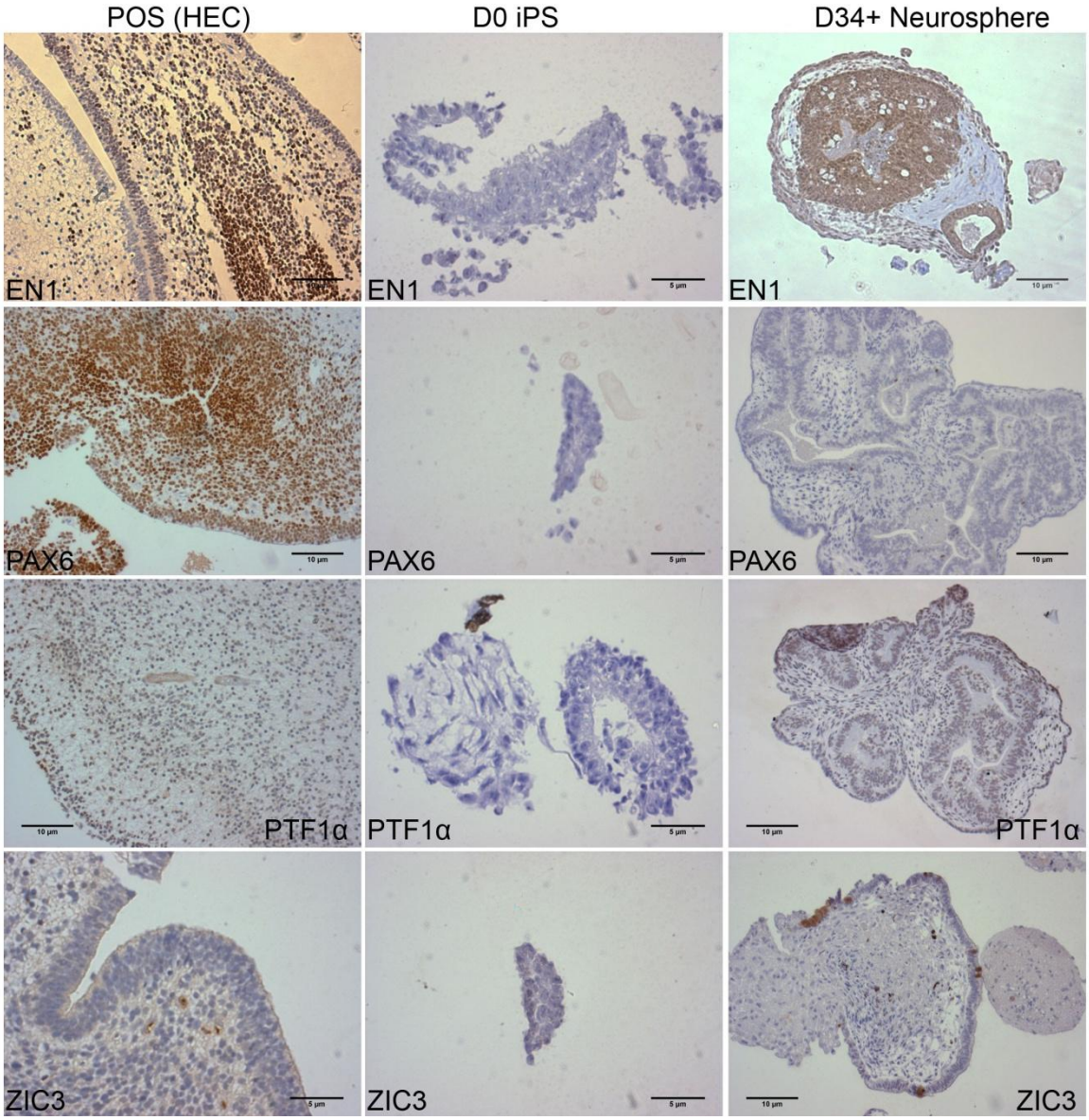

Figure 5.3C – Undifferentiated iPS cells and Neurospheres (D34+) were serially sectioned and stained for ENGRAILED1, PAX6, PTF1α & ZIC3. Human embryonic cerebellum (HEC) was used as a positive control. Scale bars are 5 & 10 µm.

Expansion of cerebellar-like neurons

When EBs were plated down and expanded after 24 days of neural induction we observed the eventual appearance of a heterogenous population of cells with neuronal morphologies including cells with small soma, multiple dendrites displaying small stubby claw-liked appendages (Figure

5.3D upper left panel). Additionally, we observed cells with glial/astrocytic type morphology (Figure 5.3D upper right panel). The continued appearance of spheroid aggregates with axon-extending neurons (lower left panel) was noted in addition to highly dense networks of axon-projecting neurons (lower right panel).

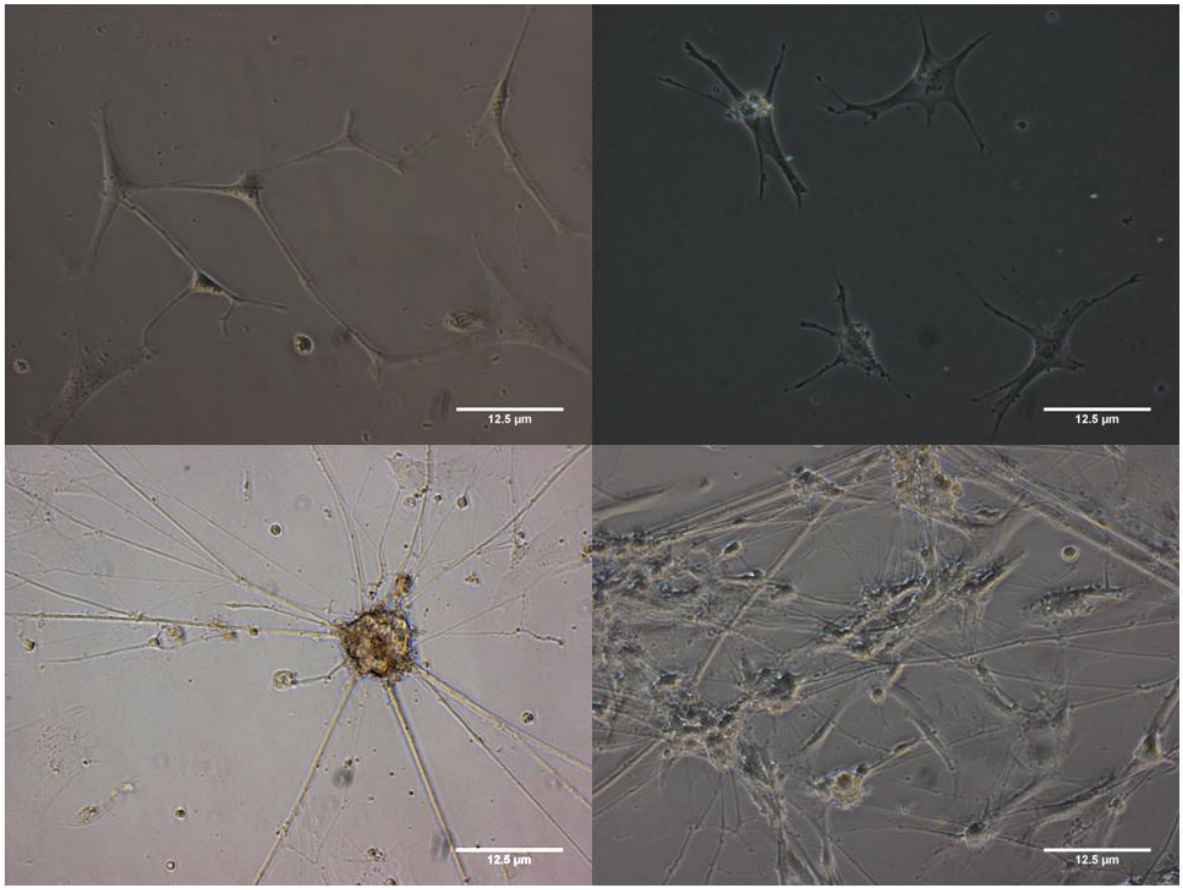

Figure 5.3D – Phase contrast microscopy of commonly observed neuronal morphologies after final neural spheroid body attachment (day 24 onwards). Scale bars are 12.5 µm.

We observed a large number of cells with morphologies consistent with the description ofgranule cells of the cerebellum. This included the appearance of stubby claw-like appendages/projections and recurrent branching of axonal projections in a T-shaped form, commonly associated with cerebellar granule cells (Figures 5.3E&F).

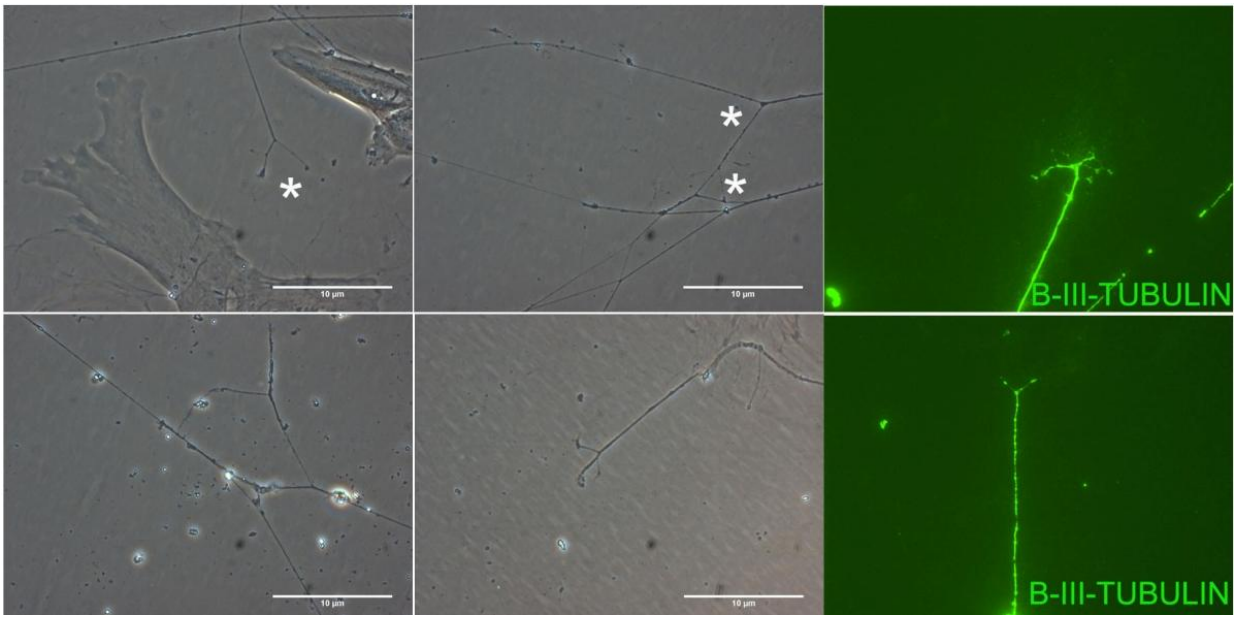

Figure 5.3E – Phase contrast and fluorescent microscopy of common T-shaped branching of axons characteristic of cerebellar granule cells (marked by asterisk). Scale bars are 10 µm.

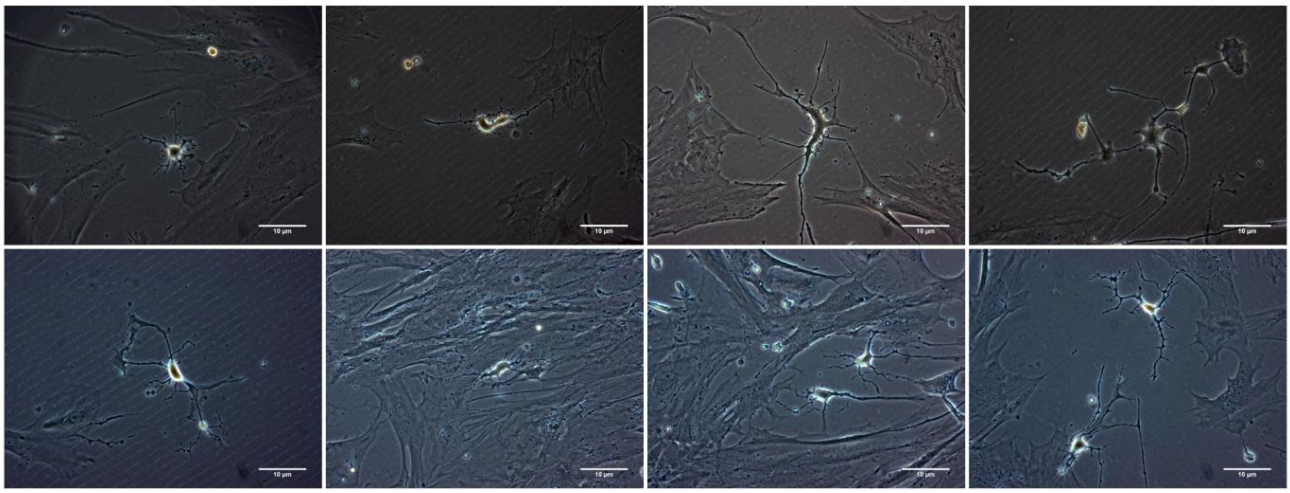

Figure 5.3F – Phase contrast microscopy of cells that show morphology consistent with developing cerebellar granule cells. Scale bars are 10 µm.

When stained with antibody for pan-neuronal marker β-III-TUBULIN, we observed morphologies consistent with that of a cerebellar granule cell including distinctive stubby claw like appendages (*), characteristically shaped soma (**) and the distinctive T-shaped branching of axons (***) (Figure 5.3G).

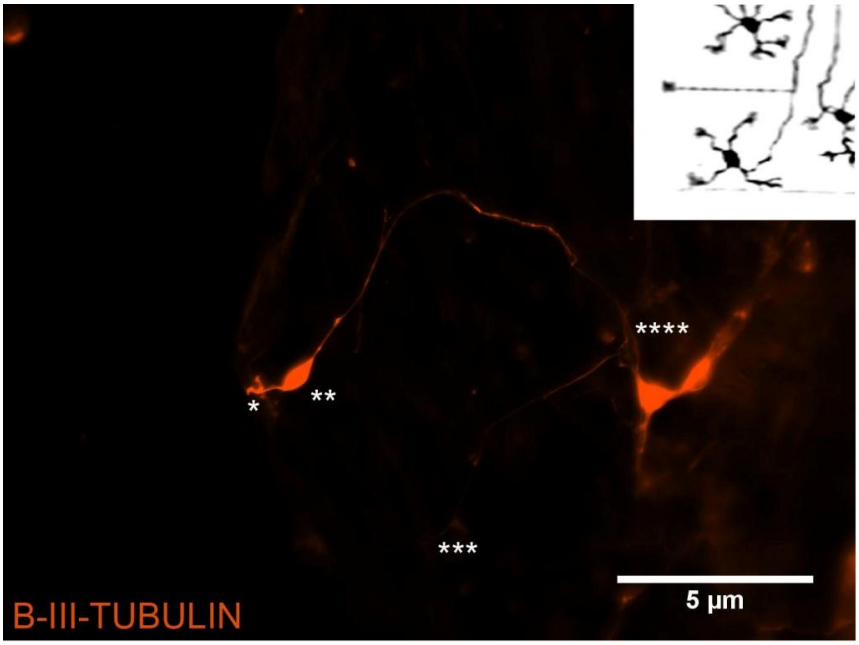

Figure 5.3G –Fluorescent microscopy of putative granule cell stained with β-III-TUBULIN exhibiting distinctive stubby claw like appendage (*), characteristic soma (**), common T-shaped branching of axons (***) and association with an adjacent neuron (****). Scale bars are 5 µm. Inlay shows a silhouette of cerebellar granule cell for comparison (Santiago Ramón y Cajal, 1899. Instituto Santiago Ramón y Cajal, Madrid, Spain).

We interpret these findings to mean this induction protocol was capable of producing cerebellar progenitors which mostly gave rise to granule cells of the cerebellum. These findings are consistent with reported induction efficiency [131] and also in keeping with what might be expected given that *in vivo* the cerebellar cortex is predominantly composed of granule cells.

After 34 days of culture we observed the sporadic appearance of cells with a large soma and multiple branching dendrites, a morphology reminiscent of Purkinje neurons (see figure 5.3H). Various degrees of dendritic complexity were observed, suggestive of Purkinje neurons at various stages of maturation. We could not, however, maintain the survival of this cell type for prolonged periods possibly due to incorrect supporting trophic microenvironment. Isolation and identification with putative markers (PCP2, CALBINDIN & NEPH3) proved unsuccessful, due to difficulties isolating this cell type. This is consistent with the work of Muguruma et al. who showed that after isolation of NEPH3 positive Purkinje cell precursors growth in conventional high-density culture settings showed gradual cell death and failure to express late Purkine cell markers such as L7 and calbindin [220].

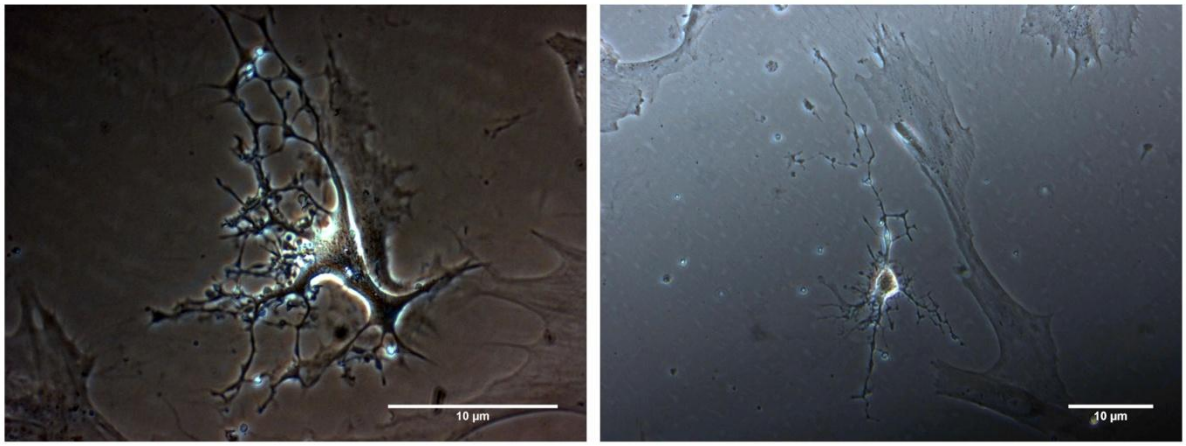

Figure 5.3H– Neuronal cells exhibitive a morphology similar to Purkinje cells (large soma and distinctive multiple branching dendrites) were generated but could not be isolated or propagated. Scale bars are 10 µm.

Our results showed that timed application of factors involved with cerebellar development induced expression of hindbrain specific transcription factors GBX2, HOXB4 and EN1, and later expression of proteins known to be expressed in the developing cerebellum (PTF1α, PAX6, ZIC3 & B-III-TUBULIN). We observed migration and expansion of neurons morphologically characteristic of granule cells which showed important hallmarks of this cell type. Our ability to

culture and propagate these cells was restricted, presumably because of the limited knowledge base regarding correct growth factor and microenvironment requirements of granule and Purkinje cells.

RNA Sequencing

To more thoroughly define this cell population and also to investigate the impact of ATM deficiency on this *in vitro* generated early cerebellar cell population, we next performed RNA sequencing to profile the expression of A–T (AT30) and control (C11) neural inductions (day 34). Three separate iPS cell cultures and neuronal inductions from individual clones were sequenced. This data is available upon request through Stemformatics (http://stemformatics.org).

Fifty to eighty per cent of reads were mapped uniquely in each of the datasets, corresponding to 30-120 million mapped reads per library; a low number of non-uniquely mapping reads (5-7% when compared to number of uniquely mapped) were also reported. Most mapped reads were mapped as pairs, with >70% of reads mapped in proper pairs across all datasets. Approximately 30% of the reads were mapped across splice junctions, which is expected given that the median exon length in humans is 120 nucleotides and that reads were sequenced using a paired end 100 bp protocol. The TruSeq protocol is designed to retain RNA strand information, and consistent with this our data shows 89-96% of reads mapped in a strand-specific manner. Overall, the mapping statistics for all datasets are comparable, and demonstrate that a good quality set of RNA sequencing libraries had been generated, enabling differential gene expression and alternative splicing analyses. Mapping statistics are presented in tab 8 of appendices.

To ensure high sequencing data fidelity and downstream alternative splicing analysis we compared junction saturation across all sequencing libraries (Figure 5.4A). For a well-annotated organism, the number of expressed genes in particular tissue is almost fixed, so the number of splice junctions should also be fixed. These are usually reflected in the reference gene model, in our case GENCODE 17, which includes data from the Illumina Body Map and other tissue atlas interrogations. All of these “tissue –characteristic" splice junctions should be rediscovered from saturated RNA-sequencing data, otherwise, downstream alternative splicing

analysis could be problematic because low abundance splice junctions are missing. Figure 5.4A illustrates that in our dataset the red curve of "known junctions" has almost reached a plateau, indicating that we have saturated known junctions and alternative splicing analysis, especially for known isoforms.

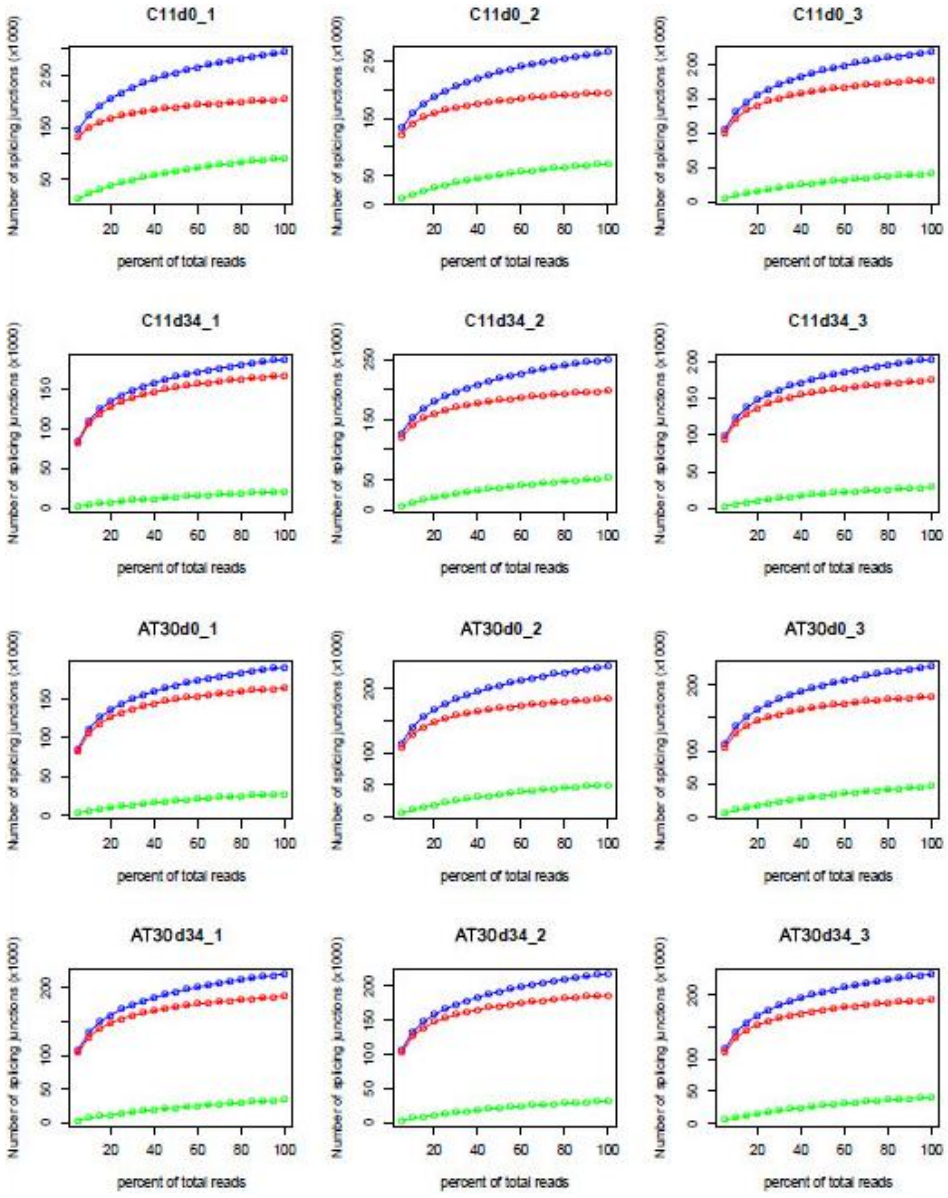

Figure 5.4A – Junction saturation in all sequenced libraries. Comparison of junction saturation across all sequencing libraries; known junctions are presented in red, novel junctions - in green, all junctions in blue.

Analysis of novel junctions (Figure 5.4B) demonstrates that a significant proportion of alternative splicing events (~10-20%) are novel in each of the datasets. This reflects the underlying diversity of the transcriptome of both the pluripotent cells and the neurons derived from them, and is encouraging for alternative splicing analysis: a subset of these novel events are likely to be unique to the A–T cells or specific to a developmental stage. Saturation was assessed by resampling 5%, 10%, 15%, ..., 95% of total alignments, then detecting splice junctions from each subset and comparing them to the GENCODE 17 reference gene model. The current sequencing depth is almost saturated for known junctions, which is discernible by the red curve reaching a plateau at when considering 80-100% of reads in the dataset. Novel junctions continue to be discovered as the depth of sequencing increases.

Figure 5.4B - Junction annotation in all sequenced libraries – comparison of splicing junctions detected in data with annotated splicing junctions in GENCODE 17. Annotated junctions are those for which both the 5’ and 3' splice sites are annotated; completely novel junctions are those for which neither the the 5’ and 3' splice sites are annotated, and partially novel are those for which either the 5' or 3' splice site is annotated, while the other site is not. A significant number of unannotated alternative splicing events are observed in the data.

Figure 5.4C illustrates that sequencing coverage across the gene body is uniform. This signifies that the library preparation method used has not preferentially enriched for shorter transcripts, which in turn enables us to be confident that our differential expression analysis is unbiased and, more critically, alternative splicing analysis is possible. The minor drop in coverage at the 5' end of genes is expected and characteristic of the current TruSeq protocols, and signifies that we may encounter difficulties in attempting to conduct alternative transcription start site analysis, but these challenges should be similar in all of the datasets generated.

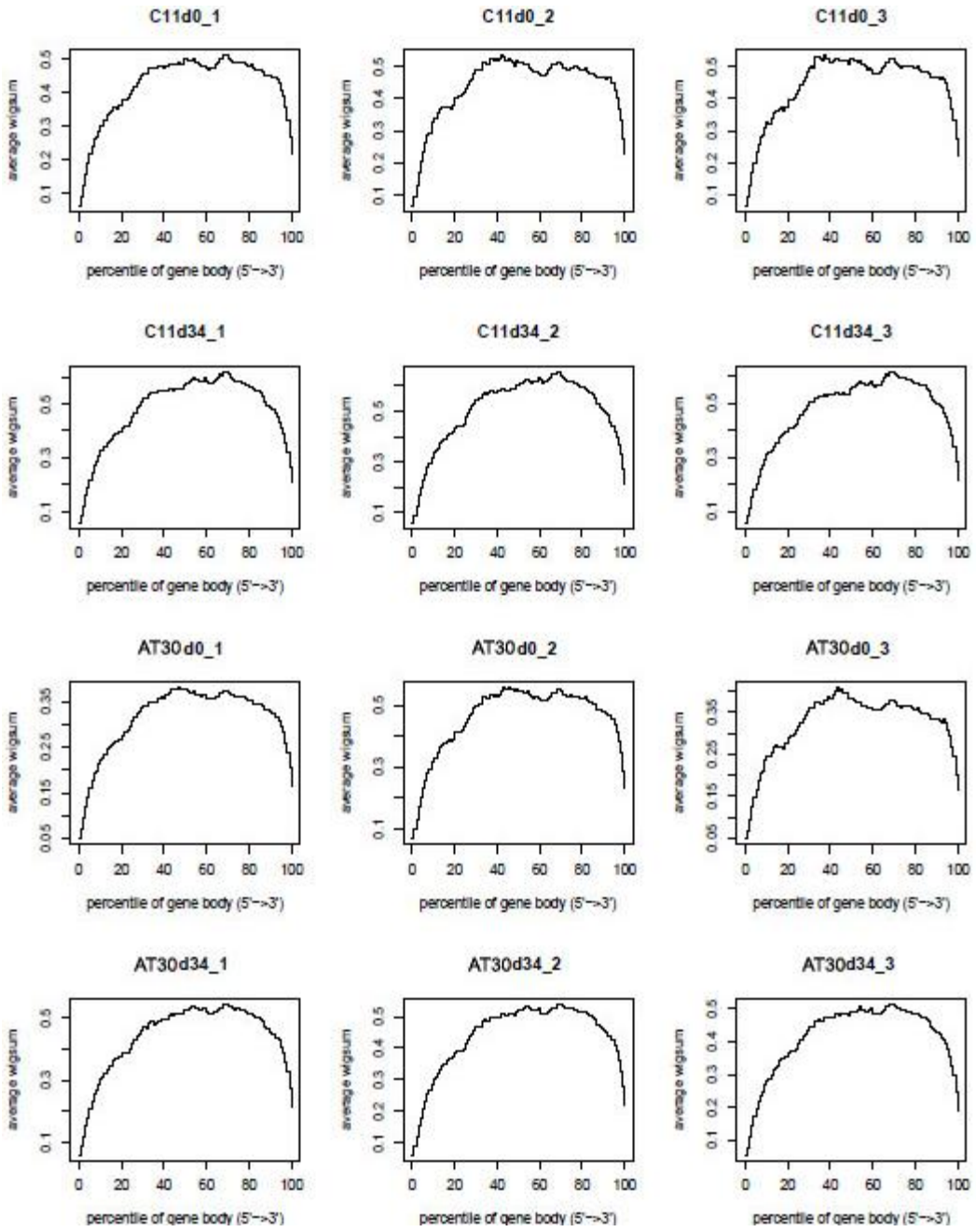

Figure 5.4C - Read coverage over gene body in all sequenced libraries.
Read coverage over gene body in all sequenced libraries was obtained by scaling all transcripts annotated in GENCODE 17 to 100 nt and calculating the number of reads covering each nucleotide position using the geneBody_coverage2.py module of the RSEQC framework). A minor 3' bias in coverage is observed in all sequencing libraries.

Generation of differential expression genelists

Differential expression genelists were generated for three main comparisons; Day 0 vs Day 34 of culture for AT30 (A–T) iPSCs to neurons, Day 0 vs 34 of culture for C11 (Control) iPSCs to neurons, and differential expression between Day 34 AT30 and C11 neurons. Volcano plots show dynamic expression of coding genes in differentiation of A–T and control iPSC-derived neurons. Volcano plots reveal significant (red points: adj. p-value <= 0.01; logFC >= 1) changes in coding gene expression after 34 days of neuronal differentiation betweem AT30 and C11 cerebellar cultures at day 34 (Figures 5.4 D & E respectively). Expected down-regulation of pluripotency-associated genes including *NANOG, SOX2, OCT4, MACC1* and *LIN28A* was observed, as well as upregulation of neuronal markers such as *EN1, HOXB4, HOXB3, ISL1* and *SOX6.*

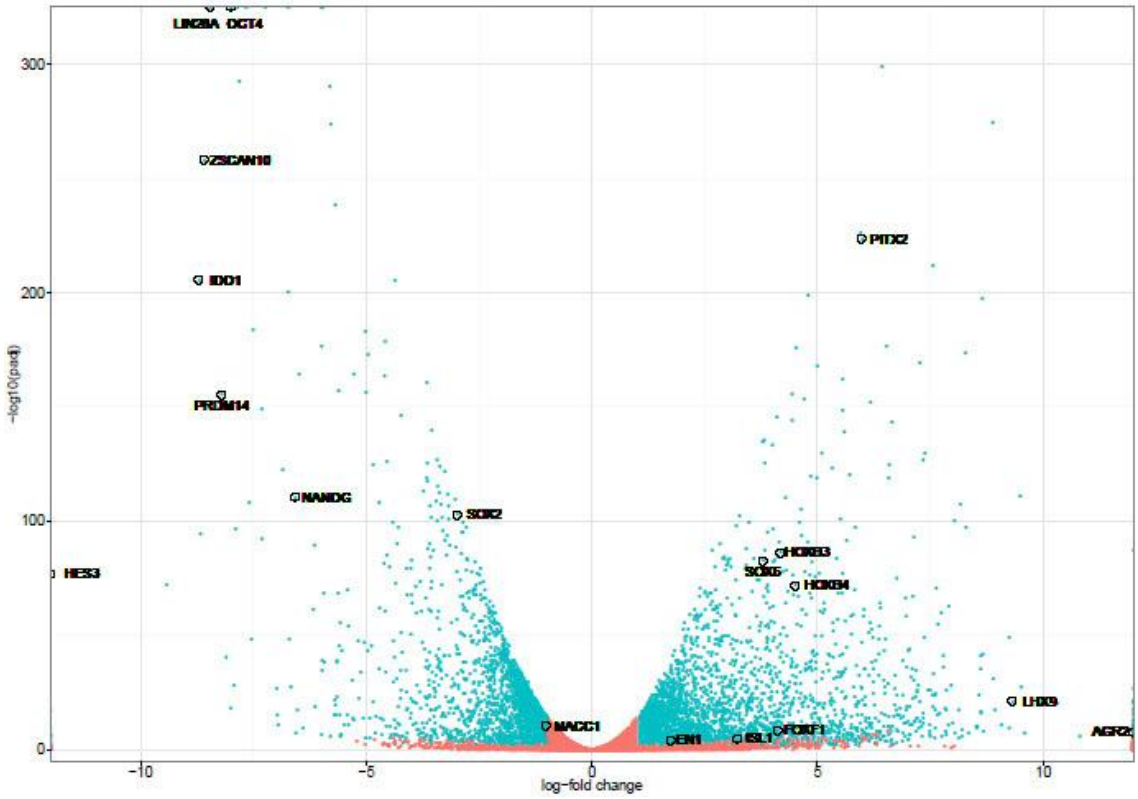

Figure 5.4D – Volcano plot shows distribution of differentially expressed genes in AT30 after 34 days of neural differentiation with log fold change (x-axis) and adjusted p-value (y-axis).

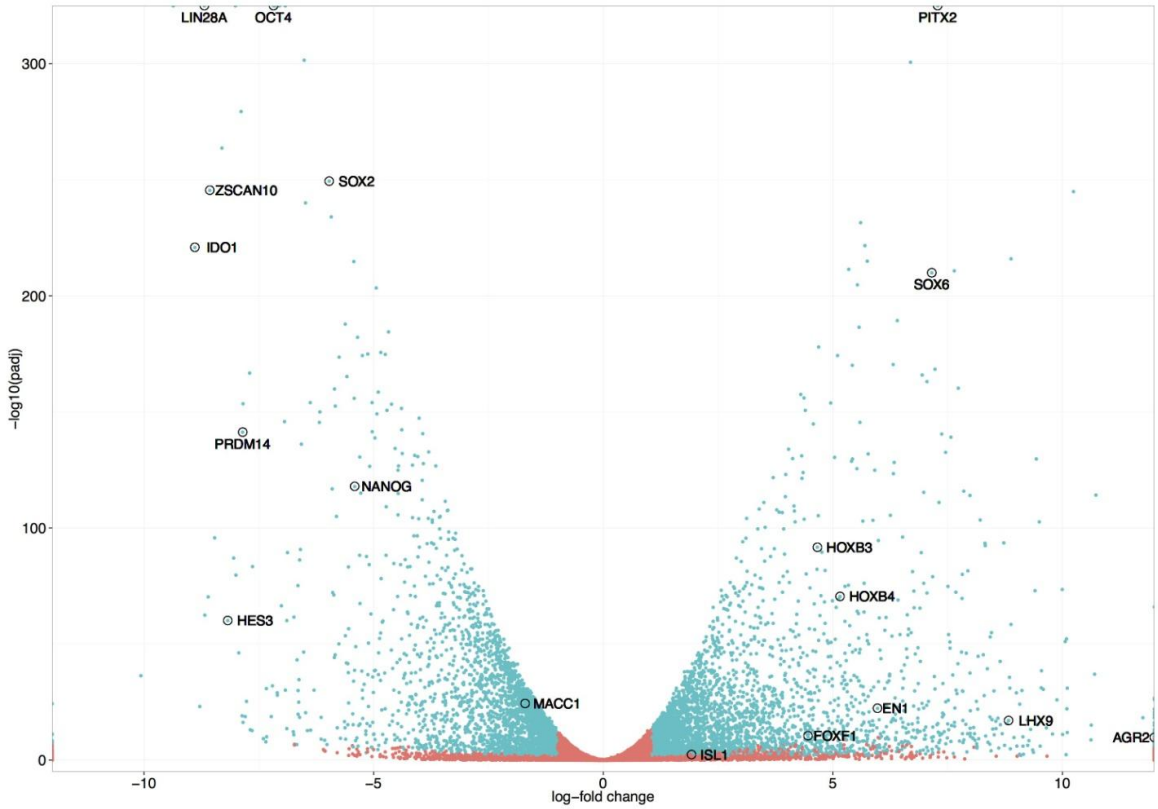

Figure 5.4E – Volcano plot shows distribution of differentially expressed genes in C11 after 34 days of neural differentiation with log fold change (x-axis) and adjusted p-value (y-axis).

Atm transcript during neuronal differentiation

We initially examined levels of *Atm* transcript in control and A–T samples over the course of the neural induction. Interestingly, *Atm* appeared to be downregulated with differentiation (Figure 5.4F). Fewer reads mapped to the *Atm* gene in AT30 at both differentiation time points indicating transcript level was lower/negligible in AT30. AT30 (a.k.a MC3) is a compound heterozygote, with two deletions in the *Atm* cDNA (8368delA and 7570delG; hg19 genomic coordinates chr11:108214045 and chr11:108202224). These are predicted to result in mRNA instability as a result of nonsense-mediated decay, since the stop codon TGA is introduced at cDNA positions 7591-7593 and 8413-8415 (hg19 genomic coordinates chr11:108,202,247-

108,202,249 and chr11:108,214,094-108,214,096, respectively). IGV snapshots demonstrating the presence of these deletions in the RNA-sequencing data are presented in Figures 5.4G and I5.4H.

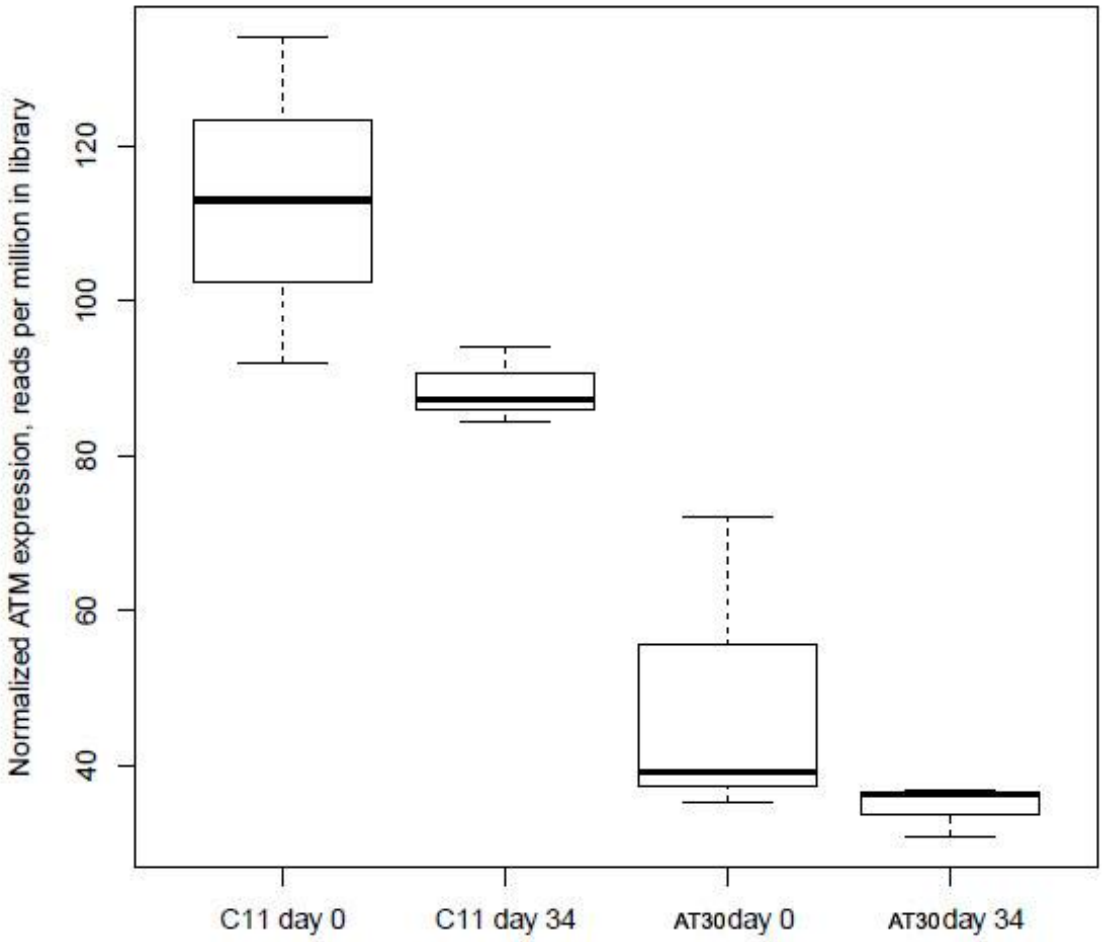

Figure 5.4F - Normalized expression of *Atm* across differentiation time course in control (C11) and AT (AT30) cells.

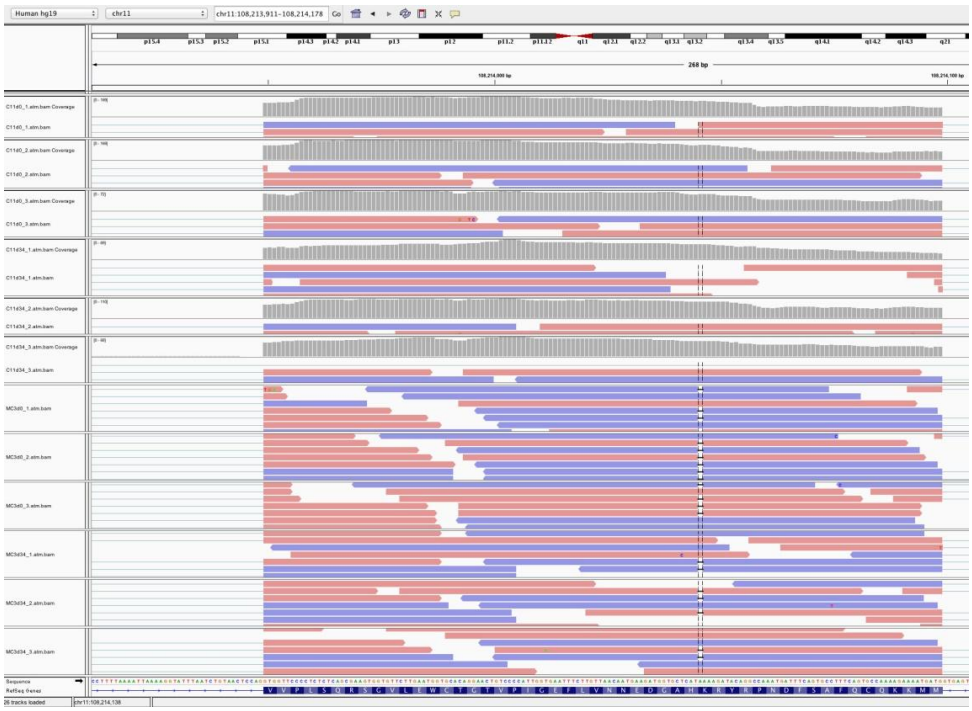

Figure 5.4G - IGV snapshot demonstrating the presence of *Atm* 8368delA mutation in AT30 (lower half of diagram) but absent in C11 controls (upper half of diagram).

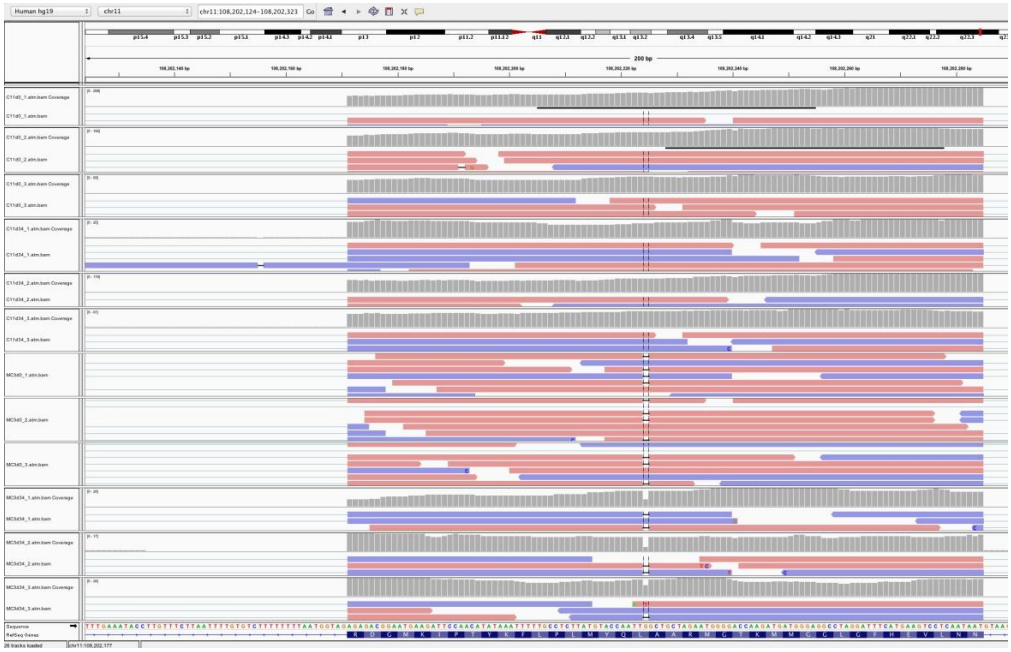

Figure 5.4H - IGV snapshot demonstrating the presence of *Atm* 7570delG mutation in AT30 (lower half of diagram) but absent in C11 controls (upper half of diagram).

Gene ontology analysis after differentiation

Gene ontology analysis was carried out using the DAVID software suite [243]. Biological process, cellular component and molecular function were annotated using GO level 1 for A-T expression data (Day 34 vs 0) (shown below Table 5.5, white background in upper section of table) and control (Day 34 vs 0) (lower section of Table 5.5A, grey background). In both A-T and control annotation sets, GO:0032502 (‘*developmental process’*) was the top pathway identified (P-values 2.03E-41 & 2.80E-34 respectively).

Category	Term	Count	%	PValue
GOTERM_BP_1	GO:0032502~developmental process	1177	23.1	2.03E-41
GOTERM_MF_1	GO:0005488~binding	3655	71.6	5.12E-21
GOTERM_BP_1	GO:0032501~multicellular organismal process	1414	27.7	1.18E-20
GOTERM_BP_1	GO:0022610~biological adhesion	291	5.7	1.11E-15
GOTERM_CC_1	GO:0044421~extracellular region part	367	7.19	4.69E-14
GOTERM_CC_1	GO:0044456~synapse part	121	2.37	5.09E-13
GOTERM_CC_1	GO:0045202~synapse	159	3.11	1.92E-12
GOTERM_BP_1	GO:0016043~cellular component organization	825	16.2	1.14E-10
GOTERM_BP_1	GO:0009987~cellular process	3042	59.6	1.92E-07
GOTERM_BP_1	GO:0065007~biological regulation	2212	43.3	2.19E-07
GOTERM_BP_1	GO:0032502~developmental process	1311	2.24	2.80E-34
GOTERM_MF_1	GO:0005488~binding	4241	7.26	9.69E-19
GOTERM_CC_1	GO:0044421~extracellular region part	418	0.72	2.44E-14
GOTERM_BP_1	GO:0009987~cellular process	3605	6.17	8.23E-13
GOTERM_BP_1	GO:0022610~biological adhesion	309	0.53	8.23E-11
GOTERM_BP_1	GO:0032501~multicellular organismal process	1556	2.66	2.45E-10
GOTERM_CC_1	GO:0045202~synapse	171	0.29	3.06E-10
GOTERM_BP_1	GO:0016043~cellular component organization	947	1.62	4.32E-10
GOTERM_CC_1	GO:0044456~synapse part	117	0.2	5.36E-07
GOTERM_BP_1	GO:0048511~rhythmic process	66	0.11	1.42E-05

Table 5.5A - Biological process, cellular component and molecular function were annotated using GO level 1. A-T (white background) and Control (grey background).

PANTHER phylogeny-aware ontologies were performed and are shown in Table 5.5B. Again '*Developmental processes*' was the top-most hit in both cases (P-values 1.72E-30 & 6.43E-14 respectively). Also present in the top five pathways were '*Ectoderm development'* and *'Neurogenesis'* indicating enrichment for primitive neuronal cells. We noted the A-T dataset to generally display a greater enrichment for processes pertaining to neuronal development.

Category	Term	Count	%	PValue
PANTHER_BP_ALL	BP00193:Developmental processes	778	15.2	1.72E-30
PANTHER_BP_ALL	BP00246:Ectoderm development	306	5.99	8.22E-27
PANTHER_BP_ALL	BP00199:Neurogenesis	270	5.29	2.69E-25
PANTHER_MF_ALL	MF00178:Extracellular matrix	162	3.17	4.37E-13
PANTHER_BP_ALL	BP00274:Cell communication	419	8.21	2.47E-12
PANTHER_BP_ALL	BP00166:Neuronal activities	222	4.35	3.42E-11
PANTHER_BP_ALL	BP00167:Synaptic transmission	124	2.43	1.04E-10
PANTHER_BP_ALL	BP00124:Cell adhesion	226	4.43	8.13E-10
PANTHER_MF_ALL	MF00040:Cell adhesion molecule	156	3.06	9.13E-10
PANTHER_MF_ALL	MF00024:Ion channel	140	2.74	5.88E-08
PANTHER_BP_ALL	BP00193:Developmental processes	800	1.37	6.43E-14
PANTHER_MF_ALL	MF00178:Extracellular matrix	175	0.3	1.01E-11
PANTHER_BP_ALL	BP00199:Neurogenesis	253	0.43	2.19E-10
PANTHER_BP_ALL	BP00246:Ectoderm development	281	0.48	3.16E-09
PANTHER_MF_ALL	MF00013:Tyrosine protein kinase receptor	47	0.08	3.49E-08
PANTHER_MF_ALL	MF00241:Protein kinase receptor	59	0.1	5.93E-08
PANTHER_BP_ALL	BP00108:Receptor protein tyrosine kinase signaling pathway	99	0.17	2.28E-07
PANTHER_MF_ALL	MF00040:Cell adhesion molecule	162	0.28	9.05E-07
PANTHER_BP_ALL	BP00274:Cell communication	441	0.75	1.07E-06
PANTHER_MF_ALL	MF00219:Annexin	42	0.07	1.81E-06

Table 5.5B - *PANTHER* phylogeny-aware ontologies at all levels are shown in A-T (white background) and Control (grey background).

Tissue similarity analysis using DAVID UP_tissue module (Table 5.5C) shows that after 34 days of differentiation the expression pattern of both A-T (white background) and control (grey background) was most similar to Brain (P-value of 3.09E-16 & 9.10E-22 respectively). Interestingly, the A-T genelist (AT30/MC3) registered 45.3% similarity to Brain, whereas control cells (C11) scored 4.66%.

Category	Term	Count	%	PValue
UP_TISSUE	Brain	2313	45.3	3.09E-16
UP_TISSUE	Plasma	107	2.1	6.14E-05
UP_TISSUE	Liver	615	12	6.28E-05
UP_TISSUE	Endothelial cell	30	0.59	1.76E-04
UP_TISSUE	Fetal brain	244	4.78	0.00101
UP_TISSUE	Lens epithelium	12	0.24	0.00216
UP_TISSUE	Epithelium	743	14.6	0.00257
UP_TISSUE	Kidney	431	8.44	0.00483
UP_TISSUE	Breast	35	0.69	0.00487
UP_TISSUE	Retinal pigment epithelium	12	0.24	0.00659
UP_TISSUE	Brain	2721	4.66	9.10E-22
UP_TISSUE	Liver	728	1.25	1.58E-06
UP_TISSUE	Epithelium	904	1.55	1.79E-06
UP_TISSUE	Placenta	1126	1.93	8.68E-06
UP_TISSUE	Plasma	118	0.2	2.90E-04
UP_TISSUE	Heart	212	0.36	5.89E-04
UP_TISSUE	Kidney	509	0.87	9.32E-04
UP_TISSUE	Tongue	154	0.26	0.00112
UP_TISSUE	Fetal brain	279	0.48	0.00169
UP_TISSUE	Amygdala	223	0.38	0.0019

Table 5.5C - Tissue similarity analysis (DAVID) using the UP_tissue module shows expression pattern from both A-T (white background) and control (grey background) differentiated cells most closely resembles Brain.

In each case while Brain was the most significant hit, there appeared to be differences that we interpreted to correspond to how terminally differentiated towards the neuronal lineage these cells had become.

IPA analysis of gene expression data following differentiation of A-T iPSCs

A genelist comprising genes that were differentially expressed between undifferentiated iPSCs and after 34 days of differentiated was uploaded to the Ingenuity Pathway Analysis (IPA) tool. Full reports are available in the appendices section.

IPA-assisted curation of the differentially expressed list of genes yielded a list of the top ten most highly and lowly differentially expressed genes (Table 5.5D). *LRRC4B* (leucine rich repeat containing 4B) is a protein of unknown function that is expressed in the brain and displays a developmentally regulated pattern of expression [246]. *AGR2* (Anterior Gradient Homolog 2) is a proto-oncogene, which is downstream of *Pou5f1* and has roles in migration, differentiation and cell growth. *NNAT* (Neuronatin) regulates segment identity and ion channels during hindbrain development and may also be involved with positive regulation of insulin secretion as well as formation and maintenance of the nervous system. Coexpression of neuronatin splice forms was shown to promote growth of medullablastoma, a granule cell progenitor tumour [246]. Kikyo et al. showed that disruption to neuronatin expression resulted in perturbation of cerebellar foliation in mice [247]. *RBP2* (Retinol binding protein-2) is a histone demethylase implicated in differentiation through chromatin modification and regulation of the cell cycle [248]. *OR51E2* (Olfactory receptor 51E2) is a G-protein-coupled receptor implicated in prostate cancer [249]. *Pln* (Phospholamban) is a substrate for PKA and involved in controlling Ca^{2}+ transport ATPase activity. *CLDN8* (Claudin 8) is a member of the claudin protein family, and is a component of the tight junction complex. *CARTPT* (Cocaine and amphetamine regulated transcript) is a neurotransmitter with roles in energy homeostasis and brain development and is an afferent marker of the developing cerebellum [250]. *IFI44* (Interferon induced Protein 44) is a non cell-type specific microtubule-associated protein. *KRT4* (Keratin 4) encodes Keratin type II, cytoskeletal 4.

Amongst the list of top downregulated transcripts were *Hes3* (a regulator of stem cell pluripotency through the Notch signaling pathway) [251], *Ventx* (displays NANOG-like activity in mammalian embryos [252]) and *Zscan10* (cell-specific transcription factor required to maintain pluripotency in ES cells***).*** Ido1 ***(***Indoleamine 2,3-Dioxygenase 1) is an enzyme that

catalyzes tryptophan catabolism to N-formyl-kynurenine. *Cldn10* (Claudin 10) encodes a claudin family member involved in tight junction complex formation. *LIN28A* is a key pluripotency factor involved in stem cell maintenance and growth. *Prdm14* (PR domain containing 14) encodes a protein with putative histone methyltransferase speculated to affect cell pluripotency by suppressing the expression of genes involved with differentiation. *Pou5f1* (*Oct4*) is one of the main drivers of pluripotency and essential for stem cell maintenance. *Dppa4* (developmental pluripotency associated 4) is a nuclear factor associated with active chromatin and involved with early embryogenesis and pluripotency. *Nmrk2* (nicotinamide riboside kinase 2) is a broadly expressed enzyme with ribosylnicotinamide kinase activity.

To summarize, the top ten most highly expressed transcripts were largely all associated with neuronal differentiation and maintenance, and the top ten lowest expressed transcripts were associated with pluripotency, grossly validating the notion that AT30 had exited the pluripotent state and acquired a neuronal phenotype.

Top Molecules	
Molecules (up)	**Exp. Value**
LRRC4B	11.757
AGR2	10.388
NNAT	10.05
RBP2	10.022
OR51E2	9.994
PLN	9.928
CLDN8	9.89
CARTPT	9.851
IFI44	9.736
KRT4	9.5

Molecules (down)	**Exp. Value**
HES3	-10.8
VENTX	-8.749
ZSCAN10	-8.597
IDO1	-8.597
CLDN10	-8.565
LIN28A	-8.502
PRDM14	-8.262
POU5F1	-8.04
DPPA4	-7.924
NMRK2	-7.864

Table 5.5D – List of Top Molecules that are upregulated (upper section) and downregulated (lower section) between A–T iPS (AT30) at Day 0 and 34

Of particular interest was defining the shift in transcription that had occurred during the 34 day differentiation process. We hypothesized we would observe a downregulation of genes involved in pluripotency and upregulation of processes involving anterior-posterior patterning and neuronal specification. As expected, amongst the top pathways identified by IPA analysis were '*Transcriptional Regulatory Network in Embryonic Stem Cells'* (p-value 7.16E-9), '*Cellular Development - Differentiation of neurons*' (p value 1.35E-11. 70), '*Embryonic development – Development of body axis*' (p-value of 8.14E-28), and '*Embryonic development - Development of rhombencephalon*' (p-value 4.94E-10).

Figure 5.5A illustrates the '*Transcriptional Regulatory Network in Embryonic Stem Cells*' annotated pathway, featuring members of the pluripotency network *Oct4, Sox2, Nanog* as well as *Foxd3,* the forkhead transcription factor required for maintenance of pluripotency [253], which are all downregulated. Also noted is upregulation of *Cx36, L1cam* involved with Neurogenesis and *Atbf1, Hand, Otx1, Meis1, Isl1* and *Pax6,* all involved with ectodermal differentiation.

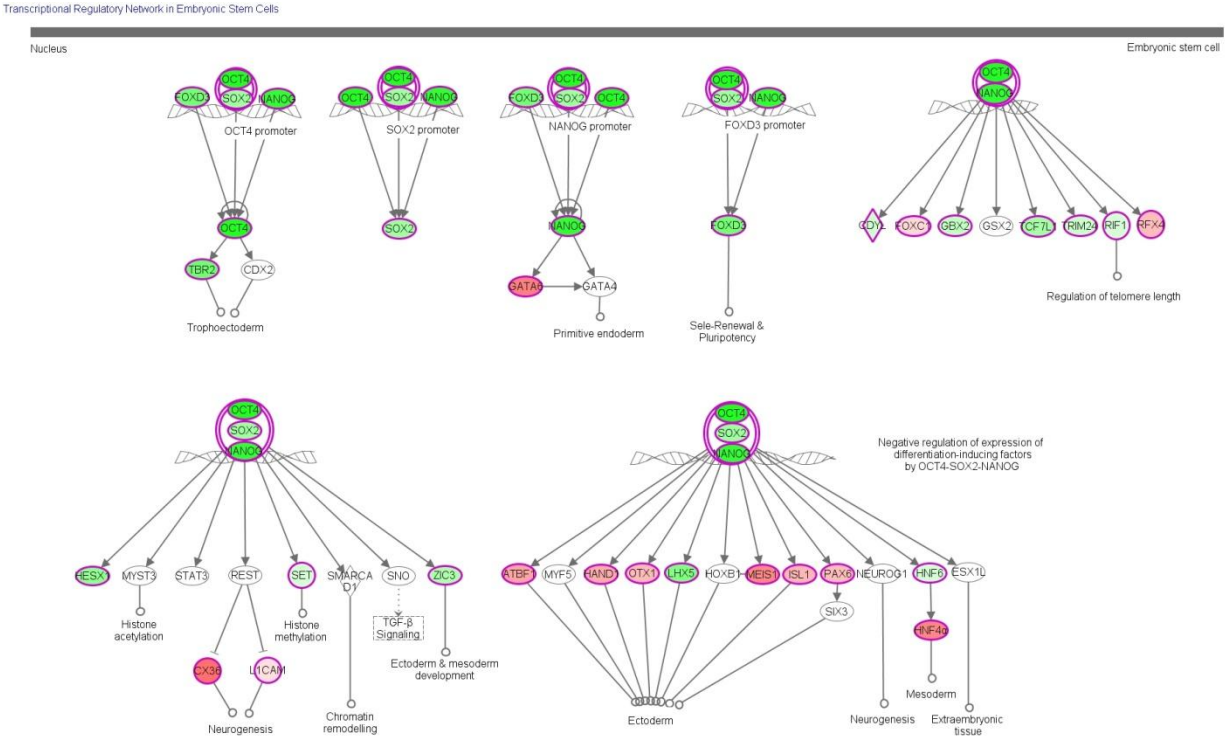

Figure 5.5A – '*Transcriptional Regulatory Network in Embryonic Stem Cells*.' (P-value 7.16E-9). Genes colored red are upregulated, genes colored green are downregulated.

Figure 5.5B depicts a number of genes annotated to the process of '*Cellular Development - Differentiation of neurons*'. Unsurprisingly, an extensive number of these genes are upregulated after 34 days of neural induction. Of particular note is the moderate expression of mid-hind brain marker *En1* (lower left), strong expression of the rhombic lip progenitor marker *Atoh1 (Math1)* (pictured lower middle of figure) and downregulation of *Otx2* (lower left hand corner of figure), a marker of anterior neuronal cells. We observed strong expression of *Dcx* (Doublecortin, middle right-hand side of figure), a microtubule associated marker of immature migrating neurons [254]. *Nf1a* (Nuclear factor 1A) exhibited upregulation – this gene is involved with co-ordination of granule cell development through regulation of cell adhesion molecules [255]. We noted the negative expression of *Lhx5,* a factor involved with forebrain specification. Similarly we could not detect expression of genes characteristic of other brain regions such as *Hb9* (spinal motor neurons) or *Nkx2-2* (motor neurons).

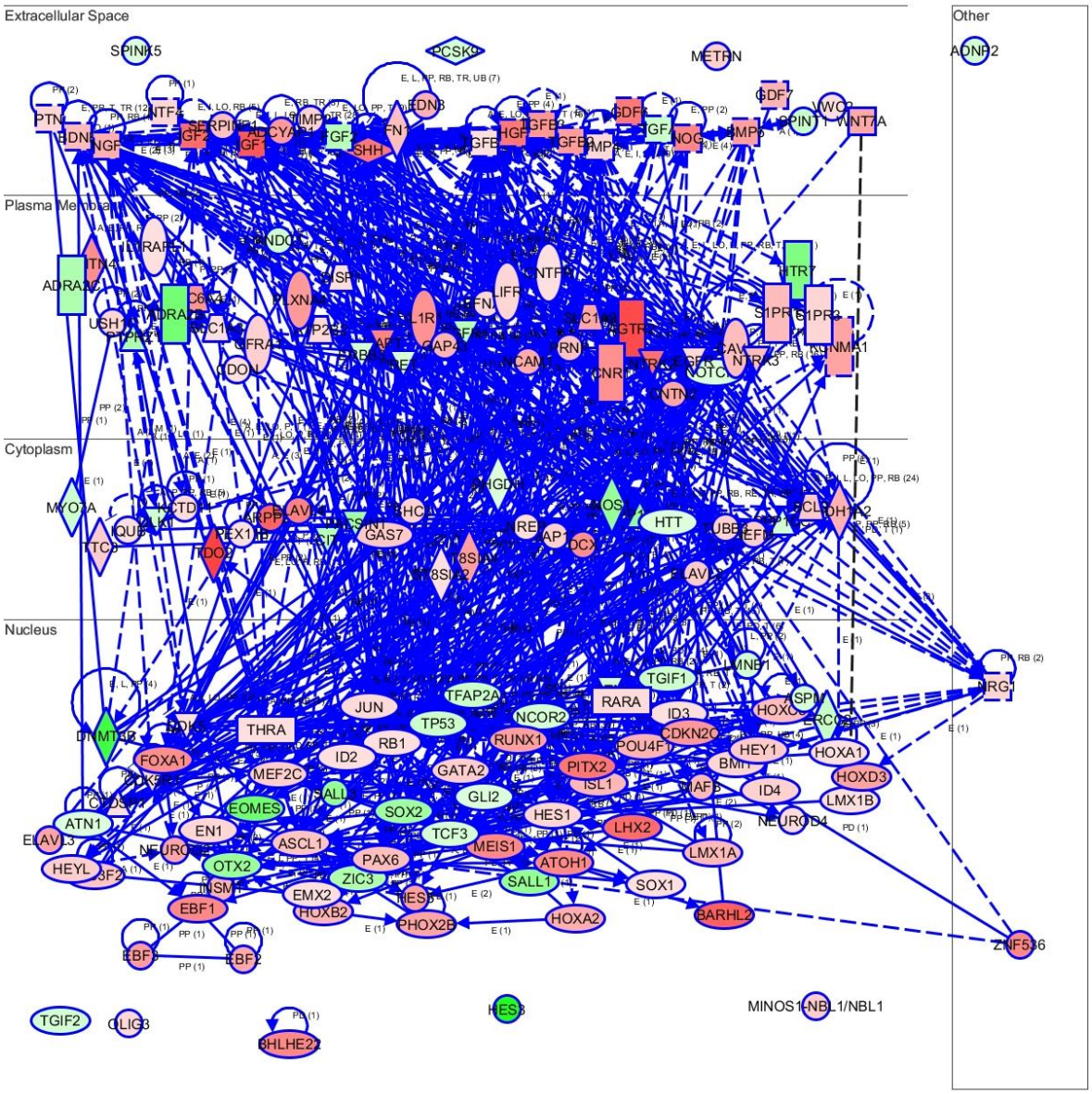

Figure 5.5B – '*Cellular Development - Differentiation of neurons*' (P-value 1.35E-11). Genes colored red are upregulated, genes colored green are downregulated.

We observed extensive activity in regulatory networks annotated to '*Embryonic development – Development of body axis*' (Figure 5.5C). This led us to examine the expression of members of the *Hox* gene family [256], a set of transcription factors that regulate development through controlling segment identity and positional specification (Table 5.5E). *Hoxa2*, which is involved in developmental patterning of the hindbrain [257] was significantly upregulated. Similarly,

expression levels of *Hoxb3* and *Hoxb4*, markers of caudal neural stem cells [245] were significantly higher after 34 days of neural induction.

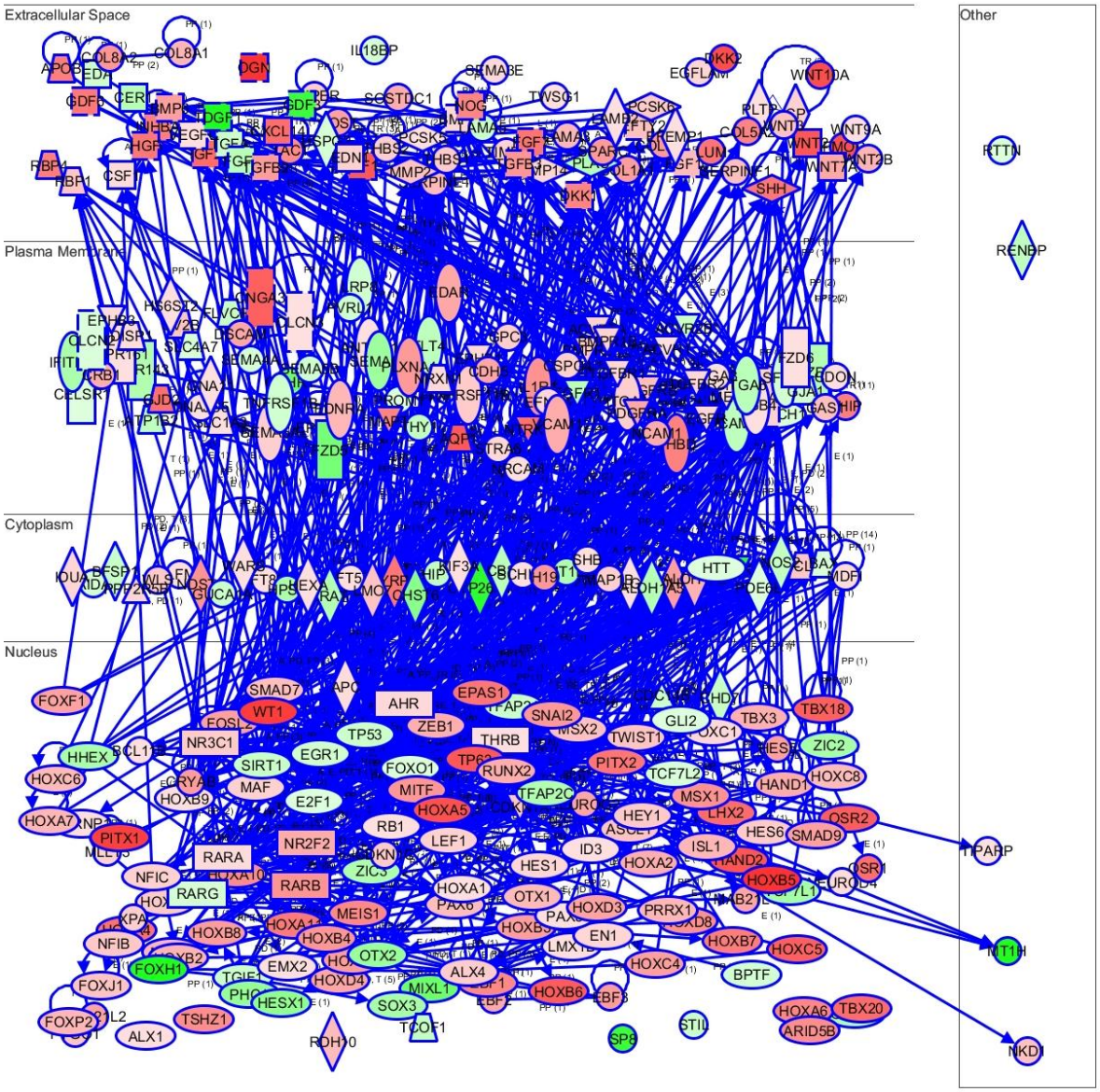

Figure 5.5C – '*Embryonic development – Development of body axis'* (P-value of 8.14E-28). Genes colored red are upregulated, genes colored green are downregulated.

Gene ID	LogFC	Gene
ENSG00000105991	1.145427	HOXA1
ENSG00000253293	4.966813	HOXA10
ENSG00000005073	5.762732	HOXA11
ENSG00000106031	7.749493	HOXA13
ENSG00000105996	3.438338	HOXA2
ENSG00000105997	4.211327	HOXA3
ENSG00000197576	6.109767	HOXA4
ENSG00000106004	7.522661	HOXA5
ENSG00000106006	5.199186	HOXA6
ENSG00000122592	3.124284	HOXA7
ENSG00000078399	2.271848	HOXA9
ENSG00000253552	4.29586	HOXA-AS2
ENSG00000254369	1.198842	HOXA-AS3
ENSG00000173917	3.209529	HOXB2
ENSG00000120093	4.166593	HOXB3
ENSG00000182742	4.501958	HOXB4
ENSG00000120075	8.942241	HOXB5
ENSG00000108511	7.030623	HOXB6
ENSG00000260027	5.628308	HOXB7
ENSG00000120068	4.291911	HOXB8
ENSG00000170689	1.17242	HOXB9
ENSG00000198353	4.102079	HOXC4
ENSG00000172789	6.863063	HOXC5
ENSG00000197757	2.993665	HOXC6
ENSG00000037965	2.883769	HOXC8
ENSG00000180806	3.325562	HOXC9
ENSG00000128652	3.971744	HOXD3
ENSG00000170166	3.853519	HOXD4
ENSG00000175879	4.788749	HOXD8
ENSG00000224189	3.138314	HOXD-AS1

Table 5.5E – List of HOX genes and log-fold expression values differentially regulated between day 0 and 34 of neural differentiation in A–T iPS cells (AT30).

Of major interest, '*Embryonic development - Development of rhombencephalon*' (Figure 5.5D) was one of the top differentially regulated pathways (P-value 4.94E-10). Expression of *Dio3* (thyroid hormone-inactivating type 3 deiodinase - top left of figure), an enzyme belonging to the iodothyronine deiodinase family was detected. *Dio3* is expressed within the embryonic and neonatal mouse cerebellum. *Dio3* knockout mice show reduced cerebellar foliation and increased disappearance of the external germinal layer with premature expansion of the molecular layer [258]. *Dner* (Delta/Notch-Like EGF Repeat Containing – top middle of figure) is a transmembrane protein, specific to neurons, which mediates Notch signaling through cell to cell interactions. *Dner* was recently shown to be essential for precise cerebellar development, where it is abundantly expressed in Purkinje and granule cells [259]. Mice lacking *Dner* display impaired cerebellar functionality [260]. *Unc5c* (Unc-5 Homolog C) belongs to the family of Netrin receptors. Netrins are secreted proteins that are involved with directing axon extension and migration during neural development. Recent results show that Unc5c played a role in dorsal guidance of axons in the developing hindbrain and that perturbation of *Unc5c* disrupted long-range dorsal guidance of inferior olivary and pontine axons within the cerebellum [261]. *Agtr2* (angiotensin II receptor, type 2 - top left of figure) that was highly expressed has been associated with a role in brain development and cognitive function. *Agtr2* was found largely expressed in the cerebellum [262]. We detected strong expression of *Zic1* and *Zic4* (Zic family members 1&4 – lower right hand side of figure). The *Zic* genes encode zinc finger proteins and are highly restricted to cerebellar granule cells and their precursors, disruption of which leads to postnatal ataxia arising from cerebellar hypoplasia [263]. Although not annotated to this network we also detected a 2.295 log fold-change of *Clbn1* (Cerebellin 1), a neuropeptide involved with synaptic integrity and plasticity in the cerebellum [264]. *Gbx2* expression was extinguished at this stage, in keeping with reports in the literature regarding its initial early involvement in inducing a self-organizing signaling centre [265, 266]. We noted the robust expression of the *Reelin* gene, a gene well characterized in cerebellar development and suspected to be downsteam of *Pax6 [267]*. Reelin is an extracellular matrix glycoprotein that regulates cerebellar corticogenesis [268]. Similarly we noted overexpression of *Shh* (top right of figure), a morphogen and critical orchestrator of cerebellar formation [269].

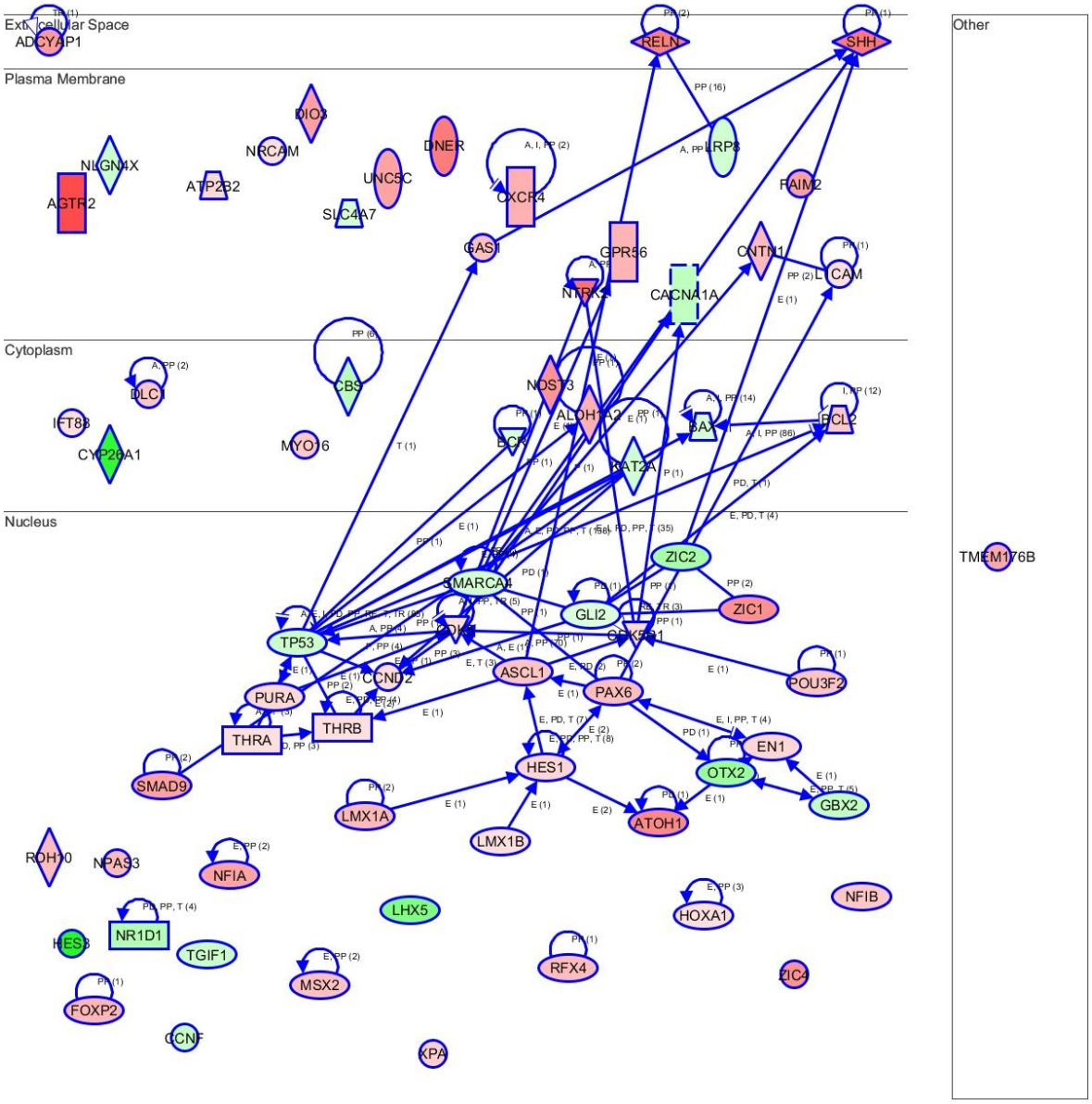

Figure 5.5D – '*Embryonic development - Development of rhombencephalon', P*-value 4.94E-10. Genes coloured red are upregulated, genes coloured green are downregulated.

To further understand what impact the loss of ATM might have in the role of commitment towards cerebellar neurons, differential expression data from between day 0 and 34 samples was overlaid on a more extensively mapped set of genes predicted to interact with ATM (not shown). The most heavily upregulated gene was *Hgf (*Hepatocyte growth factor), downsteam of ATM

and known to have a neuroprotective role in the regulation of apoptosis in cerebellar granule cells [270].

IPA analysis of gene expression data following differentiation of control iPSCs

We next examined differential expression between control (C11) iPS cells after 34 days of neural induction. Pathway report is available in Appendices.

Differential expression analysis revealed a list of the top ten most highly up and down -regulated molecules (Table 5.6A). The top most upregulated transcript was *Angptl1* (Angiopoietin-related 1), a growth factor and member of the VEGF family. Additonally, *Agr2* (Anterior Gradient Homolog 2), a proto-oncogene, which is downstream of *Pou5f1* and has roles in migration, differentiation and cell growth was the molecule second most upregulated (AGR2 also appeared in the top ten list for AT30). *C6* (Complement component 6) is a part of the membrane attack complex that is involved in the adaptive and innate immune response. Interestingly, members of the complement pathway have been implicated in regulation of neurogenesis [271]. *Cfh* (Complement factor H) is also a member of the complement family and was elevated more than 11 log-fold. *Casp4* (Caspase 4) is a well-characterized enzyme involved with apoptosis, cell migration and the inflammatory response. *Nr1h4* (Nuclear receptor subfamily 1, group H, member 4) known to interact with the Retinoid acid receptors [272]. *Agtr2* (Angiotensin II receptor type 2) regulates neuronal apoptosis. *Scrg1* (Scrapie responsive gene one) is distributed primarily in the CNS, where it associates with members of the neuronal secretory pathways. CF1 is another member of the complement family that regulates complement activation by cleaving C3b and C4b. *Ogn* (Osteoglycin) codes for a protein well known in bone formation that is also expressed in the brain.

Amongst the list of top downregulated transcripts was *Wnt8a*, (Wingless –related MMTV integration site 8A), a gene known to be involved with embryonic pattern formation. *Tdgf1 (*Teratocarcinoma-derived growth factor 1) encodes an epidermal growth factor-related protein essential for embryonic development. *Zscan10* (a cell-specific transcription factor required to maintain pluripotency in ES cells – also featured in the top 10 downregulated genes in AT30*).*

Ido1 *(*Indoleamine 2,3-Dioxygenase 1) is an enzyme that catalyzes tryptophan catabolism to N-formyl-kynurenine. *LIN28A* is a key pluripotency factor involved in stem cell maintenance and growth and was also featured in the top 10 downregulated genes in AT30. *Hes3* (a regulator of stem cell pluripotency through the Notch signaling pathway) [251], *Prdm14* (PR domain containing 14) encodes a protein with putative histone methyltransferase speculated to affect cell pluripotency by suppressing the expression of genes involved with differentiation. *Dppa2 (*developmental pluripotency associated 2) is a nuclear factor expressed specifically by pluripotent cells. *Usp44* (Ubiquitin specific peptidase 44) is a negative regulate of H2B ubiquitylation known to undergo downregulation during differentiation. *Prdm14* (PR domain containing 14) is a member of the pluripotency network. *Lect1* (Leukocyte cell derived Chemotaxin 1) is a glyosylated transmembrane protein with known roles in self-renewal and pluripotency.

In summary, and consistently with the top ten lists from AT30 analysis, the top ten most highly expressed transcripts after 34 days of neural induction in control iPS line C11 were largely all associated with neuronal differentiation and maintenance, and the top ten lowest expressed transcripts were associated with pluripotency, again grossly validating the notion that control iPS cells had exited the pluripotent state and acquired a neuronal phenotype.

Top Molecules	
Molecules (Up)	**Exp. Value**
ANGPTL1	12.11
AGR2	11.874
C6	11.349
CFH	11.163
CASP4	10.923
NR1H4	10.887
AGTR2	10.83
SCRG1	10.812
CFI	10.493
OGN	10.262
Molecules (Down)	**Exp. Value**
WNT8A	-9.438
TDGF1	-9.357
ZSCAN10	-8.743
LIN28A	-8.741
HES3	-8.711
IDO1	-8.682
DPPA2	-8.403
USP44	-8.043
PRDM14	-8.039
LECT1	-8.033

Table 5.6A – List of Top Molecules that are upregulated (upper section) and downregulated (lower section) between undifferentiated Control iPS (C11) at day 0 and 34 of neural induction.

Consistent with AT30, we could detect statistically significant differential regulation of pathways involved with self-renewal and pluripotency; including '*Transcriptional control of*

pluripotency' (Figure 5.6A, P-value 6.22E-4). Figures 5.6A illustrates downregulation of pluripotency factors including *Sox2, Sall4, Oct4, Nanog* and concordant upregulation of factors involved with differentiation including *Activin A, Noggin, Lefty, Meis1 and Gata4.*

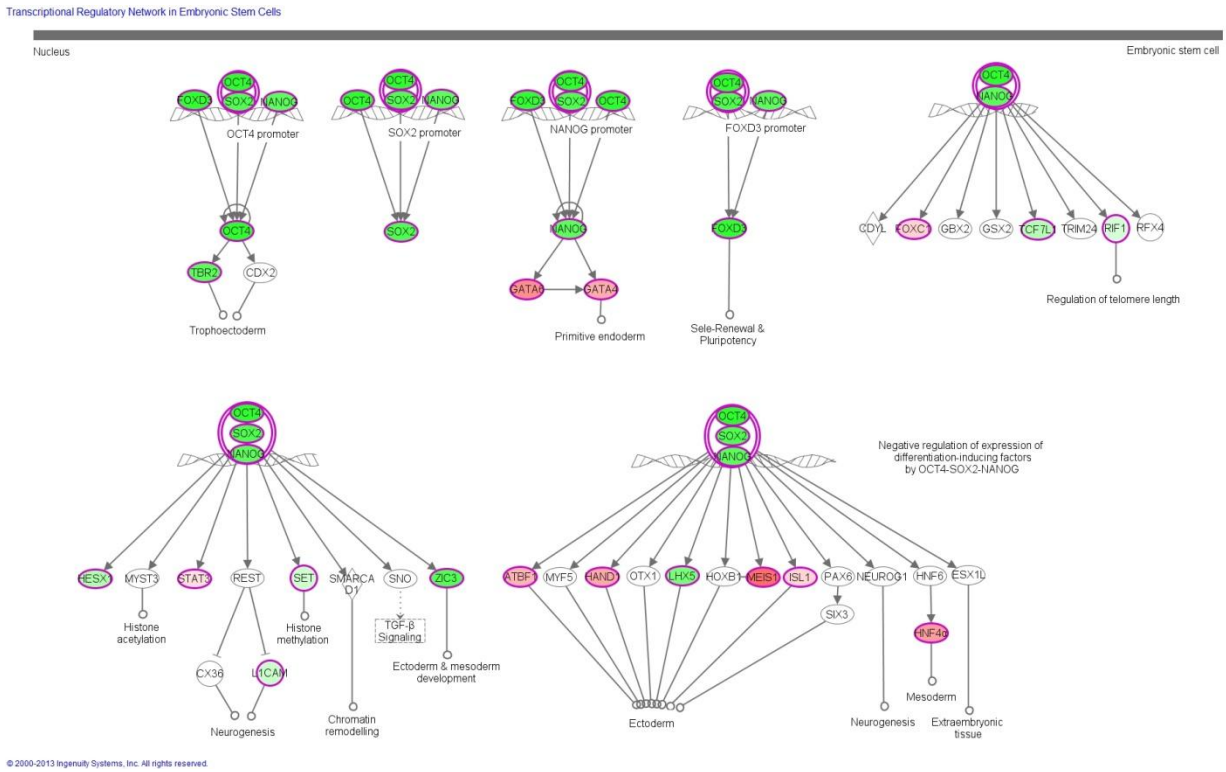

Figure 5.6B – '*Transcriptional control of pluripotency*' pathway. P-value 6.22E-4. Genes colored red are upregulated, genes colored green are downregulated.

As with analysis of AT30, IPA identified '*Embryonic development – Development of body axis'* as being a significantly over-represented network (Figure 5.6B, P-value 3.57E-19) in the C11 transcriptome after 34 days of differentiation. We again examined the expression of members of the *Hox* family (Table 5.6B). While we noticed highly similar levels of *Hox* gene expression, (Figure 5.6C) *Hoxa2* (involved with hindbrain patterning) expression was noticeably absent in comparison to AT30. Despite this, we noticed comparable levels of *Hoxb3* and *Hoxb4.* Given the role of *Hox* genes in anterior-posterior patterning and specification, these data suggest that after 34 days of neural differentiation, C11 and AT30 existed in slightly different developmental space.

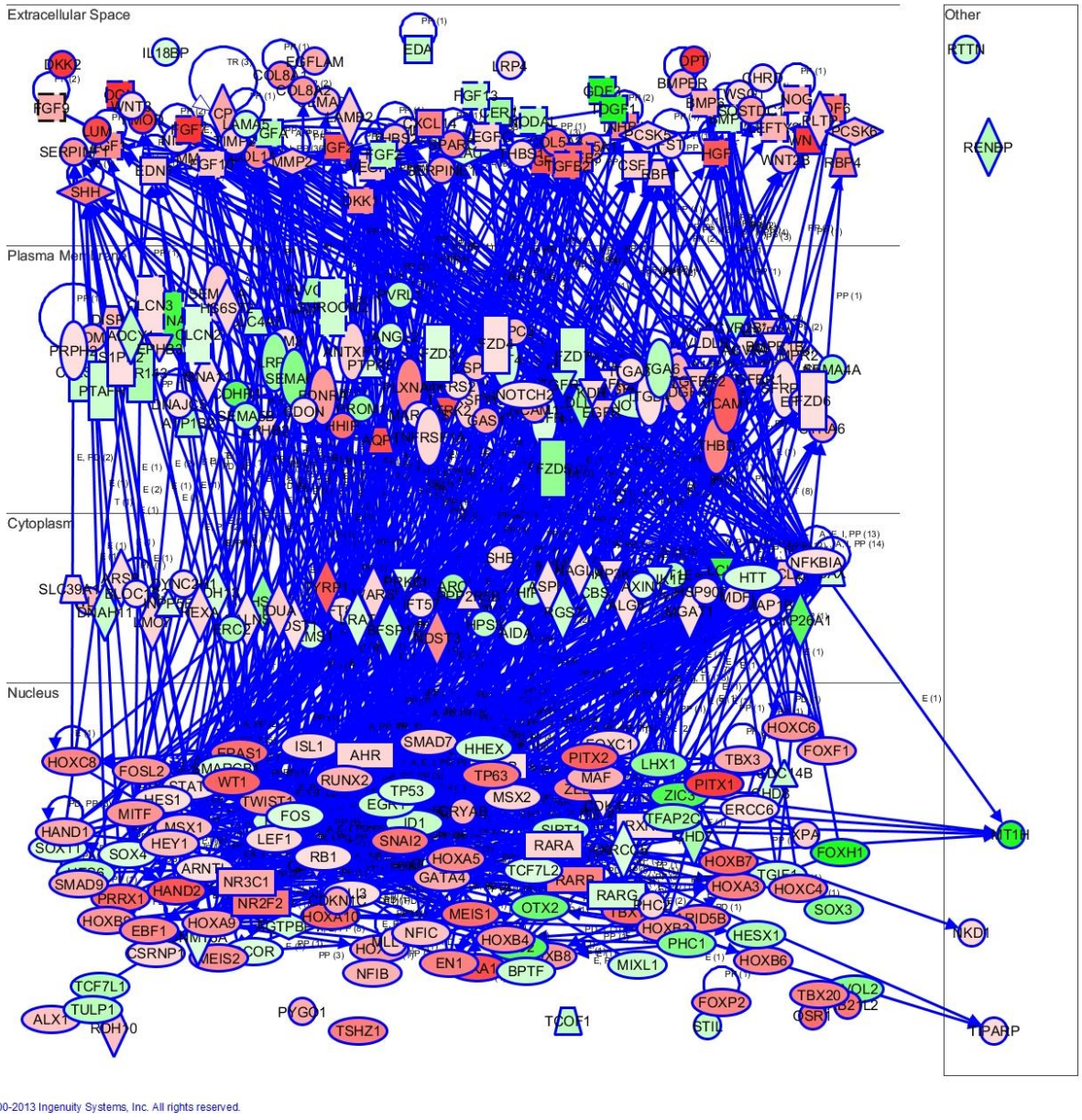

Figure 5.6B – '*Embryonic development – Development of body axis'* P-value 3.57E-19. Genes colored red are upregulated, genes colored green are downregulated.

Gene ID	LogFC	Gene
ENSG00000253293	7.06931	HOXA10
ENSG00000005073	8.252914	HOXA11
ENSG00000106031	6.558066	HOXA13
ENSG00000105997	5.920035	HOXA3
ENSG00000106004	5.390647	HOXA5
ENSG00000078399	4.650409	HOXA9
ENSG00000253552	6.67837	HOXA-AS2
ENSG00000159184	7.448134	HOXB13
ENSG00000173917	4.499966	HOXB2
ENSG00000120093	4.78546	HOXB3
ENSG00000182742	5.042186	HOXB4
ENSG00000108511	5.456975	HOXB6
ENSG00000260027	7.01179	HOXB7
ENSG00000120068	4.669538	HOXB8
ENSG00000170689	4.715488	HOXB9
ENSG00000233101	3.409145	HOXB-AS3
ENSG00000198353	5.320818	HOXC4
ENSG00000197757	4.965382	HOXC6
ENSG00000037965	5.60361	HOXC8

Table 5.6B - List of *Hox* genes and log-fold expression values differentially regulated between day 0 and 34 of neural differentiation in control iPS cells (C11).

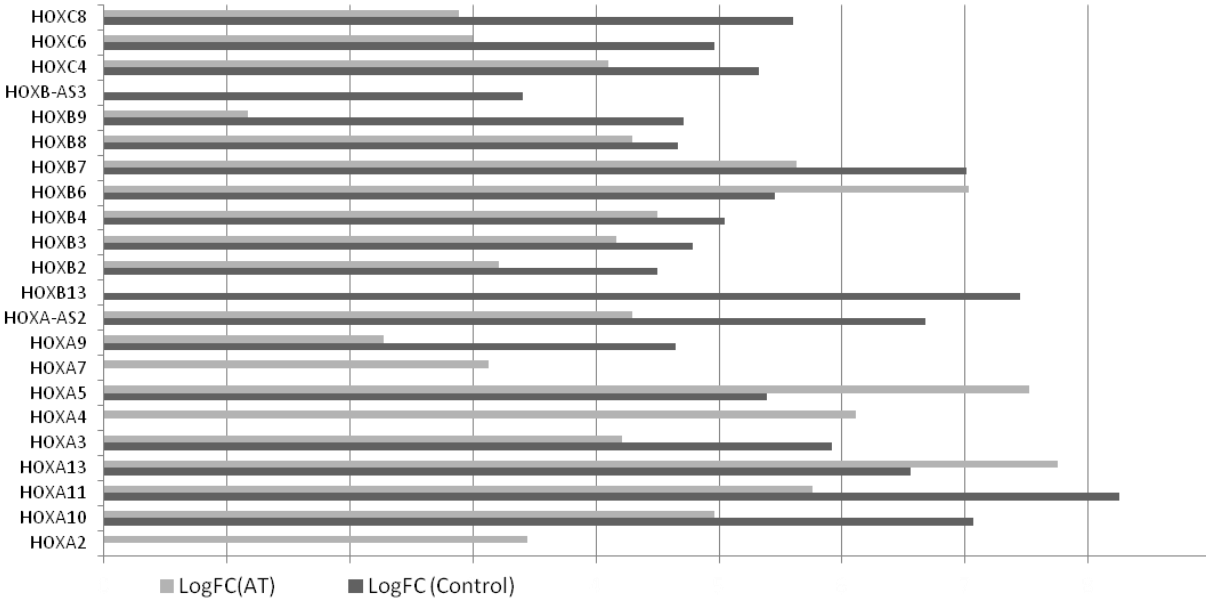

Figure 5.6C – Graph depicting relative expression (Log fold-change between undifferentiated iPS and day 34 differentiated neurons) of members of the *Hox* family.

IPA analysis again showed '*Embryonic development – Development of brain'* as a significantly altered pathway (Figure 5.6D, P-value 1.54E-8). Consistent with AT30 results we observed negative expression of *Lhx5* and *Otx2*, genes involved with forebrain and mid/forebrain specification, respectively (lower right-hand side of figure 5.6D). Upregulation of the mid-hindbrain specific transcription factor *En1* was noted, however expression of *Atoh1 (Math1)* was noticeably absent, providing further evidence that although differentiated simultaneously using identical media formulations, AT30 and C11 showed some differences in end-state. Using IPA we examined the expression patterns of a number of molecules upstream of *Atoh1* (Figure 5.6E) that were highly similar with the exception of *Hes5*, the basic helix-loop helix notch effector gene. Interestingly a recent study showed that knockdown of ATM homologue DNA-PK resulted in upregulation of *Lmx1a* activity resulting in biased regional specific neuronal specification [273].

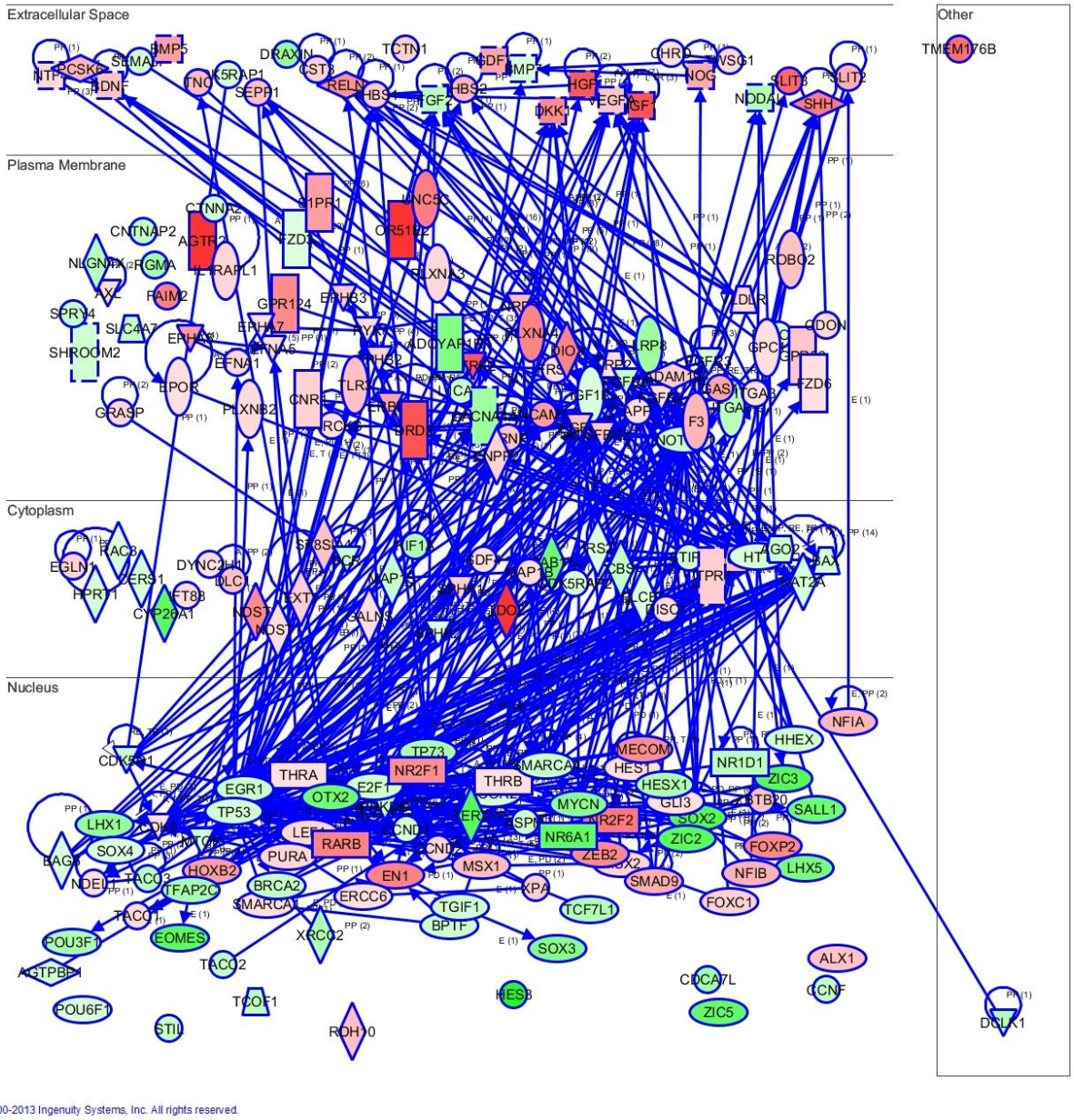

Figure 5.6D – '*Embryonic development – Development of brain'* P-value 1.54E-8. Genes colored red are upregulated, genes colored green are downregulated.

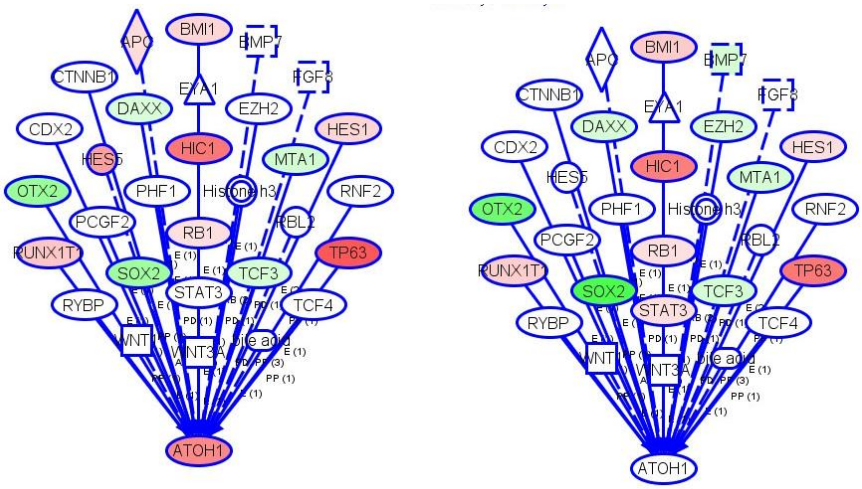

Figure 5.6E - Molecules upstream of ATOH1. Expression values are shown for AT30 (left) and C11 (right)

Hierarchical clustering and further characterisation

Both IPA (Figures 5.5 & 5.6) and DAVID gene ontology (Tables 5.5A, B & C) analysis supported the theory that both C11 and AT30 cells had lost their pluripotent phenotype and acquired neuronal fates. DAVID gene ontology showed a strong enrichment for genes associated with ectoderm development, neurogenesis, synapse and tyrosine kinase signalling, and tissue similarity analysis showed the list of differentially expressed genes was closest to genes expressed in the brain. IPA analysis supported this assertion and provided the capability to examine specific pathways. For example, '*Embryonic development – Development of Brain,*' was similar in both A-T and control genesets. While the majority of pathways that changed significantly over the course of the differentiation process were conserved between A-T and control, certain differences became apparent. For example A-T neurons showed significant upregulation of genes belonging to the '*Embryonic development - Development of rhombencephalon'* pathway, whilst control neurons did not. We noticed that *Math1* expression was much higher in A-T neurons than control. It became apparent that it would be necessary to define more specifically which developmental space these cells had entered into, before performing comparisons between the two datasets. To this end, we compared our data to a range of existing sequencing and microarray datasets by performing hierarchal clustering of ranked

RPKM values of the Illumina Body map, the Allen Brain Atlas (ABA) early prenatal sample 113 and our iPS-derived neurons. Figure 5.7A shows principal component analysis of DESeq2 variance-stabilized RNA-seq data from undifferentiated iPSCs and from cells after 34 days of differentiation in comparison to a range of Illumina Body map samples. PCA shows that undifferentiated iPSCs (pink/green left-hand side) are highly similar to each other but clearly distinct after 34 days of differentiation (purple/dark green). Samples at this time point were distinct from all tissue samples (upper right-hand corner) but could be seen to be moving in a direction consistent with brain (black, right-hand middle). A bar plot shows the percentage of variance explained by the principal components (Figure 5.7B).

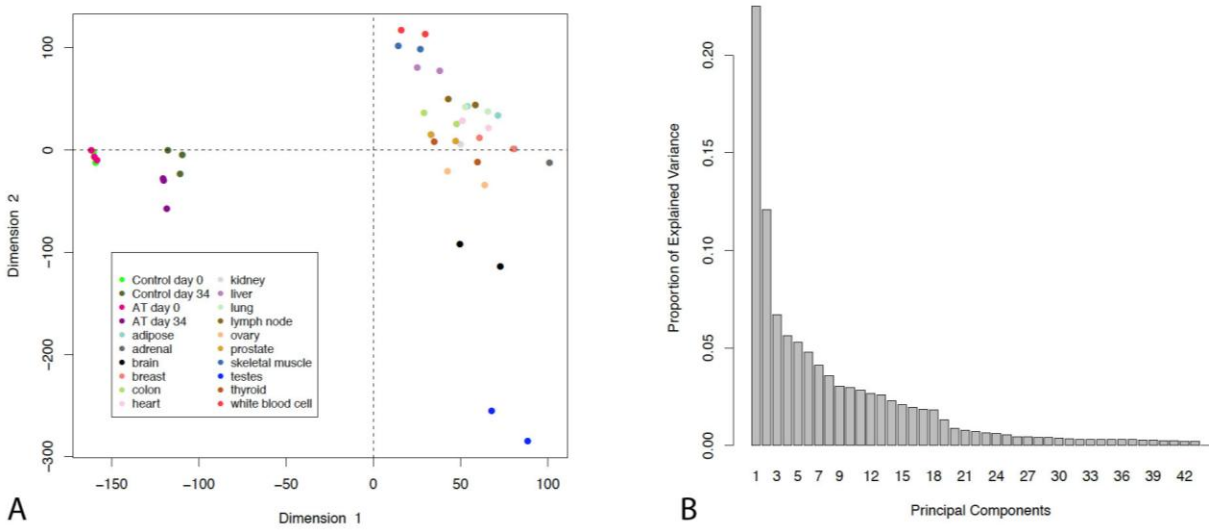

Figure 5.7 – (A) Principal component analysis of DESeq2 variance-stabilized RNA-seq data from the day 0 iPS cells and neurons and the Illumina body map. (B) Bar plot of the percentage of variance explained by the principal components.

Clustering (Figure 5.7C) shows that the transcriptome of iPS-derived neuronal cells (blue text) was most similar to that of brain and testes in the Illumina Body map (green text). The Allen Brain Atlas samples (red text) cluster away from both Illumina Body map and iPS-derived data, likely for technical reasons: both the Illumina Body Map and iPS-data were processed from reads to counts in a similar manner, while ABA data was downloaded as RPKM values from the ABA website, because raw data has not been publicly released. We could not reliably cluster our

datasets with data from the Developmental brain transcriptome, using various brain regions from several developmental time points presumably due to cross-species differences, cross-platform incompatibilities or major differences in transcriptome profiles between cultured cells/harvested tissues. This issue remains an ongoing challenge for the field to address.

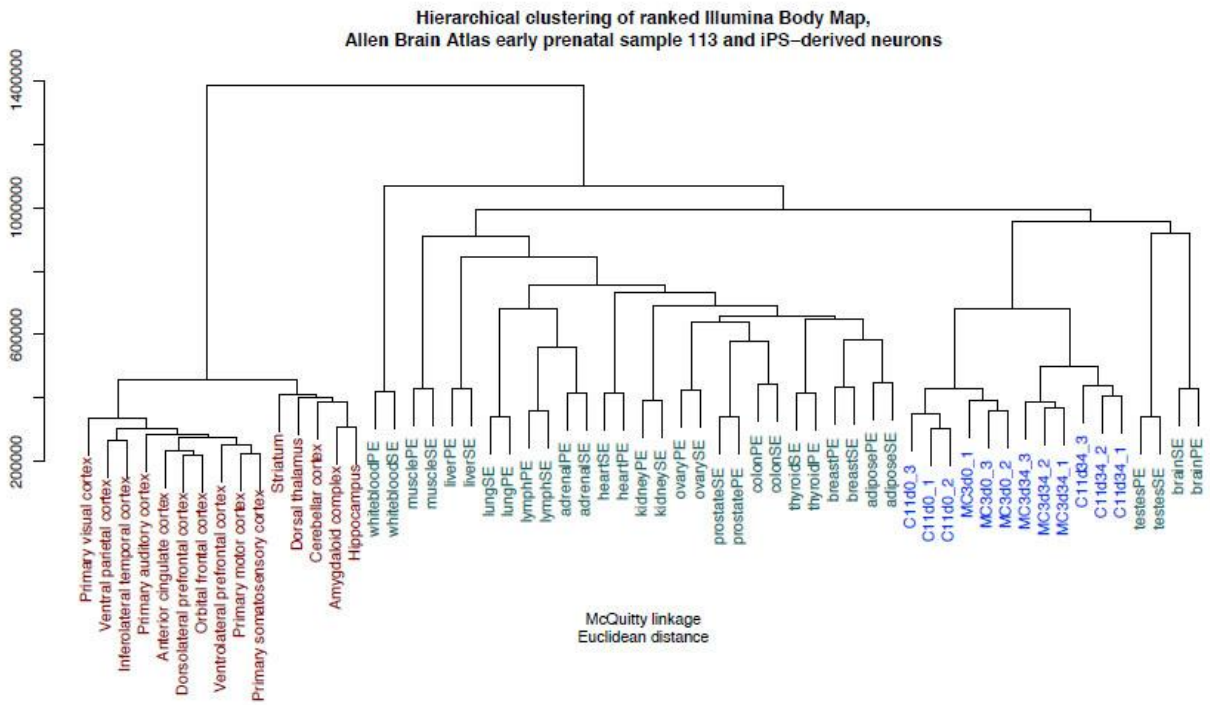

Figure 5.7C - Hierarchal clustering of ranked RPKM values of the Illumina Body map, the Allen Brain Atlas early prenatal sample 113 and iPS-derived neurons (Control, C11 and ATM mutants, MC3/AT30).

A common solution is to look at expression of a small number of important genes/transcription factors reported by the literature to make a call about cell-state and identity, which is what we have done and what is summarized in Figure 5.7D. Figure 5.7D depicts relative expression values for 10 such targets that are important markers of cerebellar identity, which we found to be well correlated (9 out of 10 genes were co-ordinately regulated). This list includes *Atoh1* (*Math1*), *En1*, *Hoxb4, Isl1*, *Lhx9, Meis1, Meis2, Nfix, Reln* and *Shh.* We found all of these

genes, with the exception of *Atoh1* to be similarly expressed in both C11 and AT30 and on this basis speculate that they exist in close developmental proximity to each other. Highly similar expression of members of the *Hox* gene family (Figure 5.6D) supports this notion.

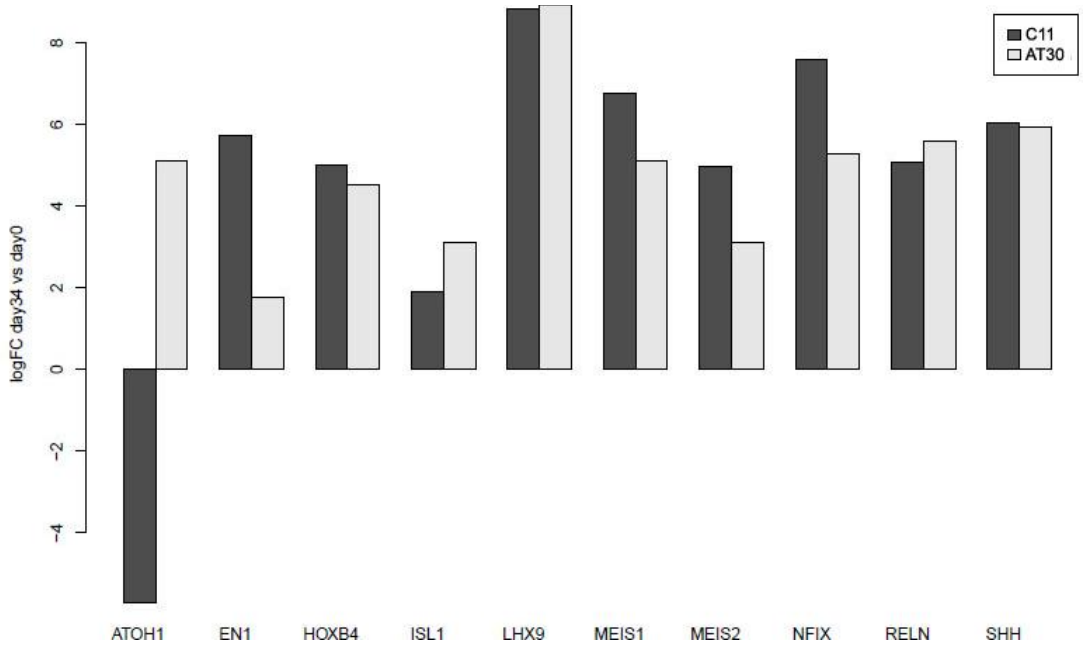

Figure 5.7D – Relative expression of ten genes critical to cerebellar development in C11 and AT30.

Additionally we looked at expression of the genes reported to define these cell types by the authors of this protocol which we show are highly similar to our data. Figure 5.7 E depicts hierarchical clustering based on separation by sample type using Pearson correlation using RPKM data from Stemformatics. A genelist was assembled from genes reprorted to be expressed after cerebellar differentiation by Erceg et al., 2010 [131] at the transcript level. Figure 5.7F shows bar graphs representing this at the gene level, highlighting those that were statistically significant (log fold-change values are shown at the gene level).

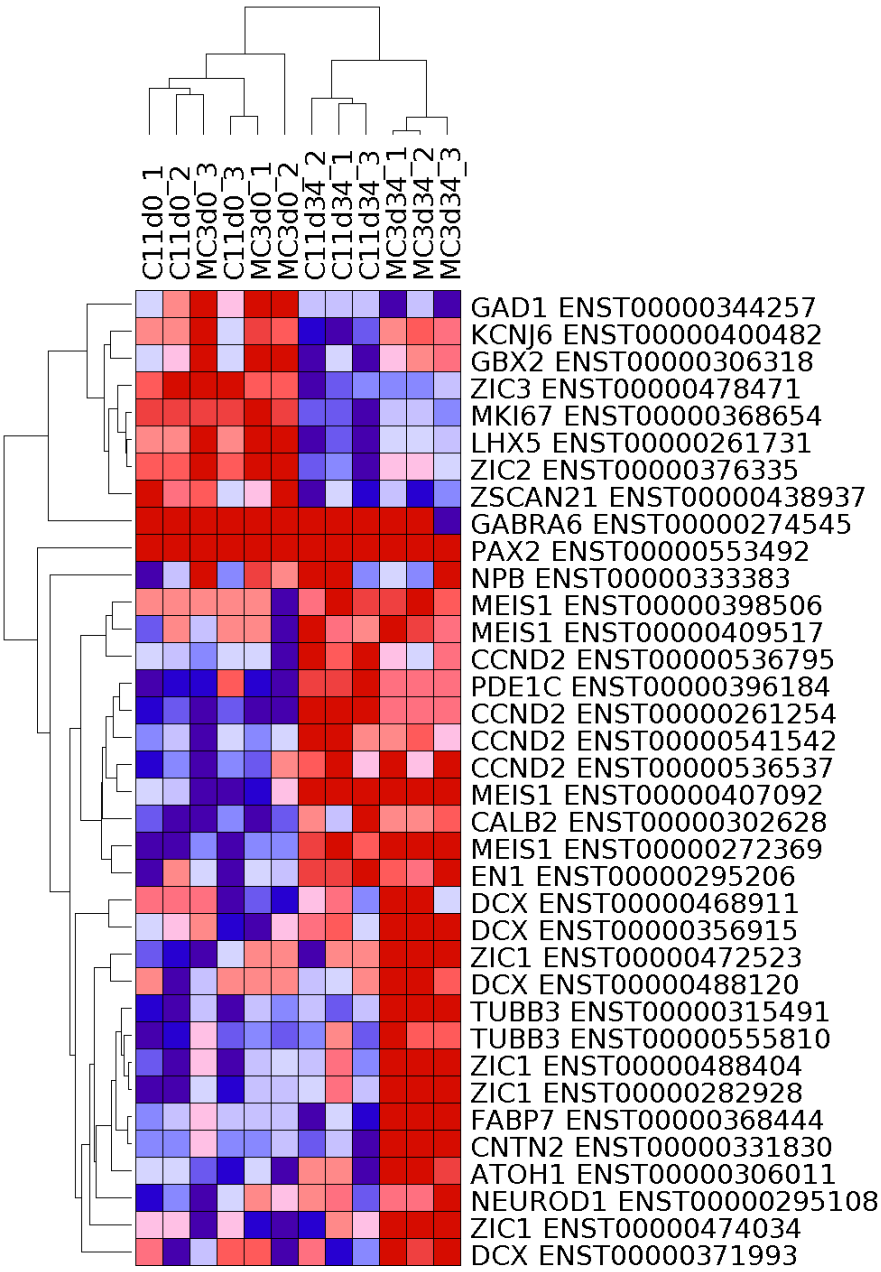

Figure 5.7E - Hierarchical clustering based on separation by sample type using Pearson correlation using RPKM data from Stemformatics. Genelist was assembled from genes reprorted to be expressed after cerebellar differentiation by Erceg et al 2010 [131]. Dominant isoforms have been selected and displayed.

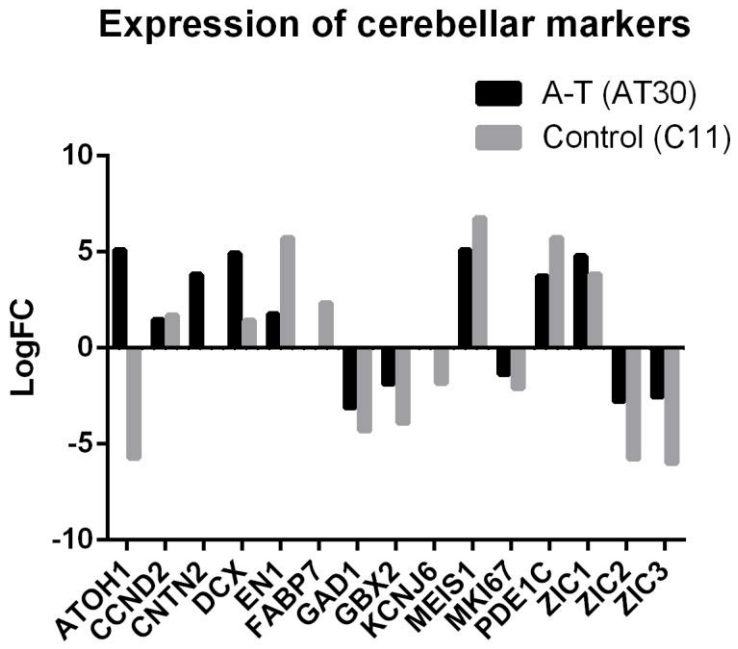

Figure 5.7F – Log fold-change gene expression values of statistically significantly differentially expressed genes using genelist compiled by Erceg et al.

It is likely given the overall expression patterns, and in particular those of *En1, Meis1* and *Atoh1* that AT30 represents a developmental stage resembling that of the upper rhomblic lip, whereas C11 may be on the cusp of this, expressing a consistent array of cerebellar markers with the exception of *Atoh1* and a greater degree of *En1*. Further supporting the theory that A-T neurons had reached a more terminally differentiated state can be seen in Figure 5.7E which shows elevated levels of *Dcx, B-III-Tubulin, Zic1 and Cntn2,* which are expressed in migrating granule neurons.

It is impossible to draw conclusions about whether this apparent inconsistency in differentiation state is attributable to normal intrinsic differentiation potential, or ATM mediated, without differentiation and sequencing of further samples. We present an analysis of the remaining data with the caveat that an absolute quantitative assessment of the similarity is currently beyond our

means and that although these cells appear to be in close developmental proximity, we cannot rule out the possibility that differences we have uncovered may be due to differences in cellular identity.

Pathway analysis between control and A-T neurons

As described above, we performed differential gene expression analysis and gene set enrichment using IPA between day 34 A–T and Control neuronal inductions (Tables 5.8A and 5.8B summaraize the results of an IPA report).

Top Networks	
Associated Network Functions	**Score**
Nervous System Development and Function, Cell Morphology, Cellular Assembly and Organization	41
Embryonic Development, Organismal Development, Cellular Development	39
Cell-To-Cell Signaling and Interaction, Nervous System Development and Function, Carbohydrate Metabolism	39
Nervous System Development and Function, Tissue Morphology, Embryonic Development	38
Embryonic Development, Endocrine System Development and Function, Nervous System Development and Function	37

Table 5.8A – Top networks identified as differentially regulated between AT30 and C11 after 34 days of neuronal induction

Top Diseases and Bio Functions		
Diseases and disorders		
Name	**p-value**	**# Molecules**
Cancer	2.69E-32 - 4.81E-04	813
Respiratory Disease	8.12E-27 - 5.40E-04	528
Hereditary Disorder	1.03E-26 - 3.79E-04	213
Neurological Disease	1.03E-26 - 6.07E-04	389
Psychological Disorders	1.03E-26 - 5.96E-04	301
Molecular and cellular functions		
Name	**p-value**	**# Molecules**
Cell-To-Cell Signaling and Interaction	6.72E-34 - 6.21E-04	226
Cell Morphology	5.13E-19 - 6.21E-04	358
Cellular Assembly and Organization	5.13E-19 - 6.21E-04	261
Cellular Development	5.13E-19 - 5.59E-04	342
Cellular Function and Maintenance	5.13E-19 - 3.78E-04	241
Physiological System Development and Function		
Name	**p-value**	**# Molecules**
Nervous System Development and Function	2.04E-34 - 6.07E-04	473
Behavior	2.03E-33 - 6.07E-04	232
Tissue Morphology	3.03E-28 - 5.59E-04	349
Organ Morphology	3.20E-22 - 5.76E-04	234
Tissue Development	2.54E-17 - 5.76E-04	368
Top canonical pathways		
Name	**p-value**	**# Molecules**
Glutamate Receptor Signaling	1.63E-08	19/71 (0.268)
Axonal Guidance Signaling	5.57E-08	63/471 (0.134)
Amyotrophic Lateral Sclerosis Signaling	1.08E-07	24/118 (0.203)
CREB Signaling in Neurons	9.98E-07	32/206 (0.155)
Cardiac b-adrenergic Signaling	3.76E-06	26/158 (0.165)

Table 5.8B - Top Diseases and Biological Functions as determined by IPA. This table is broken down into four sections listing processes that are over/under represented in this dataset and include Diseases and disorders, Molecular and Cellular Functions, Physiological System Development and Function and Top Canonical Pathways. P-values and numbers of significantly dysregulated molecules within pathways are given.

Table 5.8C shows a list of the top molecules that are upregulated (upper section) and downregulated (lower section) between A–T neurons (AT30) and control (C11) neurons at Day

34. *Nnat (*Neuronatin) regulates segment identity and ion channels during hindbrain development and may also be involved with positive regulation of insulin secretion as well as formation and maintenance of the nervous system. *ZNF285* (Zinc Finger Protein 285) is a zinc finger protein putatively involved with transcriptional regulation. *XIST (*X-Inactive specific transcript*)* is involved in developmental silencing of the second X-chromosome in females (AT30 is from a female donor, whereas C11 is male). *Atoh1* (*Math1*) is one of the major neurogenic factors involved in specification of granule cell progenitors. *GSTT1* (Glutathione S-transferase Theta 1) is an enzyme responsible for the conjugation of reduced glutathione with toxic substrates, aiding removal of these byproducts from the body. *CNTN6* (Contactin 6) is a neuronal membrane protein functioning as a cell adhesion molecule that plays a role in the formation of axon connections during development of the nervous system. *CAT* (Catalase) encodes a critical antioxidant enzyme present in the peroxisome where it converts hydrogen peroxide to oxygen and water. *H19* (Imprinteed maternally expressed transcript) expresses a non-coding RNA that has tumour suppressor roles. This gene is also imprinted, which may help explain its presence in this list. *LDOC1* (Leucine Zipper, Down-regulated in Cancer 1) is thought to orchestrate the transcriptional response mediated by NFκB. *HES5* (Hairy And Enhanced of Split 5) encodes a protein which is activated downstream of Notch, and is involved in cellular differentiation.

Amongst the most lowly expressed transcripts were *RPS4Y1* (Ribosomal Protein S4, Y-Linked 1) encodes a ribosomal component of the 40s subunit. *SLC15A4* (Solute Carrier Family 15, Member 4) is a proton oligopeptide cotransporter. *MAGEA3/MAGEA6* (Melanoma antigen family A3/6) encode members of the MAGEA family that enhance ubiquitin ligase activity of RING-type zinc finger-containing E3 ubiquitin-protein ligases and are speculated to have a role in embryonal development. *KDM5D* (Lysine (K)-Specific Demethylase 5D) is an enzyme that specifically demethylates K4 of Histone H3. *EIF1AY* (Eukaryotic Translation Initiation Factor 1A Y-linked) is involved with ribosomal subunit assembly/binding. *USP9Y* (Ubiquitin Specific Peptidase 9, Y-linked) functions as a ubiquitin-protein or polyubiquitin hydrolase and may be involved with protein turnover. It is a component of the TGF-beta/BMP signaling cascade with roles in deubiquitination of SMAD4. *HLA-DRB5* (Major Histocompatability Complex, Class II,

DR Beta 5) plays a role in the immune system by presentation of peptides from extracellular proteins. *C9orf64* (Chromosome 9 Open Reading Frame 64) encodes a protein of unknown function belonging to the member of the DUF2419 family and predicted to have a role in the peroxisome. *LOC100287163/ZNF717* (Zinc Finger Protein 717) is a zinc finger protein with unknown functionality. *PCDH11X/PCDH11Y* (Protocadherins 11X&Y) play important roles in cell to cell recognition during segmental development and function of the CNS.

Top Molecules	
Molecules	**Exp. Value**
NNAT	10.764
ZNF285	10.258
XIST	9.873
ATOH1	9.599
GSTT1	9.4
CNTN6	7.988
CAT	7.404
H19	7.03
LDOC1	6.658
HES5	6.6
RPS4Y1	-9.703
SLC15A4	-8.987
MAGEA3/MAGEA6*	-8.829
KDM5D	-8.672
EIF1AY	-8.268
USP9Y	-7.782
HLA-DRB5	-7.439
C9orf64	-7.27
LOC100287163/ZNF717	-6.882
PCDH11X/PCDH11Y	-6.006

Table 5.8C – List of Top Molecules that are upregulated (upper section) and downregulated (lower section) between A–T neurons (AT30) and control (C11) neurons at Day 34.

IPA identified the top 5 differentially expressed network functions between AT30 and C11 after 34 days of neural differentiation to include; '*Nervous System Development and Function, Cell*

Morphology, Cellular Assembly and Organization', 'Embryonic Development, Organismal Development, Cellular Development', '*Cell-To-Cell Signaling and Interaction, Nervous System Development and Function, Carbohydrate Metabolism', 'Nervous System Development and Function, Tissue Morphology, Embryonic Development'* and *'Embryonic Development, Endocrine System Development and Function, Nervous System Development and Function'*.

ERK 1 /2 is one of the central genes annotated to the '*Nervous System Development and Function, Cell Morphology, Cellular Assembly and Organization'* network. Interestingly a number of transducers of *ERK1/2* are heavily upregulated (*GPRIN1, GPRIN2, NELL2, GNAZ, SHC4, LRRN1, TMEFF2, ZNF300 & PTPRZ1*). ATM has been shown to regulate *ERK1/2* [274]. In addition, chronic activation/phosphorylation of *ERK1/2* has been implicated with loss of ATM and linked to the redox imbalance that is suspected to play a part in the pathogenesis of A–T [275]. This pathway also featured upregulation of a number of potassium channels (*KCNAB1, KCNA1, 2&3*). Aberrant activity of potassium channel activity is common in a number of neurodegenerative disorders and has previously been shown in ATM deficient cells [276].

'*Cell-To-Cell Signaling and Interaction, Nervous System Development and Function, Carbohydrate Metabolism'* was statistically significantly dysregulated. Intriguingly, the *GPCR* (G-protein couple receptor) family of molecules is heavily featured. A unique GPRC, *G2a* was found to act as an anti-proliferative cell cycle regulator and respond to various DNA damaging agents in a fashion similar to ATM [277]. Two important neurotransmitter receptors (*GRM* – Glutamate receptor metabotrophic 3) and *GABBR2* (Gamma-aminobutyric acid (GABA) B receptor 2) were upregulated. Aberrant expression levels and activity of neurotransmitter receptors has been associated with neurodegeneration in a number of cases [278].

Nervous System Development and Function, Tissue Morphology, Embryonic Development' showed *Myc*, a critical signal transducer and orchestrator of cell cycle, to be upstream of a number of genes which were misexpressed between A–T and control neurons including *DCX, SEMA4A, HES5,* & *AKAP6*. The *Myc* genes have been previously shown to be required for proper growth and development of the brain [279]. MYC was recently shown to be required for

the activation of ATM-dependent checkpoints as part of the DNA damage response [280]. *XIST* appears in this pathway network, however its appearance can be explained by the fact that C11 and AT30 are from individuals of different gender. It is widely understood that there are sex-specific differences largely brought about by incomplete or erased X-inactivation [281]. For this reason it may be pertinent to perform sex-matched differentiation experiments.

Given the assumption that the majority of the differences encapsulated by this pathway analysis should reflect the differences between individuals with functional/non-functional ATM, we were particularly interested in gene expression differences captured under the top predicted *Diseases and Disorders* by IPA, namely '*Neurological Disease'* (P-value 1.03E-26-6.07-04). Functionally annotated groups within this classification included '*Movement disorders*' (Figure 5.8A, P-value 3.08E-26), '*progressive motor neuropathy*' (Figure 5.8B, P-value 4.25E-09), *ataxia* (Figure 5.8C, '*ataxia'*) and '*cerebellar ataxia*' (Figure 5.8D, P-value 3.68E-04). Given the fact that A–T is primarily a disease of the cerebellum, and that motor control is severely affected, these lists may potentially contain targets that help explain the mechanism of neurodegeneration and targets that may be amenable to therapeutic intervention. We examined which constituents in these lists that were directly annotated as interacting with ATM, of which there were several, including; *Tdp1, Tp53, Vimentin* and *Pcna. Tdp1* (Tyrosyl-DNA phosphodiesterase 1) has a role in repair of stalled topoisomrease I-DNA complexes. ATM deficiency has recently been linked with an accumulation of DNA–Topoisomerase I covalent intermediates in neural cells [282]. Additionally *Tdp1* has been shown to have roles in defense against oxidative damage [283]. Interestingly, mutation of *Tdp1* gives rise to the disorder SCAN1 (Spinocerebellar ataxia with axonal neuropathy) [284], striking in its similarity to A–T. *Tp53* is a well known substrate of ATM and critical tumor suppressor that has been described to have roles in developmental apoptosis in specific brain regions, including the cerebellum [285]. Vimentin is a member of the intermediate filament (IF) protein family. It is expressed in neuronal and glial precursor cells during nervous system formation. Interestingly, Vimentin knock-out mice show poorly developed and abnormal Bergmann glia and stunted Purkinje cell growth [286]. These findings implicate Vimentin in the proper development of the cerebellum. *Pcna* (Proliferating cell nuclear

antigen) is an enzyme that is involved with both DNA synthesis and repair. ATM was recently shown to interact with PCNA [287], perturbation of which has been implicated with A–T [288].

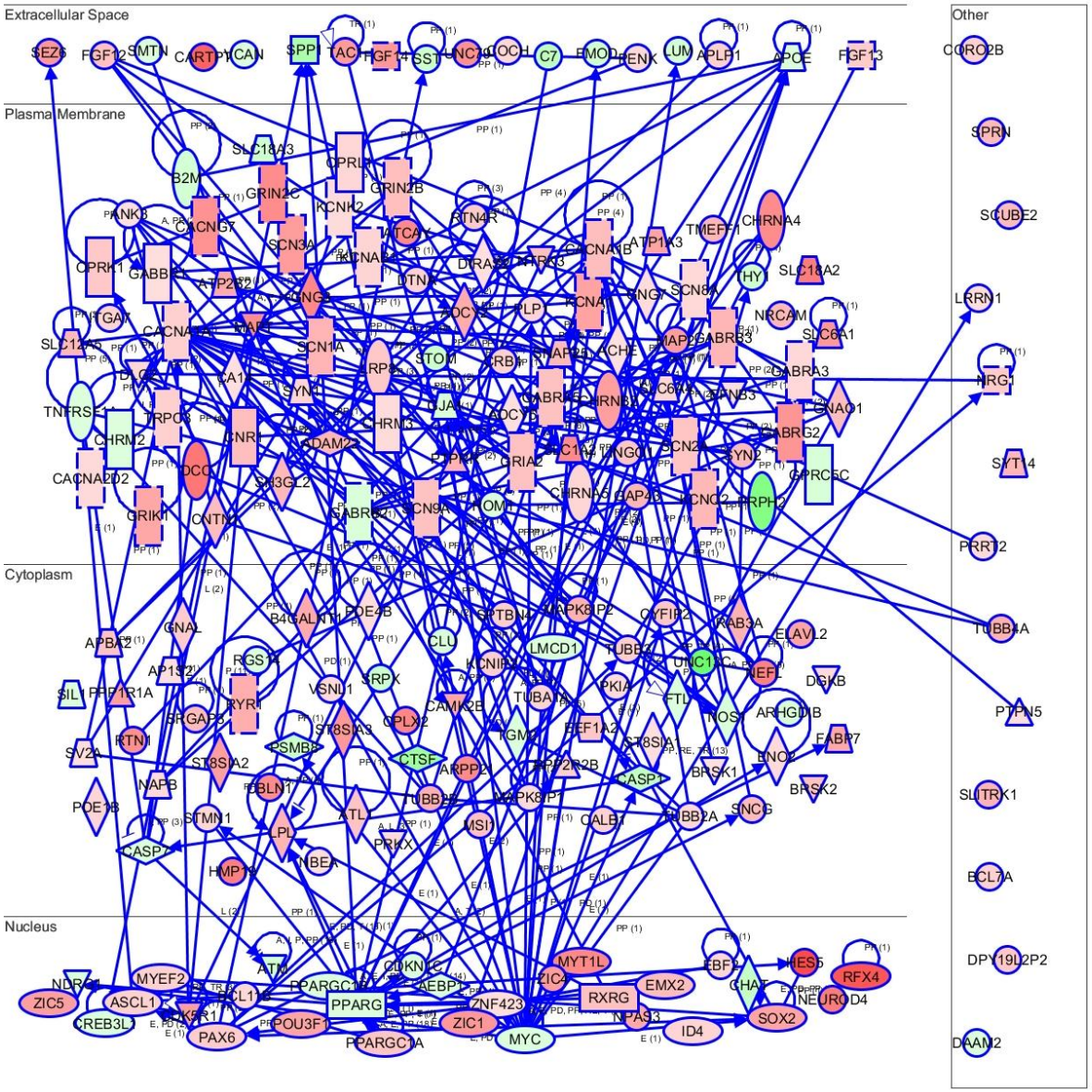

Figure 5.8A - IPA identified the network functions associated with '*Neurological Disease – Movement disorders*' as significantly differentially expressed between AT30 and C11 after 34 days of neural differentiation. Molecules in green are downregulated, red are upregulated.

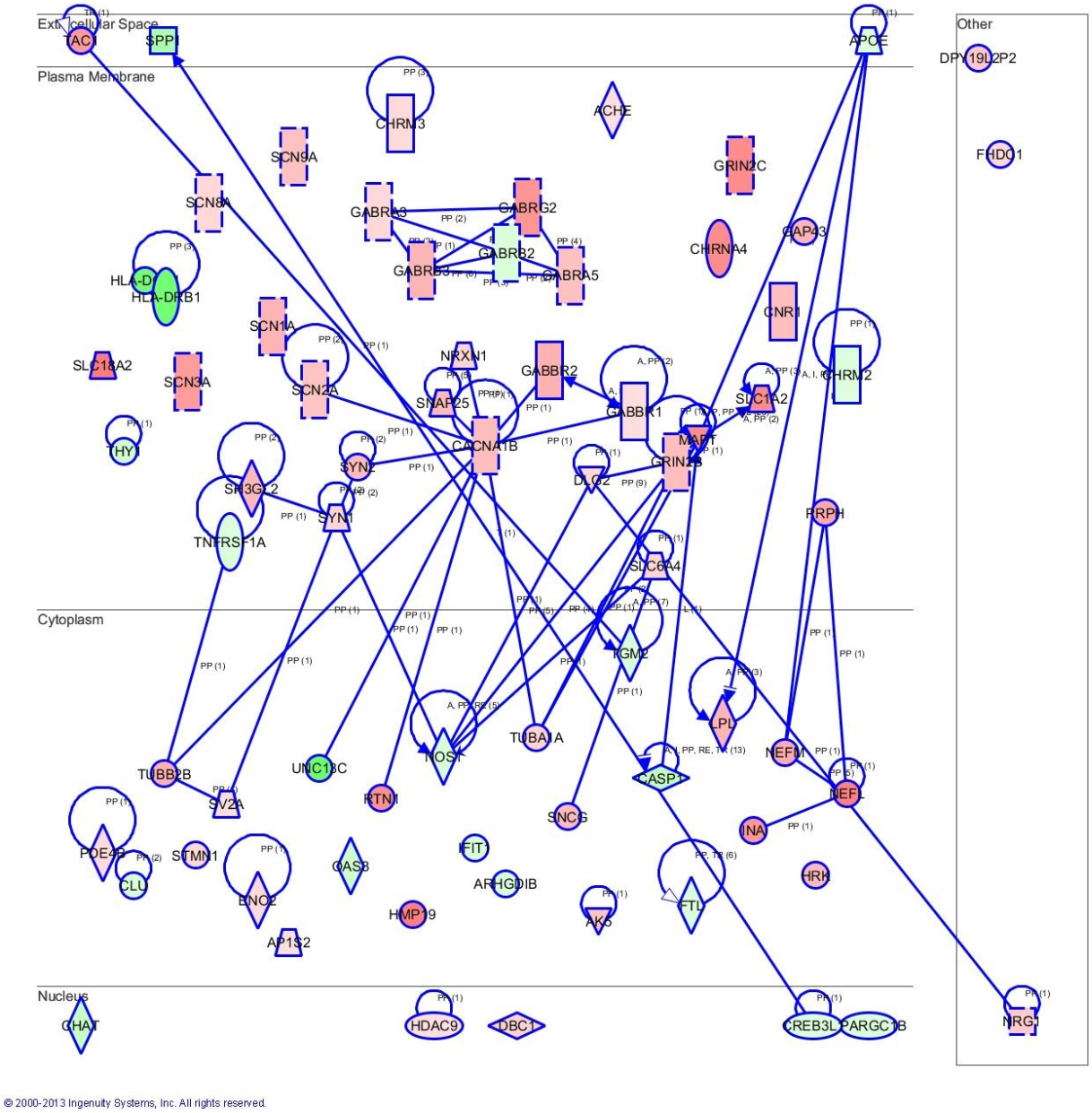

Figure 5.8B - IPA identified the network functions associated with '*Neurological Disease – progressive motor neuropathy*' as significantly differentially expressed between AT30 and C11 after 34 days of neural differentiation. Molecules in green are downregulated, red are upregulated.

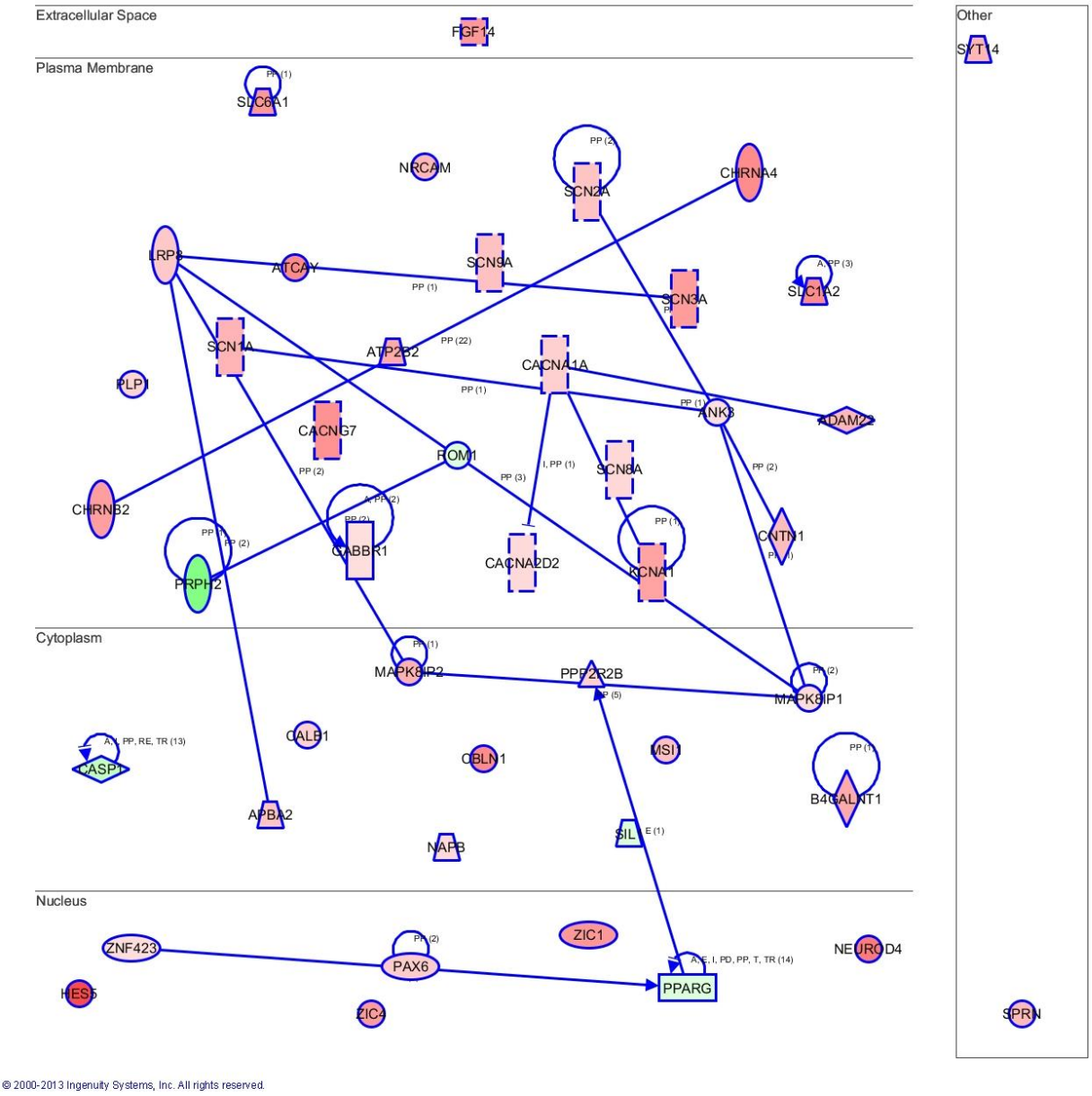

Figure 5.8C - IPA identified the network functions associated with '*Neurological Disease - ataxia*' as significantly differentially expressed between AT30 and C11 after 34 days of neural differentiation. Molecules in green are downregulated, red are upregulated.

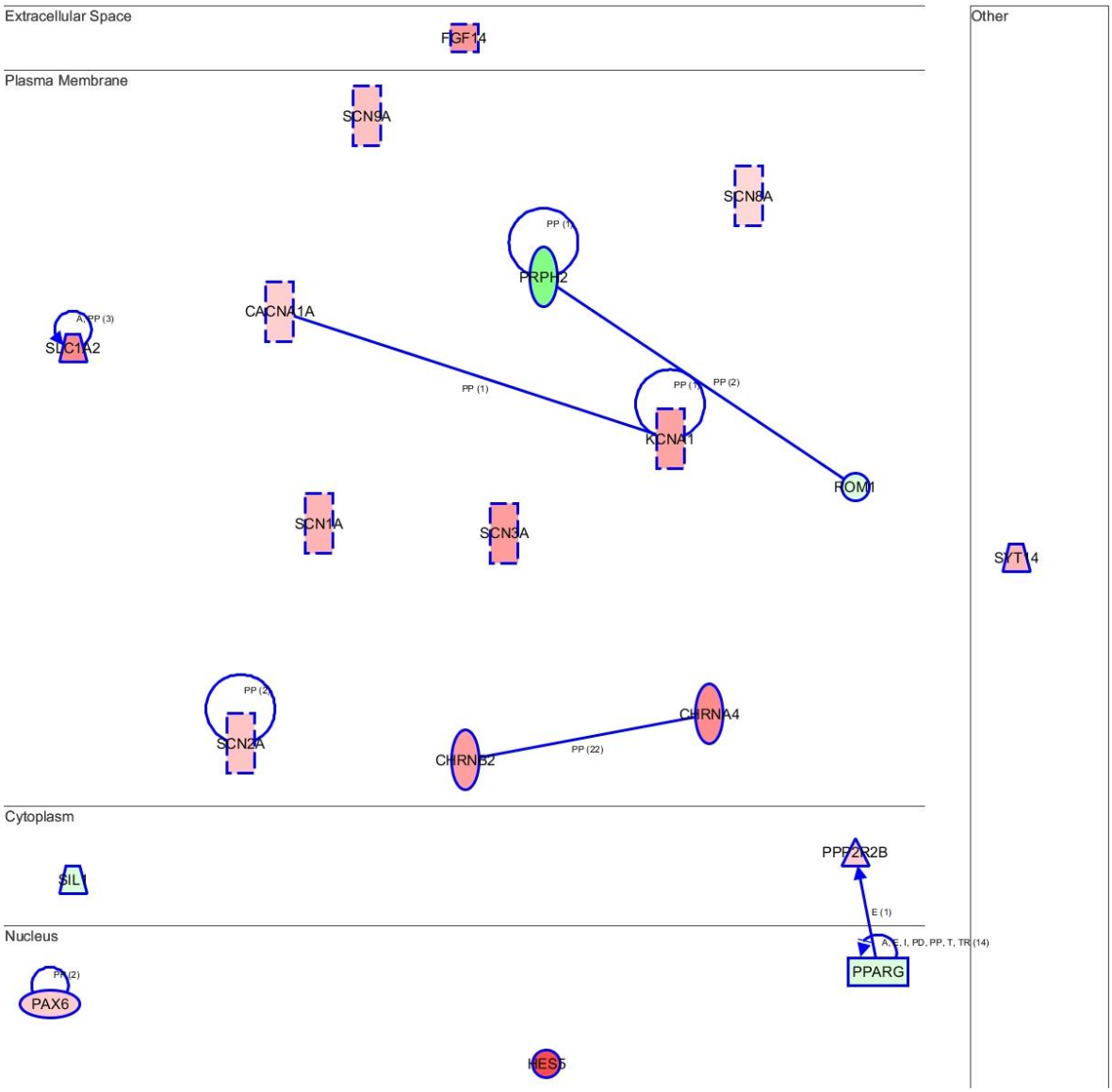

Figure 5.8D - IPA identified the network functions associated with '*Neurological Disease – cerebellar ataxia*' as significantly differentially expressed between AT30 and C11 after 34 days of neural differentiation. Molecules in green are downregulated, red are upregulated.

The top four listed differentially regulated canonical pathways were '*Glutamate Receptor Signaling*' (P value = 1.63E-08), *Axonal Guidance Signaling* (P-value = 5.57E-08), *Amyotrophic Lateral Sclerosis Signaling* (P-value 1.08E-07) & *CREB signaling in Neurons* (, P-value 9.98E-07). The observation of extensive upregulation of numerous constituents of the '*Glutamate*

receptor signaling' pathway indirectly supports the recent observation that GABAergic neurons are under-represented in the absence of ATM [212].

'*Axonal guidance signaling*' pathway, was found to be statistically significantly different after 34 days of neuronal differentiation between C11 and AT30. It has been shown that loss of ATM causes reduced dendrite numbers and complexity in cerebellar Purkinje cells. Interestingly this has been attributed to accumulation of ROS, with the observation that treatment with antioxidant could partially restore this phenotype [101]. In support of this theory we note the upregulation of the CATALASE enzyme (7.404 log-fold) as well as GSTT1 (9.4 log-fold).

CREB signaling (identified as differentially regulated between AT30 and C11) is driven largely by nuclear calcium levels and vitally important for survival and signaling in neurons [289]. ATM has been linked with CREB signaling in biochemical assays using leukemia cell lines [290] and SH-SY5Y neuronal cells [291].

Interstingly, the processes annoted to **'***Cell to cell signaling & interaction'* were significantly differentially expressed (p-value 6.72E-34 – 6.21E-04). Further investigation of this revealed A–T neuronal cells to exhibit differential regulation of genes involved with the processes annotated to '*Long term potentiation'* (Figure 5.8E, p-value –log 13.514). This is in keeping with a recent paper to explore the role of cytoplasmic ATM in the modulation of synaptic function in neurons [7]. Li et al. demonstrate a physical role for ATM in the phosphorylation of vesicle proteins VAMP2 & SYNAPSIN-1 and show that hippocampal LTP is significantly impaired in the absence of ATM.

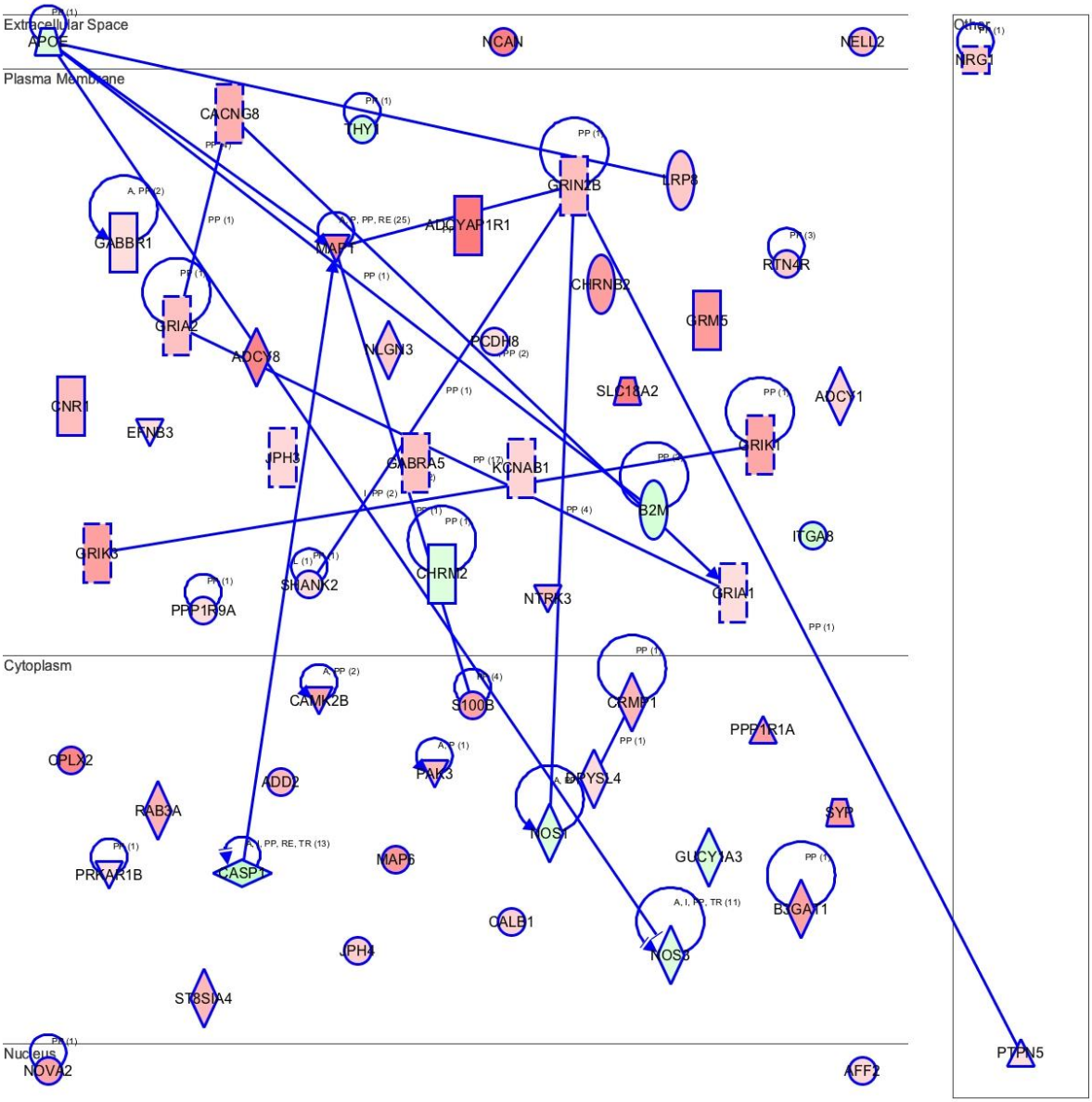

Figure 5.8E - IPA identified the network functions associated with '*Cell to cell signaling & interaction – Long term potentiation*' as significantly differentially expressed between AT30 and C11 after 34 days of neural differentiation. Molecules in green are downregulated, red are upregulated.

Dynamic differentiation-associated changes in non-coding RNA

Approximately 150 GENCODE-annotated lincRNA and ~130 processed transcripts (which are

defined as RNAs that overlap with coding genes but do not contain an open reading frame) were also found to be differentially expressed in the course of neuronal differentiation (See Figure 5.9A & B for volcano plots). We limited our analysis to ncRNAs that were differentially expressed in common between C11 and AT30 after 34 days of neuronal differentiation. This included down-regulation of known pluripotency-associated transcripts such as *linc-RoR* (> 1200x downregulated) and *DANCR* (>3x downregulated). *linc-ROR* is a miR-145 sponge expressed in pluripotent cells; it serves as a decoy for *miR-145*, which is involved in OCT4, NANOG and SOX2 repression in development [292]. Levels of the corresponding pre-miRNA (*pre-miR-145*) were also upregulated over 120 times in the course of differentiation. Differentiation-antagonizing long non-coding RNA (*DANCR*) has been characterised as critical for maintaining the potency of keratinocyte progenitors [293] and is strongly down-regulated in osteoblast and adipocyte differentiation in the ENCODE datasets [293]; the current study is the first to report of its downregulation in a neuronal differentiation paradigm.

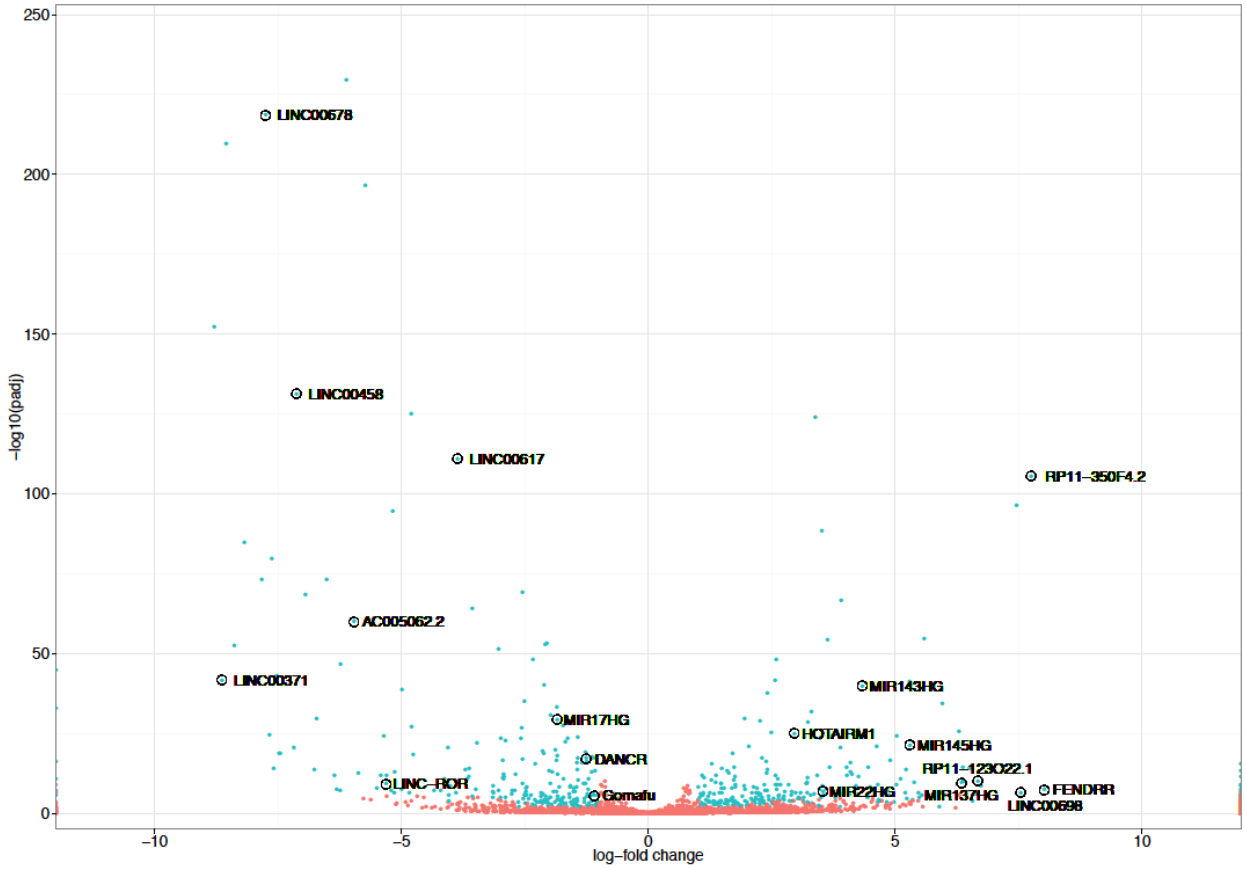

Figure 5.9A – Volcano plot depicting differentially expressed non-coding RNAs in AT30 after 34 days of neural differentiation.

Figure 5.9B – Volcano plot depicting differentially expressed non-coding RNAs in C11 after 34 days of neural differentiation.

The most strongly down-regulated ncRNA was *LINC00371*, which was expressed in iPS cells and nearly undetectable (1 read in only one of the 6 libraries) in differentiated neurons. This transcript resides on chromosome 13, <2kb upstream of the *GUCY1B2* gene; H3K27Ac data from ENCODE suggests its transcription is regulated independently of the lincRNA transcript (see Figure 5.9C). No information about roles for the enzyme or the adjacent lincRNA in the nervous system or maintenance of pluripotency has been described.

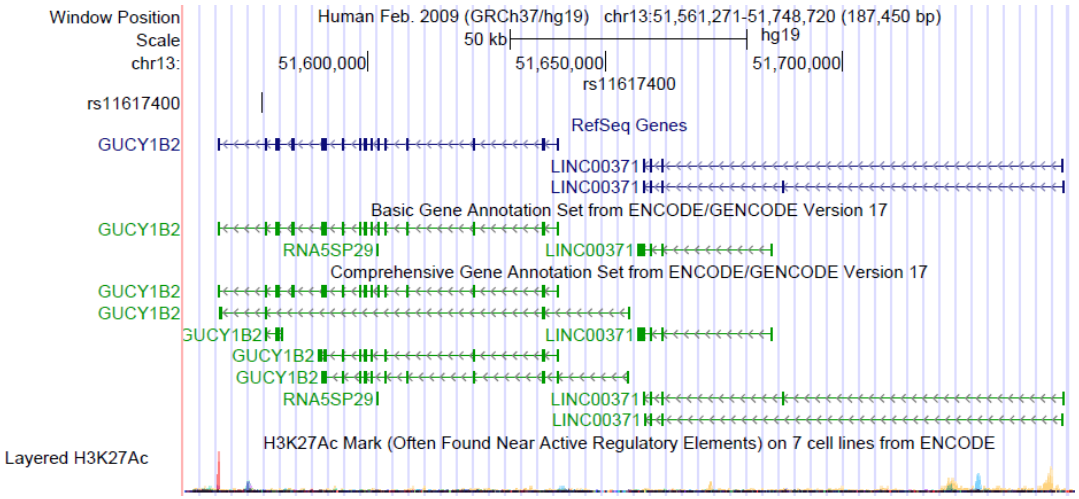

Figure 5.9C– ncRNA *LINC00371* was the most strongly down-regulated ncRNA after 34 days of neural differentiation.

One of the most strongly down-regulated transcripts was *RP11-69I8.2*, a previously uncharacterized lincRNA located in the ENPP1-CTGF locus on chr6 (see Figure 5.9D).

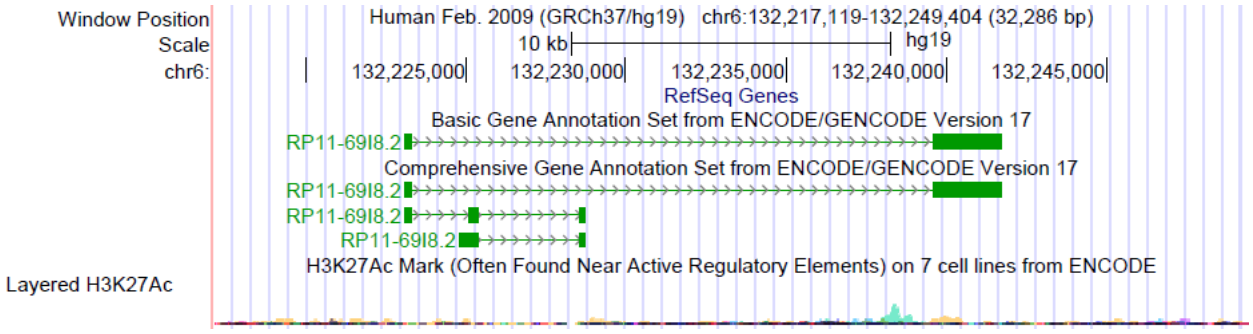

Figure 5.9D - *RP11-69I8.2*, a previously uncharacterized lincRNA located in the ENPP1-CTGF locus on chr6 was one of the most strongly down-regulated transcripts after 34 days of neural differentiation

Connective tissue growth factor (*CTGF*) has recently been shown to modulate interneuron survival in the mouse olfactory bulb [294], and was >2x upregulated with differentiation (significant only in the edgeR analysis) in both the control and A–T cells.
Similarly to a study from the Lachman group [295], who characterised the transcriptome of undifferentiated human iPS and cells following 10 days of neuronal differentiation toward a glutamatergic phenotype, strong down-regulation of the AC005062.2 lincRNA and its proximal metastasis-associated in colon cancer 1 (*MACC1*) gene were observed. *MACC1* regulates cell proliferation by modulating the transcription of *MEF*, the receptor of hepatocyte growth factor HGF [296]. Similarly to this study, strong upregulation of the *HOTAIRM1* lncRNA was also observed.

The strongest upregulation (>1000x) was observed for two poorly annotated, multi-exon lincRNA transcripts: *RP11-123O2.2* and *LINC00968,* for which no previous reports of neuronal function or expression exist.

The most strongly upregulated (>150x) annotated lncRNA was *FENDRR* (fetal-lethal noncoding developmental regulatory RNA/FOXF1 adjacent non-coding developmental regulatory RNA), a transcript identified in a screen for non-coding RNAs crucial for heart development and expressed specifically in cardiac mesoderm progenitor cells [297, 298]. Knockout of this RNA was found to cause embryonic lethality because of defects in lateral plate mesoderm resulting in omphalocele and reduced ventricle wall thickness in the heart; the molecular basis of these defects was shown to be a reduction in the expression of *FOXF1*, *IRX3,* and *PITX2*, critical mesoderm lineage specification genes, due to reduced levels of H3K4me3 at their promoters. Intriguingly, *FENDRR* was found to bind the TrxG/MLL component WDR5, which is known to be required for binding of the methyltransferase complex to H3K4me2 and for global H3K4 trimethylation [299], and the promoter regions of *FOXF1* and *PITX2* in a DNA-RNA triplex-helical configuration [297].

FOXF1 and *PITX2* were strongly upregulated after 34 days of differentiation (8x and 60x,

respectively), and while PITX2 has a well-characterised role in the development of neurons in the mouse subthalamic nucleus and midbrain; [300, 301], its role in the cerebellum is unknown. Mutations in *PITX2* cause Axenfeld-Rieger syndrome, a heterogenous disorder that in some cases can be associated with cerebellar abnormalities [302]. The highest levels of *PITX2* in a transcriptomic study of discrete human brain regions were detected in the early rhombic lip, followed by the mediodorsal nucleus of thalamus and dorsal thalamus (see Figure 5.9E).

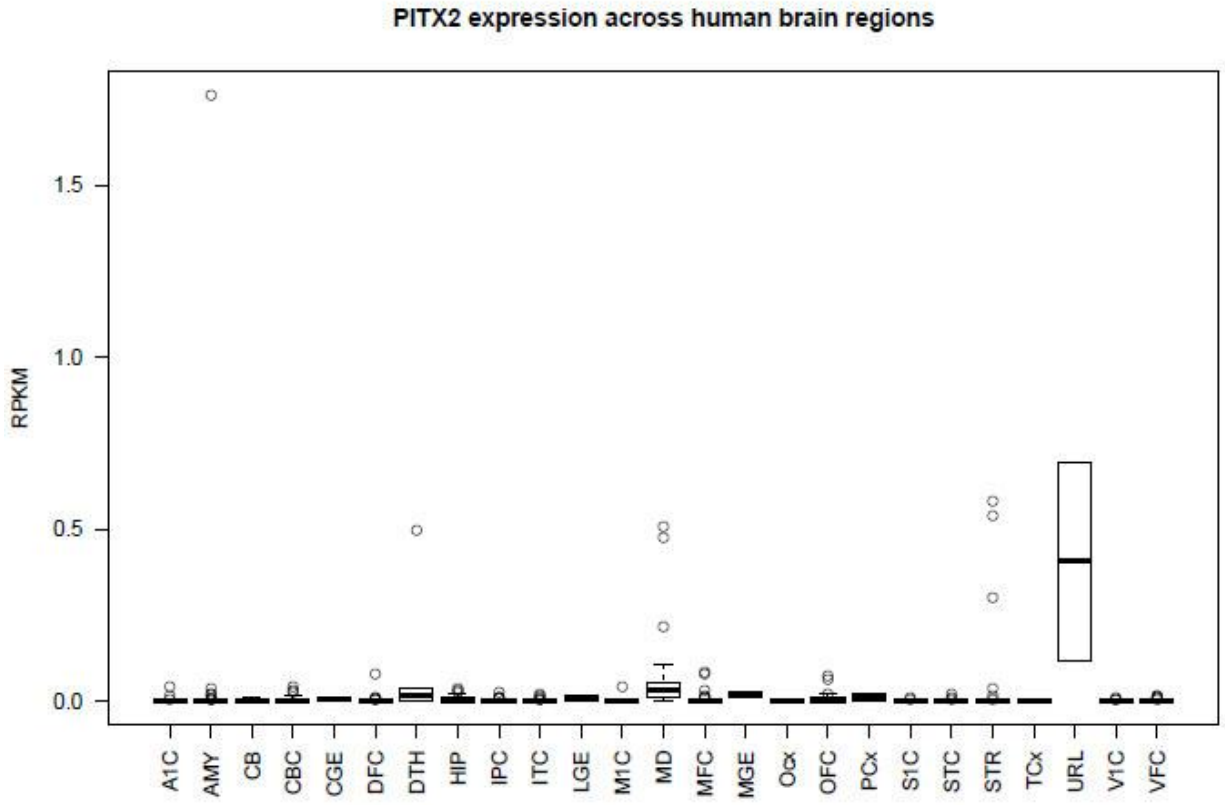

Figure 5.9E – Expression levels of *PITX2* from human brain

FOXF1 is expressed in the developing cerebellum and early low-resolution studies report its expression in astrocytes of both the cerebral and cerebellar cortex [303]; to our knowledge, no other studies describe the presence or function of this gene in the nervous system. Transcriptomic analysis shows dynamic changes in the expression of this gene in cerebellar development (Figure 5.9F), as well as across other brain regions (Figure 5.9G).

Overall, *FOXF1* and *PITX2* genes appear to be differentially expressed in our dataset and in multiple regions and developmental stages of the mouse and human brain, supporting the notion that we have generated neuronal precursors of the cerebellum.

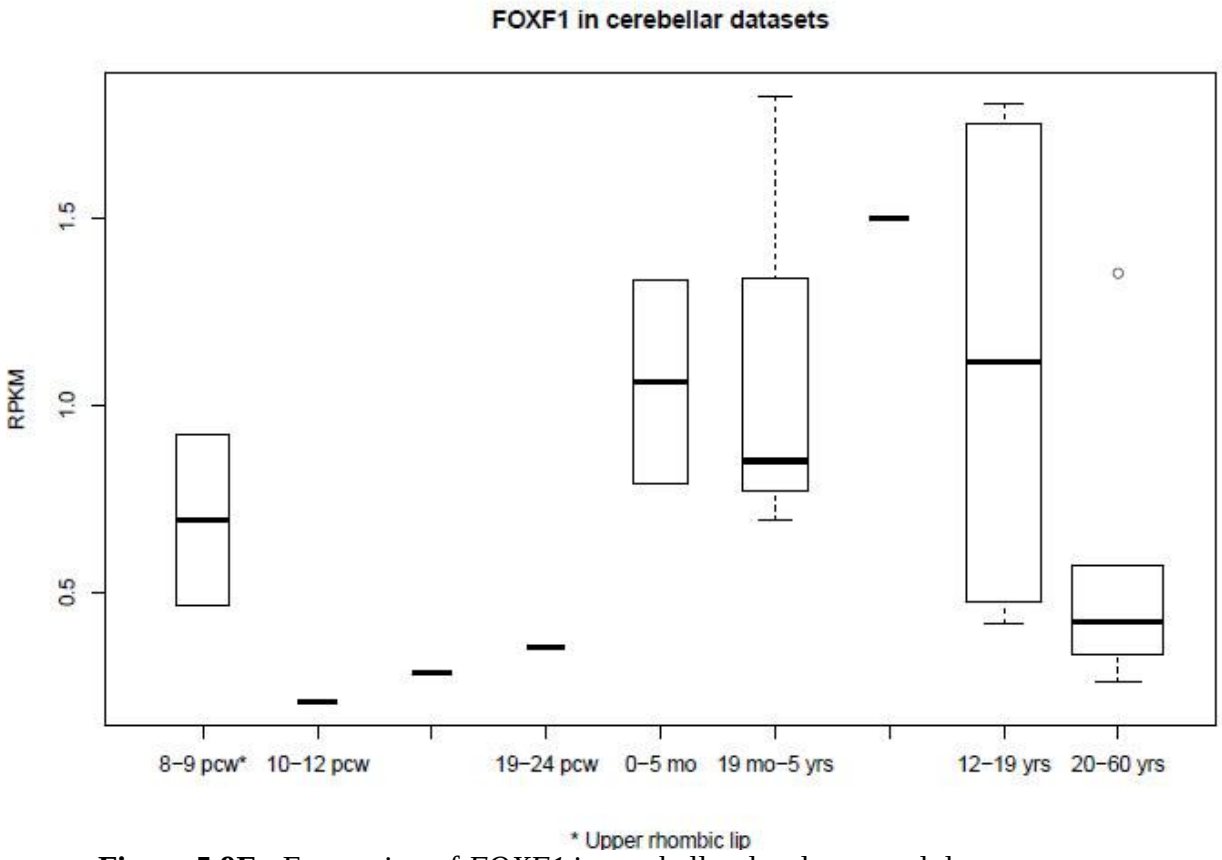

Figure 5.9F - Expression of *FOXF1* in cerebellar developmental datasets.

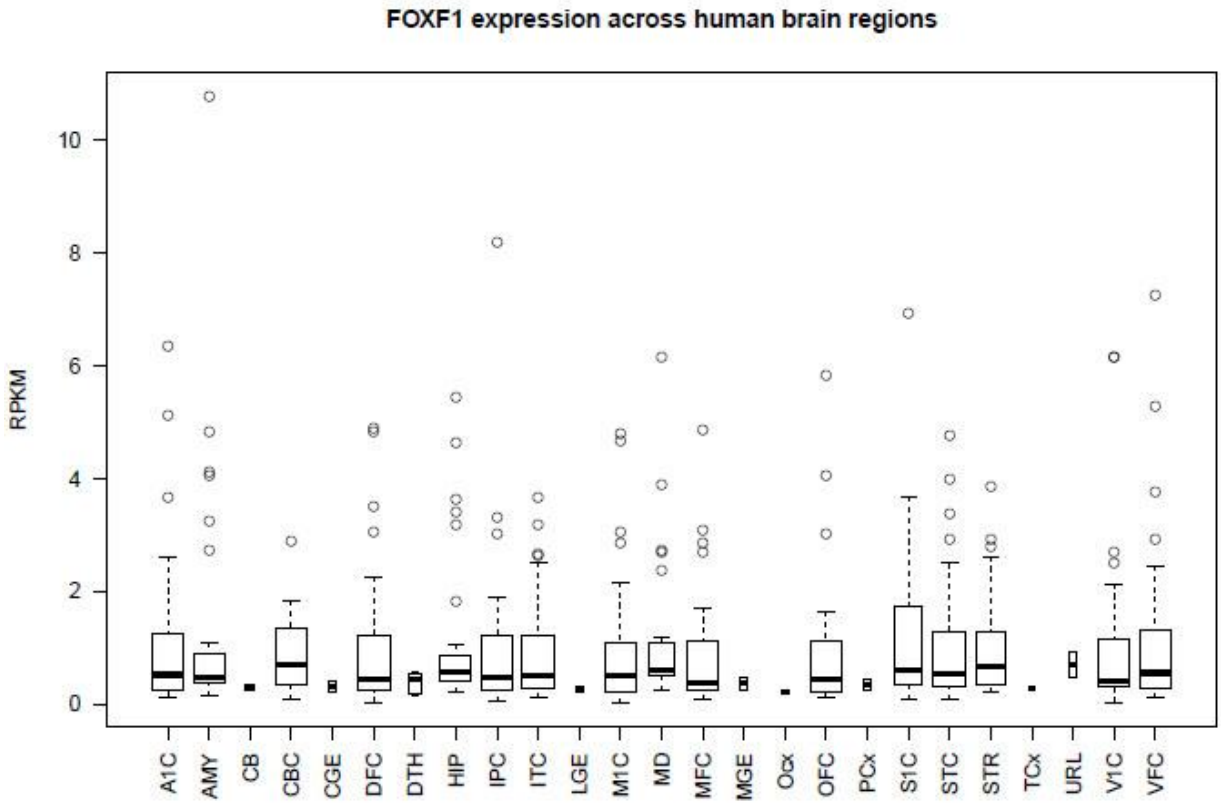

Figure 5.9G - Expression of *FOXF1* in other brain regions.

Overall, while a handful of the differentially expressed lncRNAs observed have been characterised and are discussed above, the majority remain poorly understood and await detailed functional studies to explore their roles in the nervous system and contribution to neurological disease. We provide evidence for the existence of several novel ncRNAs in our differentiated cells and also point to activity of a number of existing ncRNAs known to be involved with brain & cerebellar development *in vivo.*

Differential expression of small RNA precursors

Among the most strongly down-regulated pre-miRNAs were the precursor transcripts of *miR-145*, described above, and the *miR-17-92* cluster host gene. *miR-17-92* family members are the

most highly expressed miRNAs in medulloblastoma [304], and are associated with a constitutively activated Sonic Hedgehog signalling pathway [305]. Knockout of this cluster has recently been shown to maintain the potency of radial glial cells in the cortex and prevent their differentiation into intermediate progenitors [306]. Functionally relevant targets of these miRNAs in the cerebellum remain to be identified.

The precursor transcripts of *miR-137*, *miR-22* and *miR-143* were strongly upregulated with differentiation. *miR-137* has previously been found to be enriched in the neuronal lineage in the dentate gyrus and molecular layer of the mouse hippocampus [307] and in synaptosomes isolated from rat forebrains [308] and is required for a proper balance between proliferation and differentiation of adult neural stem cells due to its role in modulating global H3K27me3 levels via post-transcriptional repression of the Polycomb group protein EZH2 [307]. *miR-22* was shown to have a similar expression pattern in the cerebellum during mouse development as the bone morphogenic proteins BMP2 and BMP4, which inhibit the SHH-induced proliferation of cerebellar granule neuronal precursors [309], and to significantly increase cell cycle length in this system. Reduced levels of *miR-22* have been found in the brains of Huntington's and Alzheimer's disease patients [310, 311], and its overexpression suppresses neurodegeneration in primary rat cortical neuronal cultures [310]. *miR-143* has been found in nociceptive dorsal root ganglia neurons, and was down-regulated in response to inflammatory cytokines in this model system [312].

Analysis of both the coding and non-coding transcriptomes differentially regulated in development support the hypothesis that cerebellar-like neuronal cells have been generated, and that use of this human iPSC-derived model system is useful for interrogating novel cerebellar transcripts in a human neurological context.

RNAseq analysis validation - transcript analysis as a measure of differentiation status

The major finding of our cerebellar differentiation experiment (which featured differentiation of iPS cells from one A-T patient (AT30) and one control (C11) in technical triplicate) was that

these cells had lost their pluripotent phenotype and made a transition to a neuronal-like state. We describe results from several methodologies (gene ontology analysis, principal component analysis, hierarchical clustering based on published/reported genelists and manual curation/biological introspection) supporting the conclusion that these cells resembled those of the developing cerebellum and that these stages were subtly distinct from one another. Although we noted a core subset of genes annotated to hindbrain/cerebellar development that were co-ordinately regulated between A-T and control samples, it was evident that there were differences in terminal differentiation state after identical treatment.

While global gene expression signatures showed a brain-specific pattern (Fig 5.7A, Table 5.5C), they failed to be useful in ascertaining precise spatio-temporal identity. Strong expression of a number of prominent markers was used to theorize about this status (Fig 5.7D). Specifically, we noted similar expression levels of *Engrailed1* (1.73/5.73 LogFC A-T/Control respectively) and *Hoxb4 (4.50/5.00* LogFC mRNA between A-T and control) differentiation experiments. While expression of more mature cerebellar marker *Pax6 (*2.81/2.89 LogFC A-T/Control respectively*)* was also expressed similarly, the rhombic lip progenitor marker *Math1* was expressed at markedly higher levels in A-T neurons, relative to control neurons (5.08 LogFC /negligible in controls). We interpret this to mean that differentiation may have proceeded at a different rate in A-T cells relative to controls.

Whilst the sample size is small and it is known that differentiation kinetics can vary largely [313], we examined the concept that A-T neurons might be poised to differentiate at a noticeably different rate to controls. We performed differentiation using the aforementioned protocol on a further three control and three A-T iPSC lines (sex-matched donor lines were used to control for potential differentiation bias inherent to gender).

A qPCR experiment was designed to test the hypothesis that expression of transcripts informative to differentiation status during early (*Engrailed1/Hoxb4*) and late differentiation (*Math1/Pax6*) would be distinct between control and A-T samples. Primers were designed to span exon-exon boundaries to exclude the possibility of genomic DNA contamination

contributing to PCR signal, as well as DNase treatment of RNA. Primer efficiencies were calculated using pooled cDNA libraries. Melt curves indicated primers were specific via the presence of a sharp peak. A minus *Reverse transcriptase* and no template controls were included to control for reaction contamination/specificity. Nil/negliglbe levels of transcript could be detected from cDNA generated from undifferentiated pluripotent stem cells but could be detected from E16 BL6 mouse cerebellum (a kind gift from Dr Conor O'leary). Sequencing data for differentiated/undifferentiated cells was consulted to inform on suitable housekeeping primer design. *ACTB* and *GAPDH* were chosen given their steady expression at both time points (primer sequences are listed in appendices).

Figure 5.9H (panel A) shows comparable expression of *Engrailed1* mRNA in all six differentiated cell lines (no significant differences One way ANOVA, Kruskall-Wallis test with multiple comparisons). We observed a similar pattern with respect to *Hoxb4* transcript (Panel B). Interestingly, H9b showed strong much lower expression of *Engrailed1* but strong expression of *Math1* and *Pax6* (panels C & D), indicating this cell line had differentiated further than others. Results were pooled by genotype and reassessed using independent statistical methodology (not shown), of which the conclusions were the same.

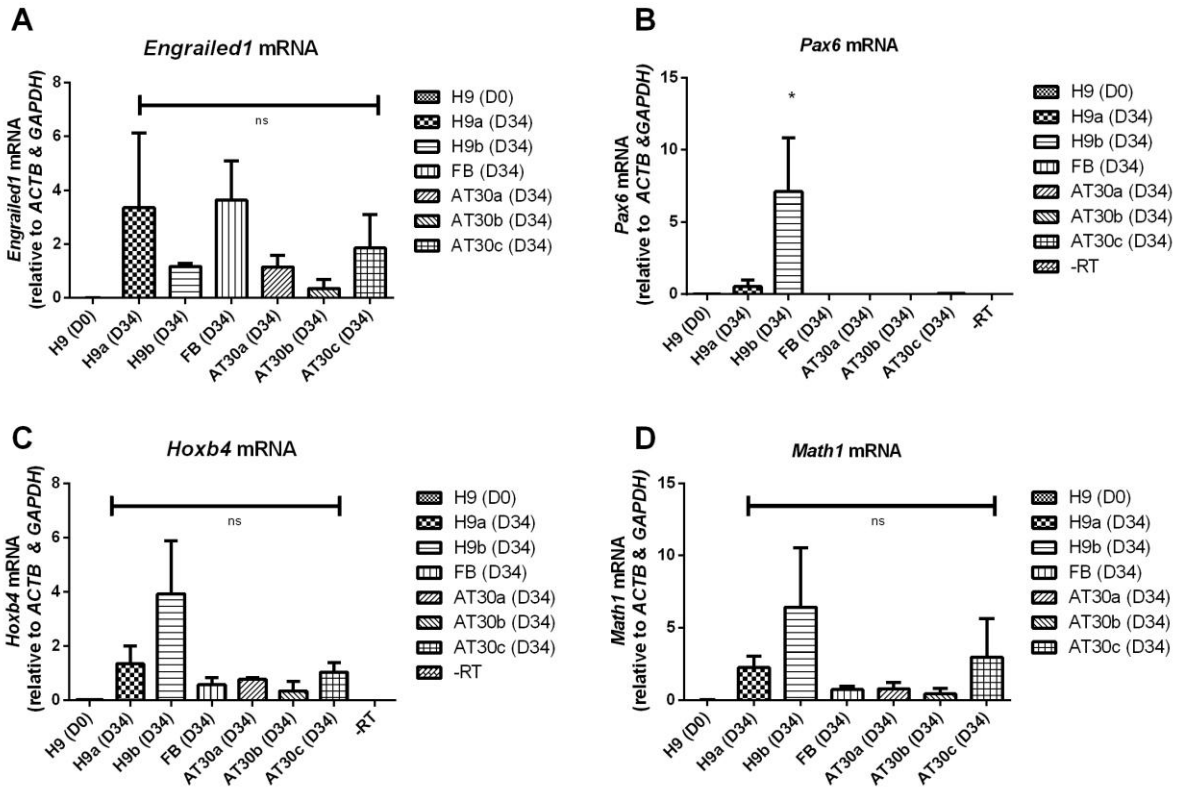

Figure 5.9H- qPCR data shows expression of mid-hindbrain specific genes (A) *Engrailed1*, *(B) Pax6, (C) Hoxb4* and *(D) Math1* after 34 days of differentiation. Transcript was not detected or detected at negligible levels in undifferentiated stem cells (D0) and also no template controls (not shown). –R T controls are shown for *Pax6* and *Hoxb4.* Data has been normalized to *ACTB* and *GAPDH.* Error bars show SEM from three independent experiments. A one way ANOVA (Kruskall-Wallis test) with multiple comparisons was used to ascertain statistical significance.

Taken together we interpret this data in several regards - firstly, we have validated that our differentiation process is reproducible in its ability to induce expression of key markers of the developing mid-hindbrain region in an independent differentiation procedure. These markers were detected in positive control tissue, but not undifferentiated stem cells. We observed that while the majority of differentiated cell lines tested expressed *Engrailed1* and *Hoxb4* at

comparable levels, one cell line showed much stronger expression of more mature markers *Math1* and *Pax6.* Given that *Math1* and *Pax6* are expressed in granule cell progenitors/developing granule neurons, we speculate that H9b represents cells that have differentiated to this stage. Importantly, this shows a strikingly similar pattern of expression (albeit simplified to four key markers) to that observed during RNA sequencing experiments. This suggests that observed differentiation bias was likely not due to ATM status or gender bias, and most probably due to innate differences in differentiation propensities between cell lines. Both of these studies highlight the need for large sample sizes and informative benchmarks or checkpoints to standardize differentiation procedures across experiments and indeed cell lines in the same experiment.

Discussion

The primary utility of induced pluripotent stem cells is to model aspects of a given disorder. This area of the field is in its infancy but developing rapidly. The relative ease with which iPSCs are generated in comparison to derivation of hESCs has made pluripotent stem cells accessible to many laboratories. Similarly, the ethical impediments associated with obtaining and working with such cells are far fewer and the capacity for disease modeling is extensive. Directed differentiation protocols capable of generating a range of cell and tissue types that encapsulate broad and complex genetic backgrounds, are currently being optimized and employed to establish disease models and drug screening platforms for many neurological diseases.

We set out to ascertain whether it was possible to generate neuronal cell types resembling those that are affected in A–T, namely Purkinje and granule cells of the cerebellum. Several groups previously have managed to generate cerebellar-like cells from murine ESCs, while only one group has used human pluripotent stem cells, however these protocols are rudimentary. We combined and optimized these protocols to produce neuroepithelial cells exhibiting gene expression patterns highly reminiscent of the developing mid-hindbrain signaling center and further, to generate hindbrain neuronal cells at high efficiency, as marked by the transcription factors EN1 and GBX2. We showed that it was possible to generate cells that exhibited

expression of transcription factors marking the two major lineages of cerebellar progenitor (MATH1 & PTF1α), which give rise to granule cells and Purkinje cells respectively, *in vivo*. Following further differentiation, these cultured cells developed morphological characteristics of immature granule cells and expression of granule cell markers such as PAX6, B-III-TUBULIN and ZIC1. Using standard culture conditions we were unable to isolate the putative Purkinje cells or culture granule cells for extended periods of time, demonstrating that further optimization of growth factor regimes and modification of the microenvironment remains to be achieved. This is in keeping with recent work by Muguruma et al. who demonstrated that after isolation of NEPH3 positive Purkinje cell precursors, growth in conventional high-density culture settings showed gradual cell death and failure to express late Purkinje cell markers such as L7 and calbindin [220]. An approach utilizing feeder layers or 3d scaffolds resembling ECM features of the developing cerebellum may assist in this regard by providing cues which are critical for processes such as neuronal activity, migration and maturation. Nevertheless, this work is, to our knowledge the only exemplification of a cerebellar disease being modeled in iPSC-derived cerebellar-like cells.

We performed RNA sequencing on control and A–T neuronal inductions, as well as their respective undifferentiated counterparts. Sequencing quality control indicated a high level of sequence coverage and a robust and reliable dataset with tight experimental replicates.

Over the course of the differentiation both AT30 and C11 downregulated pluripotency genes and upregulated neural commitment, anterior/posterior patterning gene programs. More specifically, after 34 days of differentiation both cell lines exhibited expression of a number of well characterized genes driving cerebellar development which were highly coordinately regulated, such as *Isl1, Meis1, Shh, Reelin, Lhx9* and *Nfix.* Expression of members of the *Hox* gene family were tightly regulated providing further evidence that control and A-T cells existed in a similar developmental space. We noted several important exceptions to this, namely the absence of expression of *Atoh1* and *Hoxb4* expression in C11 control iPSCs after 34 days of differentiation leading us to theorize that C11 may represent a more immature cerebellar neuronal progenitor than AT30. It should however be noted that we detected widespread activity of downstream

ATOH1 targets in both C11 and AT30 when comparing our gene expression data with a recently published ATOH1 targetome dataset [314].This may be attributable to the fact that ATOH1 targets can build up in the absence of ATOH1 to sufficient levels to sustain the differentiation process of the developing cerebellar cortex alone [314, 315].

We observed a number of non-coding RNAs and small miRNA precursors that are known to be expressed in the developing cerebellum *in vivo*, supporting the claim that we had generated cerebellar precursors.

We observed a number of differences when comparing the day 34 transcriptomes of AT30 and C11. Interestingly, IPA predicted with high confidence gene expression patterns indicative of neurological disease, and in particular progressive motor neuropathy and cerebellar ataxia, major hallmarks of A–T. This exemplifies the concept that iPS cells can be used for disease modeling purposes and presents a unique window of human brain development, which has not been previously investigated. We were able to detect gene expression evidence that is congruous with a number of theories based on other cellular systems and animal models regarding the nature of the neurodegeneration in A–T. These include the commonly held theory [180, 316] that ROS levels are misregulated and adversely affect the cerebellum – Indeed in our dataset two of the most highly upregulated genes in A–T neuronal cells were *GSTT1* and *CATALASE*, important factors in the clearance of damaging ROS intermediates. In contrast to current hypotheses our data suggest that this may be an early event in the development of the cerebellum, rather than a progressive accumulation that affects the brain later in life. In further support of this, we noticed misregulation of a number of ERK1/2 substrates. This is significant because ERK1/2 is critical in maintaining redox balance, and is a known target of ATM [275].

The equally prevalent notion that ATM maintains genomic fidelity of neural precursors and resulting progeny during development was represented in our dataset as well. We detected significant downregulation of a number of MYC substrates. MYC is required for activation of the ATM dependent DNA damage response and also critically required for neurogenesis [279,

280]. Further to this, we detected differential regulation of *Tp53* and *Pcna,* two important transducers of DNA damage and regulators of cell cycle control.

A recent study implicated cytoplasmic ATM in the regulation of long-term potentiation and vesicular release in cultured neuronal cells. Our expression profiling supports this notion by revealing significant changes in the network constituents governing the process of Long-term potentiation. While Li et al. [7] showed this defect in cultured Hippocampal neurons, our data suggest that this phenomenom extends also to cerebellar neurons, however this will require functional studies to confirm.

In contradiction to a report from Oka & Takashima [13], we noticed downregulation of *Atm* during differentiation (however it should be noted that this is relative to *Atm* expression in pluripotent stem cells). Further studies with the A–T iPSCs generated in this thesis would benefit greatly from sequencing at multiple developmental time points. It is important to examine the kinetics of *Atm* activity, as if a sharp peak in *Atm* expression could be identified and correlated with a particular developmental event, this may shed light on the origin and onset of this disease.

The capacity for using iPSCs for discovery of novel disease phenotypes and the molecular mechanisms underlying these events is promising, however in the current study we contended with the issue of low replicate number and the resulting underpowered statistical significance. Another major confounding factor centered on the comparison of a slightly different, and not fully defined, population of cells. Nevertheless a number of interesting and novel candidates for involvement in cerebellar neurodegeneration in A–T were prominent and warrant further validation. These included aberrant regulation of glutamate receptor signaling, CREB signaling and axonal guidance pathways. Interestingly, Carlessi et al. [212] showed neuronal differentiation bias after ATM knockdown with neuronal progenitors consistently producing fewer GABAergic neurons. Although we did not quantify the ratios of GLUTAmatergic to GABAergic neurons, the fact that we observe extensive upregulation of genes involved with glutamate receptor signaling may support the notion that such a bias also exists in our cultures. One of the most highly differentially expressed genes between A–T and control neurons was

Hes5, the basic helix-loop helix notch effector gene. A recent study shows knockdown of DNA-PK to result in upregulation of *Lmx1a* activity resulting in biased regional specific neuronal specification, in which *Hes5* was implicated [273]. It would be interesting to validate the proportions of neuronal progenitors at various timepoints throughout differentiation to see if such a bias exists in the absence of ATM, however this will require a greater degree of understanding regarding the temporal expression of cell-surface markers which delineate specific neuronal sub-populations, work currently underway in the Wolvetang laboratory.

This dataset provides a rich resource for examining neuronal specific isoforms and splicing events, which may be perturbed in the absence of ATM. We are pursuing both these aspects aswell as the behaviour of repeat elements such as LINE1, however this extends beyond the scope of this thesis and here we have focused on differential gene expression analysis.

These data are a valuable resource for researchers to formulate and test hypotheses regarding the early developmental events that occur in the absence of ATM. It does however represent only a snapshot in time and ideally, further timepoints, clones and patients/ATM mutants should be sequenced in order to garner more statistical confidence. Isogenic controls, generated using technologies such as TALENs or CRISPRs may help reduce biological variability in terms of background genetic differences and differenetiation potential. We hope that this dataset may also be used to obtain some insight into the origins of A–T and also reveal clues about what may constitute suitable conditions for the further growth and expansion of cerebellar neurons that could be used for drug screening to ameliorate symptoms associated with A–T.

6.0 Discussion and future direction

Since the advent of the iPS cell [16], research into development and disease has undergone a renaissance. Previously, researchers relied on tools such as fibroblasts/lymphoblastoid cell lines, animal models and pathological tissue to answer basic research questions. Now, with relative ease, iPSCs can be generated from patients with various diseases. These cells reflect the complex genetic background of a given disease and supercede models that may aim to knock down or abolish gene or protein activity with variable efficiency. Pluripotent stem cells provide insight into early developmental events that may precede the onset of disease, such as the loss of genomic integrity, dysregulation of pathways that govern pluripotency leading to differentiation bias, defective autophagy/mitophagy or other biochemical abnormalities [40, 143, 146, 147]. If the currently accepted hypothesis holds true, that iPSCs are functionally equivalent with hESCs, these models allow researchers to interrogate happenings from a very early time point of human development – the development of the blastocyst.

We reported the first generation of iPSCs from patients with Ataxia–Telangiectasia using a lentiviral-based methodology [147]. Subsequent similar reports have followed [190, 196]. Following this, we generated iPSCs from A–T patients using integration-free technologies (Unpublished data – Jian Sun). Non-virally generated iPSCs from A–T patients did not show a large difference in reprogramming efficiency indicating that the response to the viral transduction itself may have been responsible for the impaired reprogramming kinetics initially observed (data not shown). A–T is a disease with an unknown underlying etiology and no current effective treatment, thus making it an excellent candidate for the establishment of a pluripotent stem cell model.

Given the role for ATM in the maintenance of genomic fidelity, we used iPSCs generated from patients with A–T to study several aspects related to this. A large proportion of the current understanding within this area is reliant on data generated from cellular models such as fibroblasts and lymphoblastoid cells and as such, represents a snapshot of a much larger picture. In recent times, and as use of pluripotent stem cells grows more mainstream, interest has shifted to understanding the pathways and mechanisms that govern the maintenance of genomic fidelity

in pluripotent stem cells and their resulting progeny. As pluripotent stem cells give rise to the cells and tissues that completely constitute an organism, the burden to maintain a stable genome is paramount. As a result of this, expression of DNA damage repair and signaling genes are heavily upregulated [79, 82, 83]. ATM was shown to activate signaling pathways in embryonic stem cells [79, 81] and to be required for arrest at the G2M phase of the cell cycle after treatment with IR [15, 80]. We have shown this to be the case for iPSCs also, demonstrating that in iPSCs ATM undergoes activation by autophosphorylation at Serine 1981 and signals to downstream substrates involved with DNA repair and cell cycle control. We showed this process to be defective in iPSCs generated from A–T patients [147]. Similarly we demonstrated that unlike iPSCs from control individuals, A–T iPSCs were resistant to damage-induced G2M arrest and also exhibited radioresistant DNA synthesis. Although we used IR to illicit this response, an agent that may not necessarily occur during embryonic development, this concept represents a paradigm which supports the theory that loss of ATM may lead to accumulation of stem cells harboring unchecked genetic abnormalities.

There is compelling evidence that ATM is redundant for the repair of DNA damage and maintenance of genomic fidelity in the absence of exogenous DNA damage sources. ESCs are thought to primarily use HRR instead of the error prone NHEJ – a claim supported by the observation of a 10-fold higher rate of RAD51 foci formation in ESCs in comparison to differentiated astrocytes from the same cell line [84]. Our microarray data support the idea that in differentiated cells (in this case parental fibroblasts) loss of ATM dramatically impacts levels of basal cell cycle regulation and DNA repair activity, whereas disruption to these pathways are minimal in pluripotent stem cells lacking ATM.

Our microarray data point to a number of differences that warrant further investigation, including Cytoskeletal remodeling pathways, focal adhesion, ECM pathways, TGFβ receptor signaling, pentose phosphate signaling and oxidative phosphorylation. We choose to focus on differences at the level of the mitochondrion. In the transition from fibroblast to iPS cell, a shift occurs in energy consumption dynamics whereby the energy requirements of the cells are met by changing levels of oxidative phosphorylation, highlighting the distinct metabolic differences

between these two cell types. While it is a possibility that differences in oxidative phosphorylation gene expression arose because our A–T iPSCs were reprogrammed to a different state to that of our controls, we do not think this is the case for three main reasons; firstly, our A–T iPSCs adhere to all known criteria for pluripotency and cluster strongly with control iPSCs and ESCs when examining genes from the *Plurinet*. Secondly, we show a similar and overlapping subset of disruptions to oxidative phosphorylation pathways between control and A–T fibroblasts. Finally, we report differences that are consistent with recent reports in the literature, implicating ATM in mitochondrial homeostasis [5, 113, 195, 196]. While these publications point to mitochondrial differences in a variety of cells such as lymphoblastoid cells thymocytes and an undefined population of neurons, we point to differences in pluripotent stem cells which could be thought to occur upstream of the development of all these cells/tissues. This brings to light interesting questions regarding the nature of the onset of these mitochondrial differences and whether they are as a result of abnormalities that are acquired early during development. There is a rich array of literature [114, 176, 193] supporting the involvement of mitochondria in a number of other neurodegenerative diseases and we both eagerly await and are actively pursuing enlightenment in this regard with respect to A–T.

While differences in mitochondrial gene expression in iPSCs did not seem to significantly alter mitochondrial membrane potential (as a measure of mitochondrial health), we suspected that as the demand for energy increases and switches to a state more reliant on oxidative phosphorylation, such as during the process of neurogenesis and or downstream neuronal metabolism, these differences may manifest more overtly. To test this theory we subjected control and A–T iPSCs to neuronal differentiation to produce neural progenitors and comitted neuronal cells.

Through directed differentiation protocols, particular phenotypes that are localized to specific cell types can be observed, manipulated and studied [43, 55, 196]. To examine whether we could model the neurodegenerative aspect of A–T in iPSC derived neuronal cells, we embarked upon two separate lines of inquiry; a) to detect evidence that ATM deficiency resulted in gross deficits in general neuronal induction and maintenance, including differentiation efficiency, growth and

expansion and neuronal activity and b) the production of neuronal progenitors characteristic of the developing cerebellum, in order to more specifically model this disease.

Through general modeling of neurogenesis using an SB431542/Dorsomorphin based induction protocol we showed that iPSCs from patients with A–T generated neurons that could be expanded in culture at a similar rate to those of controls. Similarly, when we quantified the two main species of cells present in these inductions, we detected no evidence that loss of ATM impacted on the process of differentiation or neuronal specification. We observed that these neurons extended axons at a similar rate and formed connections with each other while expressing punctate staining for the synaptic marker SYNAPSIN. These neurons exhibited Sodium/Potassium currents and the ability to traffic calcium in response to stimulus. We examined calcium trafficking using a high throughput plate-reader based assay and the fluorescent calcium indicator FLUO-4-AM, as well as a single-cell based imaging approach using the genetically encoded calcium reporter gCaMP5. We were able to identify a reproducible defect in calcium trafficking that occurred in select lines only, which warrants further investigation. Despite the use of ATM inhibitor, calcium channel and mitochondrial inhibitors we were not able to isolate or identify the nature of this deficiency and speculate that it may be the complex culmination of genetic background and differentiation induced population dynamics.

Interestingly, we show that application of KCl induces neuronal activity in the form of calcium trafficking and upregulation of IEGs, and that this also induced an elevation in the number of DNA double-strand breaks, as marked by phosphorylation of H2AX. We observed that these breaks were accumulated and repaired with differential kinetics in A–T neuronal cells suggesting a novel potential mechanism for neurodegeneration in A–T. A recent paper [211] illustrates the induction of DNA DSBs in the brains of mice in response to exposure to novel environments. It remains to be seen what physiological roles these breaks may play and how ATM is involved.

We executed a number of experiments centered around modeling previously described aspects of A–T speculated to cause neurodegeneration, including mislocaisation of HDAC4, neurite

extension rate (in the presence and absence of novel antioxidant compound CTMIO), mitochondrial metabolism, calcium trafficking, and DNA repair. We show that this model system represents a valuable tool for investigating A–T, however, we could not point to any specific mechanisms that might be adapted for use as readouts in a drug-screening assay.

A concept that will be required if cell replacement therapies are ever to occur is that of genetic correction of the underlying pathogenic mutation (or a suitable workaround to providing a patient with their own cells, such as immune supression). We were able to show restoration of a functional DNA damage induced phenotype through delivery of mCherry-tagged ATM, demonstrating that genetic manipulation and correction of neurons/neural stem cells is possible. Although this was at low efficiency, there are a number of approaches to utilize burgeoning technologies such as TALEs and CRISPRs that may be utilized to generate, select and produce pure populations of cells that may be suitable for transplantation. These technologies can also be used to generate isogenic controls to study, which are important given that genetic variation across individuals can confound studies.

The field contends with the notion that neurological diseases can be modeled using neuronal cells generated from iPSCs. While in principle this holds true, the fact is that the brain is one of the most complicated structures known to exist and that our ability to reproduce it in part is in its primitive infancy. Two main issues crystalize this notion. The first being that there is a general trend towards publishing a disease model coupled with an unclassified ‘neuronal’ cell population, and whilst this may be useful, it makes the interpretation of data difficult and comparison between studies impossible. The genetic background of a given disease may or may not grossly affect production of neurons in a way that is informative of the *in* vivo biology of the disease. The second issue is that production of neurons *in vitro* generally gives rise to immature cells and that the existing knowledge on specific selection of subtypes of neurons is limited. While it is possible to reproduce several core elements of neurogenesis *in vitro* the environmental cues that neurons receive in the developing and postnatal brains may be vastly different than anything that is possible to produce. For example it is known that neurons are reliant on bursts of neuronal activity for various stages of maturation [317]. Model *in vitro*

systems may not be able to reproduce these processes fully and as a result the end product is an immature neuronal population. While we initially embarked upon an untargeted approach, we moved to adopt a protocol that favored the use of molecules aimed at recapitulating a normal developmental program through stepwise progression. Nevertheless, the fact that limited knowledge exists on human brain development in terms of classification of useful markers to identify and isolate particular neuronal subtypes at various time points is a formidable barrier. We showed through application of retinoic acid and FGF8 that we were able to induce gene expression changes that are highly similar to patterns known to occur in the developing mid-hindbrain junction (Upregulation of *Hoxb4* & *Gbx2* and downregulation of *Otx2*). We identified induction of GBX2 and ENGRAILED1 and the subsequent expression of MATH1 & PTF1A, marking the two main cerebellar progenitor types. Further to this we could isolate neuronal cells that were reactive with antibodies to ZIC3, PAX6 and B-III-TUBULIN and that showed largely morphology consistent with developing cerebellar granule neurons. We also noted the sporadic appearance of a much larger neuronal subtype with multiple and elaborate branching dendrites, which we could not isolate or culture for extended periods, which we speculate to be the other main constituent of the cerebellar cortex, the Purkinje cell. While a wealth of information from animal developmental biology studies aids in the understanding of the developmental cascade which unfolds *in vivo* and which we have tried to recapitulate *in vitro*, neurogenesis is still drastically different in mouse than it is in human and as a result, useful information is limited. For example it would be ideal if surface markers could be identified that delineate the different neuronal progenitor types at different stages, allowing purification, analysis and expansion. Technologies such as smart FLARES or plasmid-based selection approaches may be used to identify and derive specific neuronal sub-populations.

We carried out RNA sequencing on a population we knew to be largely positive for hindbrain specific markers, but was otherwise undefined. Analysis of this dataset showed global gene expression profiles similar to that of brain samples, however we were not able to show more definitively where our cells lay on a developmental spectrum by direct comparison to datasets from developing brain regions, because of technical differences & limitations. Gene expression from these samples, including non-coding RNAs supported the notion that we had generated

primitive cerebellar progenitors. This provides a window of insight into the development of the A–T brain with unprecedented resolution. Findings from gene ontology analysis (both DAVID_UP tissue module and PANTHER phylogeny), IPAand manual curation of the genelist supported the concept that there were innate differences in differentiation status of the cells studied. This brings to light an interesting question, being ‘How similar/well-defined must a stem cell-derived population be before comparisons are valid or the population is considered characterised?’ We suspect this is a question that many people are currently trying to answer and speculate that the solution will be at the interface between a deeper biological understanding of the cell type and smarter informatics approaches.

Examination of these datasets revealed gene expression consistent with a number of theories regarding the neurodegenerative aspect of A–T and may provide further clarity in these regards pertaining to their temporal onset and the gene regulatory networks that surround them. We are particularly interested in developing this model further to produce mature granule and Purkinje cells and hope that this dataset will be of use in predicting conditions to foster growth and expansion of these cell types. Ideally these cells would allow for the screening of drugs that could improve the lives of people living with A–T.

References and bibliography

1. Shiloh, Y. and G. Rotman, *Ataxia-telangiectasia and the ATM gene: linking neurodegeneration, immunodeficiency, and cancer to cell cycle checkpoints.* J Clin Immunol, 1996. **16**(5): p. 254-60.
2. Sanal, O., et al., *Further mapping of an ataxia-telangiectasia locus to the chromosome 11q23 region.* Am J Hum Genet, 1990. **47**(5): p. 860-6.
3. Hawley, R.S. and S.H. Friend, *Strange bedfellows in even stranger places: the role of ATM in meiotic cells, lymphocytes, tumors, and its functional links to p53.* Genes Dev, 1996. **10**(19): p. 2383-8.
4. Wood, L.M., et al., *A novel role for ATM in regulating proteasome-mediated protein degradation through suppression of the ISG15 conjugation pathway.* PLoS One, 2011. **6**(1): p. e16422.
5. Ambrose, M., J.V. Goldstine, and R.A. Gatti, *Intrinsic mitochondrial dysfunction in ATM-deficient lymphoblastoid cells.* Hum Mol Genet, 2007. **16**(18): p. 2154-64.
6. Bar, R.S., et al., *Extreme insulin resistance in ataxia telangiectasia: defect in affinity of insulin receptors.* N Engl J Med, 1978. **298**(21): p. 1164-71.
7. Li, J., et al., *Cytoplasmic ATM in neurons modulates synaptic function.* Curr Biol, 2009. **19**(24): p. 2091-6.
8. Lim, D.S., et al., *ATM binds to beta-adaptin in cytoplasmic vesicles.* Proc Natl Acad Sci U S A, 1998. **95**(17): p. 10146-51.
9. Cosentino, C., D. Grieco, and V. Costanzo, *ATM activates the pentose phosphate pathway promoting anti-oxidant defence and DNA repair.* EMBO J, 2011. **30**(3): p. 546-55.
10. Li, J., et al., *Nuclear accumulation of HDAC4 in ATM deficiency promotes neurodegeneration in ataxia telangiectasia.* Nat Med, 2012. **18**(5): p. 783-90.
11. Guo, Z., R. Deshpande, and T.T. Paull, *ATM activation in the presence of oxidative stress.* Cell Cycle, 2010. **9**(24): p. 4805-11.
12. Guo, Z., et al., *ATM activation by oxidative stress.* Science, 2011. **330**(6003): p. 517-21.
13. Oka, A. and S. Takashima, *Expression of the ataxia-telangiectasia gene (ATM) product in human cerebellar neurons during development.* Neurosci Lett, 1998. **252**(3): p. 195-8.
14. Barlow, C., et al., *ATM is a cytoplasmic protein in mouse brain required to prevent lysosomal accumulation.* Proc Natl Acad Sci U S A, 2000. **97**(2): p. 871-6.
15. Song, H., S.K. Chung, and Y. Xu, *Modeling disease in human ESCs using an efficient BAC-based homologous recombination system.* Cell Stem Cell, 2010. **6**(1): p. 80-9.
16. Takahashi, K. and S. Yamanaka, *Induction of pluripotent stem cells from mouse embryonic and adult fibroblast cultures by defined factors.* Cell, 2006. **126**(4): p. 663-76.
17. Thomson, J.A., et al., *Embryonic stem cell lines derived from human blastocysts.* Science, 1998. **282**(5391): p. 1145-7.
18. Boiani, M. and H.R. Scholer, *Regulatory networks in embryo-derived pluripotent stem cells.* Nat Rev Mol Cell Biol, 2005. **6**(11): p. 872-84.

19. Martin, G.R., *Isolation of a pluripotent cell line from early mouse embryos cultured in medium conditioned by teratocarcinoma stem cells.* Proc Natl Acad Sci U S A, 1981. **78**(12): p. 7634-8.
20. Bongso, A., et al., *Isolation and culture of inner cell mass cells from human blastocysts.* Hum Reprod, 1994. **9**(11): p. 2110-7.
21. Schwartz, S.D., et al., *Embryonic stem cell trials for macular degeneration: a preliminary report.* Lancet, 2012. **379**(9817): p. 713-20.
22. Deuse, T., et al., *Human leukocyte antigen I knockdown human embryonic stem cells induce host ignorance and achieve prolonged xenogeneic survival.* Circulation, 2011. **124**(11 Suppl): p. S3-9.
23. Campbell, K.H., et al., *Sheep cloned by nuclear transfer from a cultured cell line.* Nature, 1996. **380**(6569): p. 64-6.
24. De Felici, M., D. Farini, and S. Dolci, *In or out stemness: comparing growth factor signalling in mouse embryonic stem cells and primordial germ cells.* Curr Stem Cell Res Ther, 2009. **4**(2): p. 87-97.
25. Passier, R., L.W. van Laake, and C.L. Mummery, *Stem-cell-based therapy and lessons from the heart.* Nature, 2008. **453**(7193): p. 322-9.
26. Baker, M., *iPS cells: potent stuff.* Nat Methods, 2010. **7**(1): p. 17-9.
27. Okita, K., T. Ichisaka, and S. Yamanaka, *Generation of germline-competent induced pluripotent stem cells.* Nature, 2007. **448**(7151): p. 313-7.
28. Wernig, M., et al., *In vitro reprogramming of fibroblasts into a pluripotent ES-cell-like state.* Nature, 2007. **448**(7151): p. 318-24.
29. Maherali, N., et al., *Directly reprogrammed fibroblasts show global epigenetic remodeling and widespread tissue contribution.* Cell Stem Cell, 2007. **1**(1): p. 55-70.
30. Wernig, M., et al., *c-Myc is dispensable for direct reprogramming of mouse fibroblasts.* Cell Stem Cell, 2008. **2**(1): p. 10-2.
31. Takahashi, K., et al., *Induction of pluripotent stem cells from adult human fibroblasts by defined factors.* Cell, 2007. **131**(5): p. 861-72.
32. Yu, J., et al., *Induced pluripotent stem cell lines derived from human somatic cells.* Science, 2007. **318**(5858): p. 1917-20.
33. Zhou, W. and C.R. Freed, *Adenoviral gene delivery can reprogram human fibroblasts to induced pluripotent stem cells.* Stem Cells, 2009. **27**(11): p. 2667-74.
34. Chang, C.W., et al., *Polycistronic lentiviral vector for "hit and run" reprogramming of adult skin fibroblasts to induced pluripotent stem cells.* Stem Cells, 2009. **27**(5): p. 1042-9.
35. Zhou, H., et al., *Generation of induced pluripotent stem cells using recombinant proteins.* Cell Stem Cell, 2009. **4**(5): p. 381-4.
36. Yu, J., et al., *Human induced pluripotent stem cells free of vector and transgene sequences.* Science, 2009. **324**(5928): p. 797-801.
37. Warren, L., et al., *Highly efficient reprogramming to pluripotency and directed differentiation of human cells with synthetic modified mRNA.* Cell Stem Cell. **7**(5): p. 618-30.
38. Warren, L., et al., *Highly efficient reprogramming to pluripotency and directed differentiation of human cells with synthetic modified mRNA.* Cell Stem Cell, 2010. **7**(5): p. 618-30.

39. Woltjen, K., et al., *piggyBac transposition reprograms fibroblasts to induced pluripotent stem cells.* Nature, 2009. **458**(7239): p. 766-70.
40. Marion, R.M., et al., *A p53-mediated DNA damage response limits reprogramming to ensure iPS cell genomic integrity.* Nature, 2009. **460**(7259): p. 1149-53.
41. Chan, E.M., et al., *Live cell imaging distinguishes bona fide human iPS cells from partially reprogrammed cells.* Nat Biotechnol, 2009. **27**(11): p. 1033-7.
42. Ohi, Y., et al., *Incomplete DNA methylation underlies a transcriptional memory of somatic cells in human iPS cells.* Nat Cell Biol, 2011. **13**(5): p. 541-9.
43. Brennand, K.J., et al., *Modelling schizophrenia using human induced pluripotent stem cells.* Nature, 2011. **473**(7346): p. 221-5.
44. Dimos, J.T., et al., *Induced pluripotent stem cells generated from patients with ALS can be differentiated into motor neurons.* Science, 2008. **321**(5893): p. 1218-21.
45. Loh, Y.H., et al., *Generation of induced pluripotent stem cells from human blood.* Blood, 2009. **113**(22): p. 5476-9.
46. Tsai, S.Y., et al., *Single transcription factor reprogramming of hair follicle dermal papilla cells to induced pluripotent stem cells.* Stem Cells, 2011. **29**(6): p. 964-71.
47. Zhou, T., et al., *Generation of induced pluripotent stem cells from urine.* J Am Soc Nephrol, 2011. **22**(7): p. 1221-8.
48. Juopperi, T.A., H. Song, and G.L. Ming, *Modeling neurological diseases using patient-derived induced pluripotent stem cells.* Future Neurol, 2011. **6**(3): p. 363-373.
49. Bjorklund, L.M., et al., *Embryonic stem cells develop into functional dopaminergic neurons after transplantation in a Parkinson rat model.* Proc Natl Acad Sci U S A, 2002. **99**(4): p. 2344-9.
50. Deacon, T., et al., *Blastula-stage stem cells can differentiate into dopaminergic and serotonergic neurons after transplantation.* Exp Neurol, 1998. **149**(1): p. 28-41.
51. Kim, J.H., et al., *Dopamine neurons derived from embryonic stem cells function in an animal model of Parkinson's disease.* Nature, 2002. **418**(6893): p. 50-6.
52. Roy, N.S., et al., *Functional engraftment of human ES cell-derived dopaminergic neurons enriched by coculture with telomerase-immortalized midbrain astrocytes.* Nat Med, 2006. **12**(11): p. 1259-68.
53. Connolly, B. and S.H. Fox, *Treatment of Cognitive, Psychiatric, and Affective Disorders Associated with Parkinson's Disease.* Neurotherapeutics, 2013.
54. Maehr, R., et al., *Generation of pluripotent stem cells from patients with type 1 diabetes.* Proc Natl Acad Sci U S A, 2009. **106**(37): p. 15768-73.
55. Soldner, F., et al., *Parkinson's disease patient-derived induced pluripotent stem cells free of viral reprogramming factors.* Cell, 2009. **136**(5): p. 964-77.
56. Ebert, A.D., et al., *Induced pluripotent stem cells from a spinal muscular atrophy patient.* Nature, 2009. **457**(7227): p. 277-80.
57. Marchetto, M.C., et al., *A model for neural development and treatment of Rett syndrome using human induced pluripotent stem cells.* Cell, 2010. **143**(4): p. 527-39.
58. Zhang, N., et al., *Characterization of Human Huntington's Disease Cell Model from Induced Pluripotent Stem Cells.* PLoS Curr, 2010. **2**: p. RRN1193.
59. Liu, J., et al., *Generation of induced pluripotent stem cell lines from friedreich ataxia patients.* Stem Cell Rev, 2011. **7**(3): p. 703-13.

60. Ku, S., et al., *Friedreich's ataxia induced pluripotent stem cells model intergenerational GAATTC triplet repeat instability.* Cell Stem Cell, 2010. **7**(5): p. 631-7.
61. Raya, A., et al., *Disease-corrected haematopoietic progenitors from Fanconi anaemia induced pluripotent stem cells.* Nature, 2009. **460**(7251): p. 53-9.
62. Miranda, C.J., et al., *Frataxin overexpressing mice.* FEBS Lett, 2004. **572**(1-3): p. 281-8.
63. Coppola, G., et al., *Gene expression profiling in frataxin deficient mice: microarray evidence for significant expression changes without detectable neurodegeneration.* Neurobiol Dis, 2006. **22**(2): p. 302-11.
64. Gatti, R.A., et al., *Ataxia-telangiectasia: an interdisciplinary approach to pathogenesis.* Medicine (Baltimore), 1991. **70**(2): p. 99-117.
65. Kurz, E.U. and S.P. Lees-Miller, *DNA damage-induced activation of ATM and ATM-dependent signaling pathways.* DNA Repair (Amst), 2004. **3**(8-9): p. 889-900.
66. Su, Y. and M. Swift, *Mortality rates among carriers of ataxia-telangiectasia mutant alleles.* Ann Intern Med, 2000. **133**(10): p. 770-8.
67. McKinnon, P.J., *ATM and ataxia telangiectasia.* EMBO Rep, 2004. **5**(8): p. 772-6.
68. Gatti, R.A., et al., *Localization of an ataxia-telangiectasia gene to chromosome 11q22-23.* Nature, 1988. **336**(6199): p. 577-80.
69. Savitsky, K., et al., *A single ataxia telangiectasia gene with a product similar to PI-3 kinase.* Science, 1995. **268**(5218): p. 1749-53.
70. Brumbaugh, K.M., et al., *The mRNA surveillance protein hSMG-1 functions in genotoxic stress response pathways in mammalian cells.* Mol Cell, 2004. **14**(5): p. 585-98.
71. Savitsky, K., et al., *The complete sequence of the coding region of the ATM gene reveals similarity to cell cycle regulators in different species.* Hum Mol Genet, 1995. **4**(11): p. 2025-32.
72. Lempiainen, H. and T.D. Halazonetis, *Emerging common themes in regulation of PIKKs and PI3Ks.* EMBO J, 2009. **28**(20): p. 3067-73.
73. Lavin, M.F., *Ataxia-telangiectasia: from a rare disorder to a paradigm for cell signalling and cancer.* Nat Rev Mol Cell Biol, 2008. **9**(10): p. 759-69.
74. Xu, Y., et al., *Targeted disruption of ATM leads to growth retardation, chromosomal fragmentation during meiosis, immune defects, and thymic lymphoma.* Genes Dev, 1996. **10**(19): p. 2411-22.
75. Shiloh, Y. and M.B. Kastan, *ATM: genome stability, neuronal development, and cancer cross paths.* Adv Cancer Res, 2001. **83**: p. 209-54.
76. Brown, K.D., et al., *The ataxia-telangiectasia gene product, a constitutively expressed nuclear protein that is not up-regulated following genome damage.* Proc Natl Acad Sci U S A, 1997. **94**(5): p. 1840-5.
77. Lavin, M.F., *Radiosensitivity and oxidative signalling in ataxia telangiectasia: an update.* Radiother Oncol, 1998. **47**(2): p. 113-23.
78. Adams, B.R., et al., *ATM-independent, high-fidelity nonhomologous end joining predominates in human embryonic stem cells.* Aging (Albany NY), 2010. **2**(9): p. 582-96.
79. Momcilovic, O., et al., *DNA damage responses in human induced pluripotent stem cells and embryonic stem cells.* PLoS One, 2011. **5**(10): p. e13410.

80. Momcilovic, O., et al., *Ionizing radiation induces ataxia telangiectasia mutated-dependent checkpoint signaling and G(2) but not G(1) cell cycle arrest in pluripotent human embryonic stem cells.* Stem Cells, 2009. **27**(8): p. 1822-35.
81. Filion, T.M., et al., *Survival responses of human embryonic stem cells to DNA damage.* J Cell Physiol, 2009. **220**(3): p. 586-92.
82. Fan, J., et al., *Human induced pluripotent cells resemble embryonic stem cells demonstrating enhanced levels of DNA repair and efficacy of nonhomologous end-joining.* Mutat Res, 2011. **713**(1-2): p. 8-17.
83. Momcilovic, O., C. Navara, and G. Schatten, *Cell cycle adaptations and maintenance of genomic integrity in embryonic stem cells and induced pluripotent stem cells.* Results Probl Cell Differ, 2011. **53**: p. 415-58.
84. Adams, B.R., et al., *Dynamic dependence on ATR and ATM for double-strand break repair in human embryonic stem cells and neural descendants.* PLoS One, 2010. **5**(4): p. e10001.
85. Amit, M., et al., *Clonally derived human embryonic stem cell lines maintain pluripotency and proliferative potential for prolonged periods of culture.* Dev Biol, 2000. **227**(2): p. 271-8.
86. Becker, K.A., et al., *Establishment of histone gene regulation and cell cycle checkpoint control in human embryonic stem cells.* J Cell Physiol, 2007. **210**(2): p. 517-26.
87. Abraham, R.T., *Cell cycle checkpoint signaling through the ATM and ATR kinases.* Genes Dev, 2001. **15**(17): p. 2177-96.
88. Yao, G., et al., *Origin of bistability underlying mammalian cell cycle entry.* Mol Syst Biol, 2011. **7**: p. 485.
89. Barta, T., et al., *Human embryonic stem cells are capable of executing G1/S checkpoint activation.* Stem Cells, 2010. **28**(7): p. 1143-52.
90. Sumi, T., et al., *Apoptosis and differentiation of human embryonic stem cells induced by sustained activation of c-Myc.* Oncogene, 2007. **26**(38): p. 5564-76.
91. Wilson, K.D., et al., *Effects of ionizing radiation on self-renewal and pluripotency of human embryonic stem cells.* Cancer Res, 2010. **70**(13): p. 5539-48.
92. Goodarzi, A.A., et al., *ATM signaling facilitates repair of DNA double-strand breaks associated with heterochromatin.* Mol Cell, 2008. **31**(2): p. 167-77.
93. Meshorer, E., et al., *Hyperdynamic plasticity of chromatin proteins in pluripotent embryonic stem cells.* Dev Cell, 2006. **10**(1): p. 105-16.
94. Kawamura, T., et al., *Linking the p53 tumour suppressor pathway to somatic cell reprogramming.* Nature, 2009. **460**(7259): p. 1140-4.
95. Kinoshita, T., et al., *Ataxia-telangiectasia mutated (ATM) deficiency decreases reprogramming efficiency and leads to genomic instability in iPS cells.* Biochem Biophys Res Commun, 2011. **407**(2): p. 321-6.
96. Hussein, S.M., et al., *Copy number variation and selection during reprogramming to pluripotency.* Nature, 2011. **471**(7336): p. 58-62.
97. Woods, C.G. and A.M. Taylor, *Ataxia telangiectasia in the British Isles: the clinical and laboratory features of 70 affected individuals.* Q J Med, 1992. **82**(298): p. 169-79.
98. Barlow, C., et al., *Loss of the ataxia-telangiectasia gene product causes oxidative damage in target organs.* Proc Natl Acad Sci U S A, 1999. **96**(17): p. 9915-9.

99. Elson, A., et al., *Pleiotropic defects in ataxia-telangiectasia protein-deficient mice.* Proc Natl Acad Sci U S A, 1996. **93**(23): p. 13084-9.
100. Xu, Y. and D. Baltimore, *Dual roles of ATM in the cellular response to radiation and in cell growth control.* Genes Dev, 1996. **10**(19): p. 2401-10.
101. Chen, P., et al., *Oxidative stress is responsible for deficient survival and dendritogenesis in purkinje neurons from ataxia-telangiectasia mutated mutant mice.* J Neurosci, 2003. **23**(36): p. 11453-60.
102. Lin, C.H., et al., *Child with ataxia telangiectasia developing acute myeloid leukemia.* J Clin Oncol, 2010. **28**(14): p. e213-4.
103. Kanazawa, I., *How do neurons die in neurodegenerative diseases?* Trends Mol Med, 2001. **7**(8): p. 339-44.
104. Watters, D.J., *Oxidative stress in ataxia telangiectasia.* Redox Rep, 2003. **8**(1): p. 23-9.
105. Kim, J. and P.K. Wong, *Loss of ATM impairs proliferation of neural stem cells through oxidative stress-mediated p38 MAPK signaling.* Stem Cells, 2009. **27**(8): p. 1987-98.
106. Iourov, I.Y., et al., *Increased chromosome instability dramatically disrupts neural genome integrity and mediates cerebellar degeneration in the ataxia-telangiectasia brain.* Hum Mol Genet, 2009. **18**(14): p. 2656-69.
107. Tian, B., Q. Yang, and Z. Mao, *Phosphorylation of ATM by Cdk5 mediates DNA damage signalling and regulates neuronal death.* Nat Cell Biol, 2009. **11**(2): p. 211-8.
108. Soares, H.D., J.I. Morgan, and P.J. McKinnon, *Atm expression patterns suggest a contribution from the peripheral nervous system to the phenotype of ataxia-telangiectasia.* Neuroscience, 1998. **86**(4): p. 1045-54.
109. Hensey, C., K. Robertson, and J. Gautier, *Expression and subcellular localization of X-ATM during early Xenopus development.* Dev Genes Evol, 2000. **210**(8-9): p. 467-9.
110. Allen, D.M., et al., *Ataxia telangiectasia mutated is essential during adult neurogenesis.* Genes Dev, 2001. **15**(5): p. 554-66.
111. Khanna, K.K., et al., *Defective signaling through the B cell antigen receptor in Epstein-Barr virus-transformed ataxia-telangiectasia cells.* J Biol Chem, 1997. **272**(14): p. 9489-95.
112. Chiesa, N., et al., *Atm-deficient mice Purkinje cells show age-dependent defects in calcium spike bursts and calcium currents.* Neuroscience, 2000. **96**(3): p. 575-83.
113. Valentin-Vega, Y.A., et al., *Mitochondrial dysfunction in ataxia-telangiectasia.* Blood, 2012. **119**(6): p. 1490-500.
114. Mukherjee, R. and O. Chakrabarti, *Mitochondrial Quality Control: Decommissioning Power Plants in Neurodegenerative Diseases.* ScientificWorldJournal, 2013. **2013**: p. 180759.
115. Pinto, M. and C.T. Moraes, *Mitochondrial genome changes and neurodegenerative diseases.* Biochim Biophys Acta, 2013.
116. Eaton, J.S., et al., *Ataxia-telangiectasia mutated kinase regulates ribonucleotide reductase and mitochondrial homeostasis.* J Clin Invest, 2007. **117**(9): p. 2723-34.
117. Tao, O., et al., *Efficient generation of mature cerebellar Purkinje cells from mouse embryonic stem cells.* J Neurosci Res, 2010. **88**(2): p. 234-47.
118. Miyawaki, S., et al., *Sphingomyelinosis, a new mutation in the mouse: a model of Niemann-Pick disease in humans.* J Hered, 1982. **73**(4): p. 257-63.

119. Fatemi, S.H., et al., *Purkinje cell size is reduced in cerebellum of patients with autism.* Cell Mol Neurobiol, 2002. **22**(2): p. 171-5.
120. Nordborg, C., E. Ben-Menachem, and M. Kyllerman, *Neurovascular microdysgenesis in a case of Unverricht-Lundborg's disease.* Epilepsy Res, 1992. **13**(2): p. 121-7.
121. Yang, Q., et al., *Morphological Purkinje cell changes in spinocerebellar ataxia type 6.* Acta Neuropathol, 2000. **100**(4): p. 371-6.
122. Zhang, Y., et al., *Loss of Purkinje cells in the PKCgamma H101Y transgenic mouse.* Biochem Biophys Res Commun, 2009. **378**(3): p. 524-8.
123. Tomomura, M., et al., *Purification of Purkinje cells by fluorescence-activated cell sorting from transgenic mice that express green fluorescent protein.* Eur J Neurosci, 2001. **14**(1): p. 57-63.
124. Baptista, C.A., et al., *Cell-cell interactions influence survival and differentiation of purified Purkinje cells in vitro.* Neuron, 1994. **12**(2): p. 243-60.
125. Gatti, R.A. and H.V. Vinters, *Cerebellar pathology in ataxia-telangiectasia: the significance of basket cells.* Kroc Found Ser, 1985. **19**: p. 225-32.
126. Vinters, H.V., R.A. Gatti, and P. Rakic, *Sequence of cellular events in cerebellar ontogeny relevant to expression of neuronal abnormalities in ataxia-telangiectasia.* Kroc Found Ser, 1985. **19**: p. 233-55.
127. Swanson, G.T. and A. Contractor, *Recording in the cerebellar slice.* Curr Protoc Neurosci, 2004. **Chapter 6**: p. Unit 6 18.
128. Nakamura, H., T. Sato, and A. Suzuki-Hirano, *Isthmus organizer for mesencephalon and metencephalon.* Dev Growth Differ, 2008. **50 Suppl 1**: p. S113-8.
129. Wilson, L. and M. Maden, *The mechanisms of dorsoventral patterning in the vertebrate neural tube.* Dev Biol, 2005. **282**(1): p. 1-13.
130. Su, H.L., et al., *Generation of cerebellar neuron precursors from embryonic stem cells.* Dev Biol, 2006. **290**(2): p. 287-96.
131. Erceg, S., et al., *Efficient differentiation of human embryonic stem cells into functional cerebellar-like cells.* Stem Cells Dev, 2010. **19**(11): p. 1745-56.
132. Eggan, K., *Picking the lock on pluripotency.* N Engl J Med, 2013. **369**(22): p. 2150-1.
133. Sommer, C.A., et al., *Induced pluripotent stem cell generation using a single lentiviral stem cell cassette.* Stem Cells, 2009. **27**(3): p. 543-9.
134. Plath, K. and W.E. Lowry, *Progress in understanding reprogramming to the induced pluripotent state.* Nat Rev Genet, 2011. **12**(4): p. 253-65.
135. Polo, J.M., et al., *A molecular roadmap of reprogramming somatic cells into iPS cells.* Cell, 2012. **151**(7): p. 1617-32.
136. Schubert, R., J. Reichenbach, and S. Zielen, *Growth factor deficiency in patients with ataxia telangiectasia.* Clin Exp Immunol, 2005. **140**(3): p. 517-9.
137. Nishino, K., et al., *DNA methylation dynamics in human induced pluripotent stem cells over time.* PLoS Genet, 2010. **7**(5): p. e1002085.
138. Zhou, W., et al., *Higher methylation in genomic DNA indicates incomplete reprogramming in induced pluripotent stem cells.* Cell Reprogram, 2013. **15**(1): p. 92-9.
139. Kim, K., et al., *Epigenetic memory in induced pluripotent stem cells.* Nature, 2010. **467**(7313): p. 285-90.
140. Luong, M.X., et al., *A call for standardized naming and reporting of human ESC and iPSC lines.* Cell Stem Cell, 2011. **8**(4): p. 357-9.

141. Luong, M.X., et al., *A call for standardized naming and reporting of human ESC and iPSC lines.* Cell Stem Cell, 2010. **8**(4): p. 357-9.
142. Houldsworth, J. and M.F. Lavin, *Effect of ionizing radiation on DNA synthesis in ataxia telangiectasia cells.* Nucleic Acids Res, 1980. **8**(16): p. 3709-20.
143. Marion, R.M., et al., *Telomeres acquire embryonic stem cell characteristics in induced pluripotent stem cells.* Cell Stem Cell, 2009. **4**(2): p. 141-54.
144. Vaziri, H., *Critical telomere shortening regulated by the ataxia-telangiectasia gene acts as a DNA damage signal leading to activation of p53 protein and limited life-span of human diploid fibroblasts. A review.* Biochemistry (Mosc), 1997. **62**(11): p. 1306-10.
145. Pandita, T.K., *ATM function and telomere stability.* Oncogene, 2002. **21**(4): p. 611-8.
146. Briggs, J.A., et al., *Integration-free induced pluripotent stem cells model genetic and neural developmental features of down syndrome etiology.* Stem Cells, 2013. **31**(3): p. 467-78.
147. Nayler, S., et al., *Induced pluripotent stem cells from ataxia-telangiectasia recapitulate the cellular phenotype.* Stem Cells Transl Med, 2012. **1**(7): p. 523-35.
148. Gatei, M., et al., *ATM protein-dependent phosphorylation of Rad50 protein regulates DNA repair and cell cycle control.* J Biol Chem, 2011. **286**(36): p. 31542-56.
149. Hans, F. and S. Dimitrov, *Histone H3 phosphorylation and cell division.* Oncogene, 2001. **20**(24): p. 3021-7.
150. Parra, I. and B. Windle, *High resolution visual mapping of stretched DNA by fluorescent hybridization.* Nat Genet, 1993. **5**(1): p. 17-21.
151. Gatei, M., et al., *ATM-dependent phosphorylation of RAD50 regulates DNA repair and cell cycle control.* J Biol Chem, 2011.
152. Du, P., W.A. Kibbe, and S.M. Lin, *lumi: a pipeline for processing Illumina microarray.* Bioinformatics, 2008. **24**(13): p. 1547-8.
153. Benjamini, Y. and Y. Hochberg, *Controlling the False Discovery Rate - a Practical and Powerful Approach to Multiple Testing.* Journal of the Royal Statistical Society Series B-Methodological, 1995. **57**(1): p. 289-300.
154. Muller, F.J., et al., *Regulatory networks define phenotypic classes of human stem cell lines.* Nature, 2008. **455**(7211): p. 401-5.
155. Mar, J.C., et al., *attract: A method for identifying core pathways that define cellular phenotypes.* PLoS One, 2011. **6**(10): p. e25445.
156. Kanehisa, M., et al., *The KEGG resource for deciphering the genome.* Nucleic Acids Res, 2004. **32**(Database issue): p. D277-80.
157. Kozlov, S.V., et al., *Autophosphorylation and ATM activation: additional sites add to the complexity.* J Biol Chem, 2011. **286**(11): p. 9107-19.
158. van Veelen, L.R., et al., *Analysis of ionizing radiation-induced foci of DNA damage repair proteins.* Mutat Res, 2005. **574**(1-2): p. 22-33.
159. Bensimon, A., et al., *ATM-dependent and -independent dynamics of the nuclear phosphoproteome after DNA damage.* Sci Signal, 2010. **3**(151): p. rs3.
160. Bensimon, A., R. Aebersold, and Y. Shiloh, *Beyond ATM: the protein kinase landscape of the DNA damage response.* FEBS Lett, 2011. **585**(11): p. 1625-39.
161. Pagliarini, D.J., et al., *A mitochondrial protein compendium elucidates complex I disease biology.* Cell, 2008. **134**(1): p. 112-23.

162. Lim, J., et al., *A protein-protein interaction network for human inherited ataxias and disorders of Purkinje cell degeneration.* Cell, 2006. **125**(4): p. 801-14.
163. McKinnon, P.J. and L.A. Burgoyne, *Altered cellular morphology and microfilament array in ataxia-telangiectasia fibroblasts.* Eur J Cell Biol, 1985. **39**(1): p. 161-6.
164. Ozair, M.Z., et al., *SMAD7 directly converts human embryonic stem cells to telencephalic fate by a default mechanism.* Stem Cells, 2013. **31**(1): p. 35-47.
165. Tesseur, I., et al., *Deficiency in neuronal TGF-beta signaling promotes neurodegeneration and Alzheimer's pathology.* J Clin Invest, 2006. **116**(11): p. 3060-9.
166. Das, P. and T. Golde, *Dysfunction of TGF-beta signaling in Alzheimer's disease.* J Clin Invest, 2006. **116**(11): p. 2855-7.
167. Chen, P.C., et al., *Identification of ataxia telangiectasia heterozygotes, a cancer prone population.* Nature, 1978. **274**(5670): p. 484-6.
168. Taylor, A.M., et al., *Ataxia telangiectasia: a human mutation with abnormal radiation sensitivity.* Nature, 1975. **258**(5534): p. 427-9.
169. Morgan, S.E. and M.B. Kastan, *p53 and ATM: cell cycle, cell death, and cancer.* Adv Cancer Res, 1997. **71**: p. 1-25.
170. Biton, S., et al., *ATM-mediated response to DNA double strand breaks in human neurons derived from stem cells.* DNA Repair (Amst), 2007. **6**(1): p. 128-34.
171. Rashi-Elkeles, S., et al., *Parallel induction of ATM-dependent pro- and antiapoptotic signals in response to ionizing radiation in murine lymphoid tissue.* Oncogene, 2006. **25**(10): p. 1584-92.
172. Lee, S.A., A. Dritschilo, and M. Jung, *Role of ATM in oxidative stress-mediated c-Jun phosphorylation in response to ionizing radiation and CdCl2.* J Biol Chem, 2001. **276**(15): p. 11783-90.
173. Chen, K., et al., *Activation of p53 by oxidative stress involves platelet-derived growth factor-beta receptor-mediated ataxia telangiectasia mutated (ATM) kinase activation.* J Biol Chem, 2003. **278**(41): p. 39527-33.
174. Bruno, T., et al., *Che-1 activates XIAP expression in response to DNA damage.* Cell Death Differ, 2008. **15**(3): p. 515-20.
175. Macaulay, V.M., et al., *Downregulation of the type 1 insulin-like growth factor receptor in mouse melanoma cells is associated with enhanced radiosensitivity and impaired activation of Atm kinase.* Oncogene, 2001. **20**(30): p. 4029-40.
176. Glatz, C., et al., *Mutation in the mitochondrial tRNA(Val) causes mitochondrial encephalopathy, lactic acidosis and stroke-like episodes.* Mitochondrion, 2003. **11**(4): p. 615-9.
177. Cotan, D., et al., *Secondary coenzyme Q10 deficiency triggers mitochondria degradation by mitophagy in MELAS fibroblasts.* FASEB J, 2011. **25**(8): p. 2669-87.
178. Nakamura, M., et al., *MERRF/MELAS overlap syndrome: a double pathogenic mutation in mitochondrial tRNA genes.* J Med Genet, 2011. **47**(10): p. 659-64.
179. Yalcin, S., et al., *Foxo3 is essential for the regulation of ataxia telangiectasia mutated and oxidative stress-mediated homeostasis of hematopoietic stem cells.* J Biol Chem, 2008. **283**(37): p. 25692-705.
180. Wang, S.C., et al., *Inactivation of ataxia telangiectasia mutated gene can increase intracellular reactive oxygen species levels and alter radiation-induced cell death pathways in human glioma cells.* Int J Radiat Biol, 2011. **87**(4): p. 432-42.

181. Hrvatin, S., et al., *MARIS: method for analyzing RNA following intracellular sorting.* PLoS One, 2014. **9**(3): p. e89459.
182. Liu, W., et al., *Mitochondrial metabolism transition cooperates with nuclear reprogramming during induced pluripotent stem cell generation.* Biochem Biophys Res Commun, 2013. **431**(4): p. 767-71.
183. Bottini, A.R., et al., *Heterotopic Purkinje cells in ataxia-telangiectasia.* Neuropathology, 2011. **32**(1): p. 23-9.
184. Verhagen, M.M., et al., *Neuropathology in classical and variant ataxia-telangiectasia.* Neuropathology, 2012. **32**(3): p. 234-44.
185. Larnaout, A., et al., *Atypical ataxia telangiectasia with early childhood lower motor neuron degeneration: a clinicopathological observation in three siblings.* J Neurol, 1998. **245**(4): p. 231-5.
186. Agamanolis, D.P. and J.I. Greenstein, *Ataxia-telangiectasia. Report of a case with Lewy bodies and vascular abnormalities within cerebral tissue.* J Neuropathol Exp Neurol, 1979. **38**(5): p. 475-89.
187. Barlow, C., et al., *Atm-deficient mice: a paradigm of ataxia telangiectasia.* Cell, 1996. **86**(1): p. 159-71.
188. Spring, K., et al., *Atm knock-in mice harboring an in-frame deletion corresponding to the human ATM 7636del9 common mutation exhibit a variant phenotype.* Cancer Res, 2001. **61**(11): p. 4561-8.
189. Borghesani, P.R., et al., *Abnormal development of Purkinje cells and lymphocytes in Atm mutant mice.* Proc Natl Acad Sci U S A, 2000. **97**(7): p. 3336-41.
190. Carlessi, L., et al., *DNA-damage response, survival and differentiation in vitro of a human neural stem cell line in relation to ATM expression.* Cell Death Differ, 2009. **16**(6): p. 795-806.
191. Coufal, N.G., et al., *Ataxia telangiectasia mutated (ATM) modulates long interspersed element-1 (L1) retrotransposition in human neural stem cells.* Proc Natl Acad Sci U S A, 2011. **108**(51): p. 20382-7.
192. Lee, Y., et al., *ATR maintains select progenitors during nervous system development.* EMBO J, 2012. **31**(5): p. 1177-89.
193. Girard, M., et al., *Mitochondrial dysfunction and Purkinje cell loss in autosomal recessive spastic ataxia of Charlevoix-Saguenay (ARSACS).* Proc Natl Acad Sci U S A, 2012. **109**(5): p. 1661-6.
194. Patel, A.Y., et al., *Ataxia telangiectasia mutated influences cytochrome c oxidase activity.* Biochem Biophys Res Commun, 2011. **405**(4): p. 599-603.
195. Fu, X., et al., *Etoposide induces ATM-dependent mitochondrial biogenesis through AMPK activation.* PLoS One, 2008. **3**(4): p. e2009.
196. Lee, P., et al., *SMRT compounds abrogate cellular phenotypes of ataxia telangiectasia in neural derivatives of patient-specific hiPSCs.* Nat Commun, 2013. **4**: p. 1824.
197. Fernandez-Gomez, F.J., et al., *Involvement of mitochondrial potential and calcium buffering capacity in minocycline cytoprotective actions.* Neuroscience, 2005. **133**(4): p. 959-67.
198. Komuro, H. and T. Kumada, *Ca2+ transients control CNS neuronal migration.* Cell Calcium, 2005. **37**(5): p. 387-93.

199. Pivovarova, N.B. and S.B. Andrews, *Calcium-dependent mitochondrial function and dysfunction in neurons.* FEBS J, 2010. **277**(18): p. 3622-36.
200. Hongpaisan, J., C.A. Winters, and S.B. Andrews, *Strong calcium entry activates mitochondrial superoxide generation, upregulating kinase signaling in hippocampal neurons.* J Neurosci, 2004. **24**(48): p. 10878-87.
201. Hagenston, A.M. and H. Bading, *Calcium signaling in synapse-to-nucleus communication.* Cold Spring Harb Perspect Biol, 2011. **3**(11): p. a004564.
202. Jankowski, J., et al., *Cell death as a regulator of cerebellar histogenesis and compartmentation.* Cerebellum, 2010. **10**(3): p. 373-92.
203. Cross, J.L., et al., *Modes of Neuronal Calcium Entry and Homeostasis following Cerebral Ischemia.* Stroke Res Treat, 2010. **2010**: p. 316862.
204. Mattson, M.P. and S.L. Chan, *Neuronal and glial calcium signaling in Alzheimer's disease.* Cell Calcium, 2003. **34**(4-5): p. 385-97.
205. Kofuji, P., et al., *Functional analysis of the weaver mutant GIRK2 K+ channel and rescue of weaver granule cells.* Neuron, 1996. **16**(5): p. 941-52.
206. Kim, D.S., et al., *Robust enhancement of neural differentiation from human ES and iPS cells regardless of their innate difference in differentiation propensity.* Stem Cell Rev, 2010. **6**(2): p. 270-81.
207. Vetter, I. and R.J. Lewis, *Characterization of endogenous calcium responses in neuronal cell lines.* Biochem Pharmacol, 2011. **79**(6): p. 908-20.
208. Morizane, A., et al., *Small-molecule inhibitors of bone morphogenic protein and activin/nodal signals promote highly efficient neural induction from human pluripotent stem cells.* J Neurosci Res, 2011.
209. Yuan, S.H., et al., *Cell-surface marker signatures for the isolation of neural stem cells, glia and neurons derived from human pluripotent stem cells.* PLoS One, 2011. **6**(3): p. e17540.
210. Jakob, T.F., *[Stimulation-dependent gene expression in the central auditory system]*. HNO, 2011. **59**(3): p. 230-8.
211. Suberbielle, E., et al., *Physiologic brain activity causes DNA double-strand breaks in neurons, with exacerbation by amyloid-beta.* Nat Neurosci, 2013. **16**(5): p. 613-21.
212. Carlessi, L., et al., *ATM-deficient human neural stem cells as an in vitro model system to study neurodegeneration.* DNA Repair (Amst), 2013. **12**(8): p. 605-11.
213. Lorenzon, N.M., et al., *Altered calcium channel currents in Purkinje cells of the neurological mutant mouse leaner.* J Neurosci, 1998. **18**(12): p. 4482-9.
214. Liu, J., et al., *Deranged calcium signaling and neurodegeneration in spinocerebellar ataxia type 2.* J Neurosci, 2009. **29**(29): p. 9148-62.
215. Levine-Small, N., et al., *Reduced synchronization persistence in neural networks derived from atm-deficient mice.* Front Neurosci, 2011. **5**: p. 46.
216. Siddoway, B., et al., *Synaptic activity bidirectionally regulates a novel sequence-specific S-Q phosphoproteome in neurons.* J Neurochem, 2013.
217. Ma, N., et al., *TALEN-mediated gene correction in integration-free beta-thalassemia iPSCs.* J Biol Chem, 2013.
218. Horii, T., et al., *Generation of an ICF Syndrome Model by Efficient Genome Editing of Human Induced Pluripotent Stem Cells Using the CRISPR System.* Int J Mol Sci, 2013. **14**(10): p. 19774-81.

219. Wichterle, H., et al., *Directed differentiation of embryonic stem cells into motor neurons.* Cell, 2002. **110**(3): p. 385-97.
220. Muguruma, K., et al., *Ontogeny-recapitulating generation and tissue integration of ES cell-derived Purkinje cells.* Nat Neurosci, 2010. **13**(10): p. 1171-80.
221. Muller, F. and R. O'Rahilly, *The human brain at stages 21-23, with particular reference to the cerebral cortical plate and to the development of the cerebellum.* Anat Embryol (Berl), 1990. **182**(4): p. 375-400.
222. Gonzalez-Burgos, I. and M. Alejandre-Gomez, *Cerebellar granule cell and Bergmann glial cell maturation in the rat is disrupted by pre- and post-natal exposure to moderate levels of ethanol.* Int J Dev Neurosci, 2005. **23**(4): p. 383-8.
223. Chi, C.L., et al., *The isthmic organizer signal FGF8 is required for cell survival in the prospective midbrain and cerebellum.* Development, 2003. **130**(12): p. 2633-44.
224. Ye, W., et al., *FGF and Shh signals control dopaminergic and serotonergic cell fate in the anterior neural plate.* Cell, 1998. **93**(5): p. 755-66.
225. Segal, R.A., S.L. Pomeroy, and C.D. Stiles, *Axonal growth and fasciculation linked to differential expression of BDNF and NT3 receptors in developing cerebellar granule cells.* J Neurosci, 1995. **15**(7 Pt 1): p. 4970-81.
226. Sadakata, T., et al., *The secretory granule-associated protein CAPS2 regulates neurotrophin release and cell survival.* J Neurosci, 2004. **24**(1): p. 43-52.
227. Marshall, H., et al., *Retinoids and Hox genes.* FASEB J, 1996. **10**(9): p. 969-78.
228. Folberg, A., et al., *RARbeta mediates the response of Hoxd4 and Hoxb4 to exogenous retinoic acid.* Dev Dyn, 1999. **215**(2): p. 96-107.
229. Salero, E. and M.E. Hatten, *Differentiation of ES cells into cerebellar neurons.* Proc Natl Acad Sci U S A, 2007. **104**(8): p. 2997-3002.
230. Hashimoto, M. and M. Hibi, *Development and evolution of cerebellar neural circuits.* Dev Growth Differ, 2012. **54**(3): p. 373-89.
231. Andrews, S., *FastQC: A Quality Control tool for High Throughput Sequence Data*. 2012.
232. Li, H. and R. Durbin, *Fast and accurate short read alignment with Burrows-Wheeler transform.* Bioinformatics, 2009. **25**(14): p. 1754-1760.
233. Li, H., et al., *The Sequence Alignment/Map format and SAMtools.* Bioinformatics, 2009. **25**(16): p. 2078-2079.
234. Katz, Y., et al., *Analysis and design of RNA sequencing experiments for identifying isoform regulation.* Nature Methods, 2010. **7**(12): p. 1009-1015.
235. Kim, D., et al., *TopHat2: accurate alignment of transcriptomes in the presence of insertions, deletions and gene fusions.* Genome Biology, 2013. **14**(4): p. R36.
236. Harrow, J., et al., *GENCODE: The reference human genome annotation for The ENCODE Project.* Genome Research, 2012. **22**(9): p. 1760-1774.
237. Anders, S., *HTSeq: Analysing high-throughput sequencing data with Python*. 2010.
238. Team, R.C., *R: A Language and Environment for Statistical Computing*. 2009: Vienna, Austria}.
239. Robinson, M.D., D.J. McCarthy, and G.K. Smyth, *edgeR: a Bioconductor package for differential expression analysis of digital gene expression data.* Bioinformatics, 2009. **26**(1): p. 139-140.
240. Anders, S. and W. Huber, *Differential expression analysis for sequence count data.* Genome Biology, 2010. **11**(10): p. R106.

241. Suzuki, R. and H. Shimodaira, *Pvclust: An R package for assessing the uncertainty in hierarchical clustering.* Bioinformatics, 2006. **22**(12): p. 1540-1542.
242. Li, C.J., et al., *Pathway analysis identifies perturbation of genetic networks induced by butyrate in a bovine kidney epithelial cell line.* Funct Integr Genomics, 2007. **7**(3): p. 193-205.
243. Huang, D.W., B.T. Sherman, and R.A. Lempicki, *Systematic and integrative analysis of large gene lists using DAVID bioinformatics resources.* Nature Protocols, 2009. **4**(1): p. 44-57.
244. Sato, T., A.L. Joyner, and H. Nakamura, *How does Fgf signaling from the isthmic organizer induce midbrain and cerebellum development?* Dev Growth Differ, 2004. **46**(6): p. 487-94.
245. Gould, A., et al., *Positive cross-regulation and enhancer sharing: two mechanisms for specifying overlapping Hox expression patterns.* Genes Dev, 1997. **11**(7): p. 900-13.
246. Zhang, Q., et al., *Expression and functional characterization of LRRC4, a novel brain-specific member of the LRR superfamily.* FEBS Lett, 2005. **579**(17): p. 3674-82.
247. Kikyo, N., et al., *Genetic and functional analysis of neuronatin in mice with maternal or paternal duplication of distal Chr 2.* Dev Biol, 1997. **190**(1): p. 66-77.
248. Benevolenskaya, E.V., et al., *Binding of pRB to the PHD protein RBP2 promotes cellular differentiation.* Mol Cell, 2005. **18**(6): p. 623-35.
249. Xia, C., et al., *Identification of a prostate-specific G-protein coupled receptor in prostate cancer.* Oncogene, 2001. **20**(41): p. 5903-7.
250. White, J.J. and R.V. Sillitoe, *Development of the cerebellum: from gene expression patterns to circuit maps.* Wiley Interdiscip Rev Dev Biol, 2012. **2**(1): p. 149-64.
251. Katoh, M., *Integrative genomic analyses on HES/HEY family: Notch-independent HES1, HES3 transcription in undifferentiated ES cells, and Notch-dependent HES1, HES5, HEY1, HEY2, HEYL transcription in fetal tissues, adult tissues, or cancer.* Int J Oncol, 2007. **31**(2): p. 461-6.
252. Scerbo, P., et al., *Ventx factors function as Nanog-like guardians of developmental potential in Xenopus.* PLoS One, 2012. **7**(5): p. e36855.
253. Pan, G., et al., *A negative feedback loop of transcription factors that controls stem cell pluripotency and self-renewal.* FASEB J, 2006. **20**(10): p. 1730-2.
254. des Portes, V., et al., *A novel CNS gene required for neuronal migration and involved in X-linked subcortical laminar heterotopia and lissencephaly syndrome.* Cell, 1998. **92**(1): p. 51-61.
255. Wang, W., et al., *Nuclear factor I coordinates multiple phases of cerebellar granule cell development via regulation of cell adhesion molecules.* J Neurosci, 2007. **27**(23): p. 6115-27.
256. Krumlauf, R., *Hox genes in vertebrate development.* Cell, 1994. **78**(2): p. 191-201.
257. Eddison, M., et al., *Segmental identity and cerebellar granule cell induction in rhombomere 1.* BMC Biol, 2004. **2**: p. 14.
258. Peeters, R.P., et al., *Cerebellar abnormalities in mice lacking type 3 deiodinase and partial reversal of phenotype by deletion of thyroid hormone receptor alpha1.* Endocrinology, 2013. **154**(1): p. 550-61.
259. Saito, S.Y. and H. Takeshima, *DNER as key molecule for cerebellar maturation.* Cerebellum, 2006. **5**(3): p. 227-31.

260. Tohgo, A., et al., *Impaired cerebellar functions in mutant mice lacking DNER.* Mol Cell Neurosci, 2006. **31**(2): p. 326-33.
261. Kim, D. and S.L. Ackerman, *The UNC5C netrin receptor regulates dorsal guidance of mouse hindbrain axons.* J Neurosci, 2011. **31**(6): p. 2167-79.
262. Vervoort, V.S., et al., *AGTR2 mutations in X-linked mental retardation.* Science, 2002. **296**(5577): p. 2401-3.
263. Aruga, J., et al., *Mouse Zic1 is involved in cerebellar development.* J Neurosci, 1998. **18**(1): p. 284-93.
264. Hirai, H., et al., *Cbln1 is essential for synaptic integrity and plasticity in the cerebellum.* Nat Neurosci, 2005. **8**(11): p. 1534-41.
265. Li, J.Y., Z. Lao, and A.L. Joyner, *Changing requirements for Gbx2 in development of the cerebellum and maintenance of the mid/hindbrain organizer.* Neuron, 2002. **36**(1): p. 31-43.
266. Luu, B., D. Ellisor, and M. Zervas, *The lineage contribution and role of Gbx2 in spinal cord development.* PLoS One, 2011. **6**(6): p. e20940.
267. Ha, T.J., et al., *Genome-wide microarray comparison reveals downstream genes of Pax6 in the developing mouse cerebellum.* Eur J Neurosci, 2012. **36**(7): p. 2888-98.
268. Miyata, T., et al., *Migration, early axonogenesis, and Reelin-dependent layer-forming behavior of early/posterior-born Purkinje cells in the developing mouse lateral cerebellum.* Neural Dev, 2010. **5**: p. 23.
269. Vaillant, C. and D. Monard, *SHH pathway and cerebellar development.* Cerebellum, 2009. **8**(3): p. 291-301.
270. Zhang, L., et al., *Hepatocyte growth factor protects cultured rat cerebellar granule neurons from apoptosis via the phosphatidylinositol-3 kinase/Akt pathway.* J Neurosci Res, 2000. **59**(4): p. 489-96.
271. Moriyama, M., et al., *Complement receptor 2 is expressed in neural progenitor cells and regulates adult hippocampal neurogenesis.* J Neurosci, 2011. **31**(11): p. 3981-9.
272. Seol, W., H.S. Choi, and D.D. Moore, *Isolation of proteins that interact specifically with the retinoid X receptor: two novel orphan receptors.* Mol Endocrinol, 1995. **9**(1): p. 72-85.
273. Hunt, C.P., et al., *DNA-Dependent Protein Kinase Is a Context Dependent Regulator of Lmx1a and Midbrain Specification.* PLoS One, 2013. **8**(10): p. e78759.
274. Nyati, M.K., et al., *Ataxia telangiectasia mutated down-regulates phospho-extracellular signal-regulated kinase 1/2 via activation of MKP-1 in response to radiation.* Cancer Res, 2006. **66**(24): p. 11554-9.
275. Kim, J. and P.K. Wong, *Oxidative stress is linked to ERK1/2-p16 signaling-mediated growth defect in ATM-deficient astrocytes.* J Biol Chem, 2009. **284**(21): p. 14396-404.
276. Rhodes, N., et al., *Defective potassium currents in ataxia telangiectasia fibroblasts.* Genes Dev, 1998. **12**(23): p. 3686-92.
277. Weng, Z., et al., *A DNA damage and stress inducible G protein-coupled receptor blocks cells in G2/M.* Proc Natl Acad Sci U S A, 1998. **95**(21): p. 12334-9.
278. Traynelis, S.F., et al., *Glutamate receptor ion channels: structure, regulation, and function.* Pharmacol Rev, 2010. **62**(3): p. 405-96.
279. Wey, A. and P.S. Knoepfler, *c-myc and N-myc promote active stem cell metabolism and cycling as architects of the developing brain.* Oncotarget, 2010. **1**(2): p. 120-30.

280. Guerra, L., et al., *Myc is required for activation of the ATM-dependent checkpoints in response to DNA damage.* PLoS One, 2010. **5**(1): p. e8924.
281. Xu, J., et al., *Sex-specific differences in expression of histone demethylases Utx and Uty in mouse brain and neurons.* J Neurosci, 2008. **28**(17): p. 4521-7.
282. Alagoz, M., et al., *ATM deficiency results in accumulation of DNA-topoisomerase I covalent intermediates in neural cells.* PLoS One, 2013. **8**(4): p. e58239.
283. Ben Hassine, S. and B. Arcangioli, *Tdp1 protects against oxidative DNA damage in non-dividing fission yeast.* EMBO J, 2009. **28**(6): p. 632-40.
284. Interthal, H., et al., *SCAN1 mutant Tdp1 accumulates the enzyme--DNA intermediate and causes camptothecin hypersensitivity.* EMBO J, 2005. **24**(12): p. 2224-33.
285. Geng, Y., et al., *p53 transcription-dependent and -independent regulation of cerebellar neural precursor cell apoptosis.* J Neuropathol Exp Neurol, 2007. **66**(1): p. 66-74.
286. Colucci-Guyon, E., et al., *Cerebellar defect and impaired motor coordination in mice lacking vimentin.* Glia, 1999. **25**(1): p. 33-43.
287. Gamper, A.M., et al., *ATM protein physically and functionally interacts with proliferating cell nuclear antigen to regulate DNA synthesis.* J Biol Chem, 2012. **287**(15): p. 12445-54.
288. Yang, Y. and K. Herrup, *Loss of neuronal cell cycle control in ataxia-telangiectasia: a unified disease mechanism.* J Neurosci, 2005. **25**(10): p. 2522-9.
289. Hardingham, G.E., F.J. Arnold, and H. Bading, *Nuclear calcium signaling controls CREB-mediated gene expression triggered by synaptic activity.* Nat Neurosci, 2001. **4**(3): p. 261-7.
290. Shi, Y., et al., *Direct regulation of CREB transcriptional activity by ATM in response to genotoxic stress.* Proc Natl Acad Sci U S A, 2004. **101**(16): p. 5898-903.
291. Fernandes, N.D., Y. Sun, and B.D. Price, *Activation of the kinase activity of ATM by retinoic acid is required for CREB-dependent differentiation of neuroblastoma cells.* J Biol Chem, 2007. **282**(22): p. 16577-84.
292. Wang, Y., et al., *Endogenous miRNA sponge lincRNA-RoR regulates Oct4, Nanog, and Sox2 in human embryonic stem cell self-renewal.* Dev Cell, 2013. **25**(1): p. 69-80.
293. Kretz, M., et al., *Suppression of progenitor differentiation requires the long noncoding RNA ANCR.* Genes Dev, 2012. **26**(4): p. 338-43.
294. Khodosevich, K., et al., *Connective tissue growth factor regulates interneuron survival and information processing in the olfactory bulb.* Neuron, 2013. **79**(6): p. 1136-51.
295. Lin, M., et al., *RNA-Seq of human neurons derived from iPS cells reveals candidate long non-coding RNAs involved in neurogenesis and neuropsychiatric disorders.* PLoS One, 2011. **6**(9): p. e23356.
296. Stein, U., et al., *Circulating MACC1 transcripts in colorectal cancer patient plasma predict metastasis and prognosis.* PLoS One, 2013. **7**(11): p. e49249.
297. Grote, P., et al., *The tissue-specific lncRNA Fendrr is an essential regulator of heart and body wall development in the mouse.* Dev Cell, 2013. **24**(2): p. 206-14.
298. Grote, P. and B.G. Herrmann, *The long non-coding RNA Fendrr links epigenetic control mechanisms to gene regulatory networks in mammalian embryogenesis.* RNA Biol, 2013. **10**(10).
299. Wysocka, J., et al., *WDR5 associates with histone H3 methylated at K4 and is essential for H3 K4 methylation and vertebrate development.* Cell, 2005. **121**(6): p. 859-72.

300. Waite, M.R., et al., *GABAergic and glutamatergic identities of developing midbrain Pitx2 neurons.* Dev Dyn, 2011. **240**(2): p. 333-46.
301. Waite, M.R., et al., *Pleiotropic and isoform-specific functions for Pitx2 in superior colliculus and hypothalamic neuronal development.* Mol Cell Neurosci, 2013. **52**: p. 128-39.
302. Idrees, F., et al., *A novel homeobox mutation in the PITX2 gene in a family with Axenfeld-Rieger syndrome associated with brain, ocular, and dental phenotypes.* Am J Med Genet B Neuropsychiatr Genet, 2006. **141B**(2): p. 184-91.
303. Kalinichenko, V.V., et al., *The forkhead box F1 transcription factor is expressed in brain and head mesenchyme during mouse embryonic development.* Gene Expr Patterns, 2003. **3**(2): p. 153-8.
304. Northcott, P.A., et al., *The miR-17/92 polycistron is up-regulated in sonic hedgehog-driven medulloblastomas and induced by N-myc in sonic hedgehog-treated cerebellar neural precursors.* Cancer Res, 2009. **69**(8): p. 3249-55.
305. Uziel, T., et al., *The miR-17~92 cluster collaborates with the Sonic Hedgehog pathway in medulloblastoma.* Proc Natl Acad Sci U S A, 2009. **106**(8): p. 2812-7.
306. Bian, S., et al., *MicroRNA cluster miR-17-92 regulates neural stem cell expansion and transition to intermediate progenitors in the developing mouse neocortex.* Cell Rep, 2013. **3**(5): p. 1398-406.
307. Smrt, R.D., et al., *MicroRNA miR-137 regulates neuronal maturation by targeting ubiquitin ligase mind bomb-1.* Stem Cells, 2010. **28**(6): p. 1060-70.
308. Silber, J., et al., *miR-124 and miR-137 inhibit proliferation of glioblastoma multiforme cells and induce differentiation of brain tumor stem cells.* BMC Med, 2008. **6**: p. 14.
309. Berenguer, J., et al., *MicroRNA 22 regulates cell cycle length in cerebellar granular neuron precursors.* Mol Cell Biol, 2013. **33**(14): p. 2706-17.
310. Jovicic, A., et al., *MicroRNA-22 (miR-22) overexpression is neuroprotective via general anti-apoptotic effects and may also target specific Huntington's disease-related mechanisms.* PLoS One, 2013. **8**(1): p. e54222.
311. Hebert, S.S., et al., *Loss of microRNA cluster miR-29a/b-1 in sporadic Alzheimer's disease correlates with increased BACE1/beta-secretase expression.* Proc Natl Acad Sci U S A, 2008. **105**(17): p. 6415-20.
312. Tam Tam, S., et al., *MicroRNA-143 expression in dorsal root ganglion neurons.* Cell Tissue Res, 2011. **346**(2): p. 163-73.
313. Kajiwara, M., et al., *Donor-dependent variations in hepatic differentiation from human-induced pluripotent stem cells.* Proc Natl Acad Sci U S A, 2012. **109**(31): p. 12538-43.
314. Klisch, T.J., et al., *In vivo Atoh1 targetome reveals how a proneural transcription factor regulates cerebellar development.* Proc Natl Acad Sci U S A, 2011. **108**(8): p. 3288-93.
315. Gazit, R., V. Krizhanovsky, and N. Ben-Arie, *Math1 controls cerebellar granule cell differentiation by regulating multiple components of the Notch signaling pathway.* Development, 2004. **131**(4): p. 903-13.
316. D'Souza, A.D., et al., *Reducing mitochondrial ROS improves disease-related pathology in a mouse model of ataxia-telangiectasia.* Mol Ther, 2012. **21**(1): p. 42-8.
317. West, A.E. and M.E. Greenberg, *Neuronal activity-regulated gene transcription in synapse development and cognitive function.* Cold Spring Harb Perspect Biol, 2011. **3**(6).